Inertial-Sensor-Based Control of Functional Electrical Stimulation for Paraplegic Cycling and Swimming

vorgelegt von
Dipl.-Ing., M.A.
Constantin Wiesener

an der Fakultät IV - Elektrotechnik und Informatik
der Technischen Universität Berlin
zur Erlangung des akademischen Grades
Doktor der Ingenieurwissenschaften
-Dr.-Ing.-
genehmigte Dissertation

Promotionsausschuss:
Vorsitzender: Prof. Dr. Benjamin Blankertz
Gutachter: Prof. Dr.-Ing. Jörg Raisch
Gutachterin: Univ. Prof. Dipl.-Ing. Dr. techn. Margit Gföhler
Gutachter: Dr.-Ing. Henrik Gollee
Tag der wissenschaftlichen Aussprache: 01. Oktober 2021

Berlin 2021

Abstract

The physical activity and health of people suffering from a spinal cord injury is severely limited due to the accompanying paralysis and often in stark contrast to the physical condition before the injury, especially in young patients. However, participation in sports and therapeutic activities can reduce secondary diseases and improve precisely the overall well-being of those affected. New therapy systems make it possible to produce functional movements by Functional Electrical Stimulation of the paralyzed muscles, thus enabling to perform sports activities.

In the first part of this thesis, a novel joint-angle-based stimulation pattern for cycling is presented. Using four inertial sensors attached to the upper and lower legs, knee-joint angles are estimated. The presented stimulation pattern maps the phases of knee-joint angle on the range of 0 to 100 % and activates the muscles for flexion and extension in the corresponding ranges. To reduce the effect of dynamic latency between stimulation onset and muscle response, a correction method was developed that shifts the stimulation pattern by a defined time delay based on the stimulation pattern of the preceding revolution, thus activating the corresponding muscles earlier. The resulting FES cycling system was verified in simulations at different seating positions using a computer model – pedaling could be successfully achieved for all situation using the joint-angle-based stimulation pattern without retuning. Subsequently, the developed algorithms were integrated into the Cybathlon-RehaBike of the Hasomed team. It was shown, that the same setting and stimulation pattern for stationary ergometer cycling can be used for mobile cycling. After 18 months of intensive training, our paraplegic pilot finished fourth in the FES cycling race of the Cybathlon competition with a new personal best time of 6 min 44 s over 750 m. The results show that the joint-angle-based stimulation pattern can be used for smooth and effective FES cycling. Wireless inertial sensors as well as a wearable stimulator are presented as a starting point for the transfer of the methods into cycling systems for home use.

The second part of this thesis presents a waterproof electrical stimulation system that enables paraplegics to perform swimming exercises with their own legs for the first time. A ten weeks exploratory study demonstrated that the application with reusable silicone electrodes is safe and can be performed independently by experienced paraplegic swimmers. The study results show that swimming speed is increased by the presented stimulation procedures. In addition, it was shown that by means of an inertial sensor attached to the swimmers back, the roll angle of the trunk can be used to control the stimulation of the knee extensor muscles, allowing a synchronization of the generated leg movement with the voluntary upper body movement during front crawl swimming. This enables a new hybrid form of therapy and rehabilitation for paraplegic patients, which facilitates physical activity with the impaired legs and intact arms.

Zusammenfassung

Die körperliche Aktivität und Gesundheit von Menschen, die unter einer Rückenmarksverletzung leiden, ist aufgrund der einhergehenden Lähmung stark eingeschränkt und steht oft im starken Kontrast zum Zustand vor der Verletzung, insbesondere bei jungen Patienten. Doch gerade durch sportliche und therapeutische Aktivitäten können Begleiterkrankungen reduziert und das psychische Wohlbefinden der Betroffenen gesteigert werden. Neue Therapiesysteme ermöglichen es durch gezielte Stimulation der gelähmten Muskulatur funktionelle Bewegungen zu erzeugen und so eine Teilnahme an sportlichen Aktivitäten zu ermöglichen.

Im ersten Teil dieser Arbeit wurde ein neuartiges gelenkwinkelbasiertes Stimulationsmuster für das Fahrradfahren mittels Elektrostimulation entwickelt. Anhand von vier an den Ober- und Unterschenkeln angebrachten Inertialsensoren werden die Kniegelenkwinkel bestimmt. Das darauf basierende Stimulationsmuster bildet die Phasen der Kniegelenksbewegung in einem Bereich von 0 bis 100 % ab und aktiviert die Muskeln für Flexion und Extension in festgelegten Bereichen. Um den Effekt der dynamischen Latenz zwischen Stimulationsbeginn und Muskelreaktion zu reduzieren, wurde eine Korrekturmethode entwickelt, die das Stimulationsmuster um eine definierte Zeit anhand des Winkelverlaufs des Tretzykluses verschiebt und so die entsprechenden Muskeln früher aktiviert. Das resultierende FES-Fahrradsystem wurde in Simulationen bei verschiedenen Sitzpositionen mit einem Computermodell verifiziert - in allen Fällen konnte erfolgreich eine Trittbewegung mit dem gelenkwinkelbasierten Stimulationsmuster ohne Anpassung generiert werden. Anschließend wurden die entwickelten Algorithmen im Cybathlon-RehaBike des Teams Hasomed integriert. Es konnte gezeigt werden, dass die Einstellungen und Stimulationsmuster für stationäres Ergometer-Radfahren auch für mobiles FES-Fahrradfahren verwendet werden konnten. Nach einem 18-monatigen intensiven Training belegte unser querschnittsgelähmter Pilot den vierten Platz beim FES Radrennen des Cybathlon-Wettkampfs mit einer neuen persönlichen Bestzeit von 6 min 44 s über 750 m. Es konnte anhand der Ergebnisse gezeigt werden, dass die auf Inertialsensoren basierende Gelenkwinkelschätzung für die Generierung einer gleichmäßigen und effektiven Trittbewegung beim FES-Radsport verwendet werden kann. Für die spätere Verwendung der entwickelten Methoden in Systemen für den Heimgebrauch werden drahtlose Inertialsensoren sowie ein tragbarer Stimulator als Grundlage vorgestellt.

Im zweiten Teil der Arbeit werden ein wasserdichtes Elektrostimulationssystem und Methoden vorgestellt, die es Querschnittsgelähmten erstmals ermöglichen, Schwimmen mit ihren eigenen gelähmten Beinen zusätzlich zu den Armbewegungen durchzuführen. In einer 10-wöchigen explorativen Studie konnte gezeigt werden, dass die Durchführung mit wiederverwendbaren Silikonelektroden sicher ist und von erfahrenen querschnittsgelähmten Schwimmern selbstständig realisiert werden kann. Die Studienergebnisse zeigen, dass die Schwimmgeschwindigkeit durch die präsentierten Stimulationsverfahren erhöht wurde. Darüber hinaus konnte gezeigt werden, dass mittels eines am Rücken angebrachten Inertialsensors der Rollwinkel des Rumpfes zur Steuerung der Stimulation der Kniestreckermuskulatur verwendet werden kann. Hierdurch wird eine Synchronisation der erzeugten Beinbewegung mit der willkürlichen Oberkörperbewegung beim Kraulschwimmen erreicht. Dies ermöglicht eine neuartige hybride Therapieform und Rehabilitationsmöglichkeit für querschnittsgelähmte Patienten, bei der die körperliche Aktivität durch die gleichzeitige Verwendung der betroffenen Beine und intakten Arme maximiert wird.

Acknowledgements

I am especially indebted to my supervisors Prof. Dr. Jörg Raisch and Dr. Thomas Schauer, for supporting and motivating me throughout the process and for discussing every part of my thesis in detail. I would also like to thank all of my colleagues from the Control Systems Group at Technische Universität Berlin, in particular Markus Valtin, Christina Salchow-Hömmen, Thomas Seel, Daniel Laidig, and Astrid Bergmann, for sharing their expertise and time to discuss solutions.

Besides, I would like to thank my former students, Stefan Ruppin, Ferdinand Heinrich, Leo Blankenfeld, Simon Schneider, Björn Grzywacz, Grace McLachlan as well as Lucy McConomy, for their valuable contributions.

Some parts of this study were conducted within the project RETRAINER funded by the European Union's Horizon 2020 program and within the project STIMSWIM-REHA, funded by the Department for Economics, Energy, and Public Enterprises of the Senate of Berlin. In this context, the clinical evaluation was made possible by Dr. Andreas Niedeggen from Unfallkrankenhaus Berlin and Dr. Nikolaus Wenger from the Charité Berlin. I am immensely grateful for their medical advice and for screening and recruiting suitable patients. I would also like to thank Axelgaard Manufacturing Co. Ltd. for generously donating the waterproof adhesive stimulation electrodes.

My deepest thanks go to my mother and my brothers and sisters, who always believed in me during all these times. I also would like to thank my dear friends who accompanied me along the way. In particular, the exchange, support, motivation, and inspiration of Hanno helped me through the long intense time of my dissertation. Finally, and above all, I would like to thank my wife, Kathleen, for her understanding and for taking care of our children on many weekends, as well as for her motivation and support whenever it was most needed.

Table of Contents

Title Page **i**

List of Figures **xiii**

List of Tables **xvii**

Abbreviations **xix**

Symbols **xxi**

1 Introduction **1**
- 1.1 Spinal Cord Injury . . . 1
- 1.2 Functional Electrical Stimulation . . . 4
- 1.3 Transcutaneous Spinal Cord Stimulation . . . 5
- 1.4 Rehabilitation of Paraplegia . . . 6
- 1.5 Outline of the Thesis . . . 7
- 1.6 Main Contributions of this Thesis . . . 8
- 1.7 Related Publications by the Author . . . 9
- 1.8 Related Theses Supervised by the Author . . . 11

2 Fundamentals of Inertial Measurement Units and Orientation Estimation **13**
- 2.1 Accelerometer . . . 13
- 2.2 Gyroscope . . . 14
- 2.3 Magnetometer . . . 15
- 2.4 Orientation Estimation Using Inertial Measurement Units . . . 15
  - 2.4.1 Quaternion Algebra . . . 15
  - 2.4.2 Orientation Estimation Method . . . 17

3 Joint-Angle-Based Functional Electrical Stimulation Cycling **21**
- 3.1 Overview . . . 21
- 3.2 State-of-the-Art in FES Cycling . . . 22
  - 3.2.1 FES Cycling Systems . . . 22
  - 3.2.2 Clinical Outcome of FES Cycling . . . 23
  - 3.2.3 Pattern Generation and Involved Sensors . . . 26
  - 3.2.4 Stimulated Muscle Groups . . . 27
- 3.3 Simulation Environment for FES Cycling . . . 27

3.3.1 Overview . . . 28
3.3.2 Muscle Activation and Joint-Moment Generation . . . 29
3.3.3 Mechanical Model of Cycling . . . 30
3.3.4 Virtual Inertial Measurement Unit . . . 31
3.4 Joint-Angle Estimation . . . 32
3.4.1 Segment-Inclination Estimation . . . 33
3.4.2 Evaluation of Segment-Inclination Estimation Using a Simulation Model . . . 34
3.4.3 Experimental Verification of IMU-Based Inclination Estimation . . . 36
3.4.4 Knee- and Hip-Joint-Angle Estimation . . . 38
3.5 Joint-Angle-Based Stimulation Pattern . . . 40
3.5.1 Joint-Angle Transformation . . . 40
3.5.2 Robust Discrimination of Leg Extension and Flexion Phases . . . 42
3.5.3 Stimulation Pattern . . . 44
3.5.4 Speed-Dependent Adaptation of the Stimulation Pattern . . . 47
3.6 Calculation of Crank Angle and Cadence . . . 48
3.7 Simulative Evaluation of the Knee-Joint-Angle-Based Stimulation Pattern . . . 51
3.8 Conclusions and Future Research . . . 54

4 The Cybathlon-RehaBike - Inertial-Sensor-Driven Mobile FES Cycling 57
4.1 Introduction . . . 57
4.2 Cycling Device . . . 59
4.3 Training and Cybathlon Results . . . 62
4.4 Discussion and Conclusion . . . 65

5 Hardware Development 67
5.1 Overview . . . 67
5.2 Wireless Orientation Measurement System . . . 67
5.2.1 State-of-the-Art Wireless Inertial Measurement Units . . . 68
5.2.2 Requirements Analysis and Sensor Architecture . . . 68
5.2.3 Orientation Estimation and EMC Test Results . . . 70
5.3 Current-Controlled Neuromuscular Stimulator . . . 73
5.3.1 State-of-the-Art Neuromuscular Stimulators . . . 75
5.3.2 Requirements Analysis and Stimulator Architecture . . . 75
5.3.3 Variable High-Voltage Generation . . . 76
5.3.4 Multiplexer . . . 77
5.3.5 Current Controller . . . 78
5.3.6 Software and Hardware Architecture . . . 79
5.3.7 Results . . . 81
5.4 Conclusions and Further Improvements . . . 83

6 FES Swimming Methods and Experimental Evaluation 87
6.1 Overview . . . 87
6.2 State-of-the-Art of Swimming and Aquatic Therapy in SCI Patients . . . 88
6.3 Methods . . . 89

6.3.1 Functional Electrical Stimulation Support . . . 90
6.3.2 Transcutaneous Spinal Cord Stimulation . . . 90
6.3.3 Experimental Setup . . . 91
6.3.3.1 Stimulator . . . 91
6.3.3.2 Waterproof Stimulation Electrodes . . . 92
6.3.4 Subjects, Training Protocol, and Outcome Measures . . . 94
6.3.5 IMU-Based Motion Analysis during Swimming . . . 95
6.4 Results . . . 99
6.5 Discussion . . . 102
6.6 Conclusions . . . 103

7 Inertial-Sensor-Triggered FES Swimming in Paraplegics 105
7.1 Overview . . . 105
7.2 Methods . . . 106
7.2.1 IMU-Triggered Stimulation System . . . 106
7.2.2 IMU-Based Motion Analysis . . . 107
7.2.3 IMU-Based Control of the Stimulation Timing . . . 109
7.3 Results . . . 111
7.4 Conclusion and Future Research . . . 118

8 General Conclusions and Outlook 121
8.1 General Conclusions on the Proposed FES Cycling Methods . . . 121
8.2 General Conclusions on the Proposed FES Swimming Methods . . . 122
8.3 Future Research . . . 123

References 125

Appendix A ASIA Impairment Scale (AIS) Questionnaire 137

Appendix B Proof: Hip Extension Always Follows Knee Extension in Cycling 139

Appendix C User Requirements Specifications for the Neuromuscular Stimulator 143

List of Figures

1.1 Spinal Cord of a human with injury. 2
1.2 Longitudinal organization of the spinal cord. 3
1.3 Different types of electrodes. 4
1.4 Biphasic stimulation pulses. 5
1.5 Rehabilitation process from dependence to independence. 6

2.1 Schematic of a simplified MEMS gyroscope and accelerometer. 14
2.2 World frame $\mathcal{E}$ and sensor frame $\mathcal{S}$. 15
2.3 Orientation estimation of an IMU. 18

3.1 Schematic of recumbent FES tricycle and stationary ergometer systems. 24
3.2 Stimulated muscle groups during FES cycling. 28
3.3 Simulation Model including muscle activity, joint moments, and mechanical model. . 29
3.4 Six-bar linkage model. 30
3.5 Sensor-to-leg attachment. 34
3.6 Segment-inclination estimation setting. 35
3.7 Simulated trajectory for heading α and inclination angle φ. 35
3.8 RMS of simulation of inclination-angle estimation. 36
3.9 Experimental setting for segment-inclination verification. 37
3.10 Comparison of optical and inertial measurement. 39
3.11 Lower limb geometry for joint-angle calculation. 40
3.12 Joint-angle signal processing. 41
3.13 Simplified linkage model. 43
3.14 Different phases during one cycle for the right-knee joint. 44
3.15 Crank-angle-driven stimulation pattern. 45
3.16 Simulated knee- and hip-joint angle for different seat-to-crank configurations. 45
3.17 The stimulation interval of the quadriceps and hamstring. 46
3.18 Speed adaptation comparison. 48
3.19 Comparison of the speed-adaptation methods. 49
3.20 Crank angle with optimization. 50
3.21 Cadence estimation with and without optimization. 51
3.22 Influence of crank-angle estimation with and without optimization. 52
3.23 Cycling simulation for the joint-angle-based approach. 53
3.24 Simulation of the starting phase and normal cycling with applied torque. 54

4.1 Description of the RehaBike. 59
4.2 Seat-elevation set of Hase Bikes Kettwiesel. 60
4.3 Chain and gear assembly of the RehaBike. 61
4.4 User interface of the RehaBike. 61
4.5 All mechanical, electronic, and body worn parts which compose the RehaBike. 62
4.6 Power output for exemplary 10 min training sessions. 64
4.7 The athlete during the Cybathlon race. 65

5.1 Piconet topology. 69
5.2 PCB of the developed IMU. 71
5.3 Block diagram of the developed IMU. 71
5.4 IMU sensor software architecture of the BMD300 module. 72
5.5 Comparison of optical and inertial measurement. 73
5.6 EMC test results for the sensor. 74
5.7 Hardware architecture of the neuromuscular stimulator. 76
5.8 High-voltage generation. 77
5.9 Internal schematic of the used multiplexer HV2801. 78
5.10 Characteristic curves for an exemplary n-Channel MOSFET. 79
5.11 PI-controller for low-side current control. 80
5.12 Flow chart for pulse generation. 81
5.13 Worst-case skin model for medical-device verification. 81
5.14 Efficiency of the high-voltage generation. 82
5.15 Voltage drop and ripple during stimulation. 82
5.16 Performance characteristics of the stimulation using a skin model. 83
5.17 60601-2-10:2012 EMC test procedure. 84
5.18 EMC test results for the stimulator. 84

6.1 Lower limb muscles that act in the sagittal plane 90
6.2 Paraplegic subject with and without stimulation. 91
6.3 Stimulation-assisted swimming system. 92
6.4 Electrodes used in water. 93
6.5 IMU alignment and location at the trunk and leg. 95
6.6 Definition of the knee- and hip-extension and trunk-roll angle. 96
6.7 Illustration of the heading error for two segments are connected by a hinge joint. . . 97
6.8 Lap times of two subjects over the swim training phase. 100
6.9 Knee-joint angles during swimming without and with different support modalities. . 101
6.10 Hip-joint angles during swimming without and with different support modalities. . . 102
6.11 Roll angle during swimming without and with different support modalities. 102

7.1 IMU-triggered stimulation swimming system. 107
7.2 Sensor locations and motion parameters during swimming. 108
7.3 Trunk-roll angle and roll rate and upper-arm inclination angles during front crawl. . 110
7.4 State machine of the triggered stimulation implemented in Stateflow. 112
7.5 Distribution of maximum, minimum, and mean swimming velocity. 113
7.6 Instantaneous swimming velocity for the three different swimming methods. 114

7.7 Experimental results for swimming with no stimulation. 115
7.8 Experimental results for swimming with periodic stimulation. 116
7.9 Experimental results for swimming with triggered stimulation. 117
7.10 Photos of different swimming phases for different swimming methods. 118

A.1 The international standards for neurological classification – first page. 137
A.2 Second page of the impairment scale. 138

B.1 Simplied configuration for one leg. 139

List of Tables

3.1 Type and stimulation trigger method of selected FES cycling studies. 26
3.2 Designations of the six-bar linkage model. 30
3.3 Permutation of sensor attachment angles. 34
3.4 Sectors of the cycle percentage. 41
3.5 Cycle percentage range for each muscle group. 46
3.6 Summary of the segment-length-optimization method 51
3.7 Comparison of stimulation ranges for crank angle and cycle percentage. 53

4.1 Characteristics and results of the FES pilots and hardware during the Cybathlon. . . . 58
4.2 Preparation phases for the Cybathlon. 63

5.1 Comparison of available 9 Degrees of Freedom (DoF) IMU sensors. 70

6.1 Lap times during the swim training phase for subject A. 99
6.2 Lap times during the swim training phase for subject B. 100
6.3 Averaged lap times of the post-training assessment. 101

Abbreviations

ADC Analog-to-Digital Converter 15
ASIA American Spinal Injury Association 1

BLE Bluetooth Low Energy 9

CE European Conformity 68
CP Cycle Percentage 41

DAC Digital-to-Analog Converter 79
DMA Direct Memory Access 80
DoF Degrees of Freedom xvii

EMC Electromagnetic Compliance 72

FES Functional Electrical Stimulation 1
fps frames per second 36

GPIO General Purpose Input/Output 78

HAL Hardware Abstraction Layer 70

IC Integrated Circuit 78

LED Light-Emitting-Diode 70
LUT Look-Up Table 47

MEMS Micro-Electro-Mechanical Systems 13
MOSFET Metal-Oxide-Semiconductor Field-Effect Transistor 76

op-amp operational amplifier 79

PCB Printed Circuit Board 71
PI Proportional-Integral 47

RED Radio Equipment Directive 68
RMS Root Mean Square 34

SCI Spinal Cord Injury 1
SCS Spinal Cord Stimulation 5
SDK Software Development Kit 70
SEPIC Single Ended Primary Inductance Converter 77
SMD Surface-Mount Device 78
SoC System-on-Chip 69
SPI Serial Peripheral Interface 78

tSCS Transcutaneous Spinal Cord Stimulation 6

UART Universal Asynchronous Receiver Transmitter 75
UDP User Datagram Protocol 61

WLAN Wireless Local Area Network 61

Symbols

I Maximum current of a stimulation pulse 5

$R_{\mathbf{DS(on)}}$ Drain-to-source on resistance 76

T_{gyr} Sampling time of gyroscope 18

T Stimulation period 5

$\varphi^{\mathbf{CP}}$ Cycle percentage signal 41

α Crank angle 30

$\boldsymbol{q}^*$ Conjugate of quaternion 16

z_L Vector of left hip to the pedal joint 30

z_R Vector of right hip to the pedal joint 30

z_{S_L} Vector of left shank 30

z_{S_R} Vector of right shank 30

z_{T_L} Vector of left thigh 30

z_{T_R} Vector of right thigh 30

z_c Crank vector 30

δ Heading error 97

$\dot{\phi}_{\mathbf{TR},y}$ Trunk-roll-angle rate 109

$\gamma_{\mathbf{HAT}}$ Inclination angle of the cyclist's back 30

$\hat{l}_S$ Estimated shank length 50

$\hat{l}_T$ Estimated thigh length 50

$\hat{r}_c$ Estimated radius of circle of pedal position 49

λ Weighting factor 49

$\phi_{\mathbf{TR},y}$ Trunk-roll angle 98

$\phi_{\mathbf{i},y}$ Upper arm inclination angle (i = {LA, RA} with LA - left arm, RA - right arm) 108

$\mathcal{E}_{\mathbf{TR}}{}^{\tilde{\mathbf{a}}\mathbf{TR}}$ Instantaneous change of velocity of the trunk 108

$\mathcal{E}_{\mathbf{TR}}{}^{\mathbf{vTR}}$ Instantaneous swimming speed 109

$\boldsymbol{q}$ Quaternion 16

φ_{H_L} Left hip angle 30

φ_{H_R} Right hip angle 30

φ_{K_L} Left knee angle 30

φ_{K_R} Right knee angle 30

$\varphi_{\mathbf{IMU},S_L}$ Inclination angle of the left shank 30

$\varphi_{\mathbf{IMU},S_R}$ Inclination angle of the right shank 30

$\varphi_{\mathbf{IMU},T_L}$ Inclination angle of the left thigh 30

$\varphi_{\mathbf{IMU},T_R}$ Inclination angle of the right thigh 30

φ_{z_L} Inclination angle of z_L 30

φ_{z_R} Inclination angle of z_R 30

$d_{H,C}$ Horizontal distance between crank and hip joint 30

d Pulse width 5

f_s Sampling frequency 109

$h_{H,C}$ Vertical distance of crank and hip joint 30

$k_{\mathbf{acc}}$ Weight for accelerometer correction 18

$k_{\mathbf{mag}}$ Weight for magnetometer correction 19

l_S Shank length 42

l_T Thigh length 42

r True radius of circle of pedal position 50

1

Introduction

A Spinal Cord Injury (SCI) with accompanying paralysis of the lower extremities often means a severe restriction of physical activity and health for the person affected. Depending on the lesion height and severity of the injury, this often results in a restriction of various body functions. In addition, physical inactivity due to the injury is often in stark contrast to the condition prior to the injury, especially for young patients. However, sports and/or therapeutic activities after paraplegia can help to reduce concomitant diseases and increase the mental well-being of those affected. New therapy systems make it possible to generate movements by Functional Electrical Stimulation (FES) of the paralyzed musculature and thus enable participation in sports activities. This thesis describes the development and control of new systems for FES, which support cycling and swimming by the paralyzed lower limbs. The stimulation patterns are adapted in real-time based on inertial-sensor measurements. Both cycling and swimming are useful methods for cardiovascular training. Especially for FES assisted swimming, it combines the activity of the upper and lower extremities. This chapter gives an overview of the dissertation and provides background information on SCI and FES.

1.1 Spinal Cord Injury

A SCI often results in an interruption (lesion) of the motor and sensory pathways of the spinal cord as well as damage to nerve cells in the proximity of the injury. This manifests in a loss of musculoskeletal mobility and sensibility below the injury and a disruption of the autonomous nervous system as presented in Figure 1.1. These symptoms occur immediately after the injury. Each muscle in the body is supplied by a particular level or segment of the spinal cord and by its corresponding spinal nerve. In Figure 1.2, the segments, nerve roots, and their functions of the spinal cord are summarized. A spinal cord injury, depending on its level, leads to paraplegia or tetraplegia. For paraplegia, the lesion is localized in the thoracic or lumbar segments, while for tetraplegia in the cervical segments. For paraplegia the lower extremities and lower trunk are effected, whereas for tetraplegia the upper extremities are affected as well. The degree of paralysis, loss of motor function, and sensation constitute the severity of an SCI. To classify the severity level the American Spinal Injury Association (ASIA) impairment scale has been developed to compare research results and to facilitate communication between clinicians. The ASIA offers a special questionnaire, shown in Fig.

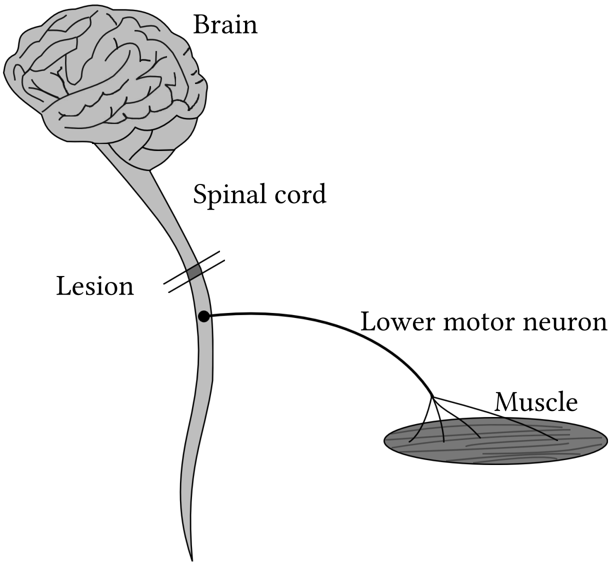

Figure 1.1: Spinal Cord of a human with an injury.

A.1 (see Appendix A). According to [1], there are 10-30 incidences of traumatic spinal cord injuries per million citizens and year in industrialized countries. The prevalence of SCI patients in Germany for 2017 was about 17,000 [2]. More than half of all spinal cord injuries occur in the cervical area, a third in the thoracic region, and the remaining injuries at the lumbar area. Most of the affected ones are young patients, in their teens or twenties. The leading causes of acute spinal cord injury in Europe include vehicular accidents 48 %, violence 6 %, falls 30 %, and sports 8 % [1].

In this work, the focus group will be paraplegics with lesions below the cervical segments. As mentioned earlier, depending on the height of the lesion there are several secondary complications besides the paralysis of the lower extremities and lower part of the abdomen. Among the described changes in the body (e.g., trophic disorders) there is an increased risk of injuries due to accidents like burns or freezes. The following list of secondary complications makes no claim to be complete but should represent the major complications.

Circulatory system Paraplegics have an increased risk of thrombosis, orthostatic hypotension, arterial hypertension, and/or bradycardia due to autonomic dysreflexia caused by injury-related immobility [1, 3].

Genitourinary system The paralysis-related bladder dysfunction may be caused by permanent complications of the affected tissue or even inadequate or incorrect bladder management complications like urinary tract infections, kidney damages, or urosepsis [1].

Spasticity A most common secondary condition for SCI patients is spasticity, which is characterized by hyperexitability of stretch-reflexes. It occurs due to a disordered control and is characterized as intermittent or sustained involuntary contractions of muscles and abnormal movements [4]. The described symptoms can cause pain, falls, or fatigue, but may also have a great influence on activities of daily living as they interfere with mobility, transfers, self-care, social participation, sleep, and more [4]. Psychologically, this can lead to lower self-esteem and a poor body image.

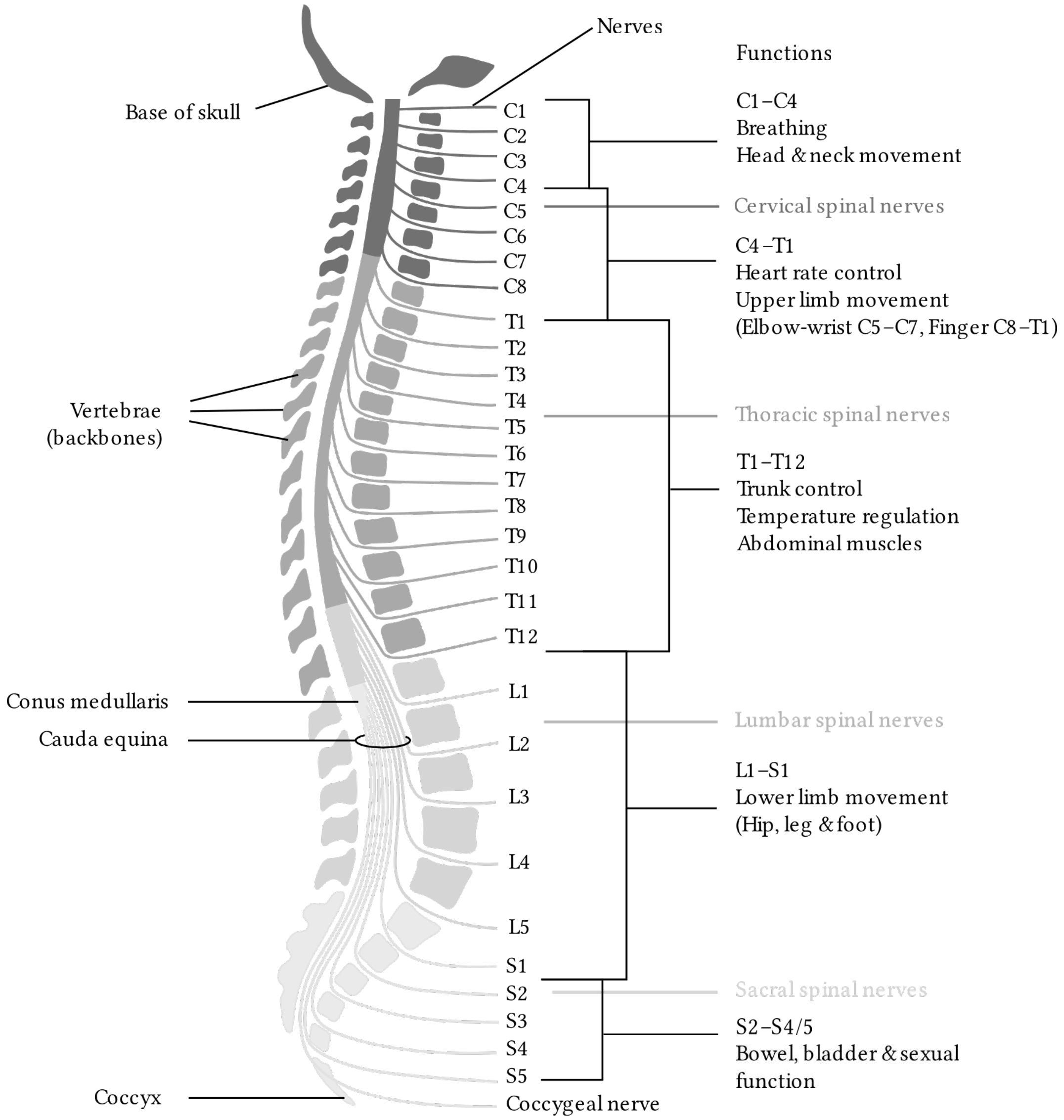
Nerves
Functions
Base of skull
C1
C2
C3
C4
C5
C6
C7
C8
T1
T2
T3
T4
T5
T6
T7
T8
T9
T10
T11
T12
L1
L2
L3
L4
L5
S1
S2
S3
S4
S5
Coccygeal nerve
C1–C4
Breathing
Head & neck movement
Cervical spinal nerves
C4–T1
Heart rate control
Upper limb movement
(Elbow-wrist C5–C7, Finger C8–T1)
Vertebrae
(backbones)
Thoracic spinal nerves
T1–T12
Trunk control
Temperature regulation
Abdominal muscles
Conus medullaris
Cauda equina
Lumbar spinal nerves
L1–S1
Lower limb movement
(Hip, leg & foot)
Sacral spinal nerves
S2–S4/5
Bowel, bladder & sexual
function
Coccyx

Figure 1.2: Longitudinal organization of the spinal cord (with cervical, thoracic, lumbar, and sacral segments shaded), spinal vertebrae, and spinal nerves and a rough representation of major functions of the spinal cord [1]

.

Bone density Osteoporosis can arise in the course of a spinal cord injury as a result of the lack of load on the bones (inactivity osteoporosis). The body begins to break down the bone substance. Due to the reduced bone density, the risk of fractures increases considerably [5].

Pain The so-called neuropathic pain originates from the lesion of the nerve fiber. Most people with SCI experience this chronic pain, which can have a significant impact on their quality of life. Neuropathic pain at the level of the lesion is also referred to as segmental, end-zone, or radicular pain. It can occur on one or both sides and expresses itself in a shot, electric, or burning. Neuropathic pain below the lesion is also referred to as central pain, dysaesthesia, or phantom pain. It appears diffuse and affects one or both sides [5].

Skin Due to the lack of sensitivity below the level of paralysis, various damages of the skin can occur. Therefore, the skin must be thoroughly protected from long exposure to heat or cold (thermal

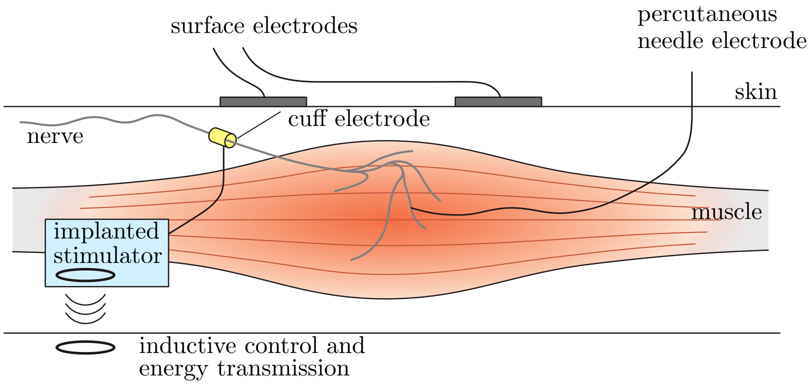

Figure 1.3: Different types of electrodes used for FES. (adapted from [7].)

hazards), from damage or injury from outside due to blunt or sharp objects (mechanical hazards), and from chemical substances, e.g., care products with high pH-value (chemical hazards).

Although there is a long list of secondary complications the life expectancy for people with SCI has intensely improved over the last years and it is no longer the main cause of death in high-income countries [1]. This progression reflects as well the improvement in clinical care, rehabilitation techniques, and improved offer of activity for SCI patients which may lead to an improved quality of life.

1.2 Functional Electrical Stimulation

Neuromodulation is the technically realized manipulation of the neuronal connections of the body using electrical or chemical stimuli. It is used to artificially restore lost or disturbed body functions or to suppress disturbances in the nervous system. Functional Electrical Stimulation (FES) describes the application of electrical pulses to nerves or muscles to produce a movement or restore a body function [6]. The restoration of motor functions by means of FES in paraplegic patients can be realized by the following two interaction mechanisms:

- Direct stimulation of intact lower motor neurons with the goal of causing muscle contractions.
- Reflex activation after afferent excitation: Stimulation of sensory (afferent) nerves can trigger spinal cord reflex activities.

If action potentials in the nerve cells shall be artificially triggered, an electric current has to be applied to the body. This can be achieved by reusable hydrogel surface electrodes which are placed on the skin over the paralyzed body part. With increasing invasiveness of the electrodes (e.g. implanted cuff electrodes, needle electrodes) the selectivity increases with respect to the excitation of nerve fibers. Figure 1.3 shows commonly used types of electrodes. The transcutaneous stimulation with surface electrodes is non-invasive. However, due to the unavoidable stimulation of receptors in the skin, higher stimulation intensities often provoke pain sensation. In case of incomplete sensory paralysis, the force generated by FES is limited by the tolerance of pain of the patient.

Charge-balanced biphasic square pulses are used for stimulation to prevent electrolysis of the tissue around the electrodes, as shown in Figure 1.4. To trigger an action potential, the stimulation pulse must have a sufficiently large charge q with respect to the first partial pulse. The charge is the

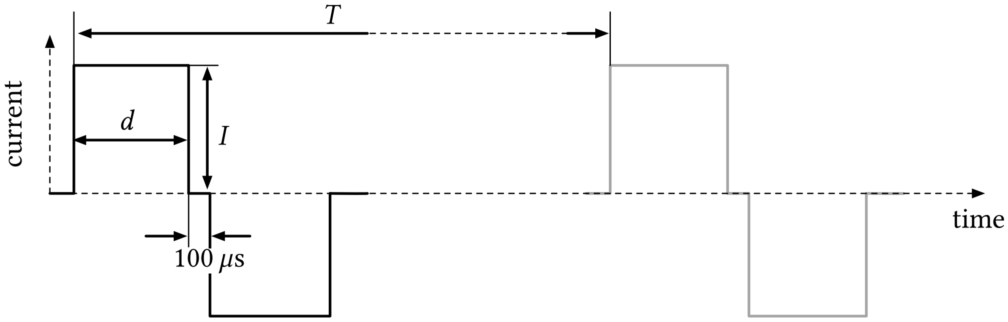

Figure 1.4: Classic biphasic stimulation pulses with current intensity I, pulse width d, stimulation period T, and a 100 μs gap in between the forward and backward pulse [7, p.339].

product of the pulse amplitude or current I and the duration or pulse width d. The muscle power generated by FES can be influenced by two mechanisms: Recruitment and frequency modulation. By changing the pulse charge, the number of recruited motor units can be controlled. The frequency is used to affect the number of action potentials per time and thus, the resulting muscle force is modulated.

Electrically stimulated muscles rapidly fatigue, which causes a nonlinear and time-variant dynamic behavior. There are multiple reasons for this [8, 9]:

1. Recruitment of motor units does not follow Hennmann's recruiting principle, but result in an inverse one. FES initially recruits the fast-fatiguing type II motor units at smaller stimulus intensities, whose large axons have a lower threshold than the smaller axons of type I. With larger stimulation intensities fatigue-resistant type I motor units are activated.
2. Another reason for the rapid fatigue is the synchronous recruitment of motor units by the electrical stimuli. The stimulation frequency of 20-50 Hz is higher than in natural asynchronous muscle activation to achieve smooth muscle contractions.
3. Another disadvantage of muscle fatigue is the fact that pulses with constant stimulus intensity activate the same motor units, and hence, no recreation can take place.

For transcutaneous stimulation spatially as well as temporal asynchronous distribution can help to mimic the natural asynchronous muscle activation and to increase the time before the onset of fatigue [10, 11]. The same technique can be used for nerve cuff electrodes to prevent the inverted recruitment of motor units by FES.

1.3 Transcutaneous Spinal Cord Stimulation

Epidural spinal cord stimulation (eSCS) is known for its use in treatment of chronic, intractable pain in the trunk and limbs since the late 1960s. Still, the control of neuropathy is its major application [12]. In the 70s, other effects of Spinal Cord Stimulation (SCS) were reported. It was observed that it improved motor function in a multiple sclerosis patient actually being treated for pain. 1978, Richardson and McLone described the effect of suppressing spasticity in SCI patients, which has been confirmed in many other studies since then. In recent years SCS experienced a resurgence of interest in spinal cord injury research and neurorehabilitation [13]. In particular, the use of electrodes, placed over the lumbar spinal cord, providing continuous stimulation resulted in a remarkable anti-spastic effect

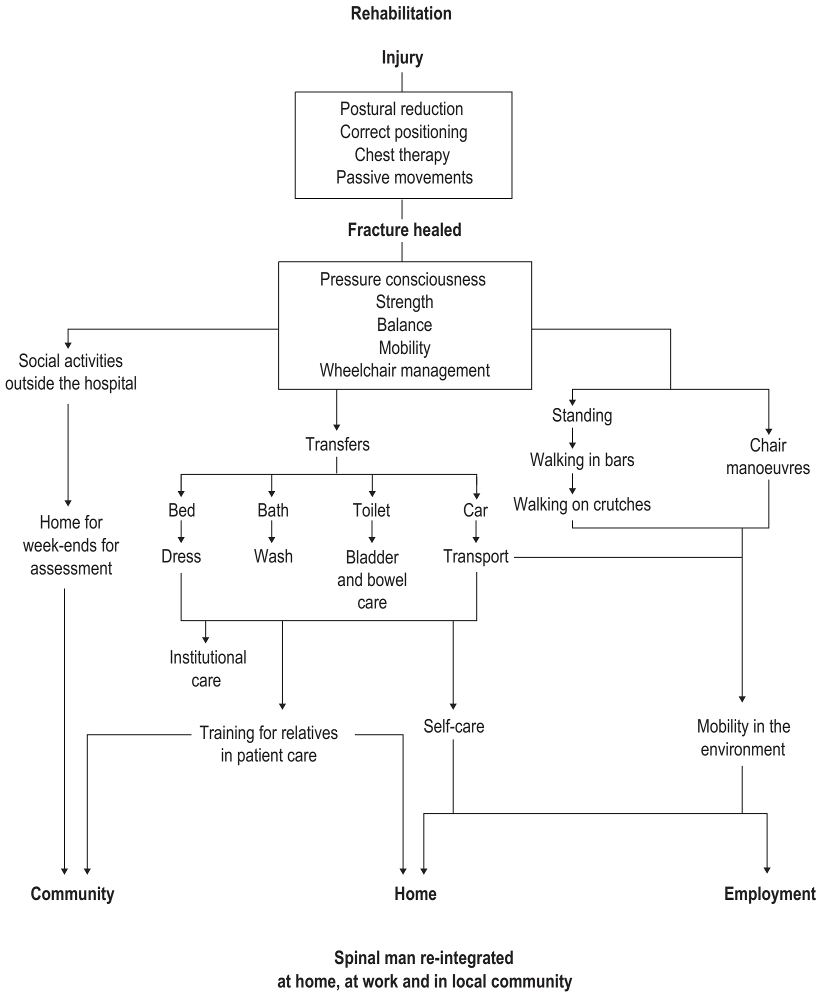
Rehabilitation
Injury
Postural reduction
Correct positioning
Chest therapy
Passive movements
Fracture healed
Pressure consciousness
Strength
Balance
Mobility
Wheelchair management
Social activities outside the hospital
Transfers
Standing
Walking in bars
Walking on crutches
Chair manoeuvres
Bed
Bath
Toilet
Car
Dress
Wash
Bladder and bowel care
Transport
Home for week-ends for assessment
Institutional care
Training for relatives in patient care
Self-care
Mobility in the environment
Community
Home
Employment
Spinal man re-integrated at home, at work and in local community

Figure 1.5: Rehabilitation process from dependence to independence [5, p.2].

across multiple lower limb muscles. This effect is present if the electrodes are placed caudal to the lesion and for stimulation frequencies of 50-100 Hz [14]. This technique is used in Chapter 6. There are further effects of Transcutaneous Spinal Cord Stimulation (tSCS) which will be described in more detail in Chapter 6.

1.4 Rehabilitation of Paraplegia

The rehabilitation of paraplegia can be summarized in an acute and a chronic phase. Focus, states, and transition of this process are summarized in Figure 1.5. Furthermore, in [15] five major goals for long-term rehabilitation are defined:

- Stabilization of vital functions,
- Prevention of secondary complications (e.g., contractures, pressure ulcers),
- Regulation of spinal spasticity,
- Psychological stabilization,
- Restoration of independence in performing daily life activities.

One major key in all of these rehabilitation goals is the retrieval of mobility. This is attained either by using a wheelchair for complete paralyzed patients or by regaining ability to walk for incomplete paralyzed patients. In the latter case, walking aids or an exoskeleton may be required. Besides the mobility, the quality of life and the preservation of body fitness depend significantly on the level of physical activity of SCI patients [16, 17]. As mentioned earlier, this work focuses on the improvement of physical activities that are available for chronic SCI patients. In [18], a scientific exercise guideline for adults with spinal cord injury has been defined. The guideline recommends for cardiorespiratory fitness and muscle strength benefits, 20 minutes of moderate to high intensity aerobic exercise and three sets of strength exercises for each major functioning muscle group two times a week at a moderate intensity. For cardio-metabolic health benefits, 30 minutes moderate to intense aerobic exercises three times a week is recommended. The guideline does not specify the type of exercise. In [19], several recommendations for exercises are made for paraplegic patients. For upper extremities e.g. wheeling, elastic resistance bands, weight machines, free weights, arm cycling, and team sports are recommended; for lower extremities body-weight-supported treadmill walking, FES cycling or rowing are recommended. Although the metabolic efficiency is low compared to able-bodied non-stimulated cycling [20], the sportive activity can improve several secondary complications [3].

In addition to land based activities, one of the most popular sports among people with paraplegia is swimming [21]. [5, 18, 19] suggest swimming as the best aerobic training for the whole body for paraplegics although the paralyzed muscles are not stimulated artificially. The benefits of swimming over ergometer training or FES cycling are both physiological and psychological. On the one hand, the condition of “zero gravity" can be achieved in the water, so that no devices for stabilizing or preventing pressure points are needed. On the other hand, paraplegics can move very similar in water compared to healthy subjects, and after a training period, they are often able to carry out the swim training without assistance. Furthermore, during rehabilitation exercises, each limb can be moved and trained independently.

1.5 Outline of the Thesis

The present dissertation aims at contributing to the improvement of FES rehabilitation systems and devices in multiple ways. Besides this introduction, this thesis consists of six further chapters and is completed by general conclusions and a outlook.

- Chapter 2 introduces the fundamentals used throughout the subsequent chapters including inertial-sensor-based orientation estimation.
- In Chapter 3, the state-of-the-art in FES cycling including recent FES cycling systems, stimulation patterns, and clinical outcomes are compared. Subsequently, a new knee-joint-angle-based stimulation pattern is introduced including a knee-joint-angle estimation algorithm. A robust discrimination between flexion and extension phases and a speed adaptation of the stimulation pattern are presented. Furthermore, an optimization method is given to calculate the crank angle and cadence using the shank- and thigh-inclination angles. All methods were evaluated using numerical simulations.
- In Chapter 4, the methods developed in Chapter 3 were integrated in a mobile FES cycling system. The design of the FES cycling system is presented. It is based on the adaptation of a

commercially available recumbent tricycle with additional sensor and electrode sleeves. During a two-year preparation phase one paraplegic subject (ASIA impairment scale A, 35 years after injury) was trained for participation at the Cybathlon in the FES race competition. The training regime as well as the race results are presented in detail.

- Chapter 5 presents a wireless sensor and a stimulation system. The sensor directly integrates the magnetometer-free orientation estimation at the sensor level to reduce the communication effort. The current-controlled stimulator can stimulate up to eight channels and offers a variable high-voltage generation. The focus of the hardware development was to build up a miniaturized, inexpensive, and versatile hardware platform for FES applications.
- The second part of this dissertation describes the research results towards FES swimming. In Chapter 6, the state-of-the-art in aquatic therapy for SCI patients and its clinical outcome is reviewed. The experimental setup and proof-of-concept for the first FES swimming device are presented including the pilot study STIMSWIM. The results indicate an improvement in swimming speed for FES swimming.
- In Chapter 7, a trunk-roll-angle synchronized is presented and compared against periodic stimulation and swimming without FES support. The trunk-roll angle is used to control the stimulation of the knee extensors and to synchronize the legs' propulsion with the volitional upper arm and trunk-roll movement in front crawl swimming. For evaluation, the upper-arm inclination, knee-joint as well as the trunk-roll angles are measured with triggered, periodic, and without stimulation support. Furthermore, the instantaneous swimming speed was calculated to compare the different swimming methods.

Conclusions and recommendations for future work are given in the final Chapter 8.

1.6 Main Contributions of this Thesis

In the following the main contributions of this thesis are summarized:

C1 In the presented thesis, a new joint-angle-based FES cycling pattern is described. The method uses four Inertial Measurement Units (IMU) to estimate the knee-joint angle of each leg, while only the accelerometer and gyroscope measurements are used to derive the orientation of each segment of the legs. Based on the estimated knee-joint angles a stimulation pattern is obtained. This pattern maps extension and flexion phases of the knee joints onto the corresponding muscles and is independent of the geometric configuration between the legs and the seat. The novel approach offers a “plug & play" system without the need for an initial calibration or manual tuning.

C2 A method for robust discrimination of flexion and extension phases is introduced without involving the angular velocity of the knee joint to guarantee a safe switching between the extension and flexion phases during mobile cycling or stationary ergometer cycling. The new criterion depends only on the segment-inclination angles and is able to reliably discriminate between flexion and extension even during the start or when the cycling was interrupted.

C3 Using the segment-inclination angles, the crank angle and cadence can be estimated using an optimization algorithm. It needs one full revolution to estimate all segment length.

C4 All methods have been evaluated in numerical models and during experiments with one paraplegic subject (ASIA impairment scale A, 35 years after injury). These developed methods were integrated in a mobile FES cycling system. The design was based on the adaptation of a commercially available recumbent tricycle with additional sensor and electrode sleeves. The used tricycle, seat position, and steering architecture allowed the paraplegic pilot to get on and off the bike without assistance. The stimulation system integrated four wired sensors and a standard FES stimulator which was controlled via an embedded control system while the gear, stimulation intensity, and frequency could be controlled by the pilot. During a two-year preparation phase the pilot was trained for participating at the Cybathlon during the FES race where he finally finished fourth. Compared to other competition contributions, the implemented stimulation pattern was able to produce a very homogeneous pedaling movement.

C5 As a technology transfer from the wired FES cycling system a lightweight and wireless inertial sensor was developed. It directly integrates the magnetometer free orientation estimation at the sensor level to reduce the communication effort. The developed sensor system was tested against an optical motion tracking system. The presented current-controlled stimulator can control up to eight stimulation channels independently while it can be configured via Bluetooth Low Energy (BLE). The variable high-voltage generation can be used to adjust the stimulation voltage in case of electrode impedance changes to save energy or for applications where only a low stimulation voltage is needed.

C6 A novel FES swimming system is developed which consists of a waterproof stimulator, electrodes and cables, and stimulation patterns for tSCS and FES. The device was evaluated in a proof-of-concept study with two complete spinal cord injured patients. The study showed an improvement in swimming speed for front crawl swimming when FES was applied.

C7 An incorporated IMU sensor is used to estimate the trunk-roll angle and trunk-roll-angle rate in real-time based on the same magnetometer-free orientation estimation used for FES cycling. The roll angle and roll-angle rate of the trunk are used to control the quadriceps stimulation and synchronize the leg propulsion with the volitional upper-body movement in front crawl swimming. This yields a more streamlined body posture and increased swimming speed.

1.7 Related Publications by the Author

The present dissertation is based in part on the publications listed below. They are grouped by the field of research to which they contribute. The cite acronym CYCx, $x \in N$, indicates contributions to the field of FES cycling including the Cybathlon.

[CYC1] S. Ruppin, C. Wiesener, and T. Schauer. "Inertial Sensor-Based Control of Functional Electrical Stimulation in Paraplegic Cycling". In: *Proc. of 20th Conference of the International Functional Electrical Stimulation Society.* IFESS. La Grande Motte, France, June 2016.

[CYC2] C. Wiesener, S. Ruppin, and T. Schauer. “Robust Discrimination of Flexion and Extension Phases for Mobile Functional Electrical Stimulation (FES) Induced Cycling in Paraplegics”. In: *IFAC-PapersOnLine* 49.32 (2016), pp. 210–215. DOI: 10.1016/j.ifacol.2016.12.216.

[CYC3] C. Wiesener and T. Schauer. “The Cybathlon RehaBike: Inertial-Sensor-Driven Functional Electrical Stimulation Cycling by Team Hasomed”. In: *IEEE Robotics & Automation Magazine* 24.4 (Dec. 2017), pp. 49–57. DOI: 10.1109/MRA.2017.2749318.

[CYC4] F. Heinrich, C. Wiesener, and T. Schauer. “Control and Optimization of FES-Cycling with Differential Evolution: A Computer Model-based Study”. In: *Autsym 2017, 8th International Symposium on AUTOMATIC CONTROL*. Vol. 8. 2017.

[CYC5] C. Wiesener, E. Ambrosini, L. Blankenfeld, S. Schneider, B. Grzywacz, and T. Schauer. “Wireless IMU- and EMG-Sensors for Controlled Functional Electrical Stimulation”. In: *Converging Clinical and Engineering Research on Neurorehabilitation III*. 1st ed. Springer International Publishing, 2018, pp. 16–20. DOI: 10.1007/978-3-030-01845-0_4.

[CYC6] C. Wiesener, M. Valtin, and T. Schauer. “Current-Controlled Stimulator with Variable High Voltage Generation”. In: *13th Int. Vienna Workshop on FES*. IFESS. Vienna, Austria, Oct. 2019.

The acronym SWIMx indicates publications on FES assisted swimming which are presented in Chapter 6 and 7.

[SWIM1] C. Wiesener, J. Axelgaard, R. Horton, A. Niedeggen, and T. Schauer. “Functional Electrical Stimulation assisted swimming for paraplegics.” In: *22th Conference of the International Functional Electrical Stimulation Society*. IFESS. Nottwill, Switzerland, Aug. 2018.

[SWIM2] C. Wiesener, T. Seel, J. Axelgaard, R. Horton, A. Niedeggen, and T. Schauer. “An Inertial Sensor-based Trigger Algorithm for Functional Electrical Stimulation-Assisted Swimming in Paraplegics”. In: *IFAC-PapersOnLine* 51.34 (2019), pp. 278–283. DOI: 10.1016/j.ifacol.2019.01.039.

[SWIM3] C. Wiesener, A. Niedeggen, and T. Schauer. “Electrotactile Feedback for FES-Assisted Swimming”. In: *Converging Clinical and Engineering Research on Neurorehabilitation III*. 1st ed. Springer International Publishing, 2019, pp. 922–925. DOI: 10.1007/978-3-030-01845-0_18.

[SWIM4] C. Wiesener, L. Spieker, J. Axelgaard, R. Horton, A. Niedeggen, N. Wenger, T. Seel, and T. Schauer. “Supporting front crawl swimming in paraplegics using electrical stimulation: A feasibility study”. In: *Journal of NeuroEngineering and Rehabilitation* 17.1 (Apr. 2020), p. 51. DOI: 10.1186/s12984-020-00682-6.

[SWIM5] C. Wiesener, T. Seel, L. Spieker, A. Niedeggen, and T. Schauer. “Inertial-Sensor-Controlled Functional Electrical Stimulation for Swimming in Paraplegics: Enabling a Novel Hybrid Exercise Modality”. In: *IEEE Control Systems* 40.6 (Dec. 2020), pp. 117–135. DOI: 10.1109/MCS.2020.3019152.

The publication [CYC2] has been awarded as best student paper of the CPHS conference 2017 in Florianopolis, Brazil. The publication [SWIM1] has been awarded with the Vodovnik Award for the best student paper of the IFESS conference 2018 in Nottwill, Switzerland. Together with Dr. Thomas Schauer the STIMSWIM research project presented in Chapter 6 and 7 has been awarded with the first price of the "Forum Junge Spitzenforscher" Award 2018 in Berlin, Germany.

1.8 Related Theses Supervised by the Author

Many of the experimental results that are described and discussed within this dissertation have been obtained with the valuable support of students whose Bachelor's thesis or Master thesis has been supervised by the author. Several side aspects that are only touched briefly or described very concisely in this dissertation can be found in further detail, and often in great clarity, within those theses. To acknowledge the valuable contribution of these students to the research projects behind this dissertation, the reference to their works here in chronological order are provided.

[TH1] S. Ruppin. "Inertial Sensor-Based Control of Functional Electrical Stimulation in Paraplegic Cycling". Master thesis. Technische Universität Berlin, 2016.

[TH2] Ferdinand Heinrich. "Control and Optimization of FES-Cycling with Differential Evolution: A Computer Model based Study". Bachelor's thesis. Technische Universität Berlin, 2017.

[TH3] L. Blankenfeld. "Entwurf und Aufbau eines über Bluetooth gekoppelten EMG-Sensormoduls". Master thesis. Technische Universität Berlin, 2018.

[TH4] S. Schneider. "Entwicklung eines mehrkanaligen Elektrostimulators mit adaptiver Spannungsanpassung". Master thesis. Technische Universität Berlin, 2018.

[TH5] B. Grzywacz. "Evaluation of Different Wireless Sensor Network Topologies Used in Controlled Functional Electric Stimulation for Rehabilitation Purposes". Master thesis. Technische Universität Berlin, 2018.

[TH6] G. Mclachlan. "Control of Neuro-prosthesis for Functional Electrical Stimulation Assisted Swimming of Paraplegics." Master thesis. University of Glasgow / Technischer Universität Berlin, 2019.

[TH7] L. Mcconomy. "An Underwater Gait Phase Detection System for Control of Functional Electrical Stimulation-Assisted Gait Training in Water After Stroke". Master thesis. University of Glasgow / Technischer Universität Berlin, 2019.

2

Fundamentals of Inertial Measurement Units and Orientation Estimation

Inertial Measurement Units (IMUs) are self-contained sensors, in which measurements produced by gyroscopes, accelerometers, and magnetometers are used to track the velocity and/or orientation of an object with respect to a fixed (inertial) coordinate system. They typically contain three orthogonal gyroscopes, accelerometers, and magnetometers, measuring angular velocity, linear acceleration, and magnetic field vector, respectively [22]. IMUs are mainly known from aerial and marine navigation. However, with the advancing progress in miniaturization of hardware, they get integrated into wearables and handheld devices to a greater extent. The sensors normally used in this consumer hardware are a combination of so-called Micro-Electro-Mechanical Systems (MEMS). These sensors are miniaturized versions of high-resolution sensors and are typically available at a low price, size, and power consumption [23].

2.1 Accelerometer

The working principle of a MEMS accelerometer is outlined in Figure 2.1. Compared to gyroscopes, which will be introduced in the following, these sensors are basic electromechanical systems. During movement, displacement of the mass produces a change of i.e., a capacitor, which can be measured by generating a voltage that is proportional to the force acting on the mass. MEMS accelerometers measure acceleration, typically in units of Earth's gravity. If three orthogonal accelerometers are used the direction of gravity can be directly measured. However, when the sensor is moved they also respond to linear acceleration. The measured acceleration of an accelerometer is normally very sensitive to noise. The major noise sources are characterized as mechanical-thermal noise and electrical-thermal noise. Mechanical-thermal noise is related to the mass and spring constant and mechanical resistance of the sensor's seismic system and can be reduced by increasing the mass and accuracy of the mass and springs or by decreasing the resonance frequency of the mechanical oscillator [23]. Another major source is electrical-thermal noise contributed by any internal or external electronics used in the measurement system, which is difficult to avoid. Furthermore, the accelerometer measurement can be affected by a bias, which is critical if the sensor information is used for velocity and position estimation.

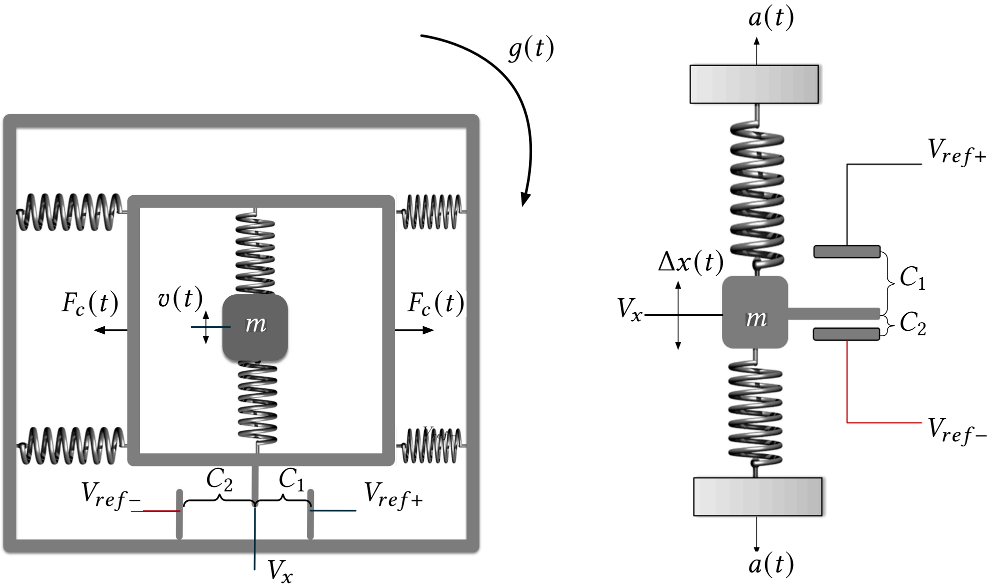

(a) MEMS gyroscope **(b)** MEMS accelerometer

Figure 2.1: Schematic of a simplified MEMS gyroscope (left) and an accelerometer (right). The working principle of the gyroscope depends on detecting the Coriolis force $F_c(t)$ acting on a vibrating proof mass in proportion to the rate of rotation along an axis orthogonal to the vibratory axis. The gyroscope drives the proof mass m into oscillation along one axis indicated by $v(t)$, regulates the mechanical amplitude so that the mass possesses a stable velocity, and senses the corresponding displacement of the same mass along an orthogonal axis. The sensed displacement is then proportional to the amplitude of the rate of rotation. For the accelerometer, the mass m is connected via springs to a fixed frame in such a way that it can move slightly up and down. When the device is accelerated, inertia effects cause a displacement (indicated by $\Delta x(t)$) of the mass [23].

2.2 Gyroscope

A gyroscope is a device that measures angular velocity on one axis where the common unit of measurement is $[°/s]$. Despite other techniques, MEMS gyroscopes measure the Coriolis effect using miniaturized vibrating elements as shown in Figure 2.1. The three-axis MEMS gyroscope consists of three one-axis gyroscopes mounted in such a way that their axes are pairwise perpendicular to each other [22]. One disadvantage of MEMS gyroscopes is that their measurements are not entirely accurate in comparison to optical gyroscopes [22]. The main source of errors for the MEMS gyroscope is the constant bias, which can be different for each axis [22]. The constant bias is a constant disagreement between the output obtained from the gyroscope and the true value. For example, if the gyroscope is not undergoing any rotational movement, the angular velocity output will not be zero. The constant bias is overlaid by a temperature-dependent bias and a bias fluctuation [22]. Since angular velocities are often integrated to obtain angles, the bias manifests itself as a drift in the angle. It is, therefore, an important quality indicator of a gyroscope.

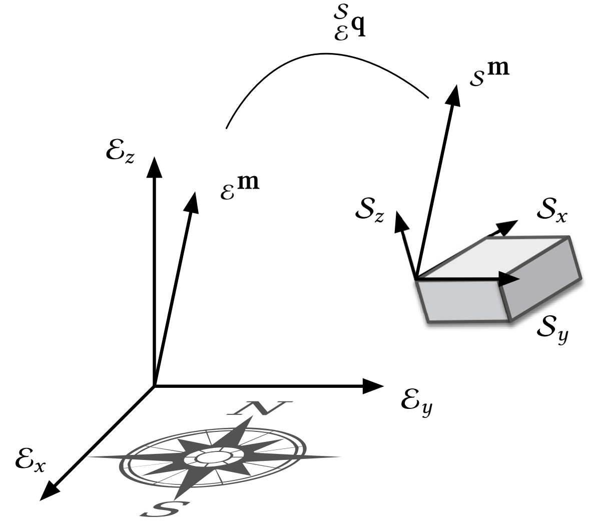
${}^{\mathcal{S}}_{\mathcal{E}}\mathbf{q}$
${}_{\mathcal{S}}\mathbf{m}$
$\mathcal{E}_z$
${}_{\mathcal{E}}\mathbf{m}$
$\mathcal{S}_z$
$\mathcal{S}_x$
$\mathcal{S}_y$
$\mathcal{E}_y$
$\mathcal{E}_x$
N
S

Figure 2.2: World frame $\mathcal{E}$ and sensor frame $\mathcal{S}$. Quaternion ${}^{\mathcal{S}}_{\mathcal{E}}\boldsymbol{q} \in \mathbb{H}$ describes the rotation (not translation) of a vector ${}_{\mathcal{S}}\mathbf{m}$ in the sensor frame with respect to the world frame. The resulting vector ${}_{\mathcal{E}}\mathbf{m}$ has the same orientation but is now described with respect to the world frame.

2.3 Magnetometer

A magnetometer is a measurement unit used to measure magnetic field strength. Modern MEMS magnetometers use the Hall effect to measure induced currents in a moving silicon plate that is proportional to the ambient magnetic field [24]. An integrated circuit translates the sensed analog current of each axis into a raw digital value via an Analog-to-Digital Converter (ADC) which can be then scaled into the more familiar Gauss unit. Three one-axis magnetometers in an orthogonal alignment form a three-axis magnetometer that can determine the north or south direction, according to the magnetic field of the earth. Magnetometers are highly affected by local disturbances of ferromagnetic materials or electrical devices. These disturbances distort the measured magnetic-field vector and change the norm of the measured output.

2.4 Orientation Estimation Using Inertial Measurement Units

The orientation describes in geometrical terms how an object is rotated with respect to the other or how an object is aligned with respect to a reference coordinate frame. Euler's rotation theorem shows that in three dimensions any orientation can be reached with a single rotation around a fixed axis assuming that all coordinate systems are right-handed Cartesian. As a convention, we assume a fixed reference frame (earth coordinate system) denoted with $\mathcal{E}$ to have a vertical z-axis and an x-axis that points horizontally to the magnetic south, as presented in Figure 2.2. To describe the coordinate transformation from a locally measured or estimated orientation in the sensor frame $\mathcal{S}$ into the defined reference frame, quaternion algebra is used.

2.4.1 Quaternion Algebra

Quaternions are a generalization of complex numbers introduced by Hamilton in the 19th century. Quaternions can be written in various ways like

$$q = q_0 + q_1 i + q_2 j + q_3 k : q_0, q_1, q_2, q_3 \in \mathbb{R} \tag{2.1}$$

or as 4-tuple

$$\boldsymbol{q} = (q_0, q_1, q_2, q_3), \quad \text{with} \quad \boldsymbol{q} \in \mathbb{H}. \tag{2.2}$$

Compared to standard complex numbers two additional imaginary parts j and k are used with the following relationship

$$i^2 = j^2 = k^2 = ijk = -1 \tag{2.3}$$

and

$$ij = k, \qquad jk = i, \qquad ki = j. \tag{2.4}$$

The multiplication of two quaternions, e.g.

$$\boldsymbol{q} = q_0 + q_1 i + q_2 j + q_3 k, \qquad q_0, q_1, q_2, q_3 \in \mathbb{R},\ \boldsymbol{q} \in \mathbb{H}$$

and

$$\boldsymbol{p} = p_0 + p_1 i + p_2 j + p_3 k, \qquad p_0, p_1, p_2, p_3 \in \mathbb{R},\ \boldsymbol{p} \in \mathbb{H},$$

is defined by

$$\begin{aligned}\boldsymbol{q} \otimes \boldsymbol{p} &= (q_0 + iq_1 + jq_2 + kq_3) \otimes (p_0 + ip_1 + jp_2 + kp_3) \\ &= (q_0p_0 - q_1p_1 - q_2p_2 - q_3p_3) \\ &\quad + (q_0p_1 + q_1p_0 + q_2p_3 - q_3p_2)i \\ &\quad + (q_0p_2 - q_1p_3 + q_2p_0 + q_3p_1)j \\ &\quad + (q_0p_3 + q_1p_2 - q_2p_1 + q_3p_0)k\end{aligned} \tag{2.5}$$

and typically non-commutative [25] which means

$$\boldsymbol{q} \otimes \boldsymbol{p} \neq \boldsymbol{p} \otimes \boldsymbol{q}. \tag{2.6}$$

The norm of a quaternion $\boldsymbol{q} \in \mathbb{H}$ is defined as follows

$$|\boldsymbol{q}| = \sqrt{q_0^2 + q_1^2 + q_2^2 + q_3^2}. \tag{2.7}$$

For the description of rotations, only unit quaternions can be used [25] which satisfy the following properties

$$|\boldsymbol{q}| = \sqrt{q_0^2 + q_1^2 + q_2^2 + q_3^2} = 1. \tag{2.8}$$

The product of two unit quaternions is a unit quaternion and the inverse of a unit quaternion is equal to the complex conjugate of a unit quaternion [25] and is defined by

$$\boldsymbol{q}^* = \boldsymbol{q}^{-1} = (q_0, q_1, q_2, q_3)^{-1} = (q_0, -q_1, -q_2, -q_3), \qquad \text{with} \ \ |\boldsymbol{q}| = 1. \tag{2.9}$$

Using these definitions, the unit quaternion can be defined which describes a rotation of angle α around a rotation axis $\boldsymbol{j} \in \mathbb{R}^3$ with

$$\alpha \in [0, 2\pi) \ @ \ \underbrace{\boldsymbol{j} = [j_x, j_y, j_z]^\intercal}_{\|j\|_2=1} \quad \cong \quad \boldsymbol{q} = \cos\left(\frac{\alpha}{2}\right) + (j_x i + j_y j + j_z k)\sin\left(\frac{\alpha}{2}\right). \tag{2.10}$$

Considering a three-dimensional vector ${}_{\mathcal{A}}\boldsymbol{m}$ in a given coordinate system $\mathcal{A}$. The rotation of this vector into another coordinate system $\mathcal{B}$ can be described with ${}^{\mathcal{B}}_{\mathcal{A}}\boldsymbol{q}$, where

$${}^{\mathcal{A}}_{\mathcal{B}}\boldsymbol{q} = {}^{\mathcal{B}}_{\mathcal{A}}\boldsymbol{q}^* \tag{2.11}$$

defines the inverse rotation. For convenience, the quaternion in Eq. (2.10) can be written in vector representation with

$${}^{\mathcal{B}}_{\mathcal{A}}\boldsymbol{q} = \begin{bmatrix} \cos(\frac{\alpha}{2}) \\ j_x \sin(\frac{\alpha}{2}) \\ j_y \sin(\frac{\alpha}{2}) \\ j_z \sin(\frac{\alpha}{2}) \end{bmatrix} = \begin{bmatrix} \cos(\frac{\alpha}{2}) \\ \sin(\frac{\alpha}{2}) \begin{bmatrix} j_x \\ j_y \\ j_z \end{bmatrix} \end{bmatrix} \qquad {}^{\mathcal{B}}_{\mathcal{A}}\boldsymbol{q}^* = \begin{bmatrix} \cos(\frac{\alpha}{2}) \\ -j_x \sin(\frac{\alpha}{2}) \\ -j_y \sin(\frac{\alpha}{2}) \\ -j_z \sin(\frac{\alpha}{2}) \end{bmatrix} = \begin{bmatrix} \cos(\frac{\alpha}{2}) \\ -\sin(\frac{\alpha}{2}) \begin{bmatrix} j_x \\ j_y \\ j_z \end{bmatrix} \end{bmatrix}. \tag{2.12}$$

Furthermore, given three frames $\mathcal{A}$, $\mathcal{B}$, and C, and given the quaternion ${}^{\mathcal{B}}_{\mathcal{A}}\boldsymbol{q}$ which defines the orientation of frame $\mathcal{B}$ expressed with respect to frame $\mathcal{A}$ and given the quaternion ${}^{C}_{\mathcal{B}}\boldsymbol{q}$ which defines the orientation of frame C expressed with respect to frame $\mathcal{B}$, the orientation of frame C with respect to frame $\mathcal{A}$ is characterized by

$${}^{C}_{\mathcal{A}}\boldsymbol{q} = {}^{\mathcal{B}}_{\mathcal{A}}\boldsymbol{q} \otimes {}^{C}_{\mathcal{B}}\boldsymbol{q} \quad \forall\, {}^{\mathcal{B}}_{\mathcal{A}}\boldsymbol{q}, {}^{C}_{\mathcal{B}}\boldsymbol{q}. \tag{2.13}$$

Additionally, for our problem stated in Figure 2.2 the vector ${}_{\mathcal{B}}\mathbf{m}$ can be described with respect to the frame $\mathcal{A}$ by multiplying the following unit quaternions

$$\begin{bmatrix} 0 \\ {}_{\mathcal{A}}\boldsymbol{m} \end{bmatrix} = {}^{\mathcal{B}}_{\mathcal{A}}\boldsymbol{q} \otimes \begin{bmatrix} 0 \\ {}_{\mathcal{B}}\boldsymbol{m} \end{bmatrix} \otimes {}^{\mathcal{B}}_{\mathcal{A}}\boldsymbol{q}^*, \tag{2.14}$$

where ${}_{\mathcal{B}}\boldsymbol{m}$ and ${}_{\mathcal{A}}\boldsymbol{m} \in \mathbb{R}^3$. For simplicity, the definition of $\otimes$ can be extended to map from $\mathbb{R}^4 \times \mathbb{R}^3 \times \mathbb{R}^4$ to $\mathbb{R}^3$ to avoid the expansion of the 3-dimensional vectors. Hence, Eq. (2.14) can then be written as

$${}_{\mathcal{A}}\boldsymbol{m} = {}^{\mathcal{B}}_{\mathcal{A}}\boldsymbol{q} \otimes {}_{\mathcal{B}}\boldsymbol{m} \otimes {}^{\mathcal{B}}_{\mathcal{A}}\boldsymbol{q}^*. \tag{2.15}$$

2.4.2 Orientation Estimation Method

In general, orientation estimation is often separated according to Figure 2.3 into a prediction and a correction which are combined to an orientation estimate using a sensor fusion algorithm.

In [26], the method used for orientation estimation for this thesis is described in detail. Here, it is assumed that the unit vectors of the x-axis and z-axis of the reference frame are defined as ${}_{\mathcal{E}}\boldsymbol{r}_{\text{mag}} = [1, 0, 0]^T$, ${}_{\mathcal{E}}\boldsymbol{r}_{\text{acc}} = [0, 0, 1]^T$ and that the coordinate systems $\mathcal{S}$ and $\mathcal{E}$ coincide initially, i.e. the initial quaternion is ${}^{\mathcal{S}}_{\mathcal{E}}\boldsymbol{q}(t_0) = [1, 0, 0, 0]^T$. Furthermore, using Eq. (2.15) the vertical unit vector in

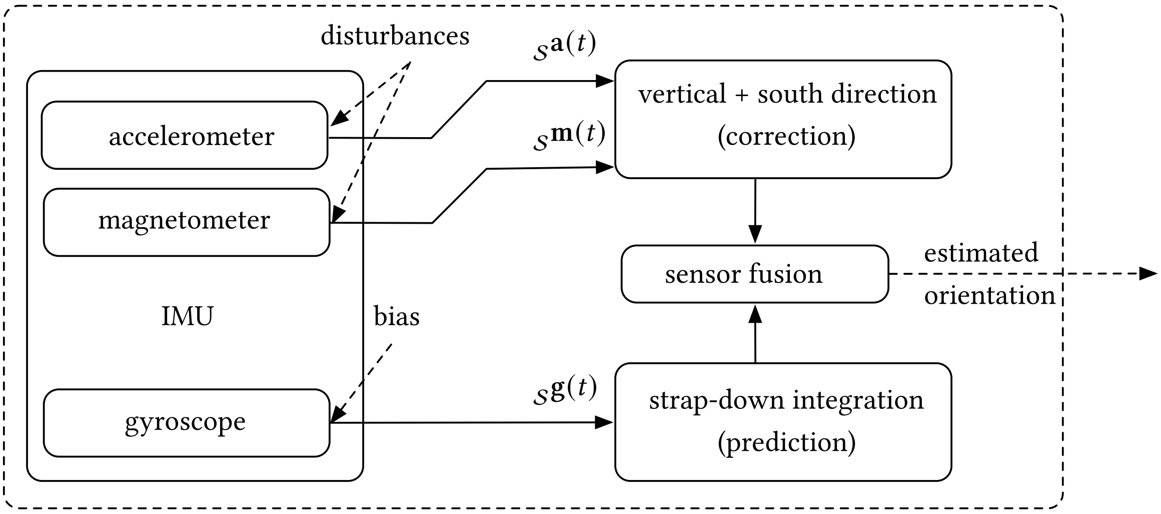
disturbances
accelerometer
magnetometer
IMU
gyroscope
bias
$_{\mathcal{S}}\mathbf{a}(t)$
$_{\mathcal{S}}\mathbf{m}(t)$
$_{\mathcal{S}}\mathbf{g}(t)$
vertical + south direction (correction)
sensor fusion
strap-down integration (prediction)
estimated orientation

Figure 2.3: Orientation estimation of an IMU with respect to a reference coordinate system $\mathcal{E}$ with a horizontal south-facing axis and a vertical axis [26], where $_{\mathcal{S}}\mathbf{g}(t)$ is the gyroscope measurement, $_{\mathcal{S}}\mathbf{a}(t)$ the accelerometer measurement and $_{\mathcal{S}}\mathbf{m}(t)$ the magnetometer measurement with respect to a sensor coordinate system $\mathcal{S}$.

the sensor frame can be defined with

$$_{\mathcal{S}}\boldsymbol{r}_{acc}(t) = {}^{\mathcal{E}}_{\mathcal{S}}\boldsymbol{q}(t) \otimes {}_{\mathcal{E}}\boldsymbol{r}_{acc} \otimes {}^{\mathcal{S}}_{\mathcal{E}}\boldsymbol{q}(t). \tag{2.16}$$

A quaternion can be formulated using the direction and norm of the angular rates for each such time interval T_{gyr} that describes the measured change in orientation by the gyroscopes

$$\boldsymbol{q}_{\mathrm{pred,gyr}}(t) = \begin{bmatrix} \cos\left(\frac{||_{\mathcal{S}}\mathbf{g}(t)||_2}{2T_{gyr}}\right) \\ \frac{\sin\left(\frac{||_{\mathcal{S}}\mathbf{g}(t)||_2}{2T_{gyr}}\right)}{||_{\mathcal{S}}\mathbf{g}(t)||_2} \, {}_{\mathcal{S}}\mathbf{g}(t) \end{bmatrix}. \tag{2.17}$$

This quaternion is then multiplied with the preceding orientation estimate ${}^{\mathcal{S}}_{\mathcal{E}}\boldsymbol{q}_{\mathrm{gyr}}(t - T_{\mathrm{gyr}})$ to obtain the prediction

$${}^{\mathcal{S}}_{\mathcal{E}}\boldsymbol{q}_{\mathrm{gyr}}(t) = {}^{\mathcal{S}}_{\mathcal{E}}\boldsymbol{q}_{\mathrm{gyr}}(t - T_{\mathrm{gyr}}) \otimes \boldsymbol{q}_{\mathrm{pred,gyr}}(t). \tag{2.18}$$

Due to the non-zero bias of the gyroscope, this quaternion is only an approximation of the true orientation [26]. Therefore, two correction quaternions are introduced, which solve the sensor fusion problem analytically. To correct for vertical drift, an accelerometer-corrected estimate of the orientation is calculated as follows:

$$\begin{aligned} {}^{\mathcal{S}}_{\mathcal{E}}\boldsymbol{q}_{\mathrm{gyracc}}(t) &= {}^{\mathcal{S}}_{\mathcal{E}}\boldsymbol{q}_{\mathrm{gyr}}(t) \otimes \boldsymbol{q}_{\mathrm{corr,acc}}(t), \text{with} \\ \boldsymbol{q}_{\mathrm{corr,acc}}(t) &= \begin{bmatrix} \cos\left(\frac{1}{2}k_{\mathrm{acc}}\,\alpha_{\mathrm{err,acc}}(t)\right) \\ \sin\left(\frac{1}{2}k_{\mathrm{acc}}\,\alpha_{\mathrm{err,acc}}(t)\right)\boldsymbol{x}_{\mathrm{corr,acc}}(t) \end{bmatrix}, \end{aligned} \tag{2.19}$$

where $k_{\mathrm{acc}} \in [0, 1]$ is a tunable weight of the sensor fusion, $\alpha_{\mathrm{err,acc}}(t) = \sphericalangle\left({}_{\mathcal{S}}\boldsymbol{a}(t), {}_{\mathcal{S}}\boldsymbol{r}_{\mathrm{acc}}(t)\right)$ is the angle between the vertical unit vector in the sensor frame and the current accelerometer reading.

Further, $\boldsymbol{x}_{\text{corr,acc}}(t)$ can be defined as the vector product for the vectors ${}_{\mathcal{S}}\mathbf{a}(t)$ and ${}_{\mathcal{S}}\boldsymbol{r}_{\text{acc}}(t)$:

$$\boldsymbol{x}_{\text{corr,acc}}(t) = \frac{{}_{\mathcal{S}}\boldsymbol{a}(t) \times {}_{\mathcal{S}}\boldsymbol{r}_{\text{acc}}(t)}{||\,{}_{\mathcal{S}}\boldsymbol{a}(t) \times {}_{\mathcal{S}}\boldsymbol{r}_{\text{acc}}(t)||_2}. \tag{2.20}$$

The vertical correction is calculated with the update rate of the accelerometer readings which can be lower than the gyroscope update rate. To correct for heading drift, a magnetometer-based correction is introduced as follows:

$$\begin{aligned}
{}^{\mathcal{S}}_{\mathcal{E}}\boldsymbol{q}_{\text{gyraccmag}}(t) \; &= \; {}^{\mathcal{S}}_{\mathcal{E}}\boldsymbol{q}_{\text{gyracc}}(t) \otimes \boldsymbol{q}_{\text{corr,mag}}(t), \qquad (2.21)\\
\boldsymbol{q}_{\text{corr,mag}}(t) &= \begin{bmatrix} \cos\left(\frac{1}{2}k_{\text{mag}}\,\alpha_{\text{err,mag}}(t)\right) \\ \sin\left(\frac{1}{2}k_{\text{mag}}\,\alpha_{\text{err,mag}}(t)\right)\boldsymbol{x}_{\text{corr,mag}}(t) \end{bmatrix},\\
\alpha_{\text{err,mag}}(t) &= \sphericalangle\left({}_{\mathcal{S}}\bar{\boldsymbol{m}}(t),\, {}_{\mathcal{S}}\boldsymbol{r}_{\text{mag}}\right),\\
\boldsymbol{x}_{\text{corr,mag}}(t) &= \frac{{}_{\mathcal{S}}\bar{\boldsymbol{m}}(t) \times {}_{\mathcal{S}}\boldsymbol{r}_{\text{mag}}(t)}{||\,{}_{\mathcal{S}}\bar{\boldsymbol{m}}(t) \times {}_{\mathcal{S}}\boldsymbol{r}_{\text{mag}}(t)||_2},
\end{aligned}$$

where $k_{\text{mag}} \in [0, 1]$ is a tunable weight of the sensor fusion and

$${}_{\mathcal{S}}\bar{\boldsymbol{m}}(t) = {}_{\mathcal{S}}\boldsymbol{m}(t) - \left({}_{\mathcal{S}}\boldsymbol{m}(t) \cdot {}_{\mathcal{S}}\boldsymbol{r}_{\text{acc}}(t)\right){}_{\mathcal{S}}\boldsymbol{r}_{\text{acc}}(t)\,, \tag{2.22}$$

is the projection of the magnetometer reading onto the horizontal plane. Here, the correction is calculated with the update rate of the magnetometer readings, which is typically lower as the gyroscope and accelerometer. For more details of the derivation of these terms refer to [26]. The combination of these three sensor fusion steps yields the orientation of the IMU sensor.

3

Joint-Angle-Based Functional Electrical Stimulation Cycling

3.1 Overview

As introduced in Section 1.4, FES is recommended throughout the guidelines for SCI patient rehabilitation and training. FES cycling ergometers are used for several decades for rehabilitation by sequentially stimulating the large muscles of the paralyzed legs to produce a cycling motion [3], often in combination with motor support. The standard approaches for FES cycling use the crank angle to generate the stimulation patterns for inducing a pedaling motion. For the majority of available systems, the SCI patient sits with her/his wheelchair in front of an ergometer for the training period whereas the mobile cycling is performed on recumbent tricycles. A measurement system for the crank angle is needed, e.g. an encoder. The muscle stimulation phases with respect to the crank angle which give positive drive torque must be determined. These phases depend on the seating position and the seat-to-crank distance (e.g., [3]). This is relevant, for instance, when the wheelchair is placed differently in front of an ergometer every day or when several subjects share a mobile cycling device.

In this chapter, a new method for joint-angle estimation is presented to perform FES cycling by using the estimated knee- and hip-joint angles instead of the crank angle to generate the stimulation pattern. To estimate the joint angles, orientation estimates of four IMUs mounted at the thighs and shanks are processed. Based on the angular velocity of the estimated knee-joint angle the flexion and extension phases of the knee and hip joint are discriminated. The corresponding muscles for extension and flexion are stimulated according to these phases to produce a useful pedaling motion.

The before described discrimination method for flexion and extension phases is sufficient as long as it is ensured that the cycling motion does not stop, and there are no disturbances resulting in a change of sign of the angular velocity prior to the correct switching points. This can only be guaranteed for stationary cycling if an assistive motor helps to overcome dead zones where no muscle is active and keeps the legs cycling. Therefore, a new robust method for flexion and extension phase discrimination has been developed for mobile FES induced cycling. As a side product the crank angle and cadence can be reliably estimated. This can be used to compare the joint-angle-based stimulation pattern against crank-angle-based methods.

To reduce the effect of dynamic latency between stimulation onset and muscle response, a correction method was developed that shifts the stimulation pattern by a defined time delay based on the stimulation pattern of the preceding revolution, thus activating the corresponding muscles earlier.

The resulting FES cycling methods have been verified in simulations at different seating positions using a complex model of a FES cycling ergometer. The presented methods offer a geometry-independent stimulation pattern while enabling “plug & play" cycling.

Copyright Statement: The methods and results presented in this chapter have been previously published in:

[CYC1] S. Ruppin, C. Wiesener, and T. Schauer. “Inertial Sensor-Based Control of Functional Electrical Stimulation in Paraplegic Cycling”. In: *Proc. of 20th Conference of the International Functional Electrical Stimulation Society.* IFESS. La Grande Motte, France, June 2016.

[CYC2] C. Wiesener, S. Ruppin, and T. Schauer. “Robust Discrimination of Flexion and Extension Phases for Mobile Functional Electrical Stimulation (FES) Induced Cycling in Paraplegics”. In: *IFAC-PapersOnLine* 49.32 (2016), pp. 210–215. DOI: `10.1016/j.ifacol.2016.12.216`.

Therefore, the text and figures in this chapter are extracted, with slight modifications, from those publications. Figures 3.1, 3.4, 3.18, 3.15, 3.16, and 3.19 and Sections 3.4.1, 3.4.2, and 3.4.3 were added. In the following, Section 3.2 gives the state-of-the-art in FES cycling technologies, and the clinical outcome of FES cycling in the context of rehabilitation. Section 3.3 introduces the simulation model based on a combination of a muscular model and a rigid body simulation. The methods for deriving the knee-joint-angle estimation are presented in Section 3.4. This estimation is then used in Section 3.5 to generate the stimulation pattern. In Section 3.5.4, a speed adaptation method is proposed to reduce the effect of dynamic latency between stimulation onset and muscle response. Based on the estimated segment inclinations the crank angle as well as the cadence can be estimated using an optimization method which is introduced in Section 3.6. Simulation results for the combination of the presented methods are given in Section 3.7. Conclusions and possible starting points for future work are presented in Section 3.8.

3.2 State-of-the-Art in FES Cycling

In this section, the state-of-the-art in FES cycling technologies and systems are presented for stationary as well as for mobile cycling including commercially available solutions. Afterwards, the clinical outcome of FES cycling in the context of rehabilitation with respect to the metabolic efficiency and the effect of the cardiopulmonary, muscular, and skeletal system of paraplegic patients has been reviewed throughout the literature. Finally, the state-of-the-art methods for stimulation pattern generation, the involved sensor systems, and the different stimulated muscle groups are summarized.

3.2.1 FES Cycling Systems

Mobile FES cycling was initially introduced by Petrofsky, Heaton, and Phillips [27] in 1983. Since this development in the early 80’s, various types of stationary and mobile FES cycling systems have been developed. In [28] different types of these systems are summarized with respect to technology, stimulated muscles, motor or flywheel involvement, and flexibility until 2005. All of these reviewed systems, including the work of [28], rely on a crank-angle measurement either for mobile or stationary cycling. The majority of systems stimulate the quadriceps, hamstrings, and gluteus maximus according to the defined crank-angle ranges. In rare cases, the tibialis anterior, iliacus, gastrocnemius, and / or pereonal nerve were stimulated.

Stationary FES cycling systems are commercially available and have been utilized as an exercise modality for years. Exemplary representives are ERGYS 2 (Therapeutic Alliances, Fairborn, Ohio, USA) and RehaMove (Hasomed GmbH, Magdeburg, Germany) shown in Figure 3.1 a) and b), respectively. For the RehaMove system the wheelchair user sits with her/his wheelchair in front of the ergometer while for the Ergys system a transfer is necessary. The feet are placed in special orthoses to fixate the ankle joint. Due to this fixation the leg posture can be determined by using the crank angle. The leg musculature is then stimulated according to the crank angle. The angle information is directly fed into the stimulator via a control interface. The RehaMove can be combined with upper extremities ergometry, while the ergometer RT300 (Restorative Therapies, USA) can be combined with upper extremities electrical stimulation for arm cranking in tetraplegics.

Mobile FES cycling was initially introduced by Petrofsky et al. in 1983 [27]. Despite technology changes and algorithmic improvements, recent mobile FES cycling systems look still (more or less) the same. They are generally constructed from a standard tricycle (see Fig. 3.1 c) and d)) with modifications, e.g. an encoder, which shows the position of the crank, as shown in Figure 3.1 d). The output of this rotary encoder is typically read by a control system, which uses this angle information to control the stimulation of the required muscle groups to generate a pedaling motion. The intensity of the stimulation is controlled by the driver via a throttle or a rotary switch. As a special case, the BerkelBike [29], shown in Fig. 3.1 c), offers the possibility to combine a mobile FES cycle with a hand bike drive. With this setting, upper and lower extremities are trained at the same time while the covered distance can be maximized, which is normally limited for leg only FES cycling. A more detailed overview of different mobile FES cycling systems used during the Cybathlon[1] 2016 is presented in Chapter 4.

3.2.2 Clinical Outcome of FES Cycling

In [30], a summary of the clinical outcome of FES cycling for SCI patients is given, although the review includes as well non-cycling FES exercise studies. Furthermore, in [31] the efficiency of FES cycling is reviewed and compared to able-bodied cycling efficiency. In the following, the therapeutic effects from both reviews are listed and discussed.

Efficiency of FES Cycling in SCI patients As stated in [32], one major problem with FES cycling is that the metabolic efficiency defined as

$$\text{efficiency} = \frac{\text{useful power output}}{\text{metabolic power input}} \cdot 100\% \tag{3.1}$$

---

[1] The Cybathlon is an international competition organized by ETH Zurich for disabled competitors using bionic assistive technology, such as robotic prostheses, brain-computer interfaces and powered exoskeletons. It is the first international competition of this kind, and took place in Zurich, Switzerland, on 8 October 2016.

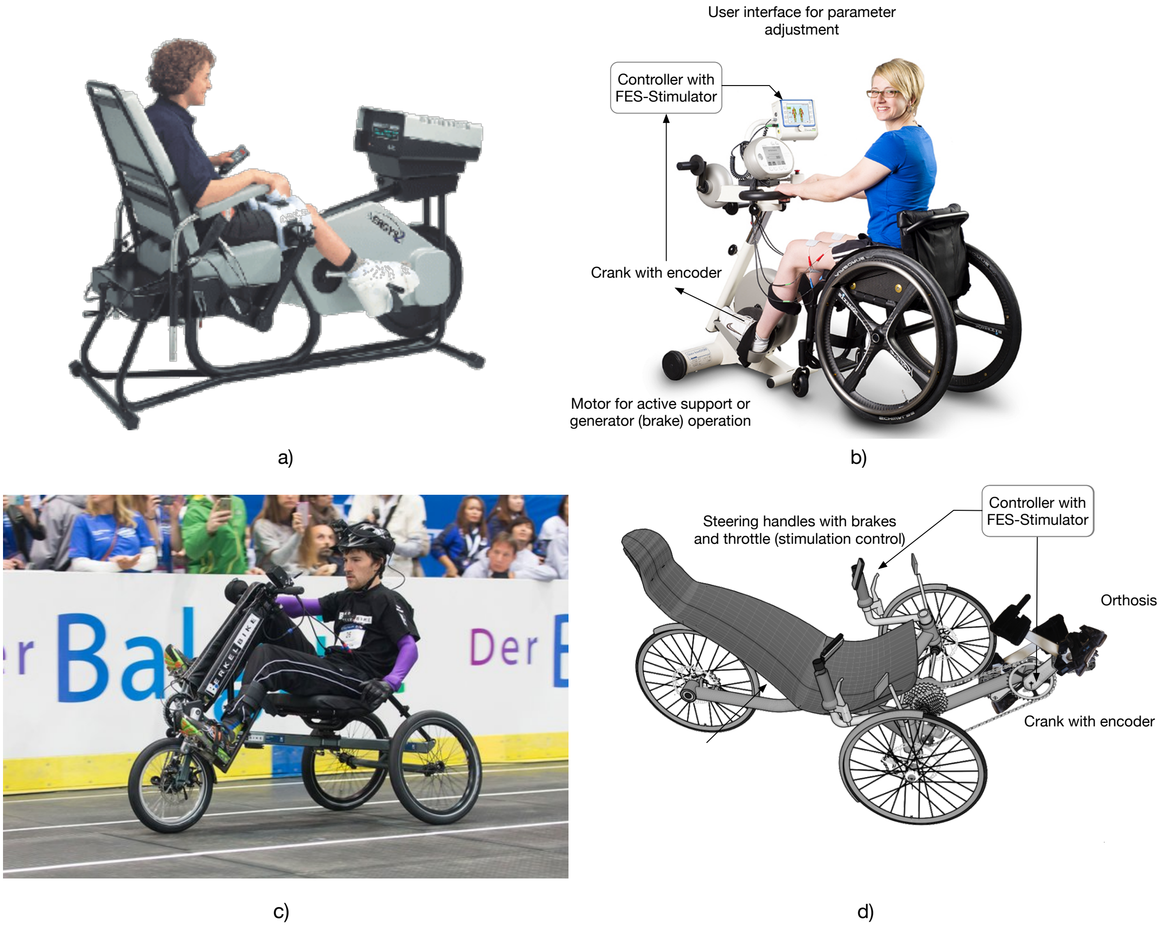
User interface for parameter adjustment
Controller with FES-Stimulator
Crank with encoder
Motor for active support or generator (brake) operation
a)
b)
Steering handles with brakes and throttle (stimulation control)
Controller with FES-Stimulator
Orthosis
Crank with encoder
c)
d)

Figure 3.1: Exemplary stationary and mobile FES cycling systems: a) The ERGYS 2 Rehabilitation System for Home and Clinics (©1996-2012 Therapeutic Alliances Incorporated, Fairborn, Ohio USA). b) RehaMove FES cycling system for upper and lower extremities (©2020 HASOMED GmbH, Magdeburg, Germany). The crank angle is read via an encoder and fed into the FES controller. Depending on the produced force by FES the motor assistance is adjusted by the ergometer. c) BerkelBike at the Cybathlon 2016, (ETH Zürich, ©Nicola Pitaro). d) Schematic of a recumbent FES tricycle consisting of an encoder attached to the crank and a throttle at the steering handle. Depending on the crank angle the requested muscles are stimulated while the stimulation intensity can be modified using the throttle. The paraplegic driver is fixed with a special belt system to prevent falling out during the course.

is very low (≈ 10%) compared to normal cycling in non-paralyzed subjects (≈ 30%). Hunt et al. [32] and Duffel et al. [20] name two factors which may be responsible:

1. "Unfavorable biomechanics due to a crude recruitment of muscle groups, non-optimal timing of muscle activation, and lack of synergistic and antagonistic joint control;"
2. As stated in Section 1.2, "a non-physiological recruitment of muscle fibers, i.e. mixed recruitment of fibers of different type and deterministic constant-frequency stimulation;"

Although several studies showed a significant improvement of the power output during a training period of several month in complete SCI subjects, the metabolic efficiency remained low [33]. Therefore, the studies by Hunt et al. [32] and Duffel et al. [20] recommend the following to improve the efficiency:

1. Alternative stimulation approaches for improved muscle activation including irregular stimulation patterns (e.g. doublets, triplets, stochastic patterns) and variable frequency stimulation trains;

2. Improvement of timing parameters for the stimulated muscle groups, and addition of more muscle groups;
3. Development of optimal stimulation protocols for muscle reconditioning and FES cycling training;
4. Individualized positioning of the stimulation electrodes;

Effects on the Cardiopulmonary System In SCI patients, the most important objective with FES cycling is to improve the cardiopulmonary fitness. This requires regular aerobic exercise, for which the body uses oxygen to release energy for physical activity. According to [34], an exercise period of 20-30 min with an increased heart rate is considered to be necessary to stimulate aerobic adaptations. However, due to the described effect of muscle fatigue during FES cycling, patients are not able to perform high-intensity training for a long period when they just started with training. Hence, to review the effect of FES cycling a long-term training has to planned during study design. Some studies on FES cycling in SCI individuals show an increase of the cross-sectional area of the arteries and the density of capillaries and improvements of the blood flow volume to the lower limbs for FES ergometer cycling [35–37]. The applied time course varied between the studies from 6 to 12 weeks, while the training frequency was 2 to 3 times a week. Furthermore, some studies reported an elevation of peak oxygen uptake after 12-26 weeks of FES cycling ergometer training by 10-20% [38, 39] or in [40] even 56%. Finally, a significant reduction in platelet activation/aggregation was demonstrated in response to FES cycling [41]. In summary, FES cycling training can improve cardiopulmonary fitness and reduce the risk of cardiovascular diseases in SCI patients.

Effects on the Muscular System An untrained SCI patient without FES cycling experience normally suffers a decreased oxidative capacity, weak muscle strength, and poor fatigue resistance. But several studies revealed that FES cycling may limit or revers muscle atrophy. An increase of muscle volume and an increase in mean power output were documented in several studies [30]. Furthermore, Pacy et al. [42] documented an improvement in the ratio between muscle and adipose tissue around the trained muscle groups. About 65%-78% of SCI patients suffer from some amount of spasticity. Depending on the subject, this includes involuntary muscle jerking, flexing, or extending of a limb, muscle spasm, and stiff or tight muscles during activity [4]. The effect of FES cycling on the spasticity of the patient is controversial as Alashram et al. [43] describe a reduction of spasticity after a certain training period while Arnold et al. [44] describe a reduction of frequency and period but an increased intensity of uncontrolled spasticity. Furthermore, some studies showed an increased range of motion and reduction of contractures for the knee joint after FES cycling training [30].

Effects on the Skeletal System As described in Section 1.1, a loss of bone density (osteoporosis) due to the inevitable immobility of the paralyzed limbs is common for all SCI patients [5]. Several reviewed studies in [30] showed no improvement in bone density of the lower limbs due to FES ergometer cycling, while [45] showed an increase in bone density for training periods greater than six months with high training intensities. Besides the described effects, there are individual studies showing a reduced risk of pressure sores [46] and type II diabetes after FES ergometer cycling [47]. These results need to be further investigated in controlled clinical studies.

Source / System	Type	Crank-angle-based	Stimulated muscles
Janssen et al. [57]	stationary	x	Q,H,G
Fornusek et al. [58]	stationary	x	Q,H,G
Schauer [28]	stationary & mobile	x	Q,H,G
Szecsi et al. [51]	stationary	x	Q,H
Hunt et al. [59]	stationary	x	Q,H,G
Hongyuan et al. [60]	stationary	x	Q,H,G
Ferrante et al. [52]	stationary	x	Q,H,G,O
Hakansson and Hull [61]	stationary	x	Q,H,G,O
Gualdi et al. [48]	stationary	x	Q,H,G,O
Shalaby et al. [62]	stationary	x	Q,H
Ambrosini et al. [53, 54]	stationary	x	Q,H,G,O
Hunt et al. [31]	stationary	x	Q,H,G
Watanabe, Karasawa, and Handa [63]	mobile	x	Q,G,O
Szecsi, Straube, and Fornusek [64]	stationary	x	Q,H
Gorgey et al. [65]	stationary	x	Q,H,G
Tong et al. [66] and Leung et al. [67]	mobile	x	Q,H
Sijobert et al. [68]	mobile	x	Q,H
Metani et al. [69]	mobile	x	Q,H,G
McDaniel et al. [70]	mobile	x	Q,H,G,O
Laubacher et al. [71]	mobile	x	Q
Bo et al. [72] and Araujo Guimarães et al. [73]	mobile	x	Q,H,G
Berkelmans and Woods [74]	mobile	x	Q,H,G
Arnin et al. [75]	mobile	x	Q,H

Table 3.1: Type and stimulation trigger method of selected FES cycling studies. The stimulated muscles in column four are abbreviated as followed: Q - quadriceps, H - hamstrings, G - gluteus maximus, O - others, e.g., tibialis anterior, gastrocnemius.

As introduced in the previous section, FES cycling is used throughout the rehabilitation and sport of mostly SCI patients since the early 1980s. Additionally, it has been applied in some studies in cerebral palsy [48–50] and stroke patients [51–56]. The results of these studies seem to be contradictory, since some studies documented an increase of muscle tone, symmetry during walking and non-assisted cycling, and walking distance as well as speed, while [56] documented no effect on mobility in a multi-center trial. Hence, further studies are needed to verify the effects on these populations.

3.2.3 Pattern Generation and Involved Sensors

In the work of Schauer [28], FES cycling systems are compared regarding their stimulated muscle groups, type of assistance, and whether the cycling system is stationary or mobile. A common feature of all studies examined in this work is that the muscle stimulation is synchronized with the measured crank angle. Therefore, only studies after 2005 have been included in Table 3.1 regarding the type of the FES cycling system, the generation of stimulation patterns, and involved sensors for controlling the stimulation. In all reviewed approaches, the timing of the muscle stimulation is determined according to the crank angle. Only two approaches use a wireless IMU attached to the crank to retrieve the crank angle [63, 73], while the rest employs traditional encoders. These IMU sensor settings were successfully used during the Cybathlon 2016 at the mobile FES race. Regardless of the type of crank-angle sensor, the relation between the lower-limb joint angles and the crank angle needs to be examined. Otherwise, the timing of the stimulation is inaccurate. This can be achieved using geometric relationships, experimental trials, or learning systems. The problem is that the relation between joint angles of the lower limbs and the crank angle can change due to variations in the sitting position (e.g., by sliding on the seat). Gföhler and Lugner [76] showed that the maximum power output for each involved muscle during FES cycling depends on the horizontal and vertical crank-to-seat distance as well as the backrest inclination angle. For bigger distances in vertical and horizontal direction, the hip- and knee-angle ranges during cycling increase and therefore the muscle lengths and moment arms change [76]. For stationary systems, the horizontal and vertical crank-to-seat distance change if the wheelchair in front of the ergometer is placed differently every day or if a new patient attends the training session. The relation is also dependent on the lengths of the lower limbs of the person who is performing FES cycling.

In summary, a new relationship needs to be established for every individual and every cycling trial. To get the perfect geometric relation, a lot of specific parameters of the device and the patient need to be taken into account. This is time-consuming and error-prone. Therefore, in this chapter a new approach of joint-angle-based FES cycling is introduced avoiding the manual determination of stimulation phases by applying a stimulation pattern based on the flexion and extension phases of the estimated hip- and knee-joint angles. All details of this new approach are discussed in the following sections.

3.2.4 Stimulated Muscle Groups

Comparing the selected FES cycling studies in Table 3.1 and the review in [28], it can be concluded that the majority of FES cycling systems achieve independent pedaling of the paralyzed individuals by activating the knee extensors via quadriceps stimulation, knee flexors via hamstrings stimulation, and hip extensors via gluteus maximus stimulation. As shown in [71], the quadriceps contributes most to the total power output in FES cycling, followed by the hamstrings and the gluteus maximus. Accordingly, FES cycling is possible with only a subset of these muscle groups depending on the condition of the paralyzed subject. Furthermore, some experimental studies, especially those involving stroke or cerebral palsy patients, used other muscle groups such as iliacus, tibialis anterior, and gastrocnemius [48, 52, 61].

Except for [70], which uses an implanted spiral cuff electrode to selectively activate the vastus lateralis, medialis, and intermedius, surface electrodes are placed over the muscle groups. Figure 3.2 shows the main joint moment of each stimulated muscle group in italics and the unwanted “side effect” in normal letters. The unwanted muscle actions of surface stimulation result from the bi-articular nature of the quadriceps and hamstring muscles. To achieve an effective and smooth cycling motion the muscle groups must be activated at appropriate times during the 360 degree crank cycle. Furthermore, the unwanted “side effects” need to be taken into account to avoid unintended joint motions and to minimize total energy expenditure of the stimulated muscles.

3.3 Simulation Environment for FES Cycling

In this section, the biomechanical model for FES cycling is described, which is used for simulations. The model is based on a combination of an artificial muscle model and a rigid-body simulation. Using such a biomechanical model has been proven (see [28, 76]) to be useful for testing new algorithms and

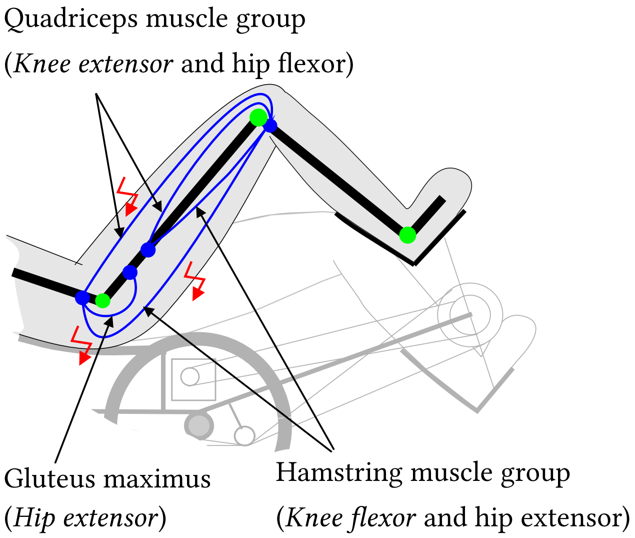

Figure 3.2: Stimulated muscle groups during FES cycling using surface electrodes. Desired muscle activities by the stimulation are shown in italics and the unwanted "side effect" in normal letters (adapted from [28]).

concepts for FES cycling. Setting up experiments, e.g., attaching the electrodes to the right positions as well as attaching the inertial sensors is time-consuming. A simulation offers a more efficient possibility to pretest different methods or scenarios and to validate and compare them before using the experimental set-up.

3.3.1 Overview

To simulate the human muscles during artificial activation, a model developed by Riener and Fuhr [77] is used. Their research provides a complete model for FES-induced movements of the lower-limb system, including nine muscles per leg (Mono-articular hip flexors, mono-articular hip extensors, hamstrings, biceps femoris (short head), rectus femoris, vasti, gastrocnemius (lat. & med. head), mono-articular ankle plantarflexors, ankle dorsalextensors). Although the model was developed for FES induced standing it has gained acceptance in the FES community to describe the dynamics of the knee in response to electrically stimulated muscle contractions. The model takes the nonlinear static and dynamic properties of the involved skeletal muscles as well as tendon tissues into account [78]. The outputs of the model are joint moments based on a certain geometry. Compared to the original model the produced ankle moment was neglected, since in the majority of FES cycling applications the ankle joint is fixated to prevent extensive flexion or extension. The model has been configured to choose the involved muscles arbitrarily. Additionally, it models muscle fatigue which has a high impact on FES applications in paraplegic subjects.

For the mechanical simulation model of the body segments, the SimScape Multibody toolbox of Matlab/Simulink$^{\text{TM}}$ (The Mathworks, Inc., USA) is used. Using this simulation framework instead of solving the equation of motion by hand, provides the ability to set-up a model fast and to change parts of the model without resolving the equations. Another reason to use this simulation framework is that it offers the possibility to simulate inertial sensors to test the complete control loop, including the generation of inertial-sensor data and the orientation estimation. Advantageously, SimScape Multibody offers an animated visualization of the simulation by default. This helps to understand

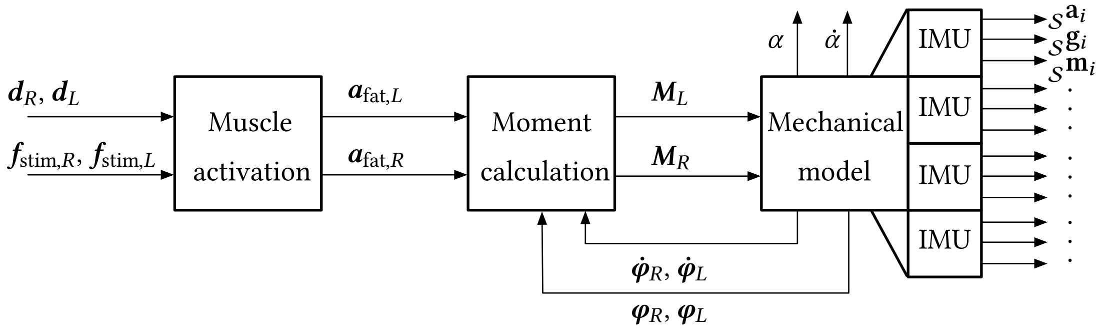

Figure 3.3: Structure of the simulation model with R and L indicating right and left leg. The model calculates the resulting muscle activation $a_{\text{fat},L}$ and $a_{\text{fat},R}$ and the generated joint moments M_L and M_R using pulse widths d_R and d_L and stimulation frequencies $f_{\text{stim},R}$, $f_{\text{stim},L}$ as inputs. The joint moments are the sum of active, passive elastic, and passive viscous joint moments. The moments are fed to the mechanical model to generate joint angles φ_R and φ_L and angular velocities $\dot{\varphi}_R$ and $\dot{\varphi}_L$. The attached virtual inertial sensors generate accelerometer ${}_S\mathbf{a}_i$, gyroscope ${}_S\mathbf{g}_i$, and magnetometer ${}_S\mathbf{m}_i$ measurements for each sensor (attached to the shank or thigh), where i indicates the sensor index. The crank angle α and crank cadence $\dot{\alpha}$ are additional outputs of the mechanical model.

problems better than just using output plots. Finally, it is an easy way to present the concept of FES cycling. The created simulation model is divided into the following four parts:

- Model of muscle activation and its dynamics;
- Passive and active joint moments generated by the muscles and tendons;
- Rigid-body skeletal mechanical model for cycling;
- Virtual inertial sensors;

The different parts are connected with each other as shown in Figure 3.3.

3.3.2 Muscle Activation and Joint-Moment Generation

For simplicity the time index t is dropped for all variables. The model of the muscle activation is used to calculate an activation factor $a_{\text{fat},R},\ a_{\text{fat},L} \in \mathbb{R}^9$ which represents the activation of nine muscles per leg, including fatigue effects. The factors are in the range of $[0, 1]$ where 0 indicates no activation and 1 full activation. The stimulation input is defined by the pulse widths $d_R,\ d_L \in \mathbb{R}^9$ and the stimulation frequencies $f_{\text{stim},R},\ f_{\text{stim},L} \in \mathbb{R}^9$. Using the activation factor and the actual joint angles as well as the angular velocities, the generated moments $M_R \in \mathbb{R}^2$ and $M_L \in \mathbb{R}^2$ for the hip and for the knee joints of both legs are calculated. The calculated total joint moments are the sum of active, passive elastic, and passive viscous joint moments and are applied to the mechanical model. This model determines the resulting joint angles $\varphi_R,\ \varphi_L \in \mathbb{R}^2$ and angular rates $\dot{\varphi}_R,\ \dot{\varphi}_L \in \mathbb{R}^2$ which are needed for the previously mentioned moment calculation. Since the mechanical model is equipped with virtual inertial sensors, their sensor data are the main output of the model. Thus, up to four sets of 3D accelerometer, gyroscope, and magnetometer data are available. Additionally, the crank angle $\alpha \in \mathbb{R}$ and crank-angle velocity $\dot{\alpha} \in \mathbb{R}$, which can also be called crank cadence, are obtained. For the model of muscle activation and moment calculation, the muscle indices and joint-angle conventions from [77] are used.

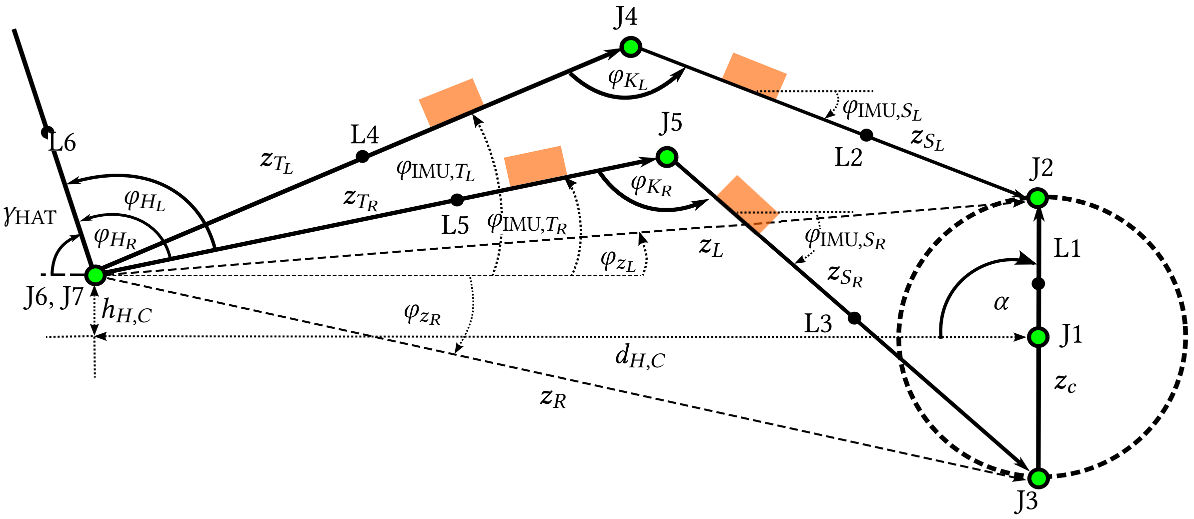

Figure 3.4: Six-bar linkage model for simulating the kinematics and dynamics of an individual during cycling. It shows the bodies L1-L6, the joints J1-J7 that are marked green, and four IMU sensors (orange boxes) at each segment. Furthermore, all relevant parameters used throughout this chapter are introduced: z_R , z_L : Vector from the hip joint to the ankle joint for the right and left leg; φ_{z_R}, φ_{z_L}: inclination angles of these vectors; z_{T_R}, z_{T_L} : Vectors of the right and left thigh; z_{S_L}, z_{S_R}: Vectors of the right and left shank; $\varphi_{\mathrm{IMU},T_R}$, $\varphi_{\mathrm{IMU},T_L}$, $\varphi_{\mathrm{IMU},S_L}$, $\varphi_{\mathrm{IMU},S_R}$: Inclination angles of the IMUs mounted at the shanks and thighs; z_c: Vector of the crank (from J3 to J2); φ_{K_L}, φ_{K_R}: Knee angles of the right and left leg; φ_{H_R}, φ_{H_L}: Hip angles of the right and left leg; α: Crank angle; $h_{H,C}$: Vertical distance between height of J1 and J6,J7; $d_{H,C}$: Horizontal distance between J6 and J1; γ_{HAT}: Inclination angle of the torso (L6).

Linkage ID	Bodies
L1	Crank shaft and arms
L2	Shank left
L3	Shank right
L4	Thigh left
L5	Thigh right
L6	Torso

Joint ID	Joints
J1	Crank shaft
J2	Pedal joint (left)
J3	Pedal joint (right)
J4	Knee joint left
J5	Knee joint right
J6	Hip joint left
J7	Hip joint right

Table 3.2: Designations of the six-bar linkage model. Left: Linkage IDs and corresponding bodies. Right: Joint IDs and corresponding joints.

3.3.3 Mechanical Model of Cycling

In the previous section, a model of muscles that react to electrical stimulation was introduced. The outputs of the previous part are the muscle and tendon-induced joint moments of the hip joint and knee joint for each leg (cf. Figure 3.3). To get the desired simulation data and to close the loop (for joint-moment calculation), a mechanical model of an individual who is performing a cycling motion is needed.

For the simulation of the kinematics and the dynamics of an individual pedaling on an ergometer and tricycle, a six-bar linkage model is created and implemented. In this model, all joints are hinge joints. This is an abstraction from reality, since the hip and knee joints have more than one degree of freedom [79] but can be simplified for the constrained cycling motion. Since all cycling devices for paraplegics restrict the movement of the ankle joint for safety reasons, these joints were modeled as a fixed orthogonal connection. The six-bar linkage model, which is implemented using Simscape Multibody™, is shown in Figure 3.4. The used designations are summarized in Table 3.2. In the presented six-bar linkage model, the distance $d_{H,C}$ and the height offset $h_{H,C}$ of the hip joint to the crank shaft can be parametrized. This offers the possibility to simulate different scenarios which can be present at some experimental set-ups. For example, by varying $d_{H,C}$ different distances for different individuals or even for different runs of the experiment, e.g., due to the wheelchair not being placed exactly the same, can be simulated.

All bodies are rigid and do not allow any twist or stretch. All body lengths can be adjusted individually and could be changed at will, but since the muscle model [77] is derived using specific lengths for these parts, the model is fed with the same lengths as in simulation study [77] to ensure compatibility.

The inputs of the presented six-bar linkage model are the muscle/tendon induced joint moments for the hip, knee, and ankle joint of each leg. Since the ankle joints are fixed, the corresponding moments are ignored. Additionally, it is possible to apply an auxiliary moment to the joint J1 which models a motor. This motor offers the possibility to set the system in motion or brake the cycling motion and to simulate any motorized device. The applied moment can also be used to simulate the inertia of a tricycle during movement. For comparability, the proposed six-bar linkage model offers the possibility to output the crank angle α. Further, it provides the cadence of the crank joint J1. The direction and starting point of α are shown in Figure 3.4.

Most importantly, the model outputs the angles and angular velocities of the hip and knee of both legs. Since those angles are used as feedback for the moment calculation, they are given accordingly to the angle definition used by [77]. Further, the angle γ_{HAT} of the torso is adjustable to model different scenarios. Additionally, the bodies L4, L5, L6, and L7 offer anchor points to place virtual inertial sensors on them (see orange boxes in Figure 3.4). The sensors can be arbitrarily orientated at those anchor points.

The complete six-bar linkage model is placed in the fixed reference frame of the Simscape Multibody simulation. To simulate different orientations of the cycling model, the possibilities to rotate the model around the z-axis as well as around the y-axis of the fixed reference frame are implemented. This results in a yaw and/or in a pitch motion of the entire linkage model with respect to the fixed reference frame. This ability can be used to validate algorithms for inertial sensors where the orientation of the model with respect to the fixed reference frame matters.

3.3.4 Virtual Inertial Measurement Unit

The simulation model needs to be capable of generating 3D inertial sensor data, i.e. acceleration data, angular rates, and magnetometer data. For creating the virtual inertial sensor, Simscape Multibody is used as well. In Simscape Multibody, every model has a so-called *World Frame*. This frame is the fixed, global reference which is denoted by $\mathcal{E}$ for every other frame placed within the model. To measure movement-based data, Simscape Multibody offers a block called *Transform Sensor*. This block measures rotations, translations, and its derivatives of one frame relative to another. The measured data is represented with respect to the coordinates of one of those frames. With these prerequisites, a new Simulink/Simscape Multibody block which simulates an inertial sensor is created.

To create a virtual inertial sensor, the introduced quaternion algebra of Section 2.4.1 is used and for simplicity the sampling index k is dropped. It is assumed that there is a Simscape Multibody model with its reference frame and an arbitrary rotated and translated frame, which is called sensor frame (see Figure 2.2). As in the previous chapter, the sensor frame represents the local coordinate system of an inertial sensor. Simscape Multibody provides

- acceleration ${}_{\mathcal{E}}\boldsymbol{a} \in \mathbb{R}^3$ of the sensor frame relative to the fixed reference frame on three axes stated in the fixed reference frame (this excludes the gravitation),
- the angular velocity ${}_{\mathcal{E}}\boldsymbol{g} \in \mathbb{R}^3$ of the sensor frame relative to the fixed reference frame on three axes stated in the fixed reference frame, and
- the orientation of the sensor frame expressed as a quaternion ${}^{\mathcal{S}}_{\mathcal{E}}\boldsymbol{q} \in \mathbb{H}$ from the fixed reference frame to the sensor frame.

The goal is to generate the

- the acceleration ${}_{\mathcal{S}}\boldsymbol{a} \in \mathbb{R}^3$ stated in the sensor frame including the gravitation,
- the angular velocity ${}_{\mathcal{S}}\boldsymbol{g} \in \mathbb{R}^3$ stated in the sensor frame, and
- the magnetic field vector ${}_{\mathcal{S}}\boldsymbol{m} \in \mathbb{R}^3$ stated in the sensor frame.

Coordinate transformations using quaternion algebra (see Equation (2.15)) are used to calculate the desired data using the provided ones by Simscape Multibody.

First of all, the direction of the earth gravitation and the direction of the magnetic field vector in the fixed reference frame are defined. Common choices for the field directions, which are also used in this work, are

$$ {}_{\mathcal{E}}\boldsymbol{e}_{\mathrm{dir}} = \begin{bmatrix} 0 & 0 & -1 \end{bmatrix} \quad \text{and} \quad {}_{\mathcal{E}}\boldsymbol{m}_{\mathrm{dir}} = \begin{bmatrix} 0 & 1 & 0 \end{bmatrix}, \tag{3.2} $$

where both direction vectors have a euclidean norm of 1. Then, the Simscape Multibody acceleration output ${}_{\mathcal{E}}\boldsymbol{a}$ is combined with the gravitation vector. Since the acceleration data is already in the fixed reference frame, adding the gravitation leads to the complete acceleration

$$ {}_{\mathcal{E}}\boldsymbol{a}_{\mathrm{g}} = {}_{\mathcal{E}}\boldsymbol{a} + 9.81\,\frac{\mathrm{m}}{\mathrm{s}^2}\,{}_{\mathcal{E}}\boldsymbol{e}_{\mathrm{dir}}, \qquad {}_{\mathcal{E}}\boldsymbol{a}_{\mathrm{g}} \in \mathbb{R}^3 \tag{3.3} $$

in the fixed frame. For simplicity the unit of the local magnetic field is set to 1. After all the data is collected in the fixed reference frame, it is required to rotate it to the sensor frame. The orientation quaternion ${}^{\mathcal{S}}_{\mathcal{E}}\boldsymbol{q}$ and Equation (2.15) are used to perform the rotation:

$$ {}_{\mathcal{S}}\boldsymbol{a} = {}^{\mathcal{S}}_{\mathcal{E}}\boldsymbol{q} \otimes {}_{\mathcal{E}}\boldsymbol{a}_{\mathrm{g}} \otimes {}^{\mathcal{S}}_{\mathcal{E}}\boldsymbol{q}^{*} \tag{3.4} $$

$$ {}_{\mathcal{S}}\boldsymbol{g} = {}^{\mathcal{S}}_{\mathcal{E}}\boldsymbol{q} \otimes {}_{\mathcal{E}}\boldsymbol{g} \otimes {}^{\mathcal{S}}_{\mathcal{E}}\boldsymbol{q}^{*} \tag{3.5} $$

$$ {}_{\mathcal{S}}\boldsymbol{m} = {}^{\mathcal{S}}_{\mathcal{E}}\boldsymbol{q} \otimes {}_{\mathcal{E}}\boldsymbol{m}_{\mathrm{dir}} \otimes {}^{\mathcal{S}}_{\mathcal{E}}\boldsymbol{q}^{*} \tag{3.6} $$

Then, all the data is given with respect to the sensor frame which provides the possibility to simulate an ideal inertial sensor using Simscape Multibody without noise and bias, and with a simulated magnetometer with exact undisturbed heading information.

3.4 Joint-Angle Estimation

To generate a cycling movement, the stimulation pattern must be chosen so that the corresponding muscles are stimulated whenever they generate a positive moment at the crank. In [28] and [76] formulas for deriving initial stimulation patterns based on the crank angle are presented. Hereby, the shank, and thigh lengths and hip to seat distance and seat height are needed. If the seat position changes due to slipping in the seat or if a new patient attends to the training, the measurement is not valid anymore, and a recalibration needs to be done. Therefore, new methods based on the knee- and hip-joint angles are presented. Using these joint angles, the stimulation timing could be aligned to ranges where certain muscles have to be active during cycling. Additionally, it would be possible to detect the flexion and extension phases of each joint and to define the stimulation timing of the corresponding muscle groups without the knowledge of the exact geometric relation of seating position and crank.

In Figure 3.4, the fundamental geometric setting for FES cycling as well as the IMU placement are illustrated for retrieving the knee- and hip-joint angles, which will be used throughout the next sections.

In [28] and [76], the pedal position is assumed to be below the heel which can be guaranteed for the majority of cycling devices. Hence, the ankle joint is very close to the pedal joint. For the majority of paraplegic cycling devices, the foot is fixed using an orthosis or customized pedal which prevents the ankle joint to overstretch in any directions. Therefore, the reduced six-bar linkage model can be assumed, where at each segment of the legs an IMU (see orange boxes in Figure 3.4) is attached using a strap or a sleeve. In the following section, the general estimation method for retrieving the segment inclination is introduced.

3.4.1 Segment-Inclination Estimation

The orientation of each sensor can be estimated using the algorithm of Section 2.4.2. Due to a high probability of magnetic disturbances, e.g. caused by the metal of the cycling device or motor coils of the ergometer, the heading of the orientation, which is the rotation of the horizontal plane around the vertical axis, will be affected by high drift. Hence, the orientation is estimated without using magnetometer measurements. Recalling, that it is assumed that the foot will be fixed using an orthosis, the abduction, adduction, and internal and external rotation of the thigh and shank segments can be neglected. As stated earlier, the sensors are assumed to be mounted at the limbs using a strap or inside a sleeve. Therefore, it can be guaranteed that the longitudinal axis of the limb is aligned with $\mathcal{S}_x$ of the sensor, as shown in Figure 3.5 to a certain degree. This should be even guaranteed if the strap or the sleeve is rotated around the limb. Using the orientation estimation algorithm introduced in Section 2.4.2, the orientation ${}^{S}_{\mathcal{E}}\boldsymbol{q}$ of the sensor can be obtained. Under the assumption, that the longitudinal axis of the segment (thigh or shank) is aligned with the intrinsic x-axis of the sensor and that the sensor intrinsic z-axis points away from the segment the inclination angle can be retrieved. First, the x-axis of the IMU in sensor-frame coordinates is given by ${}_{\mathcal{S}}\mathbf{x}_S = [1\ 0\ 0]^T$. The reference-frame coordinates of this axis are obtained by

$$ {}_{\mathcal{E}}\mathbf{x}_S = {}^{S}_{\mathcal{E}}\boldsymbol{q} \otimes {}_{\mathcal{S}}\mathbf{x}_S \otimes {}^{S}_{\mathcal{E}}\boldsymbol{q}^*. \tag{3.7} $$

Since the z-axis ${}_{\mathcal{E}}\mathbf{z}_{\mathcal{E}} = [0\ 0\ 1]^T$ of the reference frame is vertical by definition, we determine the angle between the aforementioned x-axis of the IMU and the horizontal plane as

$$ \varphi_{IMU,l} = \frac{\pi}{2} - \arccos({}_{\mathcal{E}}\mathbf{z}_{\mathcal{E}}{}^{T}\ {}_{\mathcal{E}}\mathbf{x}_{S,l}) \tag{3.8} $$

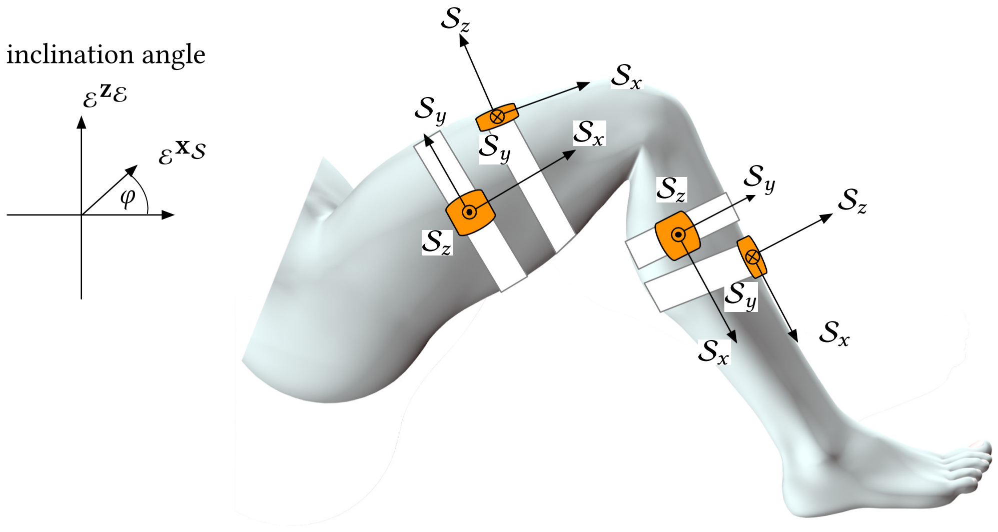

Figure 3.5: Sensor attachment if mounted with a strap or inside a sleeve, where $\mathcal{S}$ describes the local sensor coordinate system as introduced in Figure 2.2. Two possible attachments are shown for the thigh and the shank, respectively. ${}_{\mathcal{E}}\mathbf{z}_{\mathcal{E}}$ describes the z-axis of the reference frame and ${}_{\mathcal{E}}\mathbf{x}_{\mathcal{S}}$ the x-axis transformed into the reference frame. The resulting inclination angle is φ.

where l is a placeholder for the requested segment (see Figure 3.4). This formula is valid as long as the inclination of the segment remains in the range of $[-\frac{\pi}{2}, \frac{\pi}{2}]$ due to the gimbal lock. In the following section, the inclination estimation was tested for different attachment angles and during external heading and inclination movements of the limbs.

3.4.2 Evaluation of Segment-Inclination Estimation Using a Simulation Model

Using the simulation environment introduced in Section 3.3, the cylindrical bar illustrated in Figure 3.6 was simulated with the following permutation setting for γ, η, and ξ:

γ	η	ξ
0, 45, 90, ..., 315	−15, 0, 15	−15, −10, −5, ..., 15

Table 3.3: Permutation of sensor attachment angles in degree.

To simulate a cycling movement, the inclination angle φ was varied between $[-75°, 75°]$. Furthermore, during each trial the heading of the segment α was varied along a trajectory (Figure 3.7) to simulate several rotations around $\mathcal{E}_z$.

In total, 168 simulations have been executed, while the simulated and estimated inclination angles were stored and compared. In summary, it can be stated that the inclination angle estimation produces an Root Mean Square (RMS) error of 0.54 ° with an absolute maximum error of 0.76 ° for variations of γ and η. The estimation is sensitive against variations of ξ, where the RMS error of the inclination value follows ξ, as shown in Figure 3.8. As documented in Figure 3.6, a non-zero ξ results in an offset in the inclination estimation. Hence, the RMS variation increases with increasing ξ, since the inclination angle already reaches gimbal lock for the minimum and maximum simulated inclination angles. Furthermore, the simulated heading rotation during the trials did not influence the inclination-angle estimation. Hence, the main constraint of the inclination estimation is the alignment of the sensor

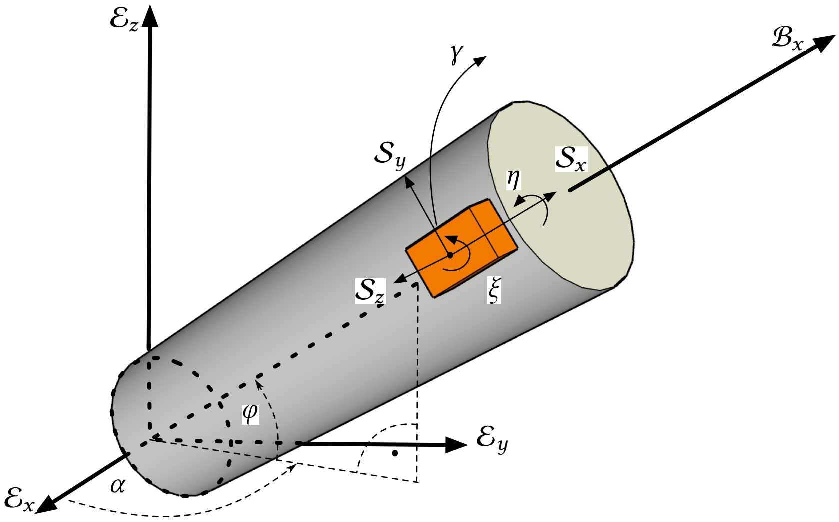
$\mathcal{E}_z$
γ
$\mathcal{B}_x$
$\mathcal{S}_y$
$\mathcal{S}_x$
η
$\mathcal{S}_z$
ξ
φ
$\mathcal{E}_y$
$\mathcal{E}_x$
α

Figure 3.6: Sensor simulation setting where $\mathcal{S}$ describes the sensor coordinate system, $\mathcal{E}$ is the reference coordinate system, α is the heading, and φ is the inclination angle of the segment. Furthermore, $\mathcal{B}_x$ is the longitudinal axis of the segment, γ is the rotation angle of the sensor around the longitudinal axis of the segment, ξ is the rotation around the $\mathcal{S}_z$, and η is the rotation around $\mathcal{S}_x$.

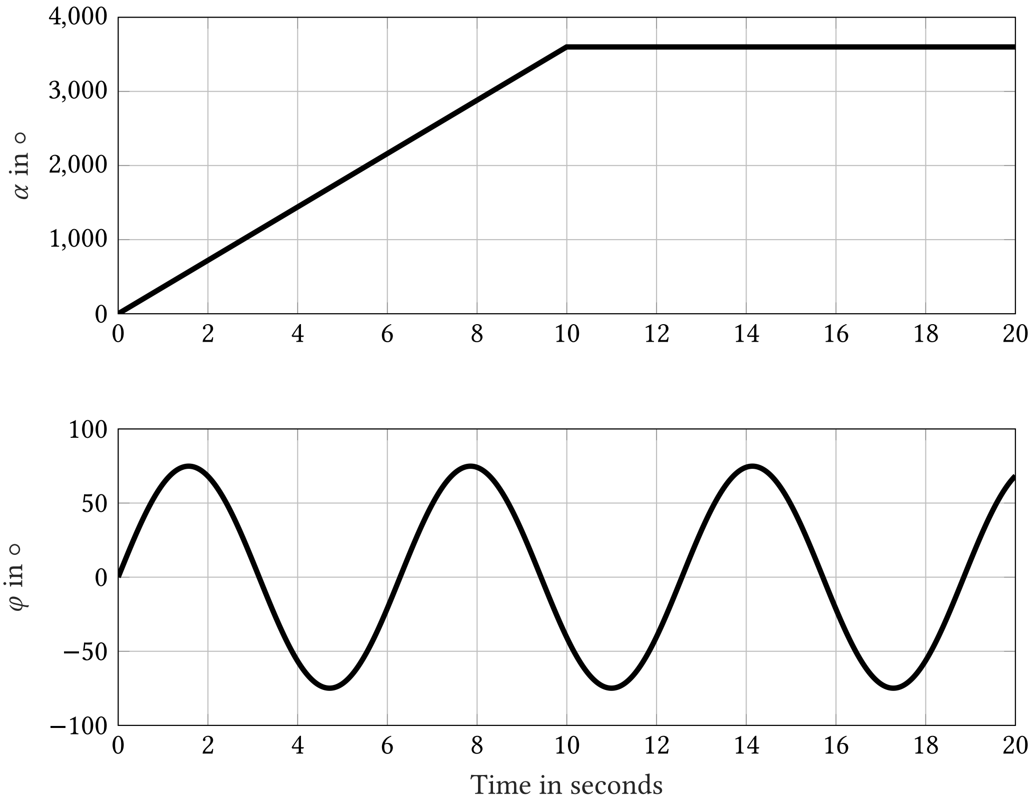

Figure 3.7: Simulated trajectory for heading α and inclination angle φ.

x-axis with the segment's longitudinal axis. This can be guaranteed if the sensor is attached via a strap or sleeve around the thigh or shank which will be shown in Chapter 4 for mobile cycling.

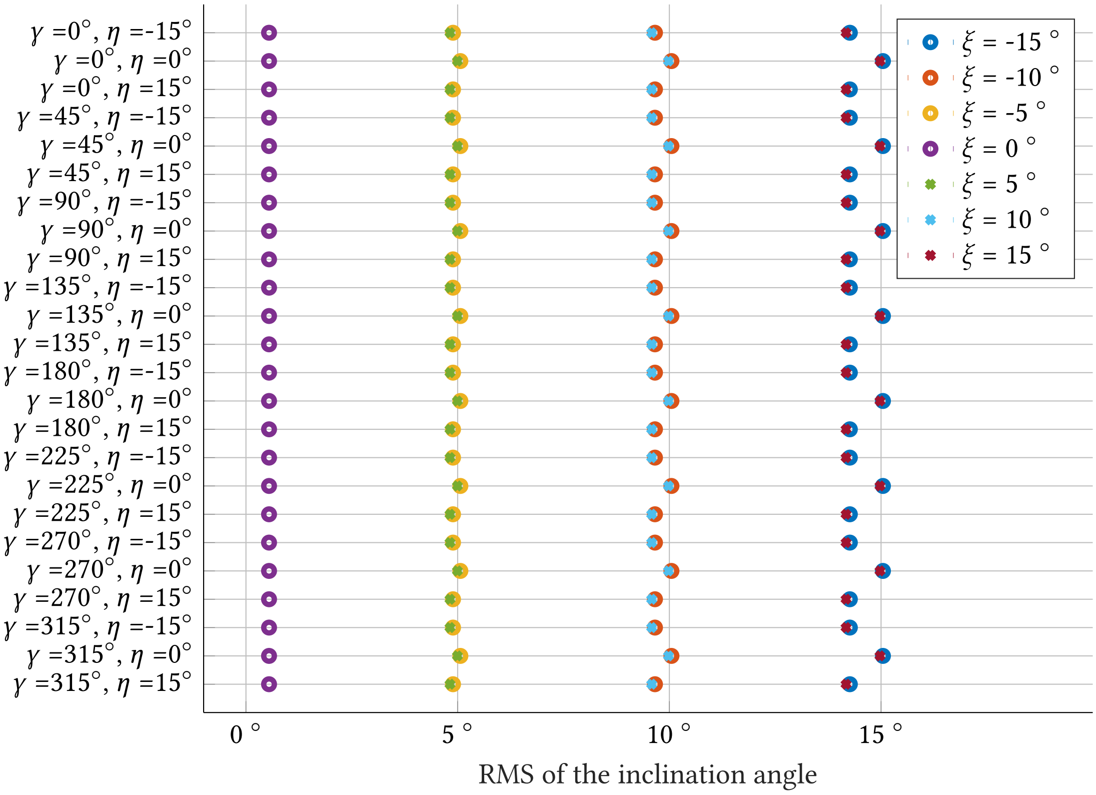

Figure 3.8: RMS of inclination-angle estimation where each marker corresponds to one simulated combination of ξ, γ and η. The x-axis represents the RMS values. The y-axis shows the corresponding γ and η angles. The markers (x and o) describe the ξ value for each experiment.

3.4.3 Experimental Verification of IMU-Based Inclination Estimation

To verify the simulative results, the IMU-based segment-inclination estimation is compared with an optical measurement system. In the first step, the optical motion capturing system OptiTrack (NaturalPoint Inc., USA), the wireless IMU system WaveTrack (Cometa srl., Italy), and the experimental setup are introduced. Secondly, the results including inclination-angle trajectories and mean and absolute-error analysis are presented.

Experimental Setup Optical motion capturing is the process of recording the movement of objects or subjects with several cameras. The captured data are then analyzed to retrieve the position as well as the orientation of the objects or people in physical space. The technology was originally developed for gait analysis in the life-science market, but is now used in a wide variety of other fields. Some of these include computer-graphics animation, robotics, and military use [80]. Basically, there are two types of motion tracking: marker and non-marker based. For this experiment, the marker-based OptiTrack system is used including twelve infrared cameras capturing the 3D position of markers at 120 frames per second (fps).

The used OptiTrack system utilizes retro-reflective markers that are tracked by the infrared cameras. Each camera tracks the six degrees of freedom (DOF) pose of one or more objects in the workspace. To improve the capture results and minimize the error when a marker leaves the working area of one camera and enters the area of the next one, virtual rigid bodies can be defined. Each rigid body is a collection of three or more markers on an object that are interconnected to each other with an assumption that the tracked object is indeformable and the position of the reflective markers

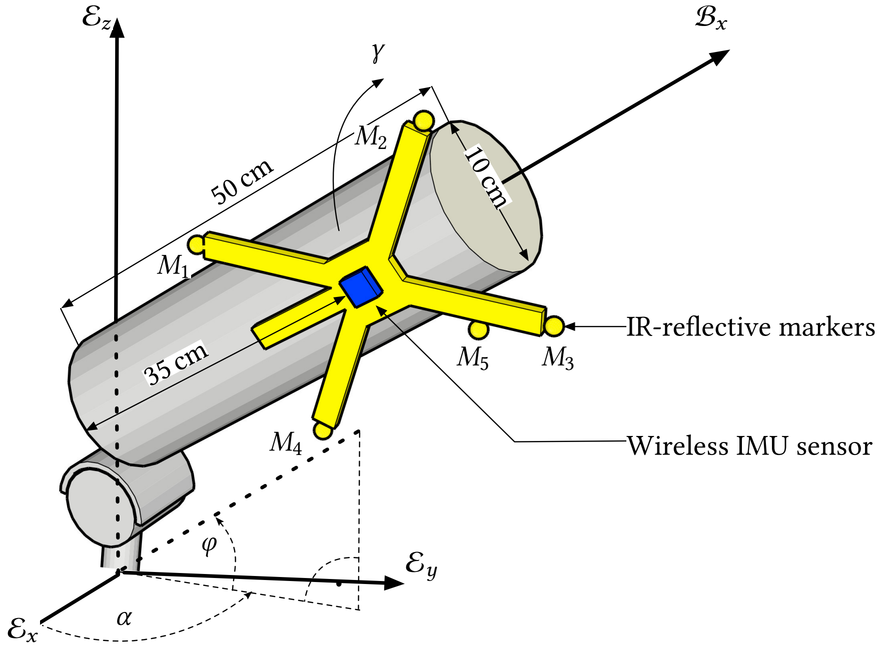

Figure 3.9: Experimental setting for segment-inclination verification where $\mathcal{E}$ is the reference coordinate system, α is the heading, and φ is the inclination angle of the segment. Furthermore, $\mathcal{B}_x$ is the longitudinal axis of the segment, and γ is the rotation angle of the sensor around the longitudinal axis of the segment. The wireless IMU sensor (blue cuboid) is rigidly attached to an optical measurement body. This includes five IR-reflective markers in a defined fixed geometry. The measurement body is attached and aligned with the cylindrical segment. The segment is attached at the ground with a hinge joint, which can be additionally rotated around the reference z-axis.

is unique [80]. If the optical measurement system is calibrated, the 3D location of markers can be resolved with sub-millimeter accuracy.

The following experimental setting shown in Figure 3.9 uses a cylinder mounted on a hinge joint. The hinge joint is fixed at a lab table and can be rotated around the reference z-axis. The IMU sensor is rigidly coupled to the yellow Optical Measurement Body (OMB). This OMB includes five IR-reflective markers M_i in a defined geometry. Using the absolute 3D position of these reflective markers, the orientation of the OMB can be retrieved. The position of the optical markers on each edge is used to calculate the orientation of the OMB. The fifth marker, which lies on the inner side of one bar, is needed so that the tracking software is able to exactly identify each marker for each orientation. In the first step, one normal vector is calculated with

$$\boldsymbol{x}_{opt} = \frac{1}{2\|\boldsymbol{x}_{M1} + \boldsymbol{x}_{M4} - \boldsymbol{x}_{M2} + \boldsymbol{x}_{M3}\|} \left(\boldsymbol{x}_{M1} + \boldsymbol{x}_{M4} - \boldsymbol{x}_{M2} + \boldsymbol{x}_{M3}\right), \tag{3.9}$$

where x_{Mi} is the absolute position in 3D coordinates in reference to the optical point of origin. The resulting vector $\boldsymbol{x}_{opt}$ is coplanar to the intersection plane of the reflective markers and points approximately in the direction of the x-axis of the IMU sensor. Since the sensor is rigidly attached to the optical measurement body the IMU x-axis and the resulting $\boldsymbol{x}_{opt}$ differ by a constant quaternion $\boldsymbol{q}_a$, which describes a fixed rotation around all three axes. This quaternion can be found by minimizing the overall error between the optical and inertial inclination error. The orientation-estimation algorithm of Section 2.4.2 has been used with gyroscope and accelerometer measurements at a frequency of 75 Hz and $k_{\text{acc}} = 1$ and $k_{\text{mag}} = 0$.

Results During one experiment five different rotation angles γ were tested. For each angle, several up and down movements of the segment were performed while the segment was rotated as well around the z-axis to simulate a heading movement. The inclination angle as well as the absolute value of the error and its RMS between the optical and inertial measurement are presented in Figure 3.10 (a) to (e). An RMS error of 0.8-1.8 ° with a maximum error of 2.8-3.2 ° was achieved for all different γ angles.

3.4.4 Knee- and Hip-Joint-Angle Estimation

To calculate the joint angles out of the previously calculated inclination angles, the general geometric structure of the cycling motion is exploited. Additionally, the assumption is made that the inclination angle of the inertial sensors represents the inclination angle of each segment. Furthermore, it is assumed that the knee joint can be approximated by a hinge joint. This should be valid, since the foot is rigidly attached to the pedal via an ankle orthosis in a fixed angle of 90 °, which constraints other movements of the knee joint. Hence, a simple triangle geometry can be applied to calculate the joint angles. The basic geometry of one leg, which is similar to the six-bar linkage model derived in Section 3.3.3, is shown in Figure 3.11. The hip-joint angle φ_{H} is defined as the angle between the thigh and the torso. Using the angle $\varphi_{\mathrm{IMU,T}}$, which is determined by using the inertial sensor on the thigh, the hip-joint angle can be calculated by

$$\varphi_{\mathrm{H}} = \pi - \varphi_{\mathrm{IMU,T}} - \gamma_{\mathrm{HAT}} \quad \text{with} \quad \varphi_{\mathrm{IMU,T}}, \gamma_{\mathrm{HAT}} \in \mathbb{R}. \tag{3.10}$$

The angle γ_{HAT} describes the inclination of the torso. This angle should be determined through the geometry of the seat or wheelchair and results in a constant offset.

The knee-joint angle is calculated analogous, but it utilizes the inertial sensors on the thigh and the shank as described by

$$\varphi_{\mathrm{K}} = \pi - \varphi_{\mathrm{IMU,T}} - \varphi_{\mathrm{IMU,S}} \quad \text{with} \quad \varphi_{\mathrm{IMU,S}} \in \mathbb{R}. \tag{3.11}$$

One of the possible main disturbances, while performing FES cycling with a moving device on a non-flat ground, is the pitch motion of the whole system. In the presented FES cycling set-up, the disturbance on the inclination of the sensors influences the hip joint-angle calculation, since there is just one sensor used. The knee-joint-angle calculation is not influenced by those disturbances, because it uses two sensors, which are equally influenced. Since this problem is caused by a variable pitch of the whole system, it does not appear while using a stationary ergometer and is related to the usage of mobile devices on non-flat ground.

If the hip-joint angle shall be used for mobile cycling, a solution to that problem is the use of an additional sensor that is not moved by the lower limbs while performing the cycling motion. Therefore, this sensor should not be placed on either the thigh or the shank. One possible placement is the seat or frame of the tricycle. Since this sensor is not influenced by the process of pedaling, it measures the inclination of the tricycle itself, which can be used to remove the tricycle pitch from the other sensors by doing a quaternion multiplication.

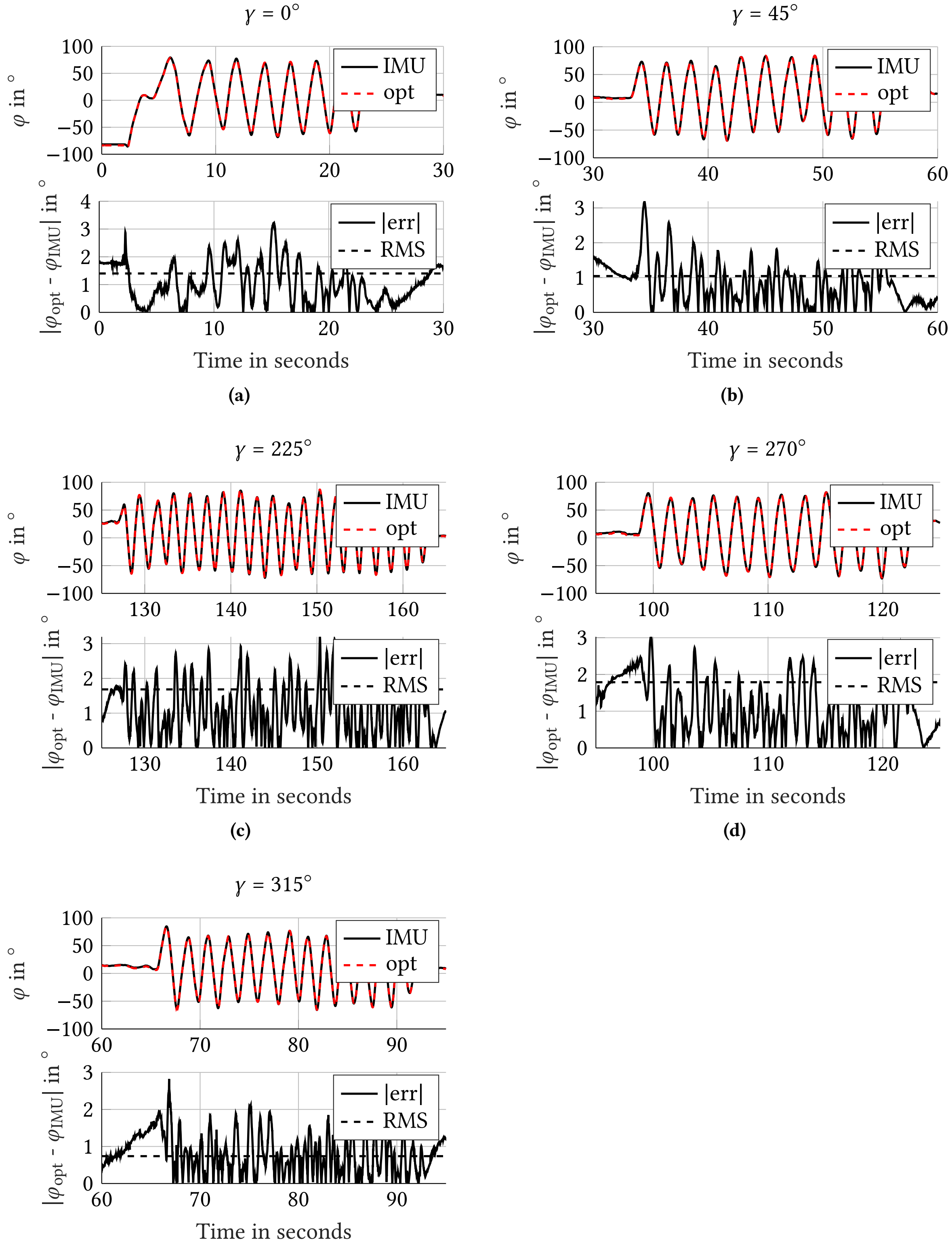

(a)

(b)

(c)

(d)

(e)

Figure 3.10: Comparison of optical and inertial measurement. For each measurement trial, the optical measurement body has been rotated around the longitudinal axis of the cylinder by $\gamma = [0°, 45°, 225°, 270°, 315°]$. For each γ configuration, several up and down movements in the range $[-70°\ldots70°]$ and rotation movements around the reference z-axis were performed.

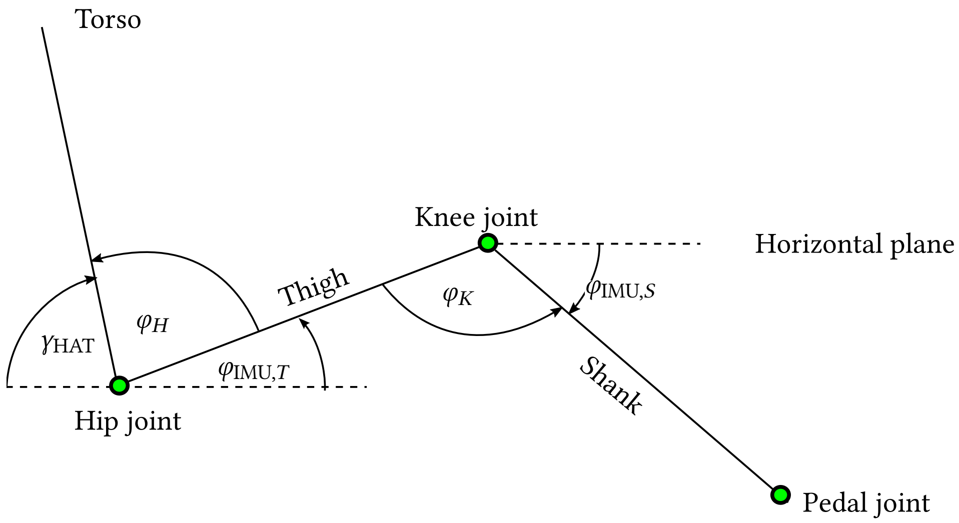

Figure 3.11: Geometry of the lower limbs of one leg for calculating joint angles based on inertial sensors. The triangle formed by the thigh, shank, and horizontal plane shows the measured inclination angles $\varphi_{\mathrm{IMU,S}}$ and $\varphi_{\mathrm{IMU,T}}$ using Eq. (3.7) and (3.8) and the joint angles φ_{H} and φ_{K} as well as the angle of the torso γ_{HAT}. Foot, pedal, and crank arm have been omitted for simplicity.

3.5 Joint-Angle-Based Stimulation Pattern

A stimulation pattern is a scheme that determines the muscle stimulation timing. It is usually driven by the crank angle as an input. Therefore, the pattern creates a mapping from the crank angle to an activation of the used muscles. One reason to use the stimulation pattern-based control is that the muscle dynamics are rather slow and have patient- and fatigue-specific delays. Hence, direct feedback mechanisms cannot be applied easily. Furthermore, the muscles have a limited functional range, which means that a certain muscle shall only be active during its support phase for the cycling motion. Such a functional range is encoded by the stimulation pattern.

3.5.1 Joint-Angle Transformation

A simple transformation is used to map the absolute joint angles of knees and hips to ranges of extension and flexion. Each joint angle, which is estimated by using the methods presented in Section 3.4.4, is mapped to the fixed range of $[0, 1[$. Such a mapping offers the possibility of specifying sectors of joint-angle flexion and extension. These sectors are independent of the seating position or geometry (e.g., thigh lengths, the distance of the seat-to-crank and seat height with respect to the crank). Thus, a stimulation pattern based on transformed joint angles can be used for most systems and individuals without modification. The transformed joint angle is denoted by the term cycle percentage (CP) in the rest of this thesis, which is determined in the range $[0, 1[$. The CP range can be divided into two parts. During joint extension, the CP value, as per definition, lies between 0.0 and 0.5, while during joint flexion it lies between 0.5 and 1.0, as summarized in Table 3.4.

Two steps are required to perform the transformation. In the first step, the estimated joint angle is continuously searched for its maximum and minimum value. The joint-angle trajectory during cycling can be approximated by a periodic oscillation. The peak detection determines the amplitude of this oscillation. Continuous peak detection is needed, since the amplitude and offset of the oscillation change due to disturbances, e.g., sliding on the seat and sensor wobbling due to soft tissue movement while stimulating. The current peaks (including the maximum peak and the minimum peak) are used

CP Range	Joint Behaviour
0.0	turning point before the joint extension
$0.0 < \mathrm{CP} < 0.5$	joint extension
0.5	turning point before joint flexion
$0.5 < \mathrm{CP} < 1.0$	joint flexion

Table 3.4: Sectors of the cycle percentage. This table shows the sectors of the CP signal and their meaning for a joint, i.e., mapping to joint extension and flexion.

to scale the signal to the range $[0, 1]$.

Let $\varphi \in \mathbb{R}$ be a joint angle which is oscillating. Furthermore, let $p_\mathrm{t} \in \mathbb{R}$ be the current maximum peak and $p_\mathrm{b} \in \mathbb{R}$ the current minimum peak. Then, the angle signal φ^B is bounded by the equation:

$$\varphi^\mathrm{B} = \frac{\varphi - p_\mathrm{b}}{p_\mathrm{t} - p_\mathrm{b}}, \qquad \varphi^\mathrm{B} \in [0, 1],\ \varphi \in [p_\mathrm{b}, p_\mathrm{t}]. \tag{3.12}$$

The resulting signal φ^B is still an oscillation but bounded to $[0, 1]$. One period of this oscillation denotes a complete cycle in the performed cycling motion. In the second step, the bounded joint angle is transformed into the Cycle Percentage (CP) $\varphi^\mathrm{CP} \in [0, 1[$, which grows from 0 to 1 and then jumps back to 0, similar to a saw-tooth signal. The CP can easily be divided into two sectors defined by

$$\varphi^\mathrm{CP} = \begin{cases} \frac{\varphi^\mathrm{B}}{2} & \text{for} \quad \dot{\varphi}^\mathrm{B} > 0 (\text{extension}) \\ 1 - \frac{\varphi^\mathrm{B}}{2} & \text{for} \quad \dot{\varphi}^\mathrm{B} \leq 0 (\text{flexion}). \end{cases} \tag{3.13}$$

At the step where φ^CP is calculated, some error corrections for real measurements can be included, e.g., a hysteresis at the switching points and smoothening, to make the CP signal a more robust stimulation trigger. The complete signal processing of a joint-angle estimate is shown in Figure 3.12 as an example.

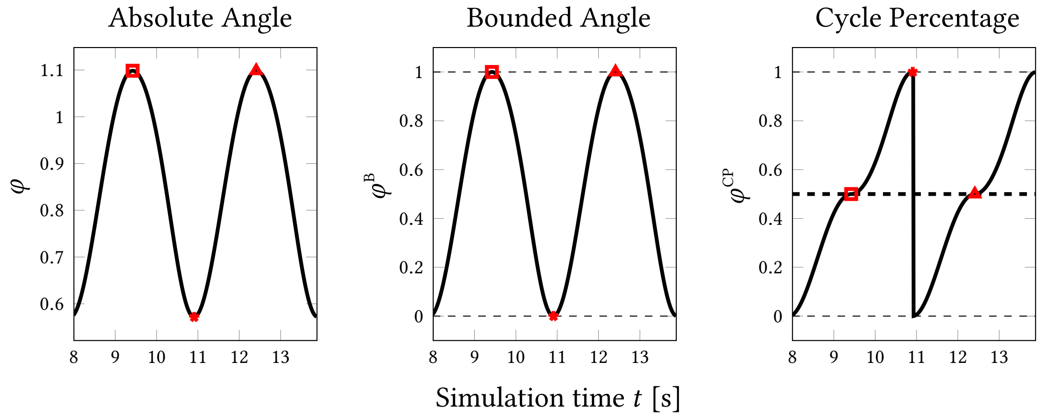

Figure 3.12: Joint-angle signal processing. Left: Absolute joint angle (black, solid) with detected peaks (red markers). Middle: Joint angle (black, solid) bounded to $[0, 1]$ with corresponding peaks (red, markers). Right: Cycle Percentage φ^CP (black, solid) with corresponding peaks (red, markers) and a sector border to delimit extension (< 0.5) from flexion sector (> 0.5).

3.5.2 Robust Discrimination of Leg Extension and Flexion Phases

The described joint-angle transformation is sufficient, as long as it is ensured that the cycling motion does not stop and there are no disturbances resulting in a change of sign of the angular velocity prior to the “correct" switching points. This can be guaranteed for stationary cycling if an assistive motor helps to overcome “dead zones", where no muscle is active and keeps the legs cycling. In the case of unassisted mobile cycling, if the pilot stops due to fatigue or spasticity, and he/she wants to start again, the pedal position is not clear. This can only be prevented if the cyclist moves his legs manually forward until the switching between flexion and extension is clear.

To guarantee a safe switching between the phases for the knee joints, a new criterion has been developed based on the polar coordinates of the right and the left leg, z_R and z_L, as introduced in Figure 3.13. Using the complex polar coordinate notation, the vectors z_{T_L} (left thigh), z_{T_R} (right thigh), z_{S_L} (left shank), and z_{S_R} (right shank) can be formulated as complex numbers

$$z_{T_L} = l_T e^{i\varphi_{IMU,T_L}} \qquad z_{T_R} = l_T e^{i\varphi_{IMU,T_R}} \tag{3.14}$$

$$z_{S_L} = l_S e^{i\varphi_{IMU,S_L}} \qquad z_{S_R} = l_S e^{i\varphi_{IMU,S_R}} \tag{3.15}$$

where l_T describes the thigh length and l_S is the shank length under the assumption that the segment lengths of the right and left side are the same. The vectors from the hip joints to the pedal joints can be now formulated with

$$z_L = z_{T_L} + z_{S_L} \tag{3.16}$$

$$z_R = z_{T_R} + z_{S_R}, \tag{3.17}$$

with the assumptions that each pedal joint is mounted approximately below the heel, and the ankle joint is fixed at 90 °. The segment lengths l_T and l_S are almost identical if the distance from the knee joint to the pedal joint is taken into account when determining l_S. This assumption is used to simplify the further steps and supersedes the measurement of the cyclist’s segment lengths. The angles of z_L and z_R can be calculated by

$$\varphi_{z_L} = \operatorname{atan2}(l(\sin\varphi_{IMU,T_L} + \sin\varphi_{IMU,S_L}), l(\cos\varphi_{IMU,T_L} + \cos\varphi_{IMU,S_L})) \tag{3.18}$$

$$\varphi_{z_R} = \operatorname{atan2}(l(\sin\varphi_{IMU,T_R} + \sin\varphi_{IMU,S_R}), l(\cos\varphi_{IMU,T_R} + \cos\varphi_{IMU,S_R})), \tag{3.19}$$

where l is the thigh and shank segment length which can be neglected due to

$$\operatorname{atan2}(b,a) = \begin{cases} \arctan\left(\frac{b}{a}\right) & \text{for} \quad a > 0 \\ \arctan\left(\frac{b}{a}\right) + \pi & \text{for} \quad a < 0, b \geq 0 \\ \arctan\left(\frac{b}{a}\right) - \pi & \text{for} \quad a < 0, b < 0. \\ \frac{\pi}{2} & \text{for} \quad a = 0, b > 0 \\ -\frac{\pi}{2} & \text{for} \quad a = 0, b < 0 \end{cases} \tag{3.20}$$

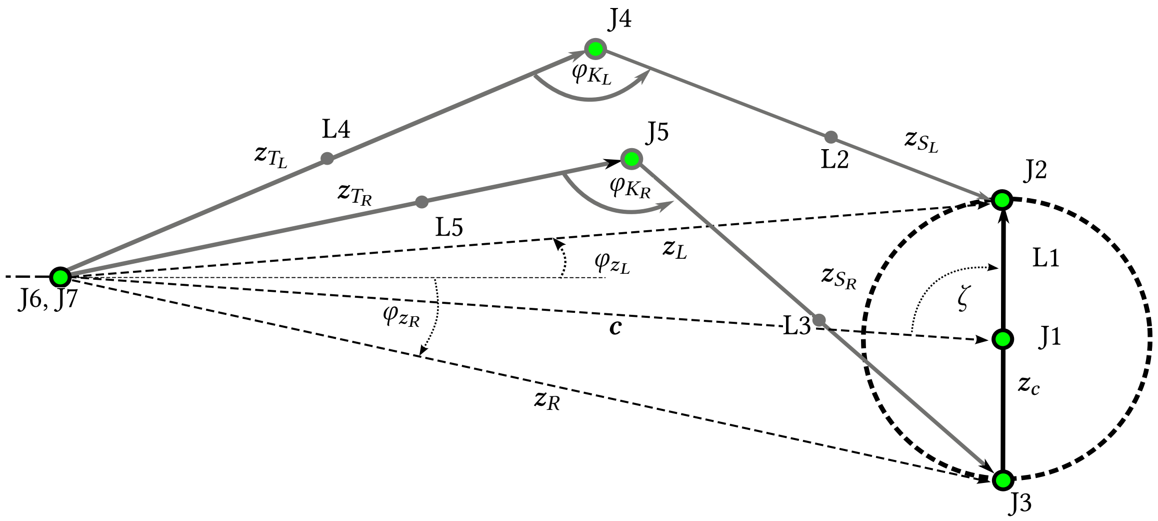

Figure 3.13: Simplified linkage model for the proof of flexion and extension phase discrimination. All relevant parameters are the same as in Figure 3.4. The vector $\boldsymbol{c}$ is introduced which is the direct connection between the hip joints J6, J7 and the crank joint J1 in the sagittal plane. Furthermore, the angle ζ describes the angle between the vectors $\boldsymbol{z_c}$ and $\boldsymbol{c}$.

Using these derived inclination angles, the transformation in (Eq. 3.13) can be changed to

$$\varphi_{K_L}^{\mathrm{CP}} = \begin{cases} \frac{\varphi_{K_L}^{\mathrm{B}}}{2} & \text{for} \quad \varphi_{z_L} > \varphi_{z_R} \\ 1 - \frac{\varphi_{K_L}^{\mathrm{B}}}{2} & \text{for} \quad \varphi_{z_L} < \varphi_{z_R} \end{cases} \qquad \text{and} \tag{3.21}$$

$$\varphi_{K_R}^{\mathrm{CP}} = \begin{cases} \frac{\varphi_{K_R}^{\mathrm{B}}}{2} & \text{for} \quad \varphi_{z_L} > \varphi_{z_R} \\ 1 - \frac{\varphi_{K_R}^{\mathrm{B}}}{2} & \text{for} \quad \varphi_{z_L} < \varphi_{z_R} \end{cases}. \tag{3.22}$$

This means that if the inclination angle of one leg gets bigger than the other, the knee-joint state switches from flexion to extension. This can be motivated with following geometric proof using Figure 3.13. If the crank $\boldsymbol{z_c}$ is rotated to the position where J2 has the farthest distance from J6, then J3 has the shortest distance from J7. With $\boldsymbol{c}$ describing the vector from the hip joint J6 or J7 to the crank joint J1, the vector $\boldsymbol{z_L}$ can be formulated as

$$\boldsymbol{z_L} = \boldsymbol{c} + \frac{1}{2}\boldsymbol{z_c}. \tag{3.23}$$

In general, by applying the law of cosines the length of $\boldsymbol{z_L}$ can be calculated with

$$|\boldsymbol{z_L}| = \sqrt{\frac{1}{4}|\boldsymbol{c}|^2|\boldsymbol{z_c}|^2 - |\boldsymbol{c}||\boldsymbol{z_c}|\cos(\zeta)}. \tag{3.24}$$

Since the length of $\boldsymbol{c}$ and $\boldsymbol{z_c}$ is constant by definition for one certain cycling configuration, the minimum of the length of $\boldsymbol{z_L}$ can be obtained for $\zeta = 0$ and the maximum for $\zeta = \pi$. For $\boldsymbol{z_R}$ the length maximum is given with $\zeta = 0$ rad and the minimum with $\zeta = \pi$. Furthermore, the maximum lengths of $\boldsymbol{z_L}$ and $\boldsymbol{z_R}$ correspond directly with the maximum knee-joint angle, while the minimum lengths of $\boldsymbol{z_L}$ and $\boldsymbol{z_R}$ correspond directly with the minimum knee-joint angle of the respective leg. Hence, as soon the inclination angle φ_{z_L} gets bigger than φ_{z_R}, the left knee-joint state switches from flexion to extension. To avoid fast switching between the states a hysteresis of 0.05 rad has been applied. In Figure 3.14, the different phases for one full rotation together with the respective signals for the right

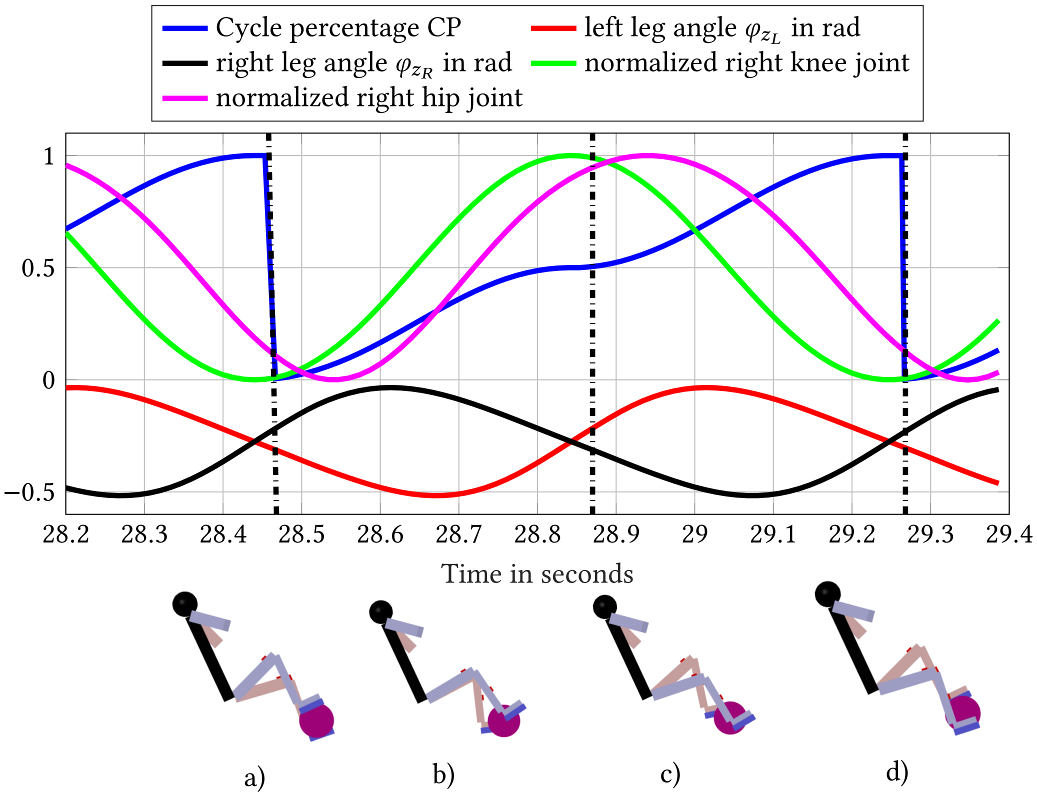

Figure 3.14: Different phases during one cycle for the right-knee joint. a) Start of extension phase, b) Extension phase, c) Start of flexion phase, and d) Flexion phase.

knee are presented. This criterion is valid even when the legs are not moving and even if the legs are rotating backwards.

Regarding the hip joint extension it can be shown, that the hip joint always follows the knee joint with respect to the flexion and extension phases. This can be proven based on Grashof's conditions for general four-segment crank-rockers [81]. A detailed proof that the start and end of the hip extension with respect to the crank angle always follow the start and end of the knee-joint extension is given in the Appendix B. The delay between the start of knee and hip extension depends on the relation of the segment lengths of thigh, shank, and crank and the displacement of hip and crank joint. The following section describes how a stimulation pattern can be derived using the cycle percentage of the knee-joint angle.

3.5.3 Stimulation Pattern

A pedaling motion at the crank can be produced if the muscles involved are stimulated exclusively at the times when they produce a positive torque at the crank. As explained in Section 3.2, the crank angle is commonly used as the stimulation-trigger signal in state-of-the-art approaches. The stimulation ranges of the crank angle are determined by empirical measurements or, if all segment lengths and distances are known, by calculation. An exemplary crank-angle range for a geometric configuration is shown in Figure 3.15. To initiate and maintain a cyclic movement, the knee extensors (via the quadriceps muscle group), the knee flexors (via the hamstring muscle group), and the hip extensors (via the gluteus maximus) must be activated by stimulation when the crank angle passes through the corresponding flexion and extension intervals (see Fig. 3.2).

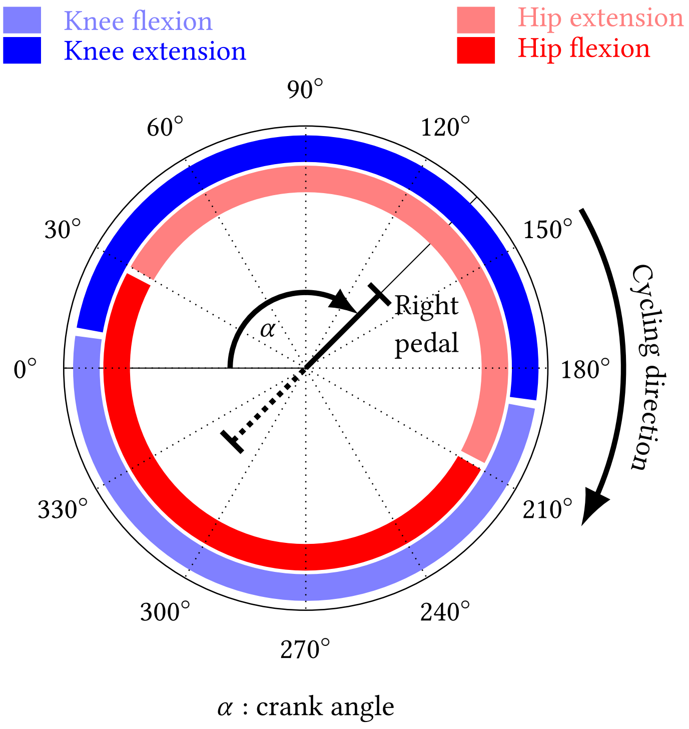
Knee flexion
Knee extension
Hip extension
Hip flexion
90°
60°
120°
30°
150°
0°
180°
330°
210°
300°
240°
270°
α
Right pedal
Cycling direction
α : crank angle

Figure 3.15: Example of the angle ranges of a crank-angle-driven stimulation pattern for the right leg. The ranges are an example for one geometric setting, e.g., specific seat height, seat-to-crank distance, and segment lengths.

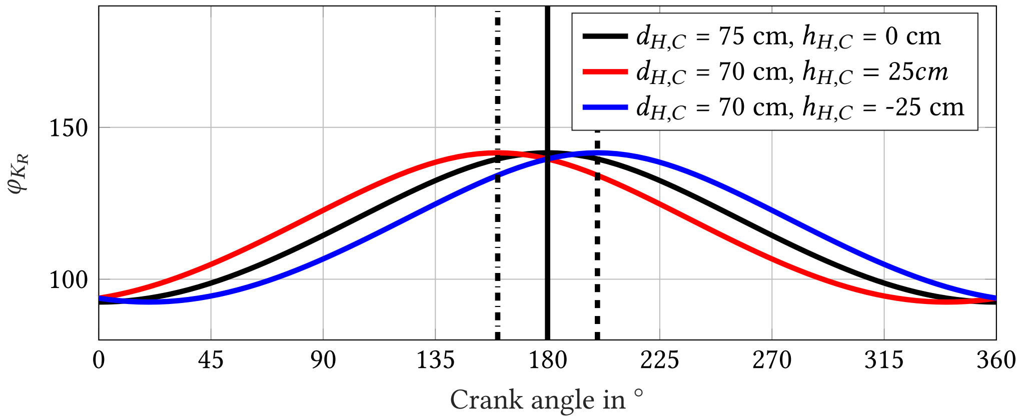

Figure 3.16: Simulated right-knee angle for different seat-to-crank configurations. The vertical lines show the crank angle for the maximum of the right knee angle for different seat-to-crank distances and seat heights.

Due to unwanted “side effects" of the stimulation, the muscle activation shall be limited to subranges in which the stimulation intensity does not produce co-activation of the muscles, which work against the cycling motion. These ranges need to be adjusted for each patient or if the cycling device or geometry is changed or adjusted.

Using the knee- and hip-joint angle, the ranges for extension and flexion of the respective joints can be directly determined based on the introduced cycle percentage (see Table 3.4). However, the muscle activation will be still limited to angular ranges of the joint angles where no unwanted “side-effect" occur. As shown in Figure 3.16, this relationship will not change if the geometry, seat-to-crank

Stimulated Muscle Group	CP Range
Quadriceps muscle group	$\varphi_{\mathrm{K}_s}^{\mathrm{CP}} \in [0.0, 0.35]$
Hamstring muscle group	$\varphi_{\mathrm{K}_s}^{\mathrm{CP}} \in [0.55, 0.85]$
Hip extensor (optional)	$\varphi_{\mathrm{K}_s}^{\mathrm{CP}} \in [0.4, 0.5]$

Table 3.5: The CP ranges for each muscle group. The stimulation pattern is symmetric – i.e., the same pattern is applied for both legs, denoted by $s \in \{L, R\}$.

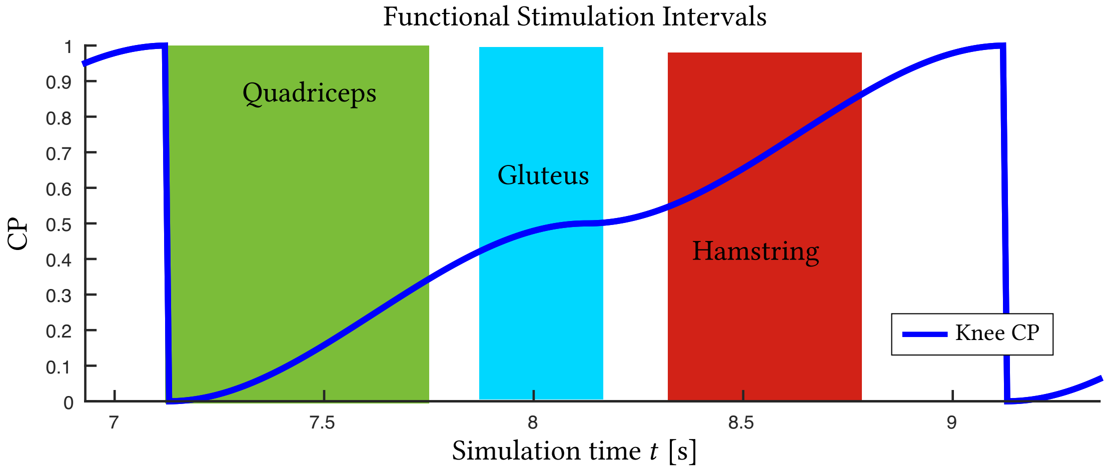

Figure 3.17: The stimulation interval of the quadriceps (green area, left), of the hamstring (red area, right), and of the gluteus (blue area, middle) muscle groups are shown. The intervals are shown for the functional range of the muscle groups.

distance, or height are changed. Here, the variation of the distance and height of the seat would demand a change in the crank-angle-based stimulation pattern, while the range of the knee-joint angle stays constant. However, the thigh inclination-angle is shifted by the amount the hip joint is inclined with respect to the crank joint, since only one sensor is involved during hip joint measurement.

The stimulation of the quadriceps muscle group is driven by the knee-joint extension, which is represented by the range $[0, 0.5]$ of $\varphi_{K_i}^{\mathrm{CP}}$ $i \in \{R, L\}$. Exploratory tests showed that stimulating for the entire extension phase of the knee joint has a negative effect at the end of the extension phase, which can result in a motion blockade. Therefore, at the end of the knee extension only the hip extensor (glueteus maximus) is stimulated, which helps to overcome dead zones, especially in mobile cycling as presented in Chapter 4. This is motivated due to the fact that the knee extension always ends before the hip extension and the knee flexion always starts before the hip extension is finished, as shown in the previous section. The stimulation of the hamstrings is driven by the knee-joint flexion, which is represented by the range $]0.5, 1.0[$ of $\varphi_{K_s}^{\mathrm{CP}}$ $s \in \{R, L\}$. Exploratory tests showed that stimulating for the entire flexion phase of the knee joint has a negative effect at the end of the flexion phase, which can result in a motion blockade. Furthermore, it must be guaranteed that the hip extension is almost finished before the knee flexor is stimulated. The resulting pattern in the form of CP ranges is shown in Table 3.5. Furthermore, in Figure 3.17, an exemplary CP trajectory of the knee joint of one leg is shown. The data is generated by implementing the joint-angle estimation of the previous Section 3.4 and the joint-angle transformation, while using the simulation environment described in Section 3.3.1. Some tuning of the stimulation pattern might still be necessary to avoid dead zones in the torque generation and to optimize the cycling performance in terms of smoothness and muscular fatigue.

The latter is directly related to the amount of required stimulation intensity and muscle activation. Depending on the seating position, there is a different leverage ratio between leg and crank. This has an influence on the transfer of muscle power to the cycling movement and thus the smoothness of cycling. In addition, as with crank-angle-based stimulation patterns, it is necessary to adjust the stimulation ranges as a function of crank speed. A method for the joint-angle-based stimulation pattern is described in the following section.

3.5.4 Speed-Dependent Adaptation of the Stimulation Pattern

The stimulation pattern described in the previous section assumed that no delay is present between stimulation and the resulting joint-torque production by the muscles. However, in reality, the torque generation is a dynamic process that must be considered when activating the muscles during cycling. A very rough approximation of the process is a simple time delay t_d of about 130 ms [28]. Therefore, muscles should be stimulated in advance during cycling to guarantee that extension and flexion torques occur exactly at extension and flexion phases of the legs, respectively. This requirement could be translated into shifted CP ranges for the simulation pattern provided in Table 3.5. Instead of shifting all the CP ranges for stimulation, the future CP value after elapse of the time delay can be estimated and used for checking the stimulation conditions based on the original CP ranges. A simple linear shift depending on a mean CP time-derivative like in crank-angle-based stimulation strategies would not work due to the much larger fluctuation of this value compared to the crank cadence. Therefore, a new method is proposed that continuously predicts the CP values after the end of the time delay by storing the cycle percentage profile of the last full revolution (between two wraps of the cycle percentage signal) and using this buffer as a Look-Up Table (LUT) for the time shifted CP signal. If the profile of the CP signal does not vary too much from one revolution to the next, then this LUT-based method produces an almost constant time-shift of the cycle percentage by t_d, as shown in Figure 3.18.

The biomechanical model of Section 3.3 is used to compare the mean CP time-derivative-based approach and LUT-based approach. In these simulations, the seat position with respect to the crank as well as the inclination angle of the cyclist's back were kept constant. A simple Proportional-Integral (PI) controller was used to maintain the mean cycling speed at target cadences of 40, 50 and 60 rpm by adjusting the pulse width and keeping f_{stim} constant. In a first simulation, the LUT-based method was tested for different time shifts in the range $50, 60, 70, ..., 200$ ms. After the PI controller reached steady-state the error between the actual and target cadence is compared. As shown in Figure 3.19.a, the shift of 100 ms results in the lowest RMSE of the cadence for all three target cadences. Afterwards, both methods were compared with respect to the RMSE of the cadence, used pulse width, and cadence variation (maximum minus minimum cadence per revolution) at steady-state. In Figure 3.19b-d the LUT-based method is compared against the mean CP time-derivative-based method. The LUT-based method produces a lower RMSE at comparable pulse widths. Compared to the mean CP time-derivative-based method the LUT-based speed adaptation produces a lower cadence variation, and therefore a smoother cycling movement is generated.

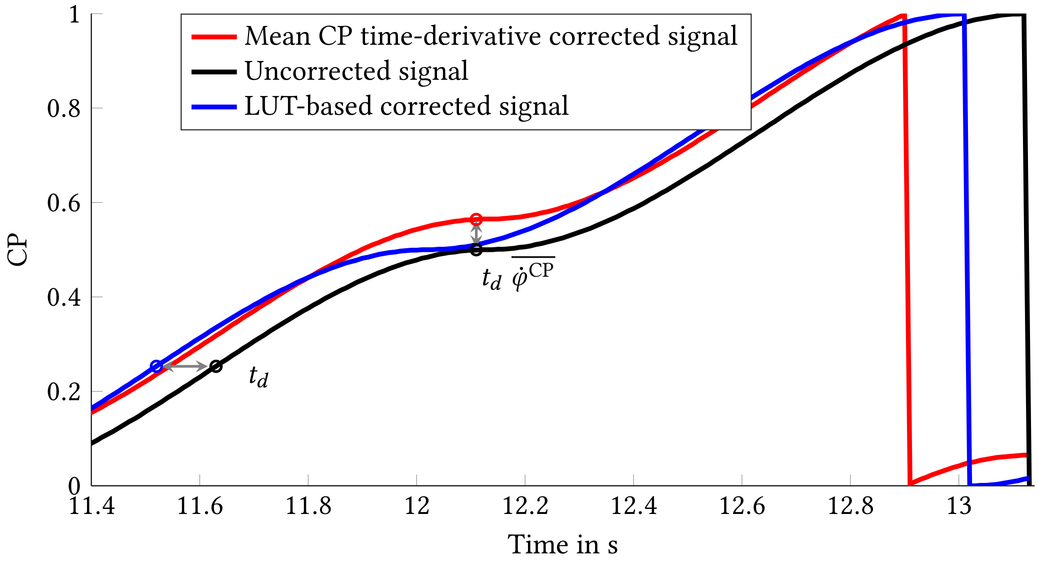

Figure 3.18: Comparison of the corrected signal (red) with an uncorrected signal (black) at cadence $\dot{\alpha} \approx 50\,\mathrm{rpm}$ with a latency time of $t_d = 130\,\mathrm{ms}$ for the mean CP time-derivative-based stimulation pattern adaptation. This method results in a variable shift of the cycle percentage signal. For the LUT-based method the cycle-percentage signal of the last revolution is used as look-up table and the corrected signal (blue) is always shifted by the same amount of time.

3.6 Calculation of Crank Angle and Cadence

Using the estimated segment-inclination angles, the crank angle can be calculated. This allows for comparing crank-angle-based approaches with the proposed joint-angle-based method without incorporating a crank-angle sensor. Furthermore, the cadence can be calculated. The crank angle can be directly derived from vector z_c in Figure 3.4. It is calculated using the inclination angles of the thighs and the shanks of both legs. As introduced earlier, the vectors z_{T_L} (left thigh), z_{T_R} (right thigh), z_{S_L} (left shank) and z_{S_R} (right shank) can be formulated as complex numbers in polar coordinate notation (see Eq. (3.14 - 3.17)). The crank vector z_c can be determined by subtracting z_R and z_L

$$z_c \quad = \quad z_R - z_L. \tag{3.25}$$

To get the crank angle $\hat{\alpha}$, the argument of z_c has to be calculated with

$$\hat{\alpha} \quad = \quad \pi - \arg(z_c) = \pi - \begin{cases} \arctan(\frac{b}{a}) & \text{for} \quad a > 0 \\ \arctan(\frac{b}{a}) + \pi & \text{for} \quad a < 0, b \geq 0 \\ \arctan(\frac{b}{a}) - \pi & \text{for} \quad a < 0, b < 0 \\ \frac{\pi}{2} & \text{for} \quad a = 0, b > 0 \\ -\frac{\pi}{2} & \text{for} \quad a = 0, b < 0 \end{cases} \tag{3.26}$$

where a and b are the real and imaginary parts of the complex number z_c and the argument is subtracted from π to get the same angle definition as shown in Fig. 3.4. The crank angle can be estimated under the assumption that all lengths of the body segments and the crank arm are known.

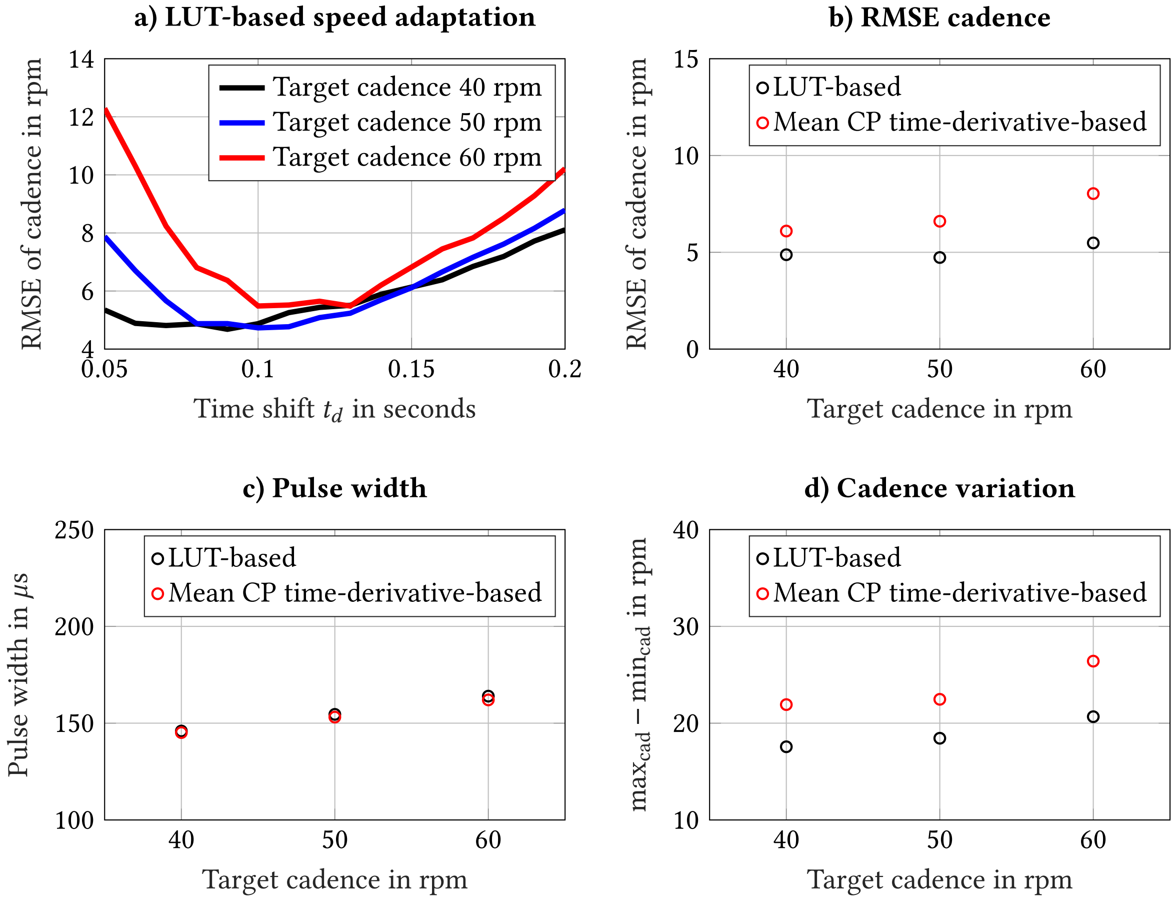

Figure 3.19: Comparison of the speed-adaptation methods. In a), the LUT-based speed adaptation method is simulated at different target cadences and for different time shifts. In b), the RMSE of the cadence is plotted for different target cadences with a time shift of 100 ms. In c), the used pulse width (controller output) is shown for different target cadences for both methods. In d), the cadence variation of the resulting stimulation patterns is presented at different target cadences.

Using the unwrapped estimated crank angle, the cadence can be derived by backward Euler differentiation and a one tap smoothing filter with

$$\dot{\hat{\alpha}}[k] = (1-\lambda)\dot{\hat{\alpha}}[k-1] + \lambda\left(\frac{\hat{\alpha}[k] - \hat{\alpha}[k-1]}{T}\right), \tag{3.27}$$

where $\lambda \epsilon]0, 1]$ is a smoothing factor, k is the sampling index, and T is the sampling period. Figure 3.20 shows a simulation of the crank-angle estimation. A small deviation of the crank angle can be observed with an RMSE ≈ 0.51 rad due to a slight mismatch of the assumed segment lengths in the calculation compared to the used segment lengths in the model. This results in a larger cadence deviation with an RMSE ≈ 2.87 rpm, since the cadence is estimated using the crank angle. To improve the results, the true lengths of the segments are needed, which can be estimated using an optimization method.

The proposed optimization can be divided into two steps. First, a data set S_{z_c} for one full cycle of the estimated polar coordinate z_c is calculated using initial lengths of the segments, e.g., $l_T = 40$ cm and $l_S = 40$ cm. For each polar coordinate z_c in S_{z_c} the radius $\hat{r}_c$ is calculated, and the difference to the measured or known true crank length is calculated and stored.

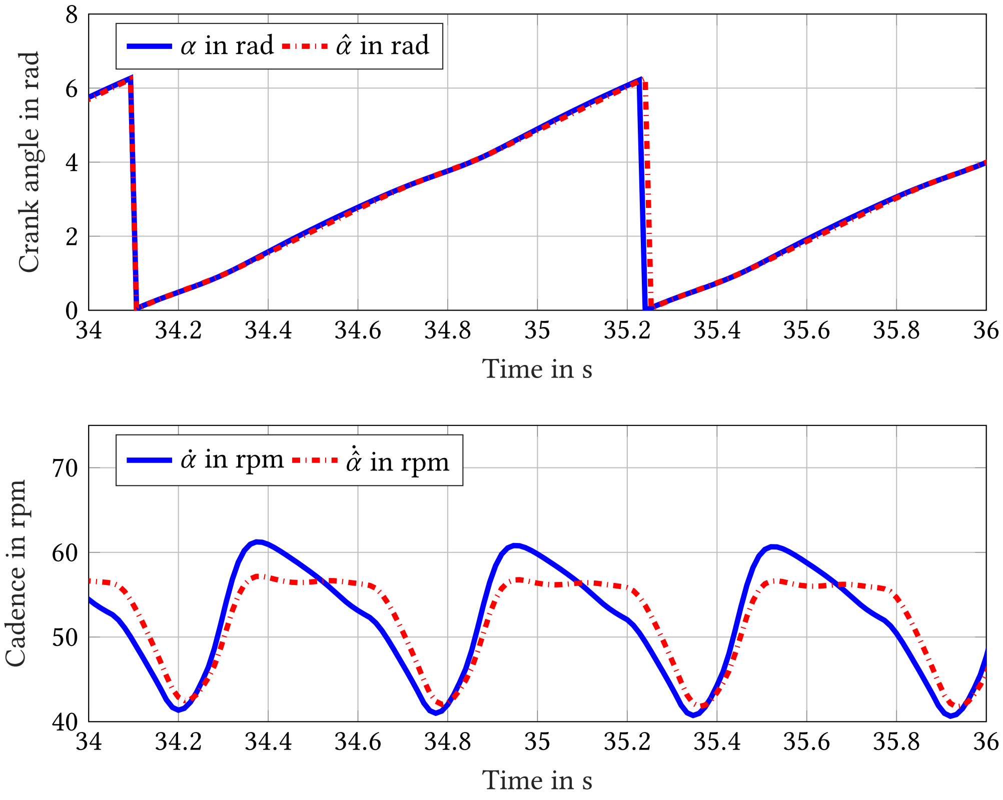

Figure 3.20: The upper graph shows a simulation with assumed thigh and shank length of 40 cm, while the true length was 45 cm. The lower graph shows the resulting cadence estimation compared to the simulated cadence with a smoothing factor $\lambda = 1.0$.

Using a nonlinear optimization method, the segment lengths can be found by minimizing the mean-squared error of the radius estimation

$$e_r = \frac{1}{N}\sum_{j=1}^{N}(r - \hat{r}_c[j])^2, \tag{3.28}$$

where N is the number of stored polar coordinates in S_{z_c}, and r is the measured or given crank-arm length. Since there might be several local minima for the optimization criteria, lower and upper boundaries are used to constrain the optimization procedure. The optimization method is summarized in Table 3.6, which solves

$$[\hat{l}_T, \hat{l}_S] = \arg\min_{l_T, l_S} e_r(l_T, l_S). \tag{3.29}$$

In Figure 3.21, the results after the estimation of the segment lengths are presented with an RMSE $\approx 4 \cdot 10^{-7}$ rad for the crank angle and an RMSE ≈ 0.58 rpm for the cadence. In Figure 3.22, the estimated pedal position is presented for the simulated crank-arm length of 12 cm for the same simulations of Figures 3.20 and 3.21. Here, the pedal position for non-optimized segment length (red line) follows an elliptical trajectory with a radius smaller than the real crank length. After the optimization, the estimated pedal position follows the true simulated position with no visible deviation.

Table 3.6: Summary of the segment-length-optimization method. The table shows the required inputs, the calculated outputs, as well as the sequence of instructions.

Inputs	joint-angle estimates φ_{IMU,S_R}, φ_{IMU,S_L}, φ_{IMU,T_R}, φ_{IMU,T_L} starting values for segment length l_T, l_S

Algorithm

```
for every sample do:
    calculate the $z_L$, $z_R$, and $z_c$
    if a set $S_{z_c}$ is complete:
        minimize $e_r$ with respect to upper and lower boundaries
end for
```

Outputs	estimated segment length: l_T, l_S

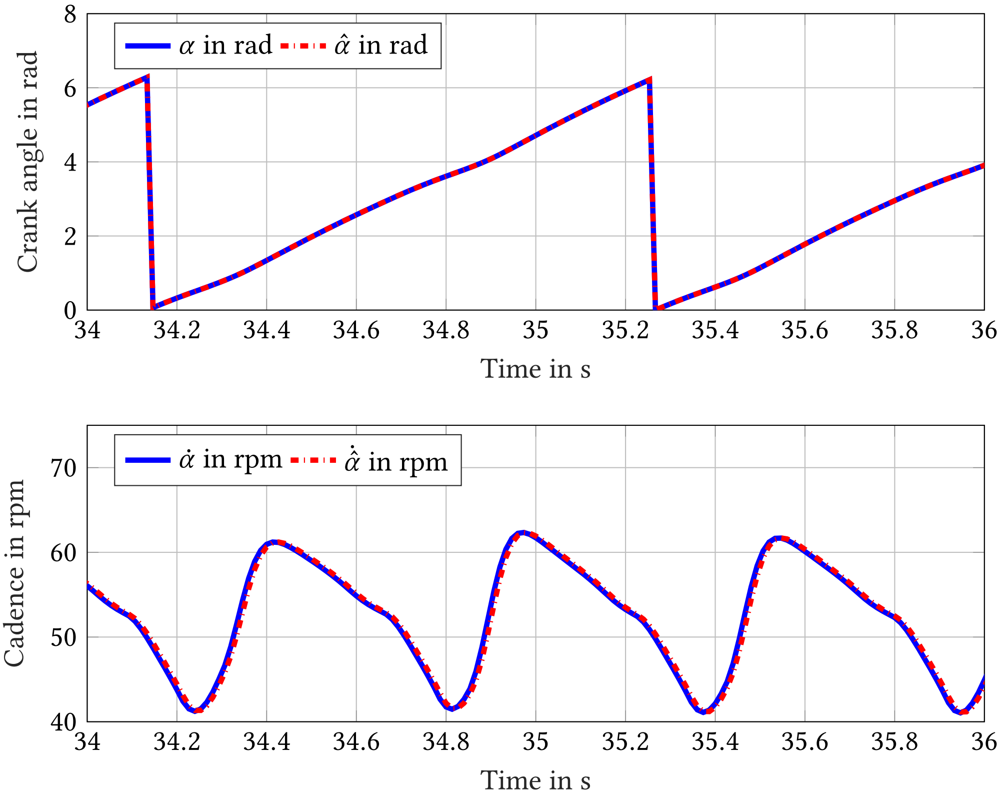

Figure 3.21: Cadence estimation with optimization. The upper graph shows the true and est. crank angle with perfectly estimated thigh length of 45 cm and shank length of 45 cm. The lower graph shows the resulting cadence estimation compared to the simulated cadence using a smoothing factor $\lambda = 1.0$.

As a main result, both crank- and joint-angle-based methods can be compared regarding the resulting stimulation pattern. Furthermore, the calculation of the crank angle can be used to check for an incorrect sensor placement, since the optimization would fail.

3.7 Simulative Evaluation of the Knee-Joint-Angle-Based Stimulation Pattern

Using the introduced stimulation pattern of the previous section, several simulations have been carried out to validate that the presented methods can induce a cycling motion without manual tuning despite changing geometric parameterizations. The biomechanical model, introduced in Section 3.3, is used to obtain simulation results for the presented methods. In these simulations, the seat position

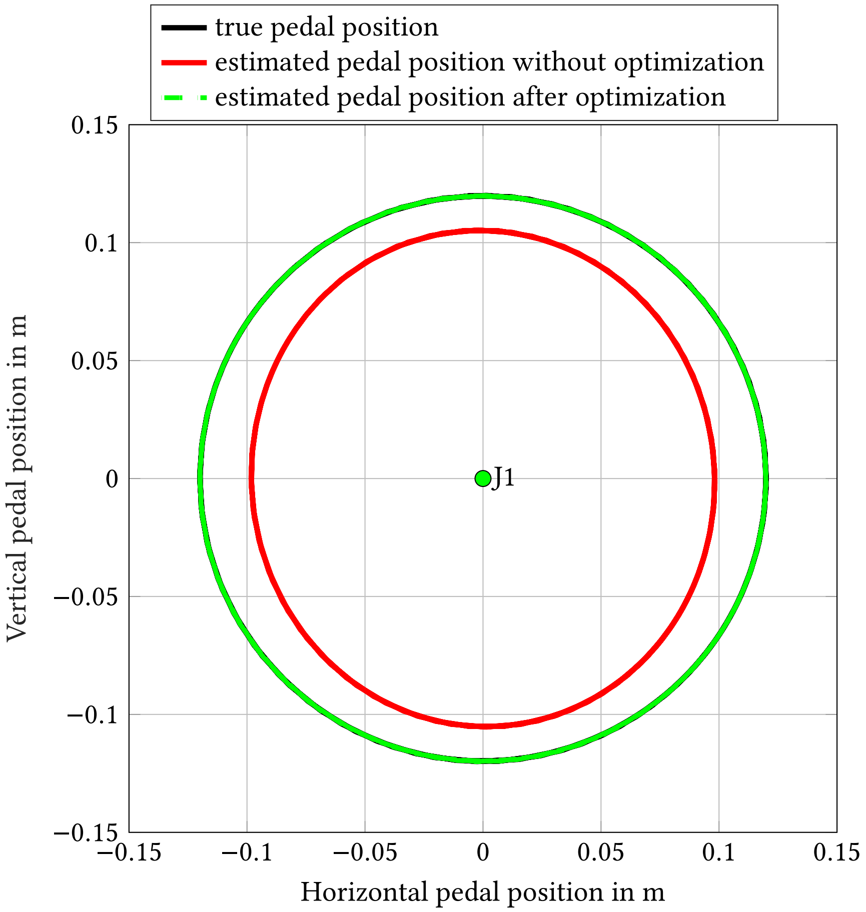

Figure 3.22: Stimulated pedal position with (green) and without (red) segment-length estimation for a simulated crank-arm length of 0.12 m. The point $(0, 0)$m represents the crank-axis location J1.

was varied in distance and height with respect to the crank. Additionally, the inclination angle of the back of the cyclist was modified. A simple PI controller was used to control the mean cycling speed to 50 rpm by adjusting the pulse width and keeping $f_{\text{stim}}(t)$ constant. As shown in Figure 3.23, the joint-angle-based approach was able to induce a cycling motion despite the geometry changes. Further, it was possible to influence and regulate the mean cadence to the desired value by changing the stimulation intensity.

As shown in the Table 3.7, the resulting crank-angle ranges of muscle activation were different for each geometric setting, while the CP ranges stayed the same over all simulations. Furthermore, the simulation shows that the cadence smoothness (deviation from the mean cadence value) depends on the seat position and inclination. While inducing a cycling motion was still possible. Sitting too close or too low to the crank decreased the cycling quality by means of cadence smoothness, due to the changed lever-arm relation. As stated earlier, some tuning of the stimulation pattern might still be necessary for optimal stimulation results.

To simulate variations of the muscle force due to fatigue, spasticity, or a lower or higher gear resistance, positive and negative torques have been applied to the crank of the model. Furthermore, a simple integral controller has been implemented, which controls the stimulation pulse width to reach a defined target cadence. Using this model, the starting phase, normal cycling, as well as critical phases can be simulated prior to real experiments. In Figure 3.24, all three simulated phases are presented. During the starting phase (time $\leq$ 20 s), a negative torque has been applied and the

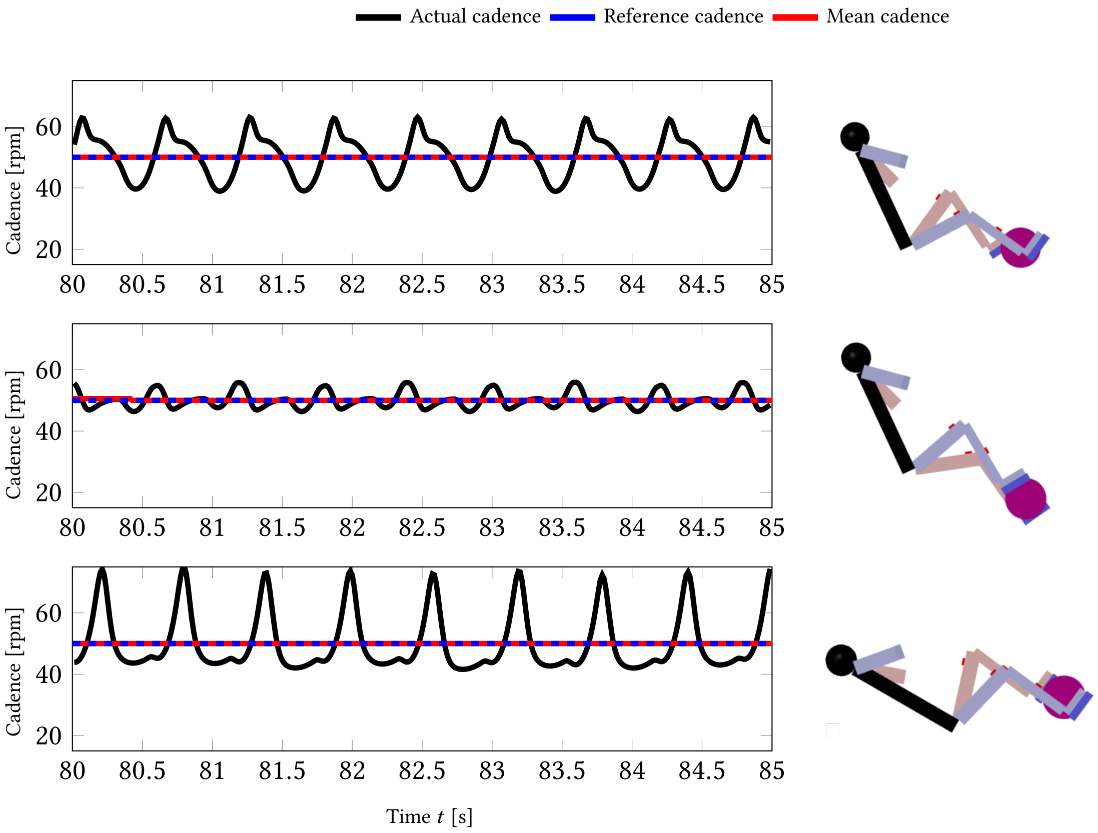

Figure 3.23: Cycling simulation for the joint-angle-based approach using different geometric parameterizations and the LUT-based speed adaptation method. The crank cadence, the mean cycling cadence, and the reference cadence are visualized for every simulation. Geometric parameters: 1st Simulation: distance to crank 0.75 m, seat height of 0 m, and back angle of 65 °, 2nd Simulation: distance to crank 0.75 m, seat height of 0.2 m, and back angle of 65 °, 3rd Simulation: distance to crank 0.75 m, seat height of -0.2 m, and back angle of 30 °.

Muscle group	Simulation (cf. Fig. 3.23)	Crank-angle range	CP range
Quadriceps	1	325 ° - 100 °	0.0 - 0.35
	2	340 ° - 125 °	0.0 - 0.35
	3	310 ° - 85 °	0.0 - 0.35
Hamstring	1	175 ° - 280 °	0.55 - 0.85
	2	205 ° - 295 °	0.55 - 0.85
	3	160 ° - 265 °	0.55 - 0.85
Gluteus maximus	1	115 ° - 150 °	0.4 - 0.5
	2	135 ° - 165 °	0.4 - 0.5
	3	100 ° - 130 °	0.4 - 0.5

Table 3.7: Resulting active crank-angle ranges for the right leg muscle groups for each simulation from Fig. 3.23 compared to the CP ranges using the joint-angle-based method.

crank is rotated backwards to estimate the required maxima and minima of the inclination angles. Afterwards, the stimulation and I-controller are started, which try to reach the target cadence of 50 rpm. After 40 seconds, assisting as well as counteracting torques are applied sequentially, which accelerate and decelerate the crank. During all disturbances, the correct joint phases (extension or

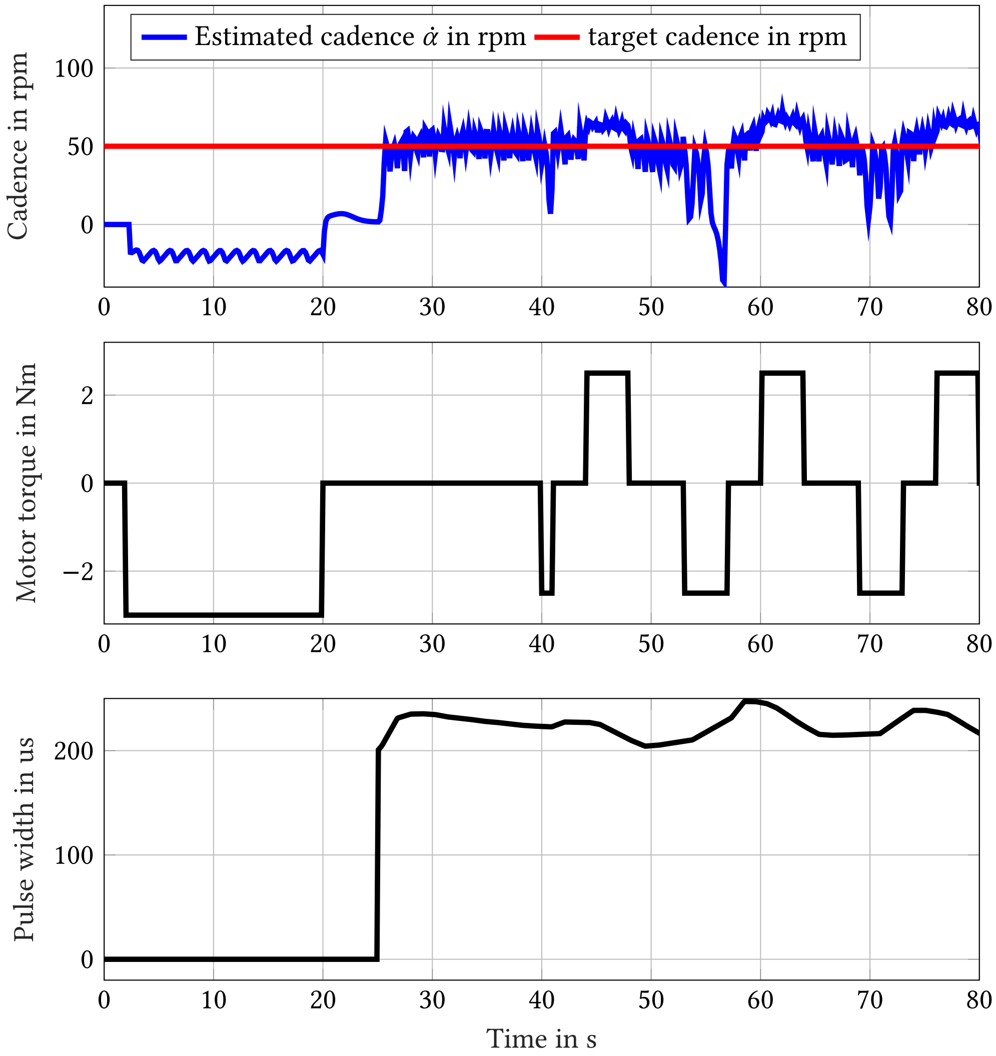

Figure 3.24: Simulation of the starting phase and normal cycling with applied counter and assisting torque. The upper plot shows the target and actual cadence. The middle plot shows the applied motor torque. The lower plot shows the applied pulse width.

flexion) were detected using the presented discrimination method. The stimulation patterns were switched correctly according to these phases. Hence, the cycling motion could be maintained or once restored using the presented methods despite the disturbances.

3.8 Conclusions and Future Research

A new joint-angle-based stimulation pattern was presented for stationary and mobile FES cycling of paraplegic subjects. The novel approach offers a “plug & play" system without the need for an initial calibration or manual tuning. The introduced method offers joint-angle estimates of the knee and hip joints by utilizing IMUs on the shank and thigh. In a first step, the inclination of each shank and thigh are estimated. Experiments resulted in an RMS error as low as 0.8-1.8 ° with a maximum error of 2.8-3.2 ° for all different attachment configurations. In a second step, the knee-joint angle is calculated by subtracting the shank from the thigh inclination. The hip-joint angle can be calculated by measuring the back inclination angle.

A simple joint-angle transformation is introduced to generate stimulation patterns based on the cycle percentage, which are independent of the geometric configuration. In addition to a simple pattern for stationary ergometer cycling, a new robust method for determining the extension and flexion phases of the knee joint was proposed. In contrast to the simple approach, that determines the extension and flexion phases based on the derivation of the normalized joint angle, the new method uses the leg inclination angles. A proof showed that the method always determines the correct turning point from extension to flexion and vice versa. Furthermore, it was possible to proof that the joint phases of the hip joint always follow the knee joint using Grashof's conditions. Finally, exploratory tests were used to determine a stimulation pattern for the corresponding muscle groups.

To account for the dynamic process of moment generation by artificially stimulated muscles during cycling, a speed-adaptation method was implemented. This method uses the past cycle percentage profile to shift the stimulation pattern forward by a fixed time offset. As a side product, the crank angle and cadence can be reliably estimated using the segment-inclination angles only. This can be used to compare the joint-angle-based stimulation pattern against encoder-based methods or to control the smoothness of inter-cycle cadence.

All presented methods were tested during simulations with disturbances to ensure that the flexion and extension phases are reliably discriminated. Furthermore, simulations showed that despite variations in the seat height, distance, and back tilt, FES cycling was possible. All presented methods have been implemented on an embedded control system and tested during training and races of the Cybathlon in 2016, which will be explained in the next Chapter 4.

For stationary cycling with an ergometer, which includes an assistive motor, a reduced sensor setting can be applied. This reduced sensor setting is not part of this dissertation but aim for future improvements. In a two sensor solution, one sensor is placed on the thigh and the other sensor is placed on the shank of the opposite leg. During the cycling motion, both legs are moving with a phase shift of 180 ° (which is forced by the crank geometry). Therefore, the crosswise placed sensors offer enough information to calculate the knee-joint angle.

Further integration could be achieved with just one sensor, e.g., the sensor can be attached to one thigh retrieving its inclination angle. Assuming a sinusoidal angular course, the thigh inclination angle of the other leg could be estimated. With some limitations, a stimulation pattern could also be defined for this reduced configuration, which should be sufficient for stationary FES ergometer training.

4

The Cybathlon-RehaBike - Inertial-Sensor-Driven Mobile FES Cycling

4.1 Introduction

On the 8th October 2016, a world premiere took place in the SWISS Arena in Kloten: ETH Zurich organized the very first Cybathlon. Athletes with physical disabilities competed side-by-side in six demanding disciplines, using the latest assistive technology. Although this was the first championship of this size and with this amount of disciplines, there were several competitions specialized on specific disciplines. In November 2004, two FES-rowers Robin Gibbons and Sol Solomou demonstrated the feasibility of FES-rowing by competing in the British Indoor Rowing Championships (BIRC) in Birmingham, UK. This historic event highlighted, for the first time, that individuals with spinal cord injury could compete on an equal basis in a national sporting event. Afterwards, the same community organized the first International FES-Sports Meeting in Cardiff in June 2006. Besides rowing, FES cycling was one of the main disciplines in races and team competitions. During these FES races neither motor nor arm support were allowed. One of the main differences between these early championships and the Cybathlon are the inclusion of robotics, brain computer interfaces, and prostheses for all kind of tasks and disabilities, and certainly the increased media exposure.

The Control Systems Group at Technische Universität Berlin, the companies Hasomed GmbH and Hempel GesundheitsPartner as well as the treatment center for spinal cord injuries at the Unfallkrankenhaus Berlin formed a collaboration with the athlete Hanno Voigt, the team Hasomed, to participate in the FES cycling race of the Cybathlon. Hanno Voigt had been paralyzed for over 35 years at the time of the Cybathlon and had no prior experience with FES cycling. The stimulation methods described in Chapter 3 were used during the training phase and race with the RehaBike. In the following sections the experimental set-up, training, and race results will be presented and finally discussed.

Rank. Team	Pilot age / lesion age	Implant	Transfer	stimulation trigger	racing time [s]
1. Cleveland (USA)	59 / 8	yes	assisted	crank angle	178
2. BerkelBike (UK)	21 / 6	no	independent	crank angle	248
3. IRPT/SPZ (SUI)	37 / 4	no	assisted	crank angle	239
4. Hasomed (GER)	55 / 35	no	independent	joint angle	395
5. MYOLYN (USA)	28 / 25	no	assisted	crank angle	309
6. FREEWheels (FRA)	47 / 33	no	assisted	crank angle	467
7. Sydney Australia (AUS)	49 / 26	no	independent	crank angle	465
8. EMA (BRA)	38 / 35	no	assisted	crank angle	183 (2)
9. Meltin MM (JAP)	47 / 26	no	assisted	crank angle	283 (1.5)
10. ENS de Lyon (FRA)	52 / 48	no	assisted	crank angle	29 (0.5)
11. Phoenix (HKG)	21 / 15	no	assisted	crank angle	480 (0.5)
DQ Mahidol/BCI (THA)	26 / 18	no	assisted	manual	-

Table 4.1: Characteristics and results of the FES pilots and hardware during the Cybathlon. Team Mahidol BCI from Thailand was disqualified (DQ) during the medical check, however, was allowed to participate in the race without scoring. The number in brackets behind the racing time indicates the number of completed laps if the pilot need to stop before finishing all five laps.

Copyright Statement: The methods and results, presented in this chapter, have been previously published in:

[CYC3] C. Wiesener and T. Schauer. “The Cybathlon RehaBike: Inertial-Sensor-Driven Functional Electrical Stimulation Cycling by Team Hasomed”. In: *IEEE Robotics & Automation Magazine* 24.4 (Dec. 2017), pp. 49–57. DOI: `10.1109/MRA.2017.2749318`.

Therefore, the text and figures in this chapter are extracted, with slight modifications, from this publication. Figure 4.5 and Section 4.1 were added. In the following, Section 4.1 gives an overview of the competing teams in the FES cycling race at the Cybathlon competition and Section 4.2 introduces the developed cycling device. The training regime and the race results are presented throughout Section 4.3. These results are finally discussed and concluded in Section 4.4.

Overview of Competing Teams at the Cybathlon 2016

There were twelve teams from ten countries participating in the Cybathlon 2016 FES race which are summarized in Table 4.1 according to [82]. The age of the pilots ranged from 21-59 while the time after injury varied between 3 and 35 years. All except our team used the crank angle for triggering the stimulation for each leg. In contrast to all other teams, team Cleveland used an implanted stimulation device, while all others used standard transcutaneous stimulation electrodes and external stimulators. Beside two commercial teams (Myolyn, BerkelBike) starting with their recent FES cycling products, universities, and research facilities designed and built the systems. While all teams used recumbent tricycles, only few of them (BerkelBike, Sidney, Hasomed) allowed an independent transfer of the cyclist to and off the bike due to an elevated seating position.

The RehaBike of team Hasomed consists of the standard TRIX tricycle of the company Hase Bikes with several add-ons and minor modifications. The details of the bike, each modification, and the assembly are described in the following section. Furthermore, the training regime, stimulation pattern, and race tactics are presented and discussed.

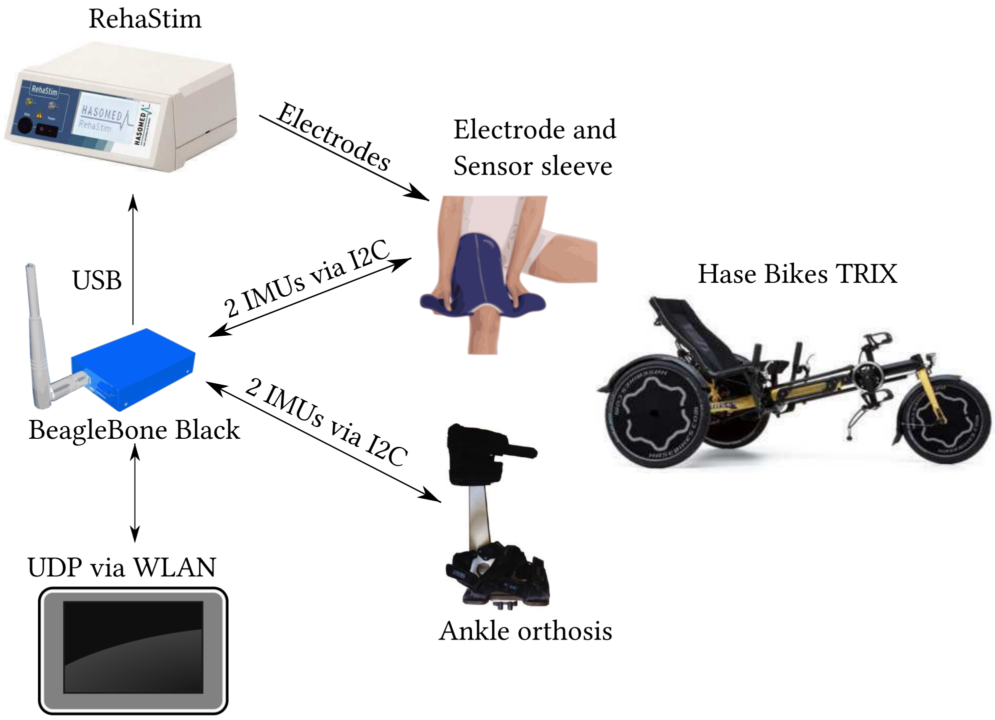

Figure 4.1: The RehaBike consists of a standard Hase Bikes TRIX with seat elevation set, ankle orthoses with two IMU sensors, an 8-channel RehaStim stimulator, a Beaglebone Black as embedded controller, an Android tablet with a Kivy App for parameterization, data visualization, and logging, and two thigh sleeves with IMU sensors and electrodes (©2017 IEEE).

4.2 Cycling Device

The RehaBike of the Hasomed Cybathlon team shown in Fig. 4.1 and summarized in Fig. 4.5 consists of a standard Hase Bikes TRIX tricycle with several modifications. The TRIX is a recumbent tricycle and an approved medical device as per the European Directive 93/42/EEC (Medical Device Directive). The distance between seat and crank can be adapted via a length adjustment and a seat elevation. To enable an easy transfer from the wheel chair to the bike, and to have the same geometric configuration as for the ergometer training, the seat elevation set for the adult bike version (Hase Bikes Kettwiesel, see Figure 4.2) was used. The TRIX is equipped with a Shimano Nexus 8-speed hub gear with a twist shifter. The hub gear allows shifting even when the pedals are not moving. A lower achievable average torque is expected in FES compared to volitional muscle activation in healthy people. Hence, the chain wheels were modified as illustrated in Figure 4.3 to allow the propulsion of the tricycle with lower crank torques at the cost of higher cadences. The aim is to enable the cyclist to initiate pedaling without the need of pushing the legs by hand. With the reduced gear wheel diameter, the resulting transmission ratios range between $1\frac{3}{4} : 1$ and $\frac{3}{4} : 1$ depending on the shifter position. This permits the pilot to start the bike with only $\approx 25\,\mathrm{N}$ tangential force at the crank arm as determined by a calibrated dynamometer (AFG 500N, Mecmesin, UK). For the cycling itself, the chosen transmission ratio translates to a cadence of 35 to 50 rpm on a flat level ground to a speed of approximately $6 - 8$ km/h for the pilot. During a full rotation of the crank, there are so-called dead zones in which no effective power transmission from the muscles to the crank can be achieved. Therefore, an oval chain wheel at the crank was used which causes a lower gear transmission-ratio at the start of the extension phase of the knee and a higher gear transmission-ratio at the start of the flexion phase.

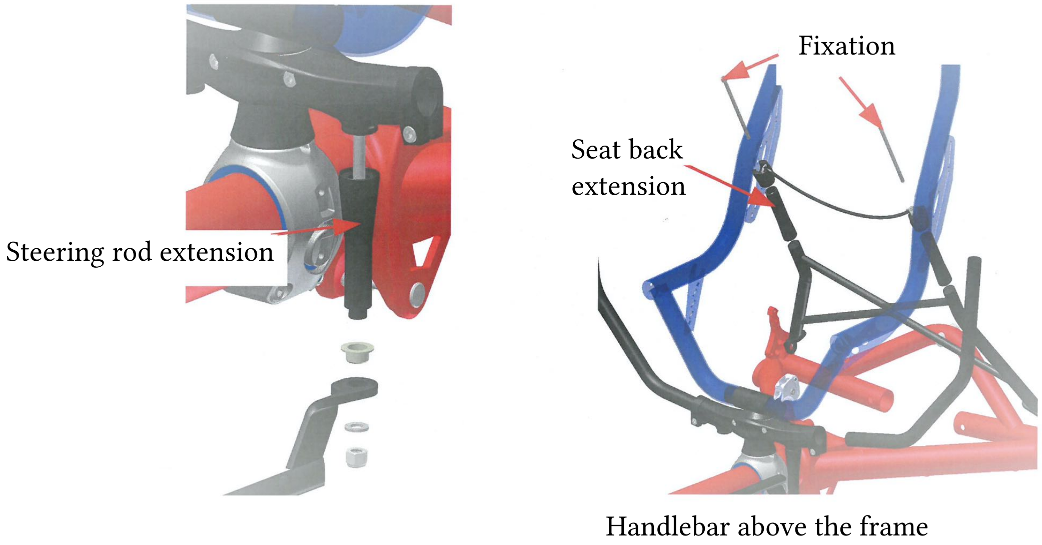

Figure 4.2: Seat elevation set of Hase Bikes Kettwiesel with a reached seat height of 46 cm and with a crank height of 30 cm measured from the ground (©2017 IEEE).

Furthermore, two chain pulleys were replaced by one chain fastener, which reduces the chain friction and weight. The TRIX has two 20" wheels at the rear and one 16" wheel at the front. The rims are made of double-walled aluminum with eyelets. The tire size at the rear is 35-406 (20 x 1.35") and at the front 50-305 (16 x 1.95") to decrease rolling resistance. The rear wheels are equipped with spoke guards that eliminate the risk of spoke-related injury. The ankle-joint orthoses, which were specially designed by the Technische Universität Wien, prevent the feet from slipping off the pedals during cycling and stabilized the ankle joints at a 90 degree angle. For the pilot, a customized cushion was designed by the company Hempel GesundheitsPartner (team partner, orthopedic supply store), which elevated the seating position (5 cm forward and upward direction). There are a lap and a shoulder belt mounted at the seat which prevent the driver from falling off the seat due to crash or tilting of the bike during the race. The closure can be opened with one hand. To generate the electrical stimulation pulses, the RehaStim device (Hasomed GmbH, Germany) was used. During the experiments, the current, pulse width and frequency can be adjusted by the pilot to modulate the stimulation intensity (e.g., to compensate fatigue effects). The RehaStim device offers the *ScienceMode* for controlling the settings for each pulse using a low-level communication protocol. To modulate the stimulation frequency, the sending routine at the embedded control system was running in a dedicated real-time thread, wherein each execution cycle triggers a stimulation pulse. The execution period can be changed via a parameter queue.

To calculate the joint angles, four wired IMUs (MPU9250, InvenSense) were mounted at each shank and thigh. Customized sleeves were used to attach the electrodes of the Hamstrings and Quadriceps muscle groups and position the thigh IMUs at the outer face of the thigh. These sleeves incorporate all needed cables and prevent electrode detachment during the cycling. The shank IMUs were attached via elastic Velcro straps.

The embedded control system consists of a standard Beaglebone Black with a customized data acquisition shield. The control system runs at a frequency of 75 Hz while the stimulation frequency can be varied between 20-40 Hz. The software was developed using Matlab/Simulink and a modified Linux ERT target [83] to generate the code and directly run the executable in Simulink External Mode. All methods including the segment-inclination estimation, the robust discrimination of leg extension

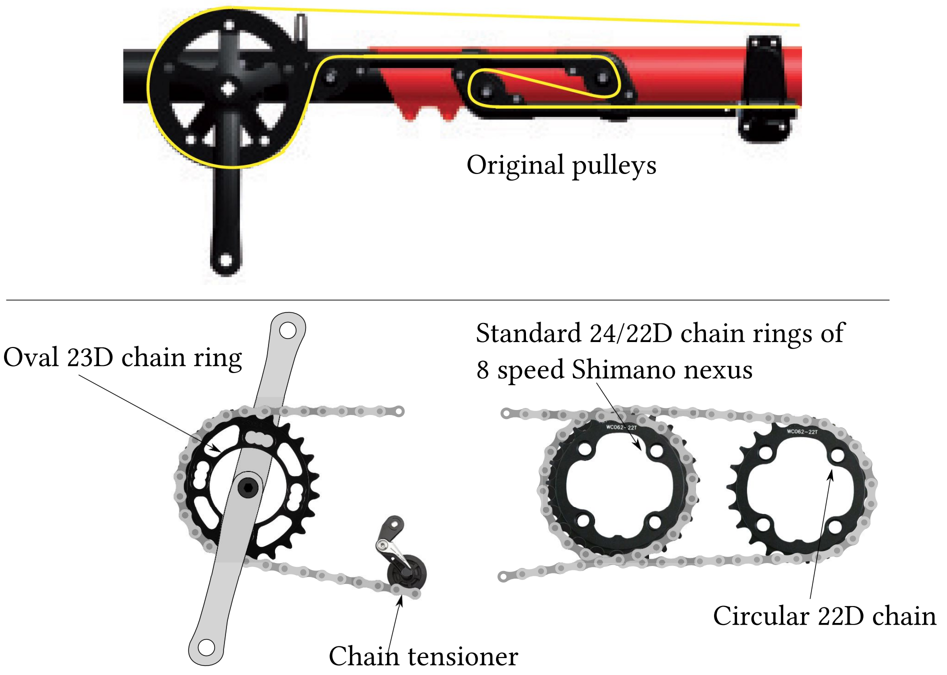
Original pulleys
Oval 23D chain ring
Standard 24/22D chain rings of
8 speed Shimano nexus
Circular 22D chain
Chain tensioner

Figure 4.3: Upper part: original chain configuration including the pulleys. Lower part: schematic of chain wheels and chain of the modified TRIX drive (©2017 IEEE).

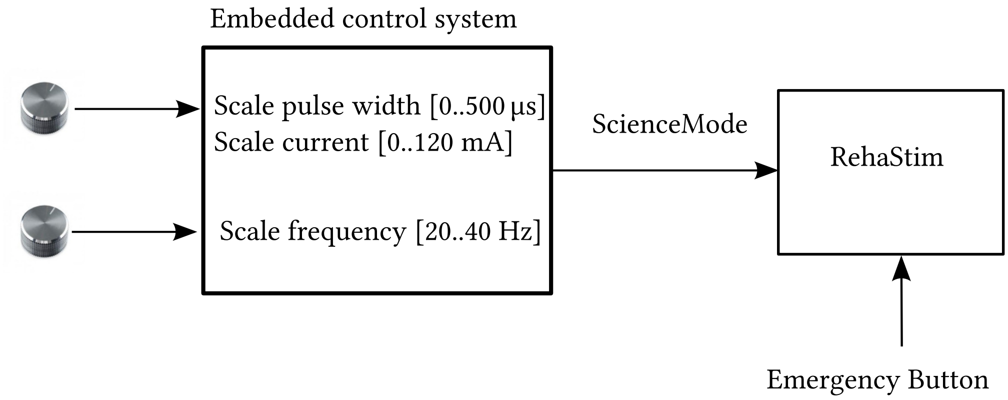
Embedded control system
Scale pulse width [0..500 µs]
Scale current [0..120 mA]
Scale frequency [20..40 Hz]
ScienceMode
RehaStim
Emergency Button

Figure 4.4: User interface of the RehaBike. The pulse width and current are adjusted with the same potentiometer while the frequency is modified with a separate potentiometer. The potentiometer offers 41 detents which are uniformly distributed over the full range which prevents unintended changes during cycling. The emergency button was integrated into the right handle bar (©2017 IEEE).

and flexion phases, the stimulation pattern, as well as the LUT-based speed adaptation method are implemented in Matlab / Simulink. The pilot has two control potentiometers at the right handlebar to increase the stimulation intensity (current 0-120 mA, pulse width 0-500 µs) and/or the stimulation frequency (20-40 Hz). Important data and parameters can be transferred over Wireless Local Area Network (WLAN) during cycling via User Datagram Protocol (UDP) to an Android tablet which ran a customized Kivy App[1] for parameter adjustment, data visualization, and logging. The CP ranges for each muscle group are set according to the values given in Table 3.5. These ranges, the stimulation latency t_d, as well as the maximum stimulation currents for each muscle group can be set individually

---

[1] https://kivy.org

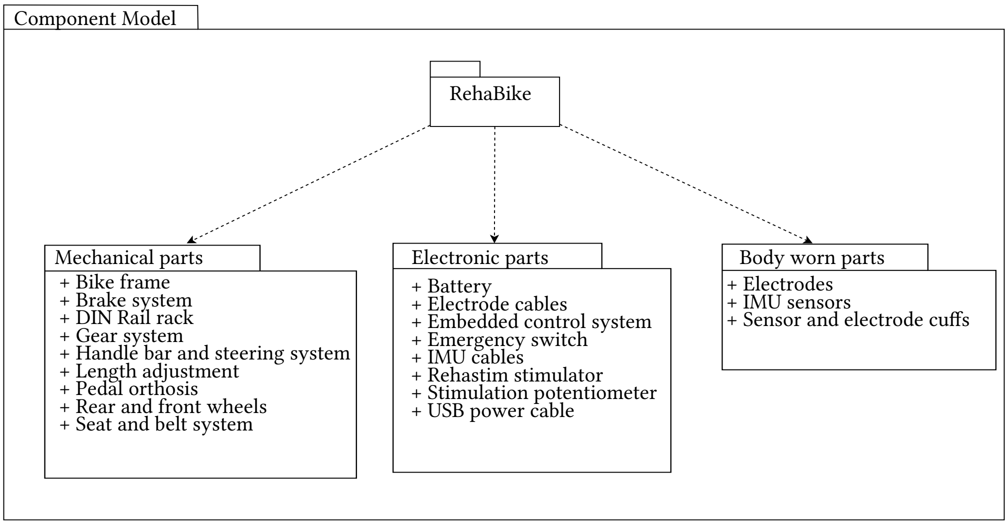
Component Model
RehaBike
Mechanical parts
+ Bike frame
+ Brake system
+ DIN Rail rack
+ Gear system
+ Handle bar and steering system
+ Length adjustment
+ Pedal orthosis
+ Rear and front wheels
+ Seat and belt system
Electronic parts
+ Battery
+ Electrode cables
+ Embedded control system
+ Emergency switch
+ IMU cables
+ Rehastim stimulator
+ Stimulation potentiometer
+ USB power cable
Body worn parts
+ Electrodes
+ IMU sensors
+ Sensor and electrode cuffs

Figure 4.5: All mechanical, electronic and body worn parts which compose the RehaBike.

via the user interface and stored for the next training session. The current intensity was scaled linearly in the range from 0 to the set maximum value of the respective muscle group, with the maximum current intensity being 120 mA. The pulse width was scaled in the range of 0 µs to 500 µs, depending on the intensity set by the user. Thus, the maximum increment of the first potentiometer results in the preset individual maximum current and 500 µs pulse width for all muscles. The embedded control system was used during the daily ergometer training of the pilot at the end of the preparation phase and during the mobile-cycling exercises.

A detailed risk analysis of the overall system, a device manual, and available safety certificates, were approved by the Cybathlon technical committee according to the standard ISO13485-2014. Furthermore, a certified confirmation by the medical team partner Dr. Niedeggen confirmed that there were no objections to the participation of the pilot in the Cybathlon from a medical point of view. Both technical and medical checks were accomplished by an on-site technical and medical check of the device and pilot at the Cybathlon.

4.3 Training and Cybathlon Results

The preparation for the Cybathlon can be divided into stationary home training and regular mobile cycling training. The home training consisted of five phases, which are summarized in Table 4.2. In the studied literature, no training regimes for long-term atrophied muscles are described with respect to FES cycling. At the time of the Cybathlon the pilot had been paralyzed for more than 30 years and had no prior experience with FES cycling. No FES-induced isometric contraction exercises have been applied before to the first cycling training sessions. According to the American Spinal Injury Association (ASIA) impairment scale his lesion was classified as Grade A, which means a complete lack of motor and sensory function below the level of injury.

The goal of phase I was to restore the full range of motion of the lower limbs, to familiarize the skin with the electrodes, and to reactivate the atrophied muscles. For the training, the RehaMove (combination of the RehaStim stimulator (Hasomed GmbH, Germany) with the MOTOmed viva2 ergometer (RECK-Technik GmbH & Co. KG, Germany) with crank-angle-based stimulation control) has been used during Phase I to III. The MOTOmed viva2 ergometer offers different operation modes,

Phases	Period	Frequency	Duration	Stimulation settings
Phase I	04/2015 - 07/2015	once a week	30 min	220 µs, 65 mA, 30 Hz
Phase II	08/2015 - 11/2015	twice a week	30 min	250 µs, 65-80 mA, 30 Hz
Phase III	12/2015 - 04/2016	every second day	30 min	280 µs, 80-90 mA, 30 Hz
Phase IV	05/2016 - 07/2016	daily	30 min	280 µs, 80-90 mA, 30 Hz
Phase V	08/2016 - 10/2016	twice a day	50-90 min	220 µs to 500 µs, 65-120 mA, 25 Hz

Table 4.2: Preparation phases for the Cybathlon

like passive (motor-driven) training, motor-assisted training, and training without motor support (the motor acts as a brake with adjustable resistance). The mechanical power actively produced by the muscles is determined by the device and presented via a display. It has large foot shells, where the patient places his feet in. The adjustable ergometer parameters during the training were the resistance level and the minimum cadence maintained by the motor in the case of absent muscle power. To minimize the difference between training and regular cycling, the ergometer training was done with the MOTOmed viva2 ergometer in combination with the inertial-sensor-based method in Phase V. During this phase the athlete trained the usage of the control interface while manipulating the load settings of the ergometer. Prior to each training, the athlete performed a five-minute warm-up at a low speed and low resistance.

During Phase I, the lowest resistance level and a minimum cadence of 25 rpm was used to protect the joints and bones of the athlete from injuries. In Phase II, the musculature was build up with caution. The ergometer was again set to the lowest resistance level, while the minimum cadence was increased to 40 rpm. Phases III and IV were the continuation of Phase II, while, herein, the minimum cadence was set to 30 rpm. Finally, in Phase V, the goal was to maximize the power. The minimum cadence was set to 35 rpm, the resistance to the highest level, and the stimulation intensity was modulated in intervals. After a short warm-up phase, the pulse width and current were increased until a power output of 20-30 W was achieved. To compensate muscle fatigue, the frequency, current, and pulse width were increased to hold the desired power output as long as possible. After these high-power intervals, the intensity was set for 5 to 10 minutes to low values reducing the power output to 5-10 W allowing the pilot's muscles to recover. The high and the low power intensity intervals were repeated sequentially until the daily training target was reached defined by a total produced energy of 150/630 kcal/kJ. At the beginning of Phase V, the pilot reached this benchmark after 90 minutes of training. Right before the Cybathlon, the benchmark was reached after 50 minutes. From Phase I to III, only a low increase of the mean power output from 5 to 8 Watt was observed. After the start of the daily training in Phase IV, an increase from 8 to 10 Watt mean power output was achieved in two months. Finally, during Phase V compared to the other phases, a further significant increase of the maximum power output and the mean power output as well as a delay of the fatigue onset was observed, as shown in Figure 4.6. To get information on the improvements for the final race, measurements were conducted in week 1, 5, and 9. During the acquisition of these measurements, the stimulation intensity was set to the maximum value and kept constant during the whole measurement phase. In summary, in Phase I-V the cadence was successively increased to the same level as during mobile cycling. Furthermore, during the Phases I to IV, only quadriceps and hamstring were involved. Additional stimulation of the gluteus maximus took only place in Phase V. The stimulation of the

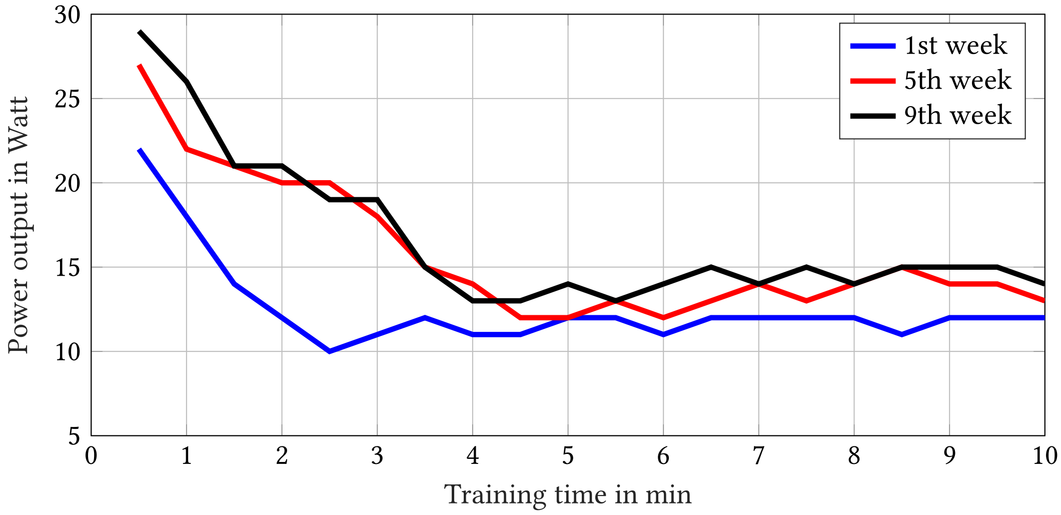

Figure 4.6: Power output for exemplary 10 min training sessions after 1, 5, and 9 weeks of training in Phase V. The power output was measured using the displayed power output of the MOTOmed viva2 ergometer. The compared results were always obtained during the first trial of the daily sessions (©IEEE).

gluteus was skipped before Phase V, because placing the electrodes at the gluteus was not possible for the athlete without assistance of a third person and would have increased the complexity of the ergometer training system. However, the stimulation of the gluteus improved the cycling performance for the mobile cycling during the dead phases of the two other muscle groups.

During the regular mobile cycling training, a control strategy was developed by the athlete, which kept the cycling cadence between 30 and 40 rpm. Below 30 rpm, a small stimulation pause could disturb the smooth cycling pattern, thus resulting in reduced cycling performance, distance, and speed. Above 40 rpm, a faster progression of fatigue could be observed. Within the first 600 m, the athlete used the gear shift and the intensity to keep the cadence in the target range. The stimulation frequency was increased for the remaining 150 m to compensate for fatigue effects and to get the maximum power for the finishing sprint. Besides the stationary ergometer training, a regular mobile cycling training with the RehaBike was performed in the corridors of the research lab and three weeks before the Cybathlon at a gymnasium. During several trials, the optimal control strategy was sought to find with a trial-and-error strategy. The main goal was to treat the muscles with care to reach the full distance, and stay below the allowed time limit of 8 min. Right before the Cybathlon, the pilote was able to cycle five times in a row the full race distance of 750 m with 5 min rest time in between.

During the preparations, the electrode placement and sizes were varied to find the optimal electrode settings for the athlete. The final settings were not changed after the start of Phase V. On the quadriceps, two electrode pairs (RehaTrode, 5cm x 9cm, Hasomed, Germany) were placed with two separate stimulation channels in a row. One pair of larger electrodes (RehaTrode, 7.5cm x 13cm) was used for the hamstrings. At the gluteus maximus muscle, one electrode pair (RehaTrode, 5cm x 9cm) was attached. Since the left leg was slightly weaker than the right, the maximum values for the current for the muscle groups of the right leg were set to 110 mA and for the left leg to 120 mA. All stimulation ranges were set for the pilot according to the Table 3.5. The optimal latency time for the pilot was determined experimentally during training and set to 130 ms as obtained during Phase IV.

During the Cybathlon, no problems or malfunctioning of the device occurred. The pilot was able to make his personal record right at the small final with a time of 6 min 44 s for the race distance of

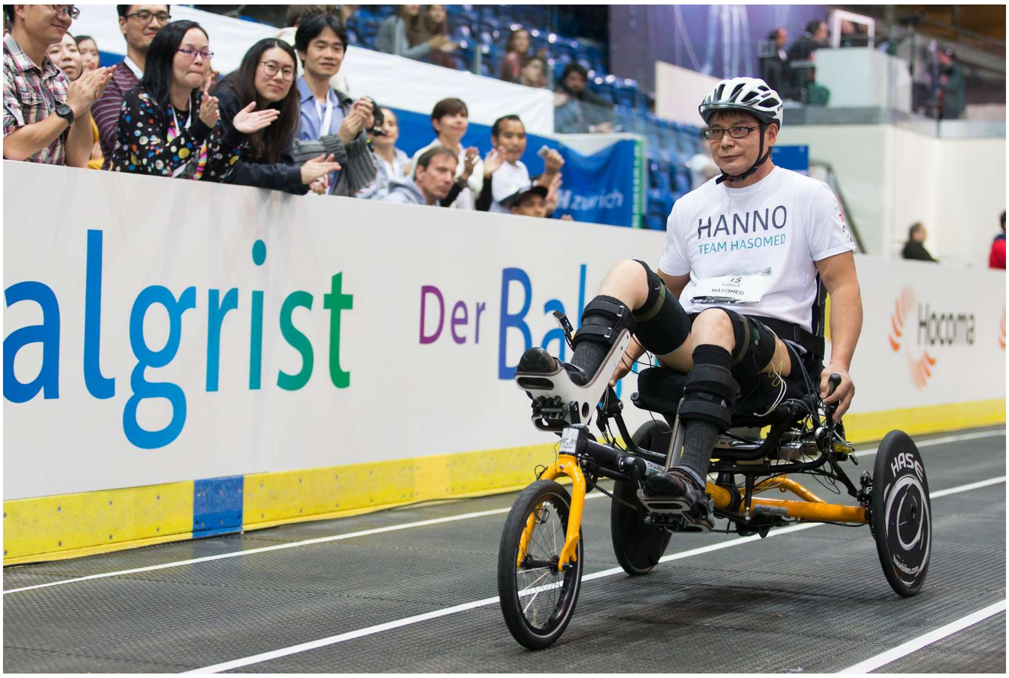

Figure 4.7: The athlete during the Cybathlon race. (©ETH Zürich, Nicola Pitaro)

750 m [1]. During all races, he showed a very smooth cycling movement and did not need to push his legs manually during dead zones. Overall, only 7 out of 11 teams completed the full distance of 750 m, while several pilots need to push their legs manually during dead zones, which was only allowed maximum three times during the race.

4.4 Discussion and Conclusion

With this work, it was possible to show that inertial-sensor-based joint-angle estimation can be used for realizing stationary and mobile FES cycling. Since the developed stimulation system is independent of the cycling device, the same setting and stimulation pattern can be used for regular and ergometer-based cycling. As shown in Figure 3.23, the same stimulation setting for the CP ranges can be used for a large range of position of the cyclist and it is still possible to achieve a cycling movement. For a crank-angle-based stimulation pattern, the stimulation ranges would probably need to be adjusted to achieve a cycling motion for each cycling position as the stimulation-angle ranges vary by up to 35 ° with respect to the crank angle.

Regarding the used bike architecture of the tricycle, the focus was on using as many standard components as possible and on enabling an easy and autonomous transfer. Among the twelve Cybathlon FES bike race pilots, only our pilot and the pilots of the two other teams, that used the BerkelBike (BerkelBike BV, The Netherlands), could get on the tricycle without assistance by a third person. For reaching the podium the next time, the focus should be changed to a weight-optimized and streamlined bike. The presented inertial-sensor-based stimulation pattern ensures positive crank torques that support cycling. But it might be further optimized inside the given stimulation ranges depending on the rider-tricycle geometry to improve mechanic and metabolic efficiency. In [32] the team IRPT presented a stimulation pattern with spatially and sequentially distributed electrodes during dynamic knee extension. With this technique an increased power output and delayed fatigue onset could be achieved. To improve cycling speed and distance, these techniques should be applied.

---

[1] Cybathlon ETH Zürich 2016 / FES Bike Race Finals `https://www.youtube.com/watch?v=G-liwPgf2dU`

The next step is the reduction of the number of used inertial sensors for ergometer cycling to two IMU sensors. Furthermore, the influence of the electrode placement shall be further investigated to overcome the dead zones without the stimulation of the gluteus maximus. Although the used joint-angle-estimation framework reduces the tuning effort, parameters for the speed compensation and the maximum current for each muscle group required manual tuning. To reduce this effort and to further improve the cycling performance, a learning algorithm shall be implemented, as presented in [84], which tries to automatically optimize the stimulation pattern after each crank revolution.

5

Hardware Development

5.1 Overview

In Chapter 4 wired sensors have been used for FES cycling. To further improve the usability and to make the technology available in a home-training device, new wireless sensors and a versatile stimulator module have been developed which will be introduced in this chapter.

Copyright Statement: The methods and results presented in this chapter have been previously published in:

[CYC5] C. Wiesener, E. Ambrosini, L. Blankenfeld, S. Schneider, B. Grzywacz, and T. Schauer. "Wireless IMU- and EMG-Sensors for Controlled Functional Electrical Stimulation". In: *Converging Clinical and Engineering Research on Neurorehabilitation III.* 1st ed. Springer International Publishing, 2018, pp. 16–20. DOI: `10.1007/978-3-030-01845-0_4`.

[CYC6] C. Wiesener, M. Valtin, and T. Schauer. "Current-Controlled Stimulator with Variable High Voltage Generation". In: *13th Int. Vienna Workshop on FES.* IFESS. Vienna, Austria, Oct. 2019.

Therefore, the text and figures in this chapter are extracted, with slight modifications, from those publications. In the following, Section 5.2 presents the developed wireless orientation-measurement system and its performance results. Afterwards, the developed current-controlled neuromuscular stimulator is presented in Section 5.3. All results are finally discussed and concluded in Section 5.4.

5.2 Wireless Orientation Measurement System

In Section 2.4.2, the orientation-estimation algorithm was introduced. There, the estimation was separated into a strap-down integration of gyroscope measurements with high frequency and vertical and south direction correction at a lower sample rate. With increasing sample frequency of the gyroscope the accuracy of the estimation can be improved. At the same time the amount of data to be sent is increased as well. Wired communication is robust in matters of communication errors or data loss and depending on the used bus technology, a high transfer rate can be achieved. But the cables are cumbersome if these wired sensors are used for daily rehabilitation purposes and during dynamic movements, since they can rip off or get stuck if used during cycling, especially if they are used without assistance by handicapped subjects. Wireless sensors are favorable in matters of usability. But they are battery powered and need to be charged regularly, the transmission rates are lower and more susceptible to interference. Furthermore, the developed sensors shall be integrated into existing rehabilitation systems. The RETRAINER system, which was developed within the European project RETRAINER [1], combines FES and robotics for upper-arm and hand rehabilitation of stroke patients. Due to the high metal content in the developed exoskeleton, the developed orientation estimation will be realized without the use of the magnetometers. Furthermore, the orientation estimation shall be integrated directly on the wireless sensor. In the following sections, the developed wireless IMU sensors will be introduced and the reached performance during orientation measurement will be presented.

5.2.1 State-of-the-Art Wireless Inertial Measurement Units

The performance of an IMU is typically characterized by bandwidth, drift, linearity, and sample rate of its sensor front-end. If these sensors are attached to segments of the body the need of small dimensions is essential. In contrast to available commercial products, existing research prototypes are typically smaller and lighter. But for critical applications the data security and compliance against electrical safety standards are mandatory, like European Conformity (CE) / Radio Equipment Directive (RED) certification. In [85] an overview of available commercial and research wireless IMU sensors is presented. The majority of these sensors deliver raw data at low sample rates if standard wireless protocols like Bluetooth Classic or ZigBee are used. In the case of customized protocols like presented in [85, 86], which use enhanced shockburst [2] and sub-1 GHz band communication, a high sample rate can be achieved. But the compliance to the radio transmission standard of the respective regulatory authority has to be certified. For precertified modules using harmonized communication standards like BLE or Bluetooth classic the certification is only needed if the antenna is modified. Furthermore, the specialized protocols are not supported by standard smart devices, which makes it necessary to build up a special receiver or dongle to receive the data via a smart device.

5.2.2 Requirements Analysis and Sensor Architecture

As remarked in Section 3.8, stationary FES cycling is possible with two IMU sensors only, attached to a shank and a thigh. Therefore, the following essential requirements can be derived to build up a system for an easy, usable, and cost effective rehabilitation setting:

- The sensor shall use BLE only for communication so that it can be used in conjunction with standard smart devices.

---

[1] REaching and grasping Training based on Robotic hybrid AssIstance for Neurological patients: End users Real life evaluation, Grant agreement ID: 644721

[2] Enhanced ShockBurst (ESB) is a basic protocol of Nordic Semiconductor supporting two-way data packet communication including packet buffering, packet acknowledgment, and automatic retransmission of lost packets. It uses the 2.4 GHz band like BLE.

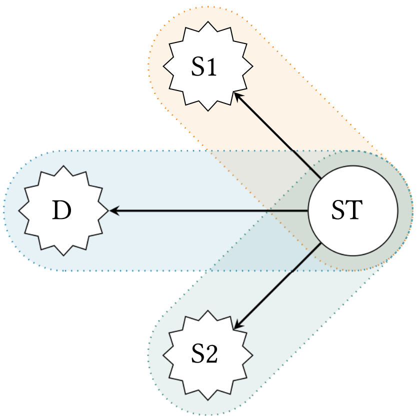

Figure 5.1: Piconet established by stimulator ST involving sensors S1, S2, and smart device D with connections over three physical channels via BLE.

- The sensor shall use an FCC precertified module to avoid certification cost if used in clinical trials.
- The sensor shall be battery powered and charged via a standard micro USB port.
- The sensor's outer dimension shall be less than 30x30x10 mm.
- To reduce the amount of data to be transferred via the wireless communication channel the orientation estimation shall run directly on the IMU.

With two sensors and a smart device for the user interface the communication topology can be represented as a so called single piconet (Figure 5.1). If BLE as a communication standard is used, then the smart device and the sensors will send advertisements to be picked up by the stimulator central device, which acts as the piconet central, initiating a connection between all devices. According to the BLE standard, a central device is permitted to establish connections to multiple peripheral devices. But it is not allowed for the peripherals to have a peer-to-peer connection to each other. In order to access the sensor measurements or send configuration messages from the smart device to the sensors, the stimulator has to act as relay and should be responsible for forwarding the packets from the smart device to the sensor. Analyzing the requirements and the available hardware the so-called nRF[3] device family of Nordic Semiconductor is favorable. This company provides energy-saving radio processors. One of the most recent developments is the System-on-Chip (SoC) nRF52832. This chip combines a 32-bit ARM Cortex-M4F processor (512 kB Flash and 64 kB RAM) and an embedded 2.4 GHz transceiver that can use different protocols like BLE, ANT and proprietary 2.4 GHz protocol stacks like Gazell and Enhanced Shockburst. The built-in Cortex-M4F processor offers in addition to accelerated digital signal processing a floating-point unit (FPU) with a fast multiplication in one clock cycle ('single-cycle basics multiply') and a hardware-accelerated division. The processor can be operated with a voltage of 1.7-3.6 V. All peripherals are flexible in dealing with energy resources and can be shut down when not used to minimize power consumption. Digital (SPI, I2C, UART, PWM) and analog interfaces are widely available. For all interfaces the pins can be arbitrary assigned via Software. The chip is available from third-parties like Rigado as a precertified BLE module (e.g. BMD-300), which can be used in body worn applications. The IMU sensors normally used in consumer

---

[3] nRF is an acronym established be Nordic Semiconductor describing a special chip family.

Sensor	BMX055	LSM9DS1TR	ICM-20948	MPU-9250
Manufacturer	Bosch	STM	InvenSense	InvenSense
Gyroscope sample rate	2 kHz	952 Hz	9 kHz	8 kHz
Gyroscope range	± 2000 $^\circ/s$	± 2000 $^\circ/s$	± 2000 $^\circ/s$	± 2000 $^\circ/s$
Gyroscope ADC resolution	16 bit	16 bit	16 bit	16 bit
Gyroscope zero-rate offset	± 1 $^\circ/s$	± 30 $^\circ/s$	± 5 $^\circ/s$	± 5 $^\circ/s$
Nonlinearity	± 0.05 %	-	± 0.1 %	± 0.1 %
Cross-axis sensitivity	± 1 %	-	± 2 %	± 2 %
Accelerometer sample rate	1 kHz	952 Hz	4 kHz	4.5 kHz
Accelerometer range	± 16 g	± 16 g	± 16 g	± 16 g
Accelerometer ADC resolution	12 bit	16 bit	16 bit	16 bit
Price (per 1000 parts)	3.39 $	3.35 $	2.90 $	4.50 $

Table 5.1: Comparison of available 9 DoF IMU sensors.

hardware are a combination of a communication processor and a so called MEMS chip, as introduced in Chapter 2. These MEMS chips are miniaturized versions of high resolution sensors and are typically available at a low price, size, and power consumption [23]. There is a high amount of miniaturized sensors available with different specifications and prices. In Table 5.1 an overview of available 9 DoF sensors, integrating 3-axis accelerometer, 3-axis gyroscope, and 3-axis magnetometer is given. Since the orientation estimation for FES cycling does not rely on magnetometer measurements, the relevant parameters are sample rates and the gyroscope zero-rate offset and sensitivities. The price of all sensors is more or less comparable and the sample rates are all over 500 Hz the zero-rate offset was identified to be the most important for uncalibrated gyroscope measurements. Therefore, the BMX055 from Bosch Sensortec was chosen.

The overall architecture of the developed IMU sensor is displayed in Figure 5.3. Besides the introduced wireless communication model and the IMU sensor chip, a power module, and a user interface is integrated. The power module handles the battery charging via a standard micro USB port and delivers the voltage level for all components. The user interface consists of a push-button controller and a RGB LED[4]. The sensor is switched on and off via the push button while the Light-Emitting-Diode (LED) indicates the operating state, e.g., BLE advertising, transmitting, or charge state. The 3D illustration of the final sensor board including dimensions is shown in Figure 5.2.

The architecture of the embedded software of the BMD300 module is shown in Figure 5.4. The low-level drivers (depicted in light gray) are part of the chip Software Development Kit (SDK), which offers the configuration and access to all hardware peripherals of the module. On top of the low-level the so called Hardware Abstraction Layer (HAL) implements the interface to the connected peripherals, e.g., the IMU sensor chip, the button, LED, and the battery. At the highest level the TaskMain component schedules the operation of the sensor. If requested, the raw data gets processed to orientation data and then scheduled for transmission to the host via the BLECommHandler, which encapsulates the interface to the underlying Bluetooth low energy protocol stack.

5.2.3 Orientation Estimation and EMC Test Results

As introduced in Section 3.4.3, the optical motion capturing OptiTrack has been used to assess the achieved accuracy of the wireless IMU sensor. The same optical measurement body was used

---

[4] A light-emitting diode (LED) consisting of a red, green, and blue LED to produce mixed colors.

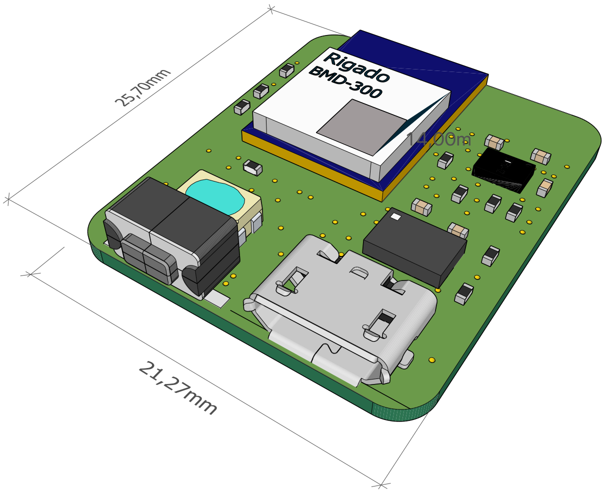

Figure 5.2: Printed Circuit Board (PCB) of the developed IMU sensor with dimensions.

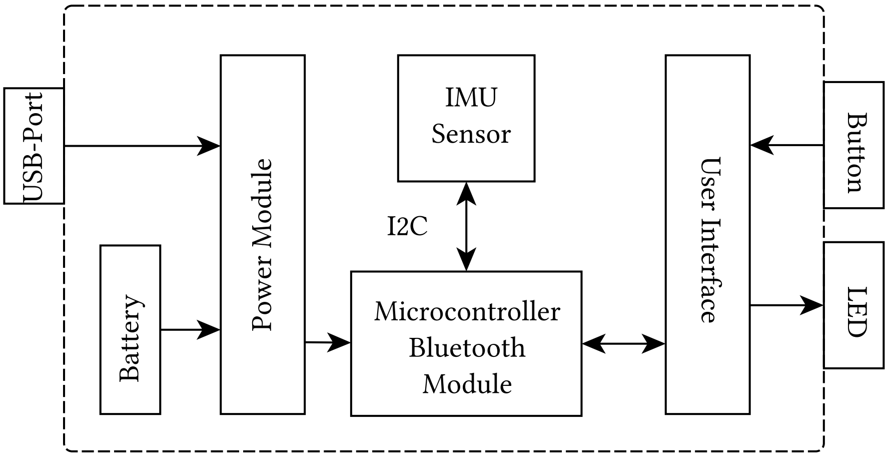

Figure 5.3: Block diagram of the IMU sensor (Adapted from [87]).

for this evaluation, but it was moved by hand inside the working area of the OptiTrack system. Both orientations were afterwards compared calculating the Euler angles according to the sequence z, y, x. The orientation-estimation algorithm of Section 2.4.2 has been used, where the strap-down integration of gyroscope was performed at a frequency of 200 Hz and the vertical-drift correction using accelerometer measurements at a frequency of 50 Hz. The strap-down integration can be executed up to a rate of 1 kHz. But it would not be possible to transmit the raw data. Hence, a lower rate was used for the experiment. The sensor fusion weights have been set to $k_{\text{acc}} = 1$ and $k_{\text{mag}} = 0$. The bias of the gyroscope was initially estimated by integrating the gyroscope measurements during the first seconds, when the sensor was at rest. This bias was then subtracted from successive gyroscope measurements during the experiment. Both, the raw data, including gyroscope and accelerometer readings, and the estimated orientation have been transferred asynchronously to a smart device at a sending frequency of 25 Hz. Each BLE package included eight raw data measurements at 200 Hz per axis and two quaternions at 50 Hz, respectively. Since the internal orientation estimation does not use the magnetometer, the absolute heading angle differs by a fixed offset from the optical measurement heading angle. Therefore, the initial heading angle of the IMU orientation was aligned with the initial heading angle of the optical measurement. Afterwards, the error between optical and

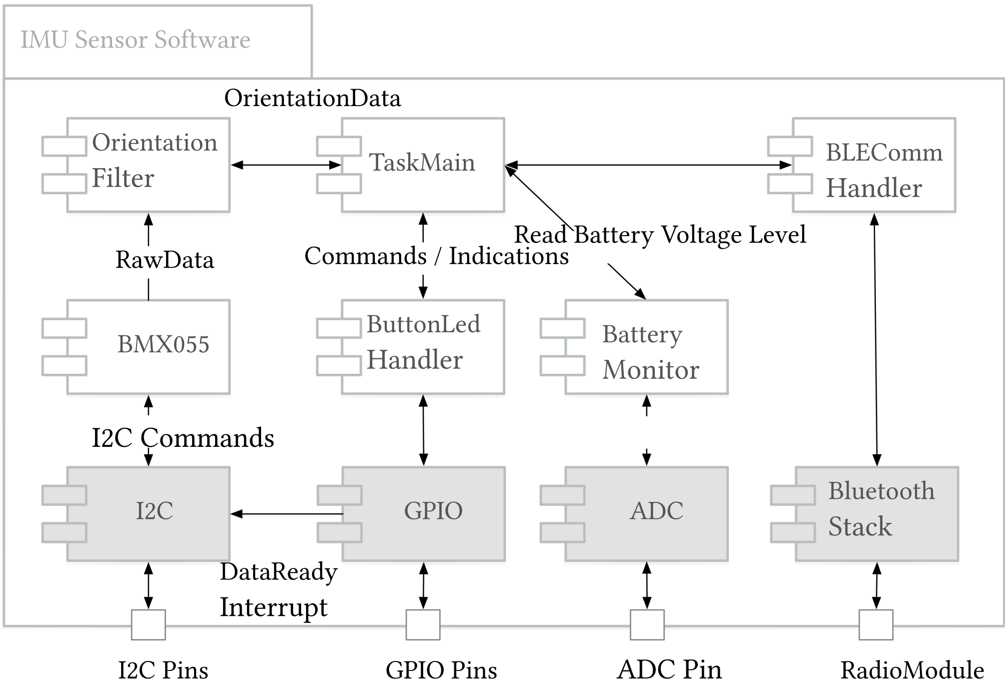
IMU Sensor Software
OrientationData
Orientation Filter
TaskMain
BLEComm Handler
RawData
Commands / Indications
Read Battery Voltage Level
BMX055
ButtonLed Handler
Battery Monitor
I2C Commands
I2C
GPIO
ADC
Bluetooth Stack
DataReady Interrupt
I2C Pins
GPIO Pins
ADC Pin
RadioModule

Figure 5.4: IMU sensor software architecture of the BMD300 module.

inertial measurement-system was calculated. As shown in Figure 5.5 the roll and heading angle show spikes in the error signal due to rotations over gimbal lock and inaccurate time alignment between both measurement systems. These spikes have been excluded from the evaluation if the respective angle wrapped at ±180° and the absolute value of the error was bigger than ±20°. Finally, an RMS of 6.13 ° for the roll, 2.2 ° for the pitch, and 4.4 ° for the heading angle error can be achieved, compared to the optical measurement reference signal. Furthermore, the initial and final deviation for heading angle is close to zero which indicates a very low drift during the test of 100 s.

After the performance of the orientation estimation fulfilled the requirements, an Electromagnetic Compliance (EMC) test was executed. Since the sensor is used in conjunction with a medical device it has to fulfill the same EMC requirements as the neurostimulator presented in the next section. For home use a maximum radiation of 30 dB (30-1000 MHz) measured in a distance of 10 meters is allowed in all directions during charging and measurement. The wireless transmission module (standard BLE 4.2) transfers the data inside the 2.4 GHz band, which is therefore not part of the measurement. As introduced earlier, the BLE module is already precertified according the FCC [5] and the RED [6]. In Figure 5.6 the EMC test results during charging (a) and measurement (b) are shown. No infringement of the threshold value could be detected for both operating modes. Furthermore, the battery lifetime was tested during real measurements and transfer to a smart device. The sensor was able to measure and transfer the orientation data for up to 10 hours with a sending frequency of 25 Hz. Afterwards, it took 90 minutes to fully recharge the battery.

---

[5] Federal Communications Commission

[6] Radio Equipment Directive (EU directive 2014/53/EU)

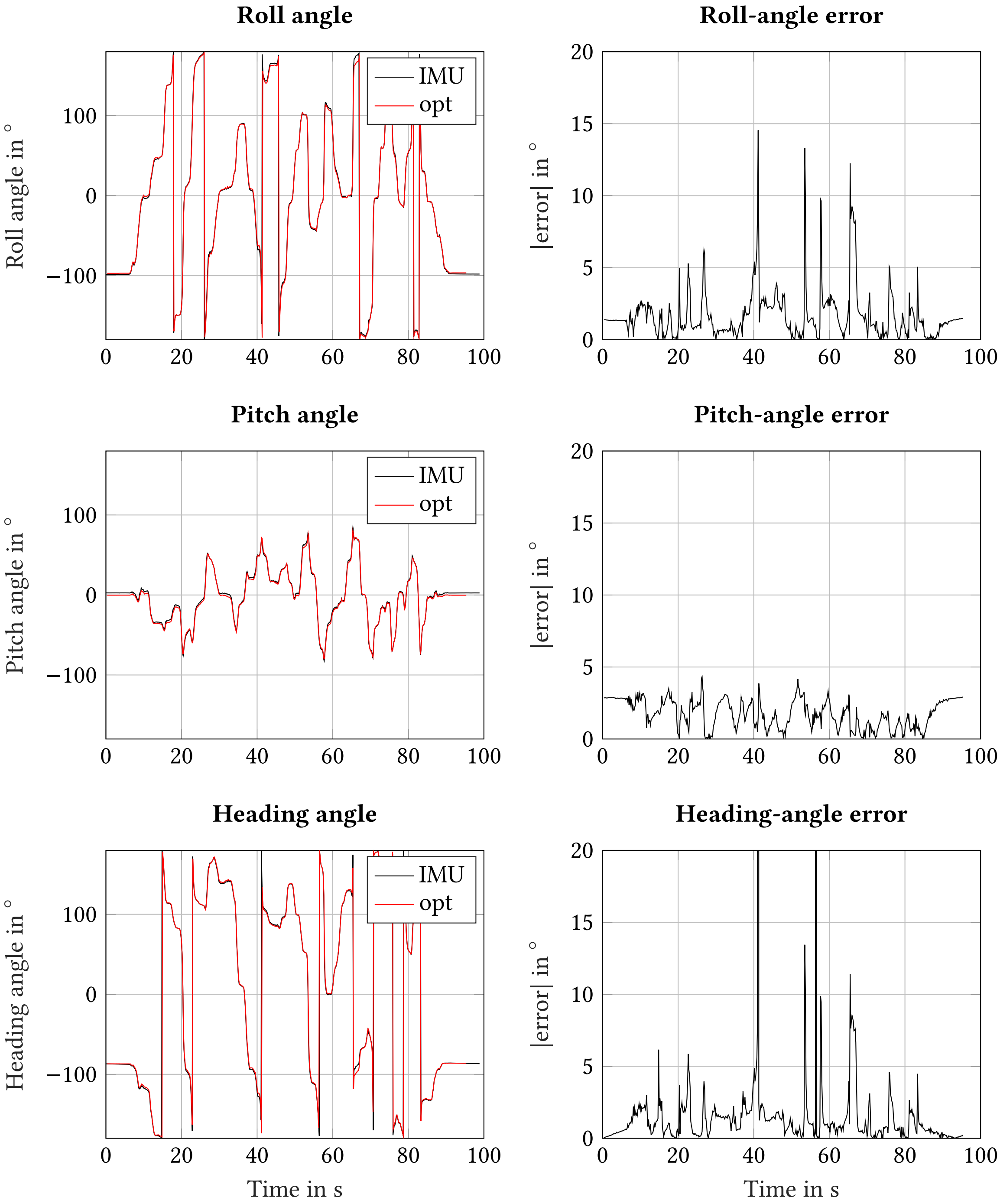

Figure 5.5: Left plots: Comparison of optical (red line) and inertial measurement (black line) of roll, pitch, and heading angle; Right plot: Error signals for roll, pitch, and heading angle. During the trial the optical measurement body has been rotated about the longitudinal and the vertical axis for several times while the pitch angle was only varied in the range [−70°...70°].

5.3 Current-Controlled Neuromuscular Stimulator

As introduced earlier, the current available and certified FES-cycling stimulation systems are tabletop units. They are not certified for portable use or to be worn at the body, e.g., the RehaMove ™, the

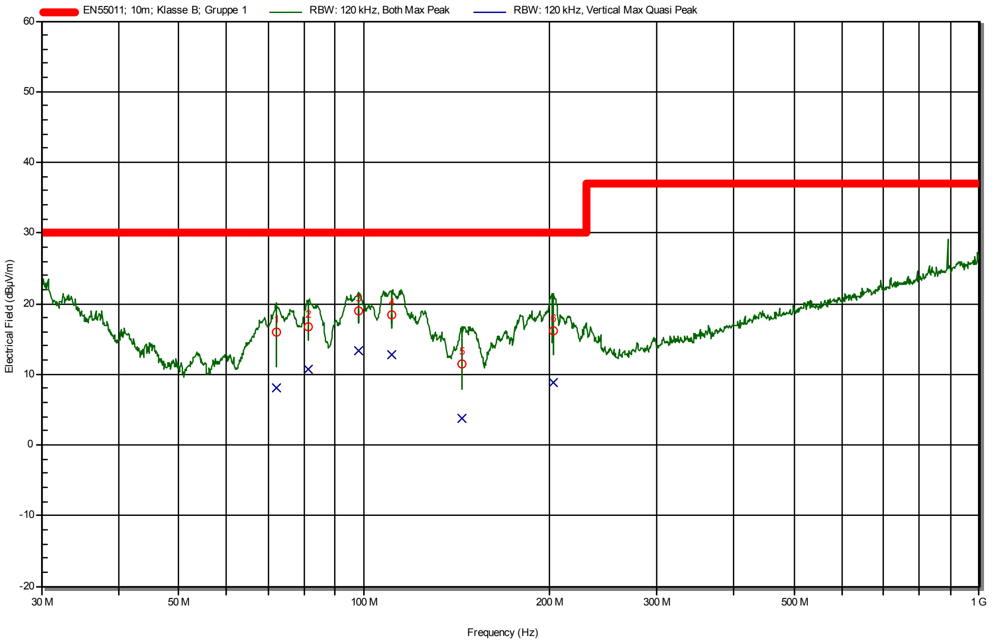

(a) Charging

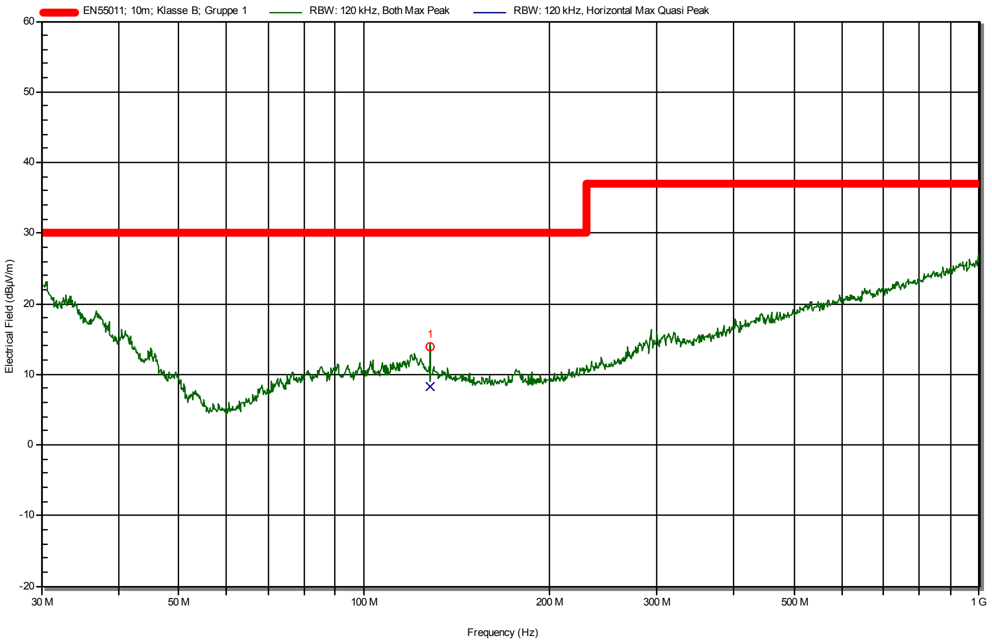

(b) Measurement

Figure 5.6: EMC test results for the sensor in the range of 30-1000 MHz

.

MyoCycle ™ , or Berkelbike ™. These systems always need the intrinsic crank information of the used ergometer or cycle. Furthermore, they only offer a standard display or LED interface and cannot be configured via a smart device. Therefore, a new stimulation module was developed which can be triggered via wireless IMU sensors. The module can be configured and controlled via a smart device. Due to its small size it might be directly integrated into a sleeve.

5.3.1 State-of-the-Art Neuromuscular Stimulators

There are many stimulation systems available for paraplegic rehabilitation. One of the most frequently used stimulators in FES cycling is the RehaMove by Hasomed GmbH, which offers the so-called Sciencemode library for stimulation configuration if used in conjunction with an ergometer or tricycle. The stimulator consists of two independent stimulation modules each with four channels, whereas each module includes a DC/DC converter cascade to produce the galvanically-isolated high voltage. The stimulation pulses are then generated via discrete H-bridges. A comparable architecture can be observed for the clinical research system Rehamove Science [88] or in scientific approaches like [89, 90]. The advantage of this architecture is that only one high-voltage source is needed and depending on the amount of H-bridges several channels can be stimulated sequentially. The main drawback is the high volume, cost, and weight of the DC/DC converters and the high amount of discrete power switches for the H-bridge realization. A different approach was presented in [91] and [92] where a flyback transformer is used for each stimulation channel which charges a capacitor. This capacitor is then directly switched to the electrodes via a current controller. Using this architecture each channel can act separately with a very low rise time of the current and with voltages up to 300 V. The drawback is the high volume, weight, and cost of the flyback transformer for each channel which limits the number of available channels. In [93] an optimization of the first architecture is presented which uses only one DC/DC converter for high voltage generation and an integrated high voltage demultiplexer for H-bridge switching. Furthermore, [94] proposes a universal stimulation system for array electrode stimulation using several demultiplexers.

5.3.2 Requirements Analysis and Stimulator Architecture

Since a neuromuscular stimulator is a class II medical device, there are several guidelines for the development and production process as well as standards to assure safety for the user and operator. According to ISO 13485, a controlled development process is mandatory, therefore essential requirements are derived, which can be found in Appendix C. In summary, to enable mobile applications, the entire circuit should be compact, portable, and battery powered only. The use of a common connector for either charging or stimulating makes it possible to omit a galvanic isolation of the high-voltage generation and the battery power. In addition, with up to 8 channels, several muscle groups shall be stimulated at the same time. Internally, a voltage source at the electrode interface of up to 115 V is needed to drive the requested currents even for high skin-electrode contact resistances, which will be explained in the next section. Furthermore, the design of the DC-DC converter has to be optimized to avoid power loss during stimulation. Finally, the stimulator shall be configured and controlled via a smart device using a wireless protocol. The resulting overall hardware architecture is summarized in Figure 5.7. The design includes an application processor that configures the respective intensities and channels based on the defined stimulation pattern. As for the wireless IMU, the application processor offers a BLE interface to adjust the stimulation settings via a smart device. The stimulation processor is configured via a Universal Asynchronous Receiver Transmitter (UART) bus and handles the processing of the stimulation pulses, the control of the high voltage, and the configuration of the channel multiplexer.

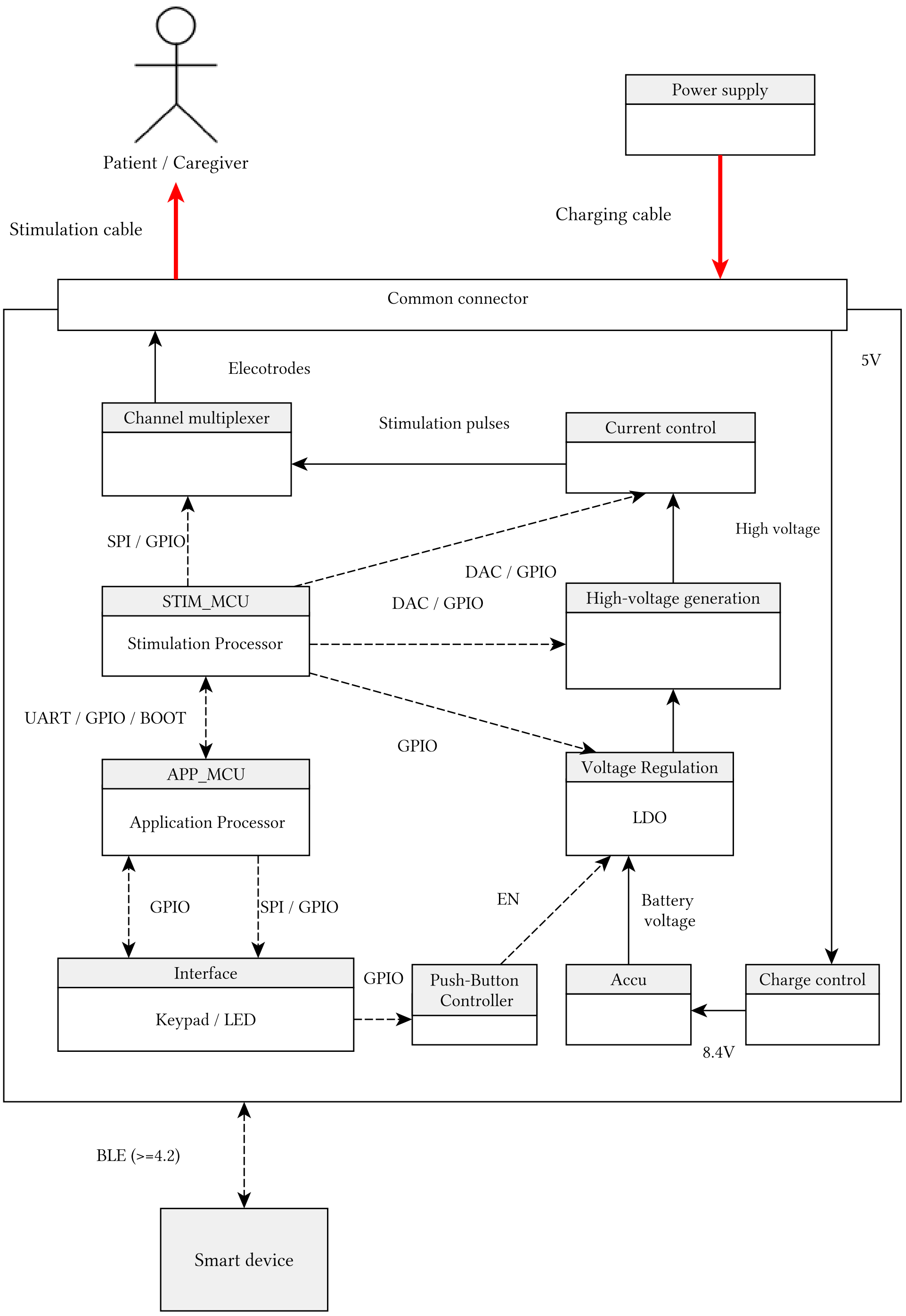
Patient / Caregiver
Power supply
Stimulation cable
Charging cable
Common connector
Elecotrodes
5V
Channel multiplexer
Stimulation pulses
Current control
High voltage
SPI / GPIO
DAC / GPIO
DAC / GPIO
STIM_MCU
Stimulation Processor
High-voltage generation
UART / GPIO / BOOT
GPIO
APP_MCU
Application Processor
Voltage Regulation
LDO
GPIO
SPI / GPIO
EN
Battery voltage
Interface
Keypad / LED
GPIO
Push-Button Controller
Accu
Charge control
8.4V
BLE (>=4.2)
Smart device

Figure 5.7: Hardware architecture of the neuromuscular stimulator. Dashed black lines describe information flow, while solid black lines describe the power lines. The interface with the patient or external components are described with solid red lines, if power signals are applied. The solid border describes the enclosure of the stimulator.

5.3.3 Variable High-Voltage Generation

A high-voltage source is needed to drive the current through the load attached at the electrodes. According to the requirements, a stimulation voltage of up to 100 V is needed at the electrode interface. A Metal-Oxide-Semiconductor Field-Effect Transistor (MOSFET), which is commonly used as high-side switch or inside a demultiplexer, exhibits a remaining $R_{\mathrm{DS(on)}}$ of several Ohms between the drain

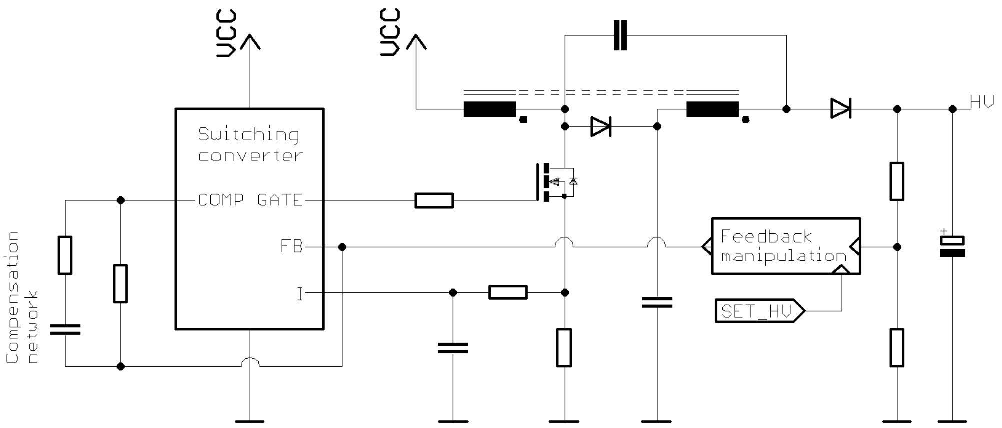

Figure 5.8: High-voltage generation consisting of a SEPIC converter with feedback manipulation.

and source when switched on. In combination with the current-control shunt, a voltage drop of up to 15 V is unavoidable. Therefore, internally, a higher voltage of 115 V is required to realize a stimulation voltage of up to 100V at the electrode interface. As stated in the introduction, the use of a common connector for either charging or stimulation makes it possible to omit the need of a galvanic isolation for the high-voltage source. An isolation of several millimeters is guaranteed due to the housing and connector isolation. Therefore, a standard switching converter can be used. The aim of the design is to minimize the size of the switching converter and at the same time to keep the efficiency as high as possible. The higher the frequency of the switching converter, the smaller the inductance can be selected. However, the duty cycle has to be kept small for high efficiency. To keep the duty cycle below 95 % a coupled inductor for a cascaded switching converter can be used, which is called Single Ended Primary Inductance Converter (SEPIC). The resulting schematic is shown in Figure 5.8. The compensation network is used to guarantee adequate phase margin of the current-mode control. The voltage VCC is directly applied from the battery power which has to be above 5 V. The resulting high-voltage generation fulfills the requested requirements. The optimized circuit only uses $7.2\,\mathrm{cm}^2$ of PCB space and still guarantees a high efficiency. With the standard SEPIC ciruit only a constant high voltage can be generated. If the electrode impedance is high, the maximum voltage level is needed to drive the requested current. If the impedance is low the unused voltage level drops over the low-side current control which results in a low efficiency due to power dissipation. Furthermore, for applications with low current requirements (e.g. facial stimulation, transcranial stimulation) the stimulation voltage shall be adjusted to a minimum level of 40 V. Hence, an adequate voltage level for the actual electrode impedance is needed. The presented feedback manipulation can be used to adjust the feedback voltage, where the feedback voltage is the control input of the switching converter. The feedback manipulation can be seen as an applied bias at the feedback line. By adding this bias, the internal high-voltage level can be controlled in the range between $[40, 115]$ V.

5.3.4 Multiplexer

To distribute the current pulses to the different channels, an integrated multiplexer is used. In order to generate bipolar current pulses, a full bridge is necessary for each channel. This results in a total of 32 discrete power transistors. Standard bipolar transistors cannot be used to avoid a corruption of the controlled stimulation current by the basis current of the transistor, which would change the

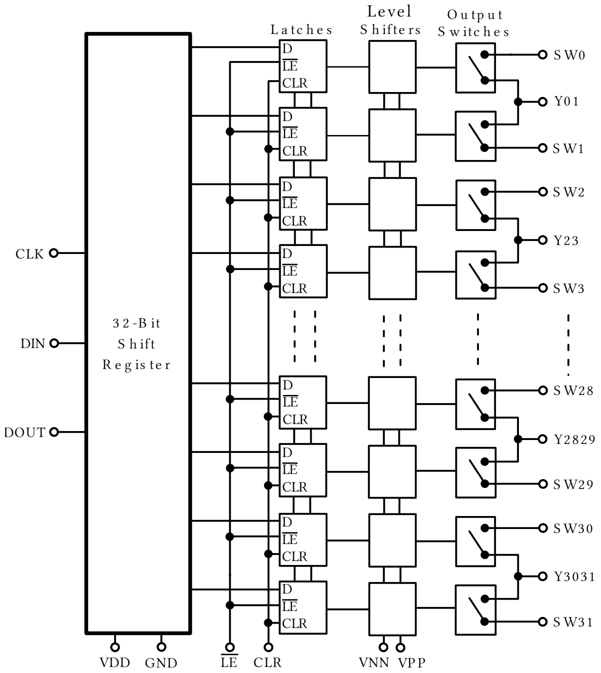

Figure 5.9: Internal schematic of the used multiplexer HV2801 [95].

current over the measurement shunt. Furthermore, a discrete assembly using Surface-Mount Device (SMD) parts would still occupy a large area of the PCB and a high number of soldering contacts. Therefore, an Integrated Circuit (IC) is used, which is controlled via Serial Peripheral Interface (SPI). The IC contains eight full bridges with level converters for high-voltage signals. There are several IC available with different number of channels and voltage levels. The HV2801 shown in Figure 5.9 consists of 32 high-voltage MOSFETs in half bridges which can be connected to form 8 full bridges with a maximum differential voltage of up to 220 V. The output voltage can be switched off in several micro seconds via one General Purpose Input/Output (GPIO) line, while each switch can be controlled via SPI. With a 64-Lead QFN package, the design is small, but could be still soldered by hand. The overall quiescent current for a switching rate of approx. 100 Hz is rated in the data sheet with approx. 78 µA. Furthermore, the 32 switches can be used to access array electrodes, where several stimulation channels are combined to form virtual electrodes. The maximum configuration consists of 15 anodes and one cathode.

5.3.5 Current Controller

Controlling the current through the skin means, controlling the current through a combined capacitive and resistive load that is not connected to the ground of the stimulator. This means that either low- or high-side current control can be applied. Because N-type transistors in general can control more current than P-types, they are preferable for switching heavy loads. Low-side switching with N-type devices is easier than high-side switching and can often be done without the need for special drivers. Furthermore, low-side control means that the low voltage of V_{SIG}, which will be switched by the demultiplexer, will be $> 0V$ due to the voltage drop over the low-side switch.

For this task it is conceivable to use an n-channel MOSFET as the control switch. If the MOSFET is directly driven by an analog output of the micro controller a certain drain current can be realized. The characteristic drain-current-to-drain-source relation is a nonlinear and temperature-dependent

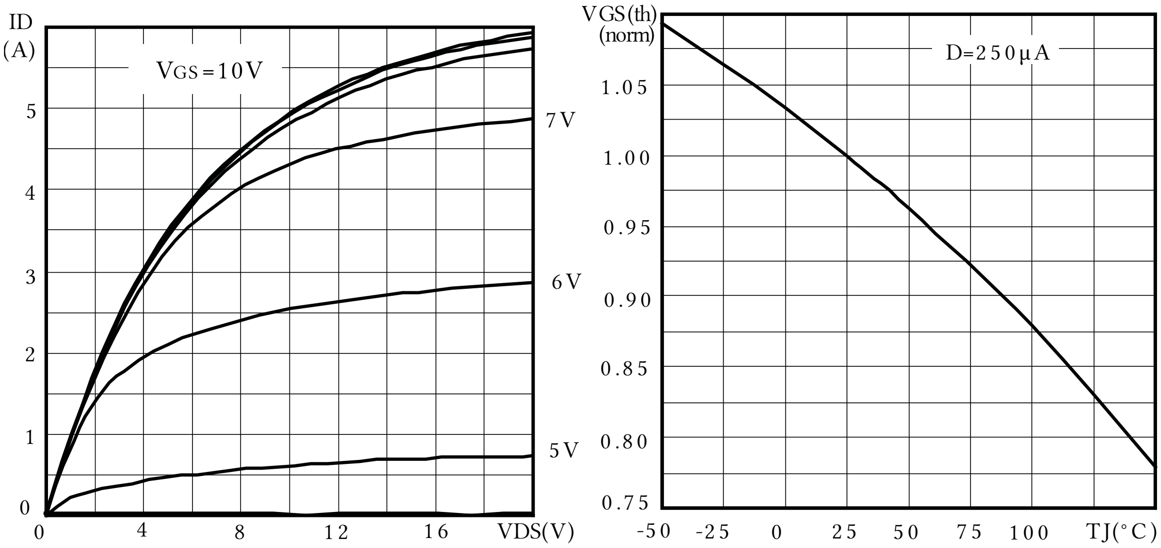

(a) Output characteristics I_D over V_{DS} for a fixed V_{GS} **(b)** Temperature characteristic V_{GS} over T_J

Figure 5.10: Characteristic curves for an exemplary n-Channel MOSFET STN1NF20 which can be used for low-side current control [96].

function (see Fig. 5.10), which cannot be predetermined. At the low-side MOSFET, a certain power loss can be expected, which results in a temperature variation of up to 30 °C. According to the exemplary characteristic temperature curve in Figure 5.10, a variation of up to 5 % for the gate-source threshold voltage $V_{GS(th)}$ is expected. Hence, the open loop structure does not satisfy the requirements of a desired steady-state-error of less than 2 %. Therefore, an analog PI controller is used that controls the MOSFET in the linear mode, above the gate-source threshold voltage. The controller is build up using a non-inverting integrator circuit with varying gain. The gain was tuned empirically to guarantee a fast stimulation onset of less than 2 µs, while having a small overshoot of less than 5 %. Furthermore, the resulting gain should be realizable with standard values for the E-series of resistors and capacitors. The values $R_1 = 162\,\Omega$, $R_2 = 1.8\,\mathrm{k}\Omega$, and $C_1 = 270\,\mathrm{pF}$ gave the best results in all experiments. The value for the set-point current is provided via a Digital-to-Analog Converter (DAC) channel of the stimulation processor, which will be explained in the next section. The actual value of the current is measured via a shunt resistor between the source of the MOSFET and ground. This additionally realizes a negative current feedback, which ensures a higher temperature stability of the analog current controller. To assure a fast control behavior, the analog controller is designed with a single operational amplifier (op-amp) as shown in Figure 5.11. The potential at the shunt is marginally affected by the op-amp. Therefore, no additional impedance converter is needed. Dependencies on the drain voltage and temperature are adequately adjusted by this topology. To avoid a wind-up of the controller output during the pause between pulses, the output of the op-amp is shorted using a power mosfet. The actual current signal is fed to an ADC input of the micro controller to check if an electrode connection error is present during stimulation.

5.3.6 Software and Hardware Architecture

The stimulation processor (see Fig. 5.7) handles the high-voltage control, pulse generation, and electrode-error detection. Different digital interfaces such as SPI and UART are necessary to communicate with peripheral parts and the application controller. The same application controller as

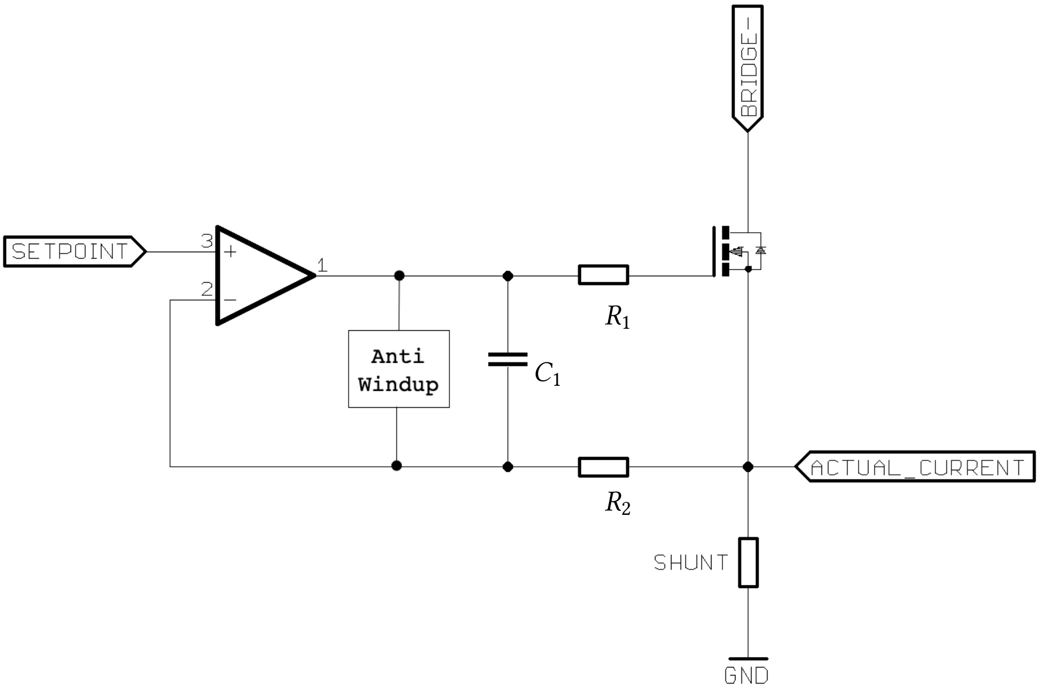

Figure 5.11: PI-controller for low-side current control with a switch for en- and disabling the control output. The BRIDGE- signal is connected with the low-side parts of the multiplexer. The SETPOINT signal is fed via the DAC of the micro-controller. The Anti-Windup control is realized with a controllable switch, which shorts the output of the op-amp with negative feedback path during stimulation pauses.

for the IMU sensor is used to handle the cycling application and all supporting tasks, e.g., battery monitoring, user interface, etc. This chip incorporates a standard Arm Cortex M4F processor and a BLE radio module. The application and stimulation processor can be programmed in C/C++ and are shipped with an SDK for low-level driver access. The stimulation controller uses a 32-Bit hardware timer to guarantee a high resolution of the pulse generation. Furthermore, the stimulation current and voltage are monitored via ADCs. The target values for current and high-voltage control are applied via integrated DACs.

The stimulation-pulse routine is running inside a timer-interrupt routine according to the following flow diagram in Figure 5.12 for each channel. In a first step, the target current value for the low-side control is set via the DAC, and the DEMUX configuration for the dedicated channel and the positive pulse are set. In the second step, the DEMUX is enabled and the current control is activated for the duration of the pulse width. Furthermore, the ADC is enabled to measure the voltage over the low-side shunt during the positive pulse via a Direct Memory Access (DMA) channel. In the third step, the stimulation is stopped. During this interphase interval the current controller is disabled and the measured shunt current is averaged and stored. Additionally, the switch configuration for the negative pulse is set. Now, in the fourth step the negative pulse is executed the same way the positive pulse was generated including the current measurement. At the end of the negative pulse, in the fifth step, the switch matrix is set to OFF, the current controller is deactivated, and the DAC voltage is set to 0. Now both measured current values for the positive and negative pulses are evaluated. If the measured current is below 10 % of the target current the electrode was not contacted or the electrode impedance was too high. In this case, an electrode error is indicated via an LED and notified to the user interface.

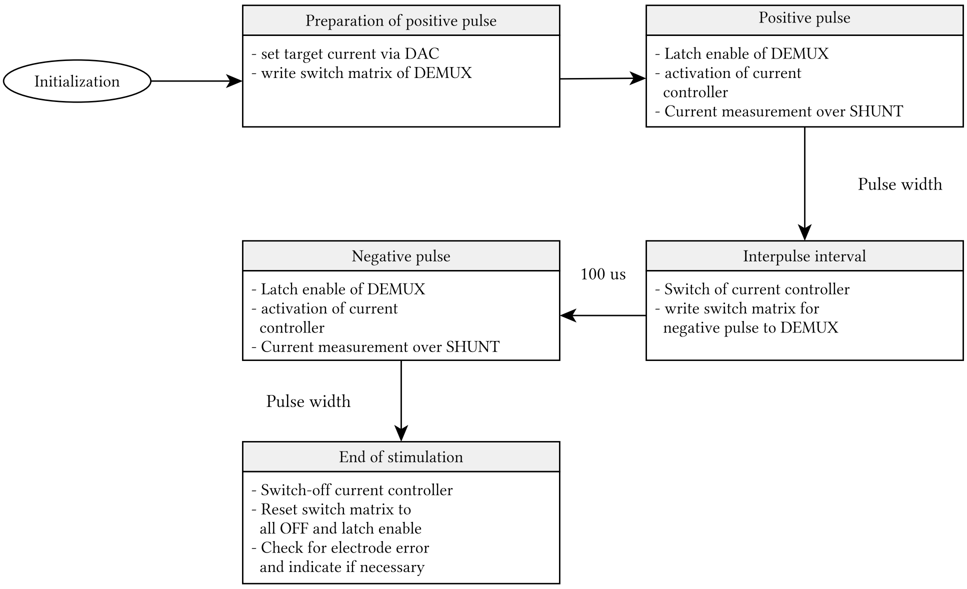
Initialization
Preparation of positive pulse
- set target current via DAC
- write switch matrix of DEMUX
Positive pulse
- Latch enable of DEMUX
- activation of current controller
- Current measurement over SHUNT
Pulse width
Interpulse interval
- Switch of current controller
- write switch matrix for negative pulse to DEMUX
100 us
Negative pulse
- Latch enable of DEMUX
- activation of current controller
- Current measurement over SHUNT
Pulse width
End of stimulation
- Switch-off current controller
- Reset switch matrix to all OFF and latch enable
- Check for electrode error and indicate if necessary

Figure 5.12: Flow chart of the pulse generation, which is executed for each channel using a timer-interrupt routine.

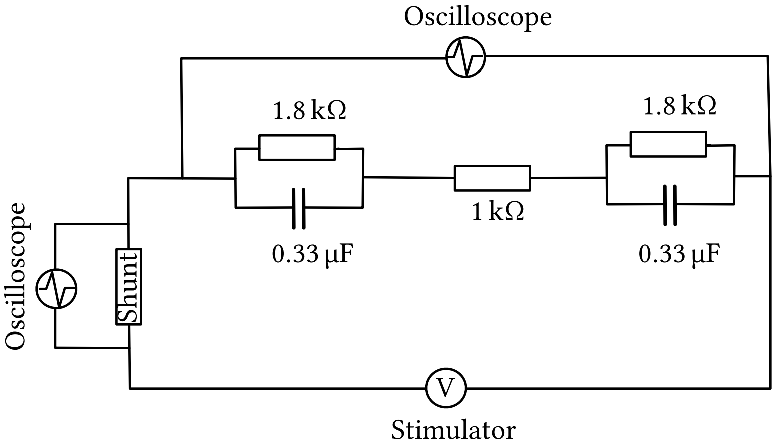
Oscilloscope
1.8 kΩ
1.8 kΩ
1 kΩ
0.33 µF
0.33 µF
Oscilloscope
Shunt
V
Stimulator

Figure 5.13: Worst-case skin model for medical-device verification (Guideline 09-01 03/2007 MDS-Hi).

5.3.7 Results

In summary, all requested requirements (see Appendix C) could be fulfilled. The majority is realized by design decisions, e.g., controller, battery, or connector selection. Especially, the results for the performance requirements shall be discussed in this section. This includes the high-voltage accuracy, stimulation-pulse characteristics, and the EMC performance. To test the stimulation device a so-called skin model is used, which mimics the impedance of both electrode-skin interfaces and the tissue in between (see Figure 5.13). The generated high voltage was tested for different input and output voltages, as shown in Figure 5.14. Here, the output voltage V_{Out} for a fixed output current I_{Out} is given over different battery-voltage levels. The resulting efficiency varies between 77-85 % for a low and between 86-90 % for a high electrode impedance. During active stimulation the SEPIC is not able to transfer enough charge into the buffer capacitor. Hence, the high voltage starts to drop by ≈ 1.5 V during stimulation and rises during stimulation pause, as shown in Figure 5.15. This results in a voltage ripple of 1.5 V peak-to-peak depending on the stimulation pulses. The current controller

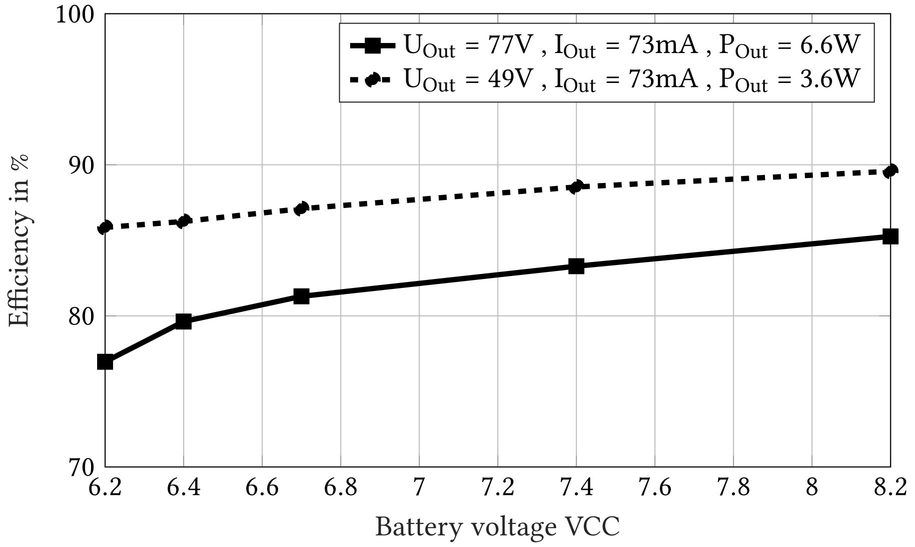

Figure 5.14: Efficiency of the high-voltage generation consisting of a SEPIC converter with feedback manipulation.

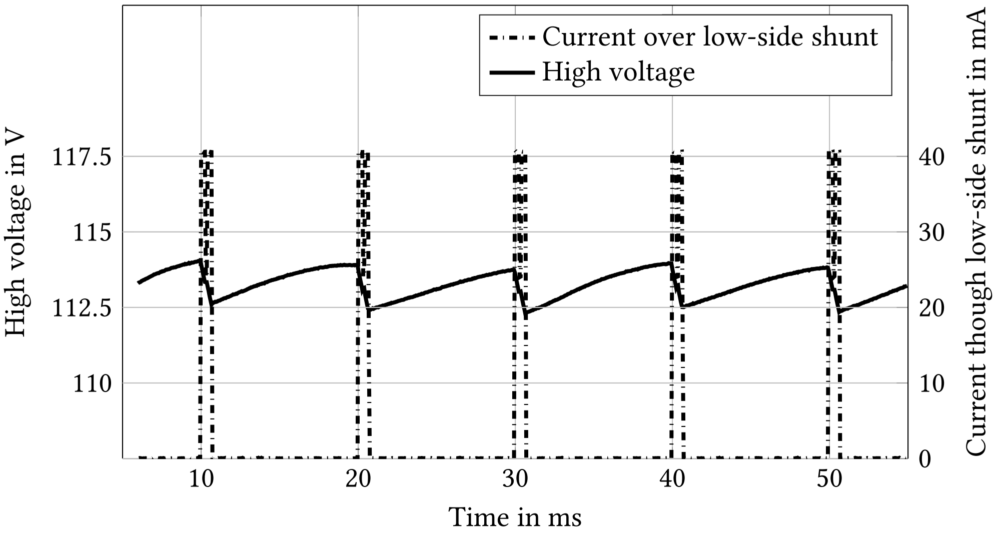

Figure 5.15: Voltage drop and ripple during stimulation with 40 mA over worst-case skin model with 100 Hz and 300 µs pulse width (biphasic stimulation pulse). The high voltage was set to 115 V. Through the low-side shunt, the current always flows in the same direction even if it is a biphasic current.

fulfills the required performance parameters in all aspects. Figure 5.16a shows the stimulation voltage (black solid line with 50 V/Div) and the resulting stimulation current at a skin model (dashed line, 20 mA/Div) for an exemplary bipolar stimulation pulse with 40 mA and a pulse width of 300 µs. The ascending slope of the voltage during the stimulation is common for a capacitive load as well as the remaining charge during the interpulse phase, which results in a nonzero voltage level at the beginning of the negative stimulation pulse. Consequently, this leads to a small overshoot of the stimulation current at the beginning of the negative pulse. In Figure 5.16b, the ascending slope of the stimulation pulse is shown in more detail, where the stimulation voltage is scaled with 20 V/Div and the stimulation current is shown with 20 mA/Div. The current control needs approximately 1.5 µs to reach the target current. But the slope starts with a small switching artifact of the demultiplexer's discharge current. These artifacts cannot be avoided by the current controller since the current does not flow through the low-side shunt as long as the controller is disabled.

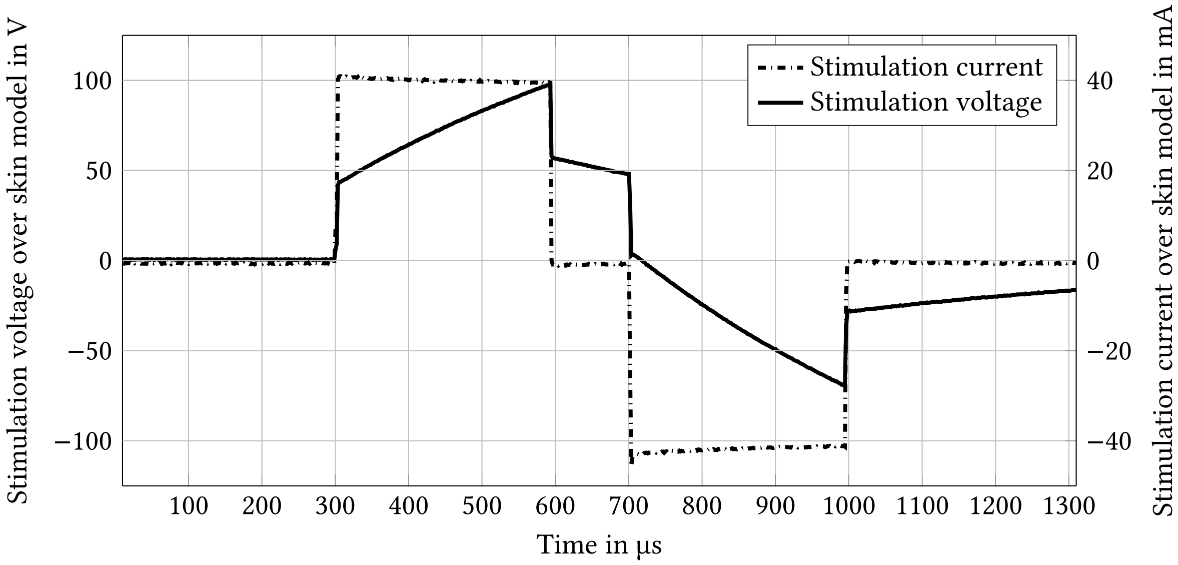

(a) Biphasic stimulation pulse (40 mA, 300 µs)

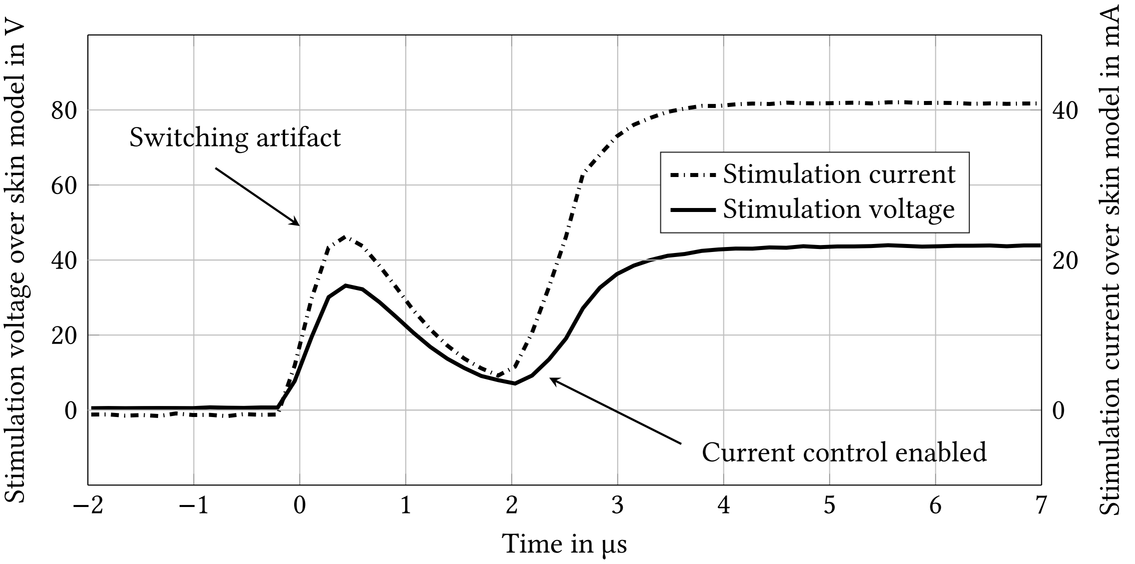

(b) Onset of the same stimulation pulse

Figure 5.16: Performance characteristics of the stimulation using a skin model.

After the performance tests fulfilled the requirements, an EMC test was executed. According to the standard IEC 60601-2-10:2015 the test setup presented in Figure 5.17 has to be applied. Therefore, a worst-case setting was defined which was set to all channels stimulating at 80 mA, with 350 µs pulse width at frequency of 25 Hz. With this setting, the high-voltage source is permanently recharging the high-voltage capacitor which might produce the electromagnetic disturbances. Over the full frequency range the maximum allowable threshold for radiation in home use was not infringed as shown in Figure 5.18.

5.4 Conclusions and Further Improvements

In Section 5.2, a wireless IMU sensor was developed with integrated orientation estimation. With a full battery charge, the sensor is capable of transmitting packages with inertial measurements (200 Hz

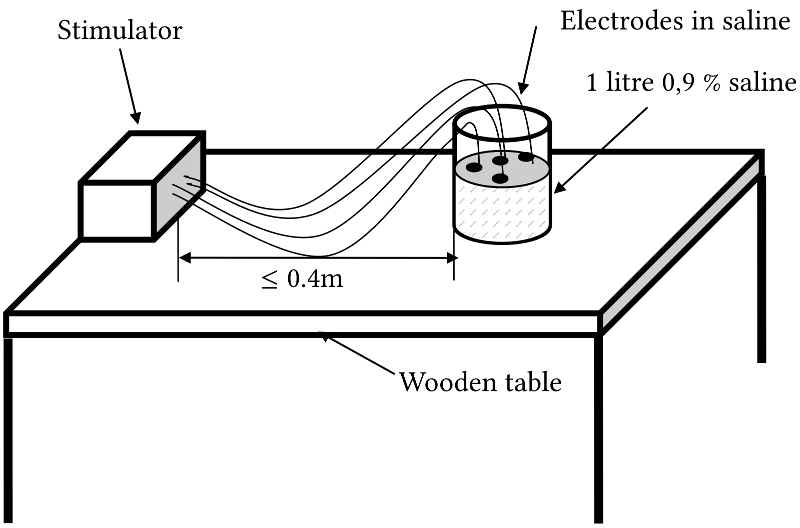

Figure 5.17: EMC test procedure according to 60601-2-10:2012 for nerve and muscle stimulators (adapted from [97]). All electrodes have to be connected to the stimulator, while the endings attached to the electrodes have to be inserted in 0.9 % saline in a cable distance of 0.4 m.

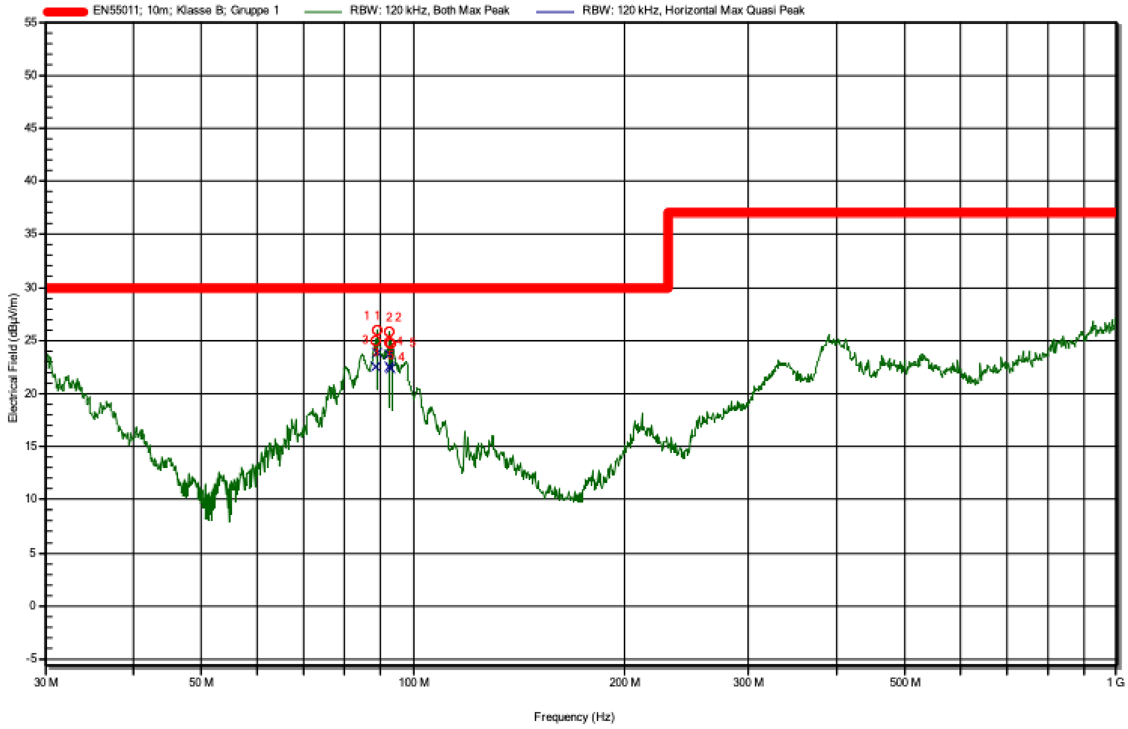

Figure 5.18: EMC test results for the stimulator according to ISO 60601-2-10:2015 for home use. The red line indicates the maximum allowable threshold for radiation in home use. The test was performed during the stimulation of all channels at 80 mA, with 350 µs pulse width, and at frequency of 25 Hz

.

gyroscope measurements, 50 Hz accelerometer and magnetometer measurements) and the estimated orientation (50 Hz) at a sending frequency of 25 Hz for up to ten hours. The orientation estimate provides a very small drift for the relative heading angle without using the magnetometer. Thus, the sensor can be used not only for movements against the gravitational acceleration but also for more complex movement patterns.

The presented current-controlled stimulator fulfills all requested requirements while being ultra-compact. Up to eight stimulation channels can be independently controlled or 16 array electrodes

(15 anodes and one cathode) can be accessed, while the stimulator can be configured via a standard smart device. The variable high-voltage generation can be used to adjust the max. stimulation voltage in the case of electrode impedance changes. For the final release of the device, this adaptation can be used for energy saving or applications where only a low stimulation voltage is needed. Finally, if the demultiplexer is configured with a constant switching-matrix configuration for one permanent stimulated channel, low DC currents can be generated with up to 30 mA for iontophoresis applications. For one channel at a 1 kΩ load the stimulator can drive up 100 mA for up to 1 ms at a frequency of 100 Hz, while an onset time of approximately 1.5 µs can be achieved. If all channels are activated, the stimulator can drive up to 80 mA with a pulse width of 350 µs at a frequency of 25 Hz which results in an average charge of 5.6 Coulomb. During FES cycling, the muscles are stimulated one after the other, so that a maximum of two channels are stimulated simultaneously (e.g., knee extensor of the left leg and knee flexor of the right leg), if both legs are stimulated. Taking the maximum settings used during the Cybathlon a charge of 4.8 Coulomb would be required. Thus, the developed stimulation module should be able to generate sufficient charge to enable FES cycling. Due to the regulations for medical devices, it is not possible to test devices on patients without the certification by a notified body. Therefore, no tests on patients could be performed within the scope of this dissertation. As next steps, a user interface concept and waterproof housing is needed as well as electrical-safety tests to prepare the device for clinical trials.

6

FES Swimming Methods and Experimental Evaluation

6.1 Overview

As introduced in Section 1.1, a spinal cord injury is often associated with paralysis of the upper and/or lower extremities which means a severe restriction of physical activity and health for the affected subjects. Depending on the level and severity of the injury, this involves functional limitation of various body sensory and motor functions below the level of lesion. Functional electrical stimulation is used successfully in cycling or rowing as presented in Chapter 3. In this chapter, a pilot study with two proficient front crawl swimmers (both ASIA A SCI, T5/6) is presented who performed a ten-week swim training with stimulation support. In addition to the functional electrical stimulation, tSCS was applied in order to reduce spasticity and to increase trunk stability [13, 14]. IMU-based motion analysis is further introduced to study joint angles of the lower limbs as well as roll angles at the lower and upper trunk during swimming. In a post-training assessment, this method has been applied to understand performance differences that have been observed when using the different support modalities during the training sessions. The suitability of reusable silicon electrodes for FES and tSCS stimulation in water has been investigated as well during the post-training assessment.

Copyright Statement: The methods and results presented in this chapter have been previously published in:

[SWIM1] C. Wiesener, J. Axelgaard, R. Horton, A. Niedeggen, and T. Schauer. "Functional Electrical Stimulation assisted swimming for paraplegics." In: *22th Conference of the International Functional Electrical Stimulation Society*. IFESS. Nottwill, Switzerland, Aug. 2018.

[SWIM2] C. Wiesener, T. Seel, J. Axelgaard, R. Horton, A. Niedeggen, and T. Schauer. "An Inertial Sensor-based Trigger Algorithm for Functional Electrical Stimulation-Assisted Swimming in Paraplegics". In: *IFAC-PapersOnLine* 51.34 (2019), pp. 278–283. DOI: `10.1016/j.ifacol.2019.01.039`.

[SWIM3] C. Wiesener, A. Niedeggen, and T. Schauer. "Electrotactile Feedback for FES-Assisted Swimming". In: *Converging Clinical and Engineering Research on Neurorehabilitation III*. 1st ed. Springer International Publishing, 2019, pp. 922–925. DOI: `10.1007/978-3-030-01845-0_18`.

[SWIM4] C. Wiesener, L. Spieker, J. Axelgaard, R. Horton, A. Niedeggen, N. Wenger, T. Seel, and T. Schauer. "Supporting front crawl swimming in paraplegics using electrical stimulation: A feasibility study". In: *Journal of NeuroEngineering and Rehabilitation* 17.1 (Apr. 2020), p. 51. DOI: `10.1186/s12984-020-00682-6`.

[SWIM5] C. Wiesener, T. Seel, L. Spieker, A. Niedeggen, and T. Schauer. "Inertial-Sensor-Controlled Functional Electrical Stimulation for Swimming in Paraplegics: Enabling a Novel Hybrid Exercise Modality". In: *IEEE Control Systems* 40.6 (Dec. 2020), pp. 117–135. DOI: `10.1109/MCS.2020.3019152`.

Therefore, text and figures in this chapter are extracted, with slight modifications, from those publications. In the following, Section 6.2 gives the state-of-the-art in aquatic therapy in SCI patients. Section 6.3 introduces the developed methods, experimental setup, and study protocol of the STIMSWIM pilot study. The results of the study are presented in Section 6.4, which are finally discussed in Section 6.5 and concluded in Section 6.6.

6.2 State-of-the-Art of Swimming and Aquatic Therapy in SCI Patients

As introduced in 1.4, body weight-supported treadmill walking, FES ergometer cycling, and rowing are recommended for lower-leg rehabilitation in SCI patients. Furthermore, [5, 18, 19] suggest swimming as the best aerobic training for the whole body for paraplegics, even if the paralyzed legs are not moved. The standard method for paraplegics to relearn swimming or unaided movements in water is the Halliwick method that teaches independence in the water [98]. The method suggests that the swimmer should first adjust to the water and then learn to change their position in the water so that they can always move into a position that allows safe breathing. During the relearning phase, the swimming instructor teaches the patient how to perform precise symmetrical strokes because asymmetrical strokes easily cause the paralyzed limbs to roll and make it difficult to maintain a straight course [5]. Depending on the height of the lesion, different swimming styles are recommended for example backstroke, breaststroke, and crawl stroke. After the relearning phase, most patients are able to swim without further assistance [98]. Besides the method for relearning simming after SCI, there are only a few studies on the effect of swimming in paraplegics in particular, although, it is a Paralympic sport since 1960. In [99], the effect of high-frequency swim training on the cardiorespiratory capacity of SCI patients was evaluated. After three years, an increase of four times compared to baseline was observed, while the control group (conventional land-based training) had no significant increase in cardiorespiratory capacity.

Besides the few research articles regarding the effect of paraplegic swimming, aquatic therapy (e.g. aquarobics, underwater treadmill training, or aqua jogging) is used for the rehabilitation of incomplete SCI patients. Three systematic reviews of the medical benefits of aquatic therapy for patients with incomplete spinal cord injury are available in the literature [100–102]. Due to the lack of randomized controlled trials, all three reviews conclude that the current research quality in the specific area of clinical rehabilitation in water is rather low. Despite the different measures across the reviewed studies, aquatic exercise sessions showed a positive impact on physical function in all studies [100]. The reason might be that the aquatic environment directly promotes and maximizes the participants' residual motor function, leading them to feel more independent in the aquatic environment after an adaptation period [103]. Similar results can be formulated for cardiorespiratory fitness [104–106]. In several studies with only few patients, improvement of cardiorespiratory fitness could be observed. Some studies showed that heart rate was lowered in SCI patients who exercised in warm water. Furthermore, the patients improved their thermoregulatory response on physical exercise. This allowed patients to exercise longer and thus increased their aerobic capacity [104, 107]. In the study in [103], it was reported that muscle spasticity was significantly reduced due to the training, which ultimately led to the reduction of the daily Baclofen dose. Additionally, [100] lists several other studies that demonstrated an increased range of motion of the lower extremities and reduced spasticity.

Electrical stimulation for massage and iontophoresis in water has been proposed a hundred years ago in [108]. The latter is used to transfer pharmaceuticals solved in water into the human body by placing one electrode on the body of the subject above the water and the counter electrode inside the water without direct contact to the subject. In [109], electrodes inside the water are used to produce a sensation feedback to the arm via electrical stimulation pulses. However, to my best knowledge, there is no prior work on FES-assisted swimming or aquatic therapy.

6.3 Methods

The human leg can be modeled as a kinematic chain with three segments and at least six rotational degrees of freedom. While the hip joint has three degrees of freedom – flexion/extension, adduction/abduction, internal/external rotation –, the human knee and ankle joint exhibit only one and two functional degrees of freedom, respectively, and barely admit any motion in the other directions. These degrees of freedom are actuated by numerous muscles, many of which excite more than one degree of freedom of a joint or even span across more than one joint. Figure 6.1 shows the major muscle groups of the lower limbs acting in the sagittal plane. Most of the muscles can be recruited by electrical stimulation via skin electrodes: the gluteus maximus muscles (1), which extend the hip joints; the quadriceps muscles (2), which primarily extend the knee joints and secondarily flex the hips; the hamstring muscles (3), which primarily flex the knees and secondarily extend the hips; the tibialis anterior muscles (4), which dorsiflex the ankle joints; the triceps surae muscles (5), which primarily pronate the ankle joints and secondarily flex the knees. Unfortunately, the hip flexors (6) are difficult to activate artificially by transcutaneous electrical stimulation.

The first question regarding FES support of paraplegic swimming is, which leg movement and swimming style can and should be assisted by FES. As mentioned earlier, there are different preferred swimming styles for paraplegics depending on their swimming ability, degree of paralysis, and lesion level. For normal breaststroke in unimpaired swimmers, the so-called frog kick is used as a leg technique. It includes knee flexors and extensors, thigh adductors and abductors, gluteus maximus, and the plantar flexors. In own preliminary tests, it was found that – due to the high number of involved muscle groups – a complex movement like the frog kick is currently not feasible with FES.

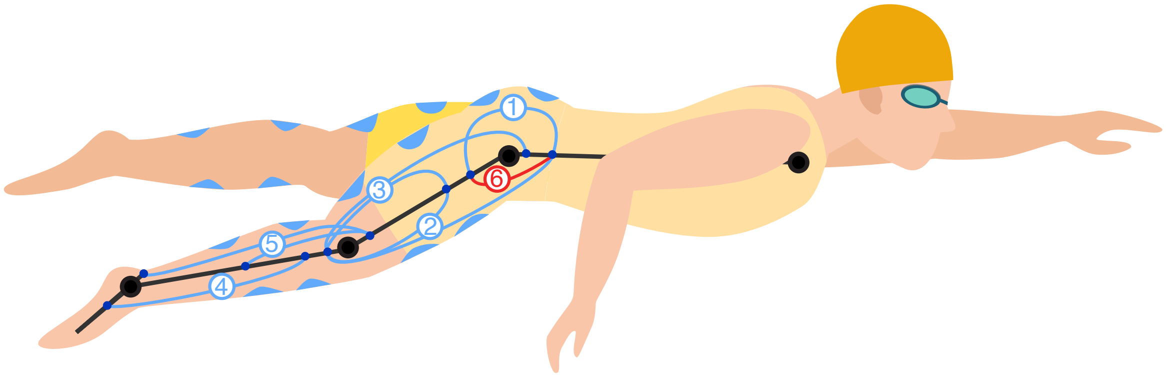

Figure 6.1: Lower limb muscles that act in the sagittal plane on the hip, knee, and ankle joints. Muscles that are well triggered by non-invasive FES and their corresponding stimulation electrodes are highlighted in blue: (1) gluteus maximus, (2) quadriceps, (3) hamstring, (4) tibialis anterior, (5) triceps surae, (6) hip flexors (©2020 IEEE).

The easier so-called flutter kick can be used for backstroke and front crawl. It involves mostly the hip and knee extensors and flexors. In [110, 111], the knee angle for healthy non-expert swimmers during front crawl was analyzed. After a short and strong extension phase, a plateau phase can be observed where the knee joint is fully extended. During this plateau phase, the contra-lateral knee is flexed to 40 to 50 degrees and then directly extended to the same plateau phase. In preliminary tests, it was shown that the stimulation of gluteus maximus muscle is difficult to realize, since the electrodes could not be placed precisely by paraplegics themselves without assistance and the stimulation-induced hip-angle change was quite low. Furthermore, the hip position of a paraplegic in backstroke swimming depends on the level of control over the hip. In further own investigations, it was found that the more flexed the hip is, the less propulsion can be achieved by stimulating the knee flexors and extensors. Patients who are proficient in backstroke and front crawl will therefore profit most from stimulation support of the flutter kick during front crawl swimming.

6.3.1 Functional Electrical Stimulation Support

Based on above reported initial tests and conclusions, it was decided to use FES-induced flutter kicks for proficient front crawl swimmers. Furthermore, floats are attached to the ankles that lead to knee flexion and an upward movement of the ankle in a non-stimulated leg. On the one hand, this results in a more streamlined posture in the water. On the other hand, it implies that the desired knee movement can be realized by alternating between FES-induced knee extension and passive knee flexion caused by the floats. Hence, only two stimulation channels are needed. The quadriceps muscles of both legs are alternately stimulated with the stimulation electrodes placed at the proximal part of the rectus femoris and the motor point of the vastus medialis of each leg. The stimulation, which is applied with a stimulation frequency of 25 Hz, is switched on and off at a rate of 1 or 2 Hz, which results in approximately one or two leg kicks per arm stroke depending on the arm-stroke frequency. The amplitude and pulse width can be varied in the ranges 0–100 mA and 0–500 µs, respectively. Both values are increased/decreased simultaneously to control the generated muscle contraction.

6.3.2 Transcutaneous Spinal Cord Stimulation

Transcutaneous spinal cord stimulation is used in addition with the aim to reduce lower-limb spasticity during and after swimming [112]. Therefore, the afferent fibers of the L2–S2 posterior roots are

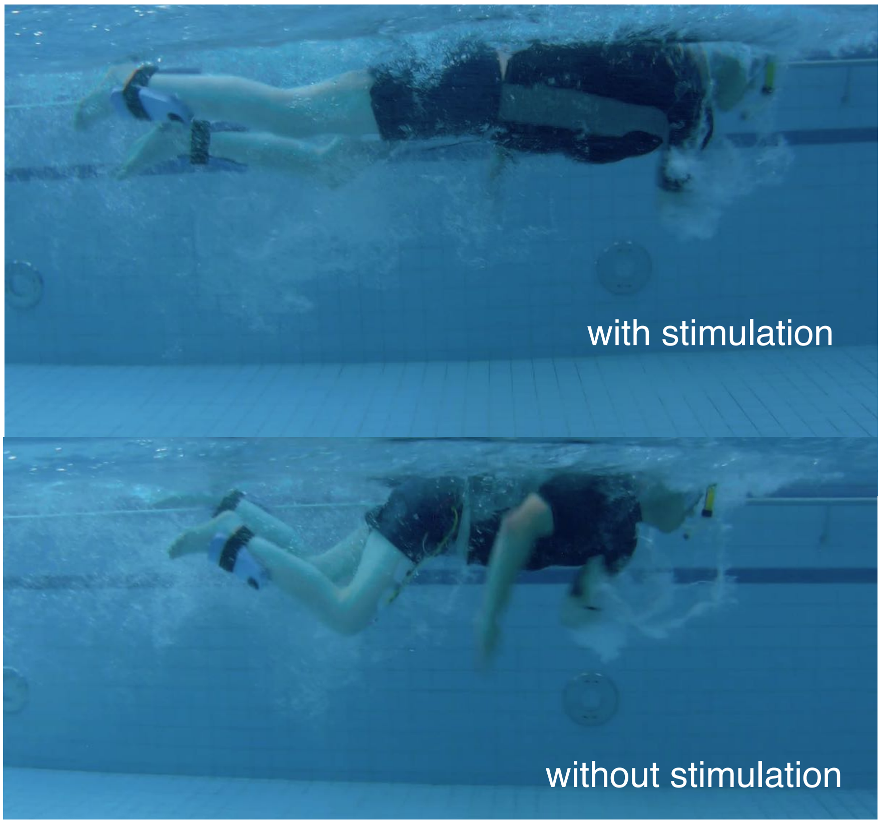

Figure 6.2: Paraplegic subject (Th5/6, ASIA scale A) with and without stimulation (FES+tSCS) using floats at the ankles and a snorkel.

stimulated continuously at 50 Hz using biphasic pulses with 1 ms pulse width over the T11/12 region at the spinal cord according to [112]. The electrode position at the back and stimulation amplitude has been determined as outlined in [112]. By switching on the tSCS, the trunk musculature is activated at a motor level as a positive side effect. This improves trunk stability and straightens the upper body. As shown in Fig. 6.2, a streamlined swimming position can be achieved with FES and tSCS compared to no stimulation in a paraplegic subject.

6.3.3 Experimental Setup

6.3.3.1 Stimulator

The stimulation system for swimming shown in Fig. 6.3 employs a CE-certified stimulator (RehaMove3, Hasomed GmbH, Germany) with customized firmware. A single current source is integrated into the device, and the output of the source is multiplexed for up to four channels. The stimulator is placed inside a waterproof bag under the swimmer's T-shirt. All stimulation cables are tunneled through the bag and drained with silicone to prevent water intrusion. The bag is attached with a strap on the swimmer's back between the shoulder blades. The stimulator can be controlled via the membrane keypad, i.e., the stimulation program can be selected, started/stopped, and the stimulation intensity can be adjusted. The stimulator is battery-powered, and the high-voltage source is galvanically isolated from the battery power. Hence, the current conduction is always constrained between the positive and the negative electrode of each stimulation channel.

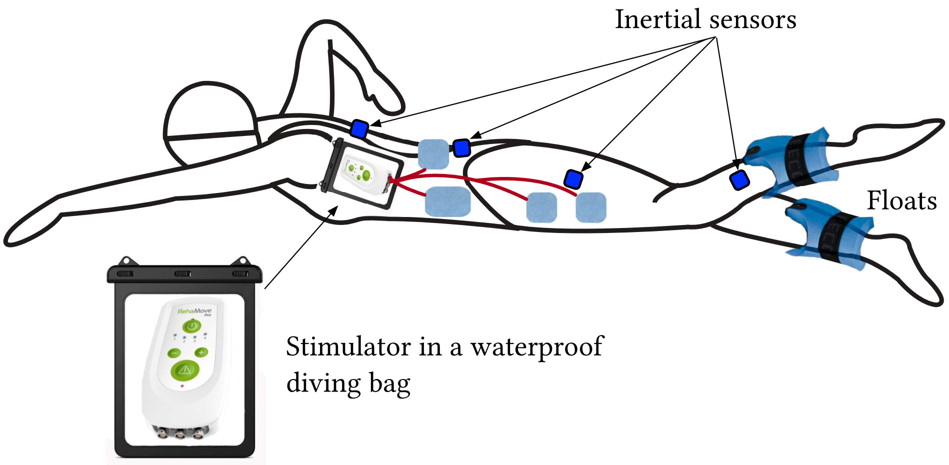

Figure 6.3: Stimulation-assisted swimming system including a waterproof stimulator, waterproof inertial sensors, floats at each shank, and waterproof electrodes.

6.3.3.2 Waterproof Stimulation Electrodes

Due to the fact that chlorinated water in swimming pools has a conductance of 2.5 mS/cm to 3 mS/cm, which results in resistance of 333 Ω/cm to 400 Ω/cm, a direct stimulation with non-waterproof electrodes would produce a parasitic short circuit between electrodes during stimulation. Therefore, the device-integrated electrode-error detection might not detect a bad connection between the electrode and the skin. If both electrodes float in water, then the muscles would not be stimulated, because the current always takes the path of the least resistance directly through the water and not the body. If only one electrode floats in water, then the current will still pass through the remaining firmly attached electrode and will still cause a muscle contraction beneath this electrode. The only potentially dangerous situation would occur when the conductive side of a detached and floating electrode would accidentally be pressed against the skin of the upper body, since then electrical currents might flow through sensitive organs, such as the heart. To minimize this risk and because of the limited electrode-error detection, the electrodes need to be safely and thoroughly attached to the skin. Furthermore, the electrode side facing away from the body needs to be isolated against water. Possible measures are waterproof transparent film dressing, straps, or swimming cloths.

Currently, there are no waterproof stimulation electrodes available on the market. Most transcutaneous electrodes consist of a conductive hydrogel adhesive, which is connected via conductive film to a lead wire or metal snap-stud and isolated with an insulating cover. If the hydrogel adhesive gets into contact with water, it starts to absorb water, while the thickness increases. Hence, the area with direct contact to the water increases. Furthermore, the adhesive function of the electrode is reduced. Approaches for underwater EMG measurement in [113, 114] used several layers of waterproof wound plaster with tunneled holes for the lead wires to waterproof standard adhesive EMG electrodes. The same procedure can be used for stimulation electrodes where standard electrodes are waterproofed with adhesive films, like Tegaderm$^{\text{TM}}$ (3M Co., USA) or OpSite$^{\text{TM}}$ (Smith & Nephew, Great Britain).

For the training sessions of the pilot study, which is described in the next subsection, special electrodes developed by Axelgaard Manufacturing Co. Ltd. (USA) have been used, as shown in Figure 6.4a). A single electrode consists of a standard electrode with an oversized waterproof backing. The snap adapter is tunneled through this backing. The remaining task is then to connect the electrode

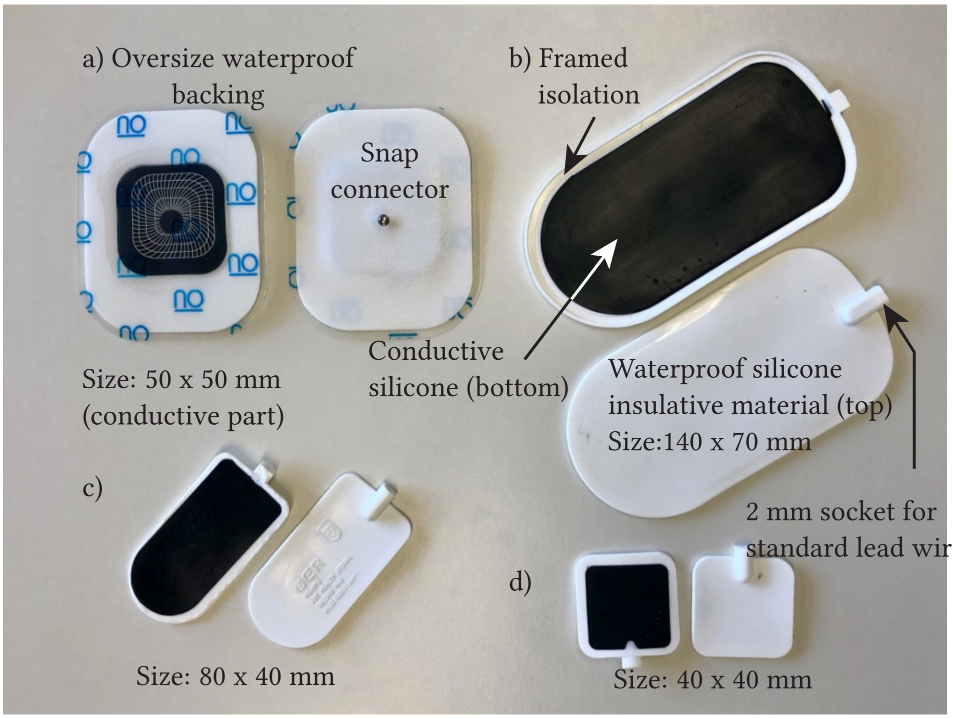
a) Oversize waterproof backing
Snap connector
b) Framed isolation
Conductive silicone (bottom)
Size: 50 x 50 mm (conductive part)
Waterproof silicone insulative material (top)
Size:140 x 70 mm
c)
2 mm socket for standard lead wire
d)
Size: 80 x 40 mm
Size: 40 x 40 mm

Figure 6.4: Electrodes used in water: a) Axelgaard Ultrastim® snap electrode with oversize waterproof backing with an electrode area of 22.9 cm^2 [115, 116] for tSCS (4 electrodes electrically connect for the abdomen and one over the spine) and FES (two electrodes for each quadriceps), b) to d) Safety silicone electrodes (VITAtronic Limited, Germany) consisting of an insulative and waterproof cover material and a conductive bottom material for tSCS (2 x (b) electrically connect for the abdomen and 1 x (d) for the back) and for FES (2 x (c) for each quadriceps).

lead (converter from the snap adapter to 2 mm socket) and seal it with a waterproof transparent film dressing (Tegaderm, 3M Co., USA). All cables and cable connections have to be waterproof as well. Otherwise, parasitic short circuits occur. Removable tight silicone tubes showed to be efficient in covering the connection between the electrode lead and the stimulation cable.

A drawback of adhesive electrodes with oversized waterproof backing is that after a single contact with water they cannot be reused. Hence, for each swimming session, a new set of electrodes is needed. To reduce costs and to save the environment, the suitability of reusable safety silicone electrodes shown in Figure 6.4b) to d) has been investigated in a post-training assessment session. These electrodes are available in different sizes (VITAtronic Ltd., Germany) and can be directly connected via a standard 2 mm electrode connector to the simulation cable. Due to the non-conducting upper side and the framed isolation on the conductive skin side, no parasitic short circuit can occur when firmly attaching the electrodes to the skin. The material is non-adhesive, which reduces skin irritation during the doffing phase but implies that it must be fixed with tight sleeves, straps, waterproof transparent film dressing, or with tight knee-length swimsuits. During swimming a small water film between the skin and the conductive part of the silicone electrode is present. Hence, no additional hydrogel was added. Straps and knee-length swimsuits have been used in this study for the leg electrodes. The electrodes for tSCS have been fixated by waterproof transparent film dressing.

6.3.4 Subjects, Training Protocol, and Outcome Measures

A feasibility study, named STIMSWIM, was carried out at the Treatment Centre for Spinal Cord Injuries in Berlin[1]. The aim of the study was to investigate the effects of stimulation-supported swimming in two SCI patients with complete paralysis of the lower extremities after spinal trauma with a lesion above Th10. Participants had to be proficient front crawl swimmers. Both recruited subjects (A: age 40, time since injury 10 years, B: age 58, time since injury 36 years) are ASIA impairment scale A with lesion level Th5/6 and gave written informed consent. At the time of the study, they both complained of a moderate clonus of the lower extremities and the abdomen during position changes, and subject A experienced leg extensor spasms from time to time. Subject B suffered from a hip-joint contracture.

After the recruitment and initial assessment, the subjects were asked to carry out a four-week FES cycling training at home. During this land training, they trained at least three times a week for 30 minutes with a standard FES cycling ergometer (RehaMove, Hasomed GmbH, Germany). This preliminary FES cycling training was needed to build up a defined baseline strength and endurance for the swimming phase. During the swimming phase, FES cycling activity was reduced to two times a week.

The entire swim training lasted for ten weeks. Subjects were asked to attend the weekly swim training session that lasted between 30 to 45 minutes (excluding donning and doffing). As a safety measure, the swim sessions were always accompanied by a trained pool guard. Furthermore, all recruited subjects were able to swim without stimulation. The training was done at a 16 m pool. Subject A used a snorkel during front crawl swimming. Prior to the first use of tSCS during swimming, the electrode position at the spinal cord and the stimulation intensity for spasticity treatment were identified according to [112] and documented. The found appropriate stimulation intensity was applied in all training sessions when tSCS was on.

The stimulation amplitudes for both quadriceps were identical and have been chosen to cause an almost full knee extension while the subjects rested at the edge of the swimming pool with an upright upper body. Before each lap, the leg movement was reevaluated and the stimulation amplitude increased, if necessary, to compensate for muscle fatigue. A break of at least one minute was kept between the laps.

At the beginning of each swim training session, lap times were measured. Therefore, the subjects were instructed to swim each 16 m lap as fast as possible. When comparative measurements were taken, first the times for swimming without support were taken, then with FES support and finally the times for FES + tSCS support. This order was applied so that the results for trials with increasing amount of support are more affected by muscular fatigue than the trials with less or no support. After this initial assessment, training with the preferred support (FES or FES + tSCS) took place for the rest of the session at self-selected swimming speed. If FES + tSCS has been selected as preferred support, then tSCS was always active, also in the breaks between the laps while FES was switched off during these breaks.

There are three main questions that should be answered in this pilot study:

- Does the swimming speed, assessed by lap times, increase compared to non-assisted swimming?
- Does the general well-being of the subject improve during the trial?
- How is the acceptance of the technology by the user?

---

[1] Ethical approval of Berlin Chamber of Physicians Eth-28/17

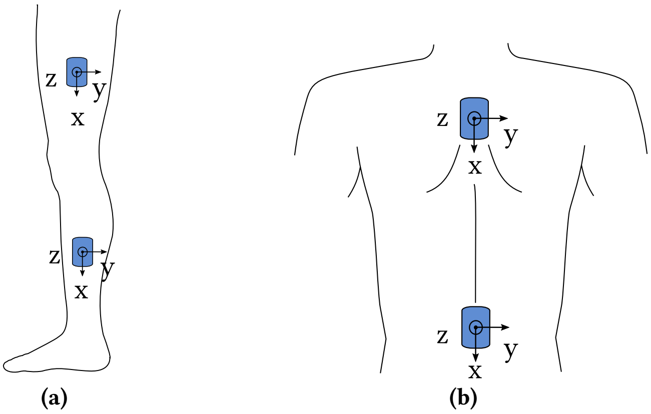

Figure 6.5: (a) IMU alignment and location on the left leg. The local x-axes are aligned with the longitudinal body axis. The z-axis points laterally to the left. (b) IMU alignment and location on the upper and lower back. The local x-axis is aligned with the longitudinal body axis, while the y-axis points to the right.

The subjects were asked to rate the therapy on the basis of predefined statements using a five-grade scale between full agreement and no agreement. Using the result of the questionnaire the last two questions can be answered.

6.3.5 IMU-Based Motion Analysis during Swimming

Post-training assessment Nine months after completion of the entire swim training phase, after a suitable measurement system was acquired, an additional swimming session with each of the two subjects was performed to monitor the effects of the different stimulation programs on the leg and trunk motion. Both subjects were instructed to repetitively swim laps with no support, tSCS support, FES support, and FES + tSCS support as fast as possible.

Sensor setup A wearable sensor setup was used. The employed system WaveTrack (Cometa srl, Italy) is a wireless and waterproof inertial-sensor system consisting of several time-synchronized IMUs. These inertial sensors provide three-dimensional measurements of the acceleration, angular velocity, and magnetic field vector at a frequency of 286 Hz. The sensor data were used to determine the joint angles of both knees and both hips and the roll-orientation angles of the trunk on the cervical and lumbar level.

As all the sensors are located under water during the whole measurement, wireless data transfer (streaming) is not an option. Therefore, an offline data recording is carried out. The data acquisition and time synchronization of the sensors is initiated by means of a remote control. The recording begins before the subject enters the pool. After leaving the pool the recording is stopped and the data are transferred from the sensors to a PC. The software EMGandMotionTools (Cometa srl, Italy) was used for data transfer and sensor settings. Due to the loss of communication between the sensors when located under water, a synchronization drift is educed. However, since this drift does not exceed a few milliseconds per hour and all acquisitions last between approximately 30 to 45 minutes, the effect on the data is considered irrelevant.

All sensors were attached to the skin by means of double-sided adhesive tape for rough fixation. Subsequently, a transparent Tegaderm film was used in order to prevent movement and loosening of the sensors during the swimming process.

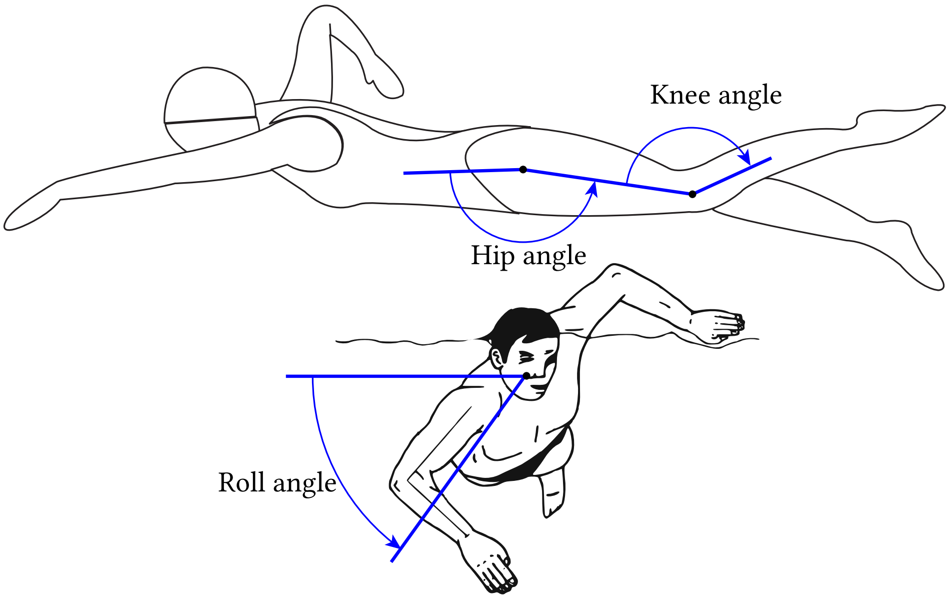

Figure 6.6: Definition of the knee- and hip-extension angle as well as the trunk-roll angle (©2020 IEEE).

To this end, four IMUs were bilaterally attached to the exterior thigh and shank, and two IMUs were located on the upper and lower back, as shown in Fig. 6.5a and Fig. 6.5b. For each of those six IMUs, the intrinsic x-axis is aligned with the longitudinal axis of the body segment and points from proximal to distal, while the intrinsic z-axis always points laterally away from the skin. Careful sensor attachment is required, since the sensor-to-segment orientation is crucial for determining body-segment-related motion parameters such as joint angles from IMU-related motion parameters [117]. Although it was demonstrated in [117, 118] that careful sensor placement is not the only way to assure knowledge of the sensor-to-segment orientation. One can use a sequence of precisely conducted calibration motions around isolated degrees of freedoms of the joints to determine the corresponding joint axis coordinates in case of non-precise or arbitrary sensor placement [117, 118]. Beyond this rather restrictive approach, it is possible to determine the sensor-to-segment orientation from arbitrary motions by real-time parameter estimation methods that exploit the kinematic constraints of the joints between the body segments. This has been demonstrated successfully for the upper limbs and the lower limbs [119–122]. Such methods will become highly relevant for future developments of the controlled FES swimming system and in non-supervised application scenarios. However, in the supervised setting of the present study, it was chosen to perform sensor-to-segment alignment by careful attachment to reduce the complexity of the data analysis. The resulting angles for knees, hips, and the trunk are defined as follows.

Joint-Angle Estimation Denote the raw accelerometer and gyroscope measurements of an IMU $i \in \{\mathrm{TR}, \mathrm{LB}, \mathrm{LT}, \mathrm{RT}, \mathrm{LS}, \mathrm{RS}\}$ by ${}_{\mathcal{S}_\mathrm{i}}\mathbf{a}_i(t)$, ${}_{\mathcal{S}_\mathrm{i}}\mathbf{g}_i(t)$ in the intrinsic coordinate system of the IMU at the upper trunk (TR), the lower back (LB), the left (LT), and right thigh (RT), and the left (LS) and right shank (RS), respectively. Since the FES system is supposed to work reliably in indoor environments and near ferromagnetic materials and electronic devices, the incorporation of magnetometer readings was avoided and the quaternion-based six-axis sensor fusion algorithm introduced in Chapter 2 was used to determine the quaternions ${}^{\mathcal{S}_i}_{\mathcal{E}_i}\mathbf{q}$ that describe the orientations of the intrinsic sensor frames $\mathcal{S}_i$ with respect to the reference frames $\mathcal{E}_i$. It must be noted that orientations obtained by such

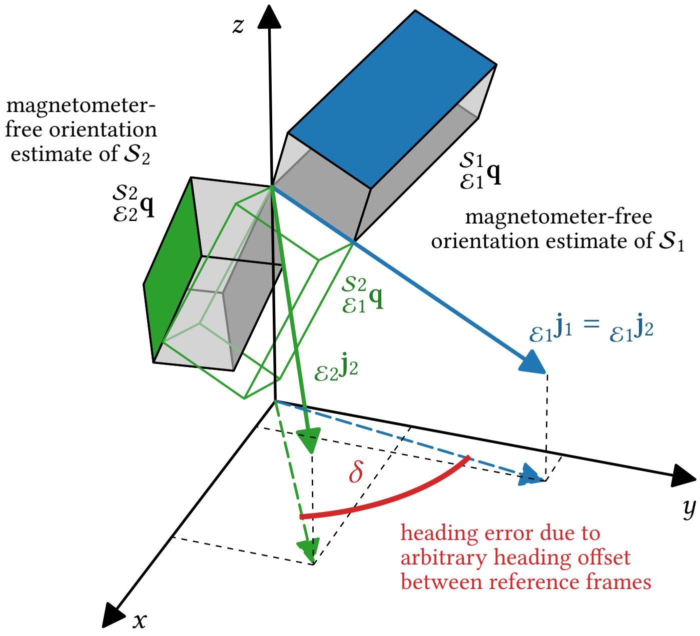
z
magnetometer-free orientation estimate of $\mathcal{S}_2$
${}^{\mathcal{S}_2}_{\mathcal{E}_2}\mathbf{q}$
${}^{\mathcal{S}_1}_{\mathcal{E}_1}\mathbf{q}$
magnetometer-free orientation estimate of $\mathcal{S}_1$
${}^{\mathcal{S}_2}_{\mathcal{E}_1}\mathbf{q}$
${}_{\mathcal{E}_1}\mathbf{j}_1 = {}_{\mathcal{E}_1}\mathbf{j}_2$
${}_{\mathcal{E}_2}\mathbf{j}_2$
δ
heading error due to arbitrary heading offset between reference frames
y
x

Figure 6.7: Illustration of the heading error for two segments are connected by a hinge joint. If their orientations are estimated by magnetometer-free inertial sensor fusion, there is an arbitrary heading offset between them. This heading error δ can be obtained from the projections of the joint axes into the horizontal plane.

a six-axis sensor fusion cannot be used for joint-angle calculation directly, since they exhibit an arbitrary heading offset and drift slowly around the vertical axis. With accurate bias estimation, that drift can be as slow as one degree in ten seconds, but it will not be reduced to perfect zero.

To overcome this drawback of the magnetometer-free approach, approximate kinematic constraints of the hip and knee joints are exploited. During the considered flutter kick motion of the legs, hip and knee move approximately like hinge joints – flexion/extension is the dominant motion, while adduction/abduction and internal rotation occur only to a limited degree. These approximate kinematic constraints are exploited by using the relative-heading tracking algorithm recently published in [123]. That algorithm takes the orientation quaternions of both segments adjacent to the joint and corrects the heading of the distal segment's orientation such that the joint constraint is fulfilled in a weighted least-squares sense. This method is applied repeatedly, starting from the upper segment and moving distally towards the shanks.

Hip- and knee-joint angle estimation The joint angles for each hip and knee joint are estimated using the same methods. For simplicity only the knee-joint-angle estimation is elaborated. As stated earlier, the knee is assumed to be an approximate hinge joint. The intrinsic coordinates ${}_{\mathcal{S}_{\mathrm{LT}}}\mathbf{j}_{\mathrm{L}}$, ${}_{\mathcal{S}_{\mathrm{LS}}}\mathbf{j}_{\mathrm{L}}$, ${}_{\mathcal{S}_{\mathrm{RT}}}\mathbf{j}_{\mathrm{R}}$, ${}_{\mathcal{S}_{\mathrm{RS}}}\mathbf{j}_{\mathrm{R}}$ of the knee-joint axes $\mathbf{j}_{\mathrm{L}}$ and $\mathbf{j}_{\mathrm{R}}$ of the left and right knee, respectively, are all assumed to be equal to $[0, 0, 1]^T$ due to the precise sensor attachment described above. These intrinsic coordinates are constant and do not change when the leg moves, since the sensors and the joint axes are rigidly connected to each other by the thighs and shanks – at least if the noisy influence of soft-tissue motion is ignored.

Recall that there is a heading offset between the reference frames of different IMUs. Therefore, transforming the joint axis into reference-frame coordinates yields, in general, different results for the thigh and shank sensor of the same leg, see Figure 6.7 for an illustration. This disagreement is only zero if the arbitrary heading offset between both reference frames happens to be zero or if the joint axis is perfectly vertical. However, it has been shown for one-dimensional joints [124] and for two-dimensional joints [123] that this disagreement between transformed joint-axis vectors can be used to determine and eliminate the heading offset. Using this kinematic-constraint-based approach, the relative orientation of the thigh and shank from six-axis inertial data can be estimated, which means without using magnetometer readings. As further explained in [124, 125], the rotations ${}^{\mathcal{E}_{\text{LS}}}_{\mathcal{E}_{\text{LT}}}\mathbf{q}$ and ${}^{\mathcal{E}_{\text{RS}}}_{\mathcal{E}_{\text{RT}}}\mathbf{q}$ are determined that eliminate the heading offsets and one can calculate the relative orientation of the shanks with respect to the thighs as follows

$$
\begin{aligned}
{}^{\mathcal{S}_{\text{LS}}}_{\mathcal{S}_{\text{LT}}}\mathbf{q} &= {}^{\mathcal{S}_{\text{LT}}}_{\mathcal{E}_{\text{LT}}}\mathbf{q} \otimes {}^{\mathcal{E}_{\text{LS}}}_{\mathcal{E}_{\text{LT}}}\mathbf{q} \otimes {}^{\mathcal{E}_{\text{LS}}}_{\mathcal{S}_{\text{LS}}}\mathbf{q}, &\quad (6.1)\\
{}^{\mathcal{S}_{\text{RS}}}_{\mathcal{S}_{\text{RT}}}\mathbf{q} &= {}^{\mathcal{S}_{\text{RT}}}_{\mathcal{E}_{\text{RT}}}\mathbf{q} \otimes {}^{\mathcal{E}_{\text{RS}}}_{\mathcal{E}_{\text{RT}}}\mathbf{q} \otimes {}^{\mathcal{E}_{\text{RS}}}_{\mathcal{S}_{\text{RS}}}\mathbf{q}. &\quad (6.2)
\end{aligned}
$$

These relative orientation quaternions are decomposed into intrinsic Euler angles with the first rotation describing the joint angles φ_{K_L} and φ_{K_R}, respectively, and the second and third angles describing small additional abduction/adduction and internal/external rotation of the knee joints. The hip-joint angles φ_{H_L} and φ_{H_R} are estimated similarly, while in Eqs. (6.1) and (6.2) the thigh quaternions are replaced with the quaternion of the lower back sensor (LB) and the quaternions of the shanks are replaced with the ones of the thighs, respectively.

Trunk-roll-angle estimation The trunk-roll angle was separately estimated using the sensor attached to the upper trunk (TR) and lower back (LB). Both angles are estimated with the same method. Therefore, only the roll-angle estimation for the upper trunk is elaborated. The motion of the trunk during front crawl swimming can be characterized by the inclination of its principal axes. The longitudinal axis of the trunk remains almost horizontal, while its left-to-right axis oscillates between pointing up and down, as the trunk rolls around its longitudinal axis, cf. Fig. 6.5b. The angle that these trunk axes confine with the vertical axis (or the horizontal plane) is independent of the heading of the body segment. It is calculated as follows. Let ${}_{\mathcal{S}_{\text{TR}}}\mathbf{y}_{\mathcal{S}_{\text{TR}}}$ be the y-axis of the trunk IMU with intrinsic coordinates ${}_{\mathcal{S}_{\text{TR}}}\mathbf{y}_{\mathcal{S}_{\text{TR}}} = [0, 1, 0]^T$. The orientation quaternion ${}^{\mathcal{S}_{\text{TR}}}_{\mathcal{E}_{\text{TR}}}\mathbf{q}$ is determined again using the six-axis inertial sensor fusion algorithm introduced in Chapter 2. The reference frame coordinates of the aforementioned y-axis are then given by

$$
{}_{\mathcal{E}_{\text{TR}}}\mathbf{y}_{\mathcal{S}_{\text{TR}}} = {}^{\mathcal{S}_{\text{TR}}}_{\mathcal{E}_{\text{TR}}}\mathbf{q} \otimes {}_{\mathcal{S}_{\text{TR}}}\mathbf{y}_{\mathcal{S}_{\text{TR}}} \otimes {}^{\mathcal{E}_{\text{TR}}}_{\mathcal{S}_{\text{TR}}}\mathbf{q}, \tag{6.3}
$$

where ${}^{\mathcal{E}_{\text{TR}}}_{\mathcal{S}_{\text{TR}}}\mathbf{q}$ is the inverse quaternion of ${}^{\mathcal{S}_{\text{TR}}}_{\mathcal{E}_{\text{TR}}}\mathbf{q}$ and the operator $\otimes$ denotes quaternion multiplication and interprets vectors from $\mathbb{R}^3$ as their corresponding pure quaternions. Since the z-axis ${}_{\mathcal{E}_{\text{TR}}}\mathbf{z}_{\mathcal{E}_{\text{TR}}} = [0, 0, 1]^T$ of the reference frame $\mathcal{E}_{\text{TR}}$ is vertical by definition, the angle $\phi_{\text{TR},y}$ is determined between the aforementioned y-axis and the horizontal plane as

$$
\phi_{\text{TR},y} = \frac{\pi}{2} - \arccos\left({}_{\mathcal{E}_{\text{TR}}}\mathbf{z}^T_{\mathcal{E}_{\text{TR}}} \; {}_{\mathcal{E}_{\text{TR}}}\mathbf{y}_{\mathcal{S}_{\text{TR}}}\right). \tag{6.4}
$$

Note that this trunk-roll angle is positive if the left-to-right axis of the trunk points up, which is typically the case if the right shoulder is above the water surface, and that the angle is negative if the left-to-right axis of the trunk points down, which is typically the case if the left shoulder is above the water surface as shown in Fig. 6.6.

	Average 16 m lap time [s]			Reduction [%]	
Day	No support	FES	tSCS + FES	FES	tSCS + FES
0	33.8	28.0	–	17.3	–
17	35.3	28.3	27.7	19.9	21.5
22	32.0	27.5	26.7	14.0	16.7
43	29.0	26.0	23.3	10.3	19.7
57	–	–	22.3	–	–
64	–	–	22.9	–	–
Average	32.5	27.4	24.6	15.4±3.6%	19.3±2.0%

Table 6.1: Lap times during the swim training phase for subject A. The reduction in lap time with respect to the lap time without support is reported.

Segmentation A segmentation of the recorded data is performed based on the norm of the 3D acceleration vector by detecting rest and motion phases. Only the first lap of each support modality is exported and investigated. From the extracted lap data a time course over seven strokes in the middle of the lap has been selected to analyze the joint and roll angles by using boxplots. Consequently, the start and stop phases of each lap are excluded from data analysis.

6.4 Results

Both subjects completed the ten weeks of training, but both subjects did not take part in all possible swim sessions due to personal reasons. Once the pool was not available either. In total, the subjects A and B completed six and seven sessions, respectively. Within each swim training, about 15 laps have been finished by each subject. After the first use of FES + tSCS, both subjects chose this as their preferred support. Hence, the major part of the training was performed with this support.

The stimulation intensities for the quadriceps for subject A were set to initially 30 % (30 mA, 150 μs) and then increased to up to 50 % (50 mA, 250 μs) to compensate fatigue. Subject B started initially with 40 % (40 mA, 200 μs) intensity, which was increased up to 60 % (60 mA, 300 μs) depending on the fatigue state. The optimal intensity for tSCS was determined as 40 mA for both subjects. The used on/off rates for the quadriceps were 1 Hz and 2 Hz for the subjects A and B, respectively, with both subjects being asked to choose the rate at which they felt more comfortable in the first session.

In Fig. 6.8, the mean values of the measured lap times in each training session are shown together with the calculated trend lines for all assessed support modalities (No support, FES, FES + tSCS). One to three laps have been measured in each session with the stopwatch for each investigated type of swimming support at the beginning. Tables 6.1 and 6.2 also reveal the lap times and the calculated reductions of the lap times with respect to swimming with no support when adding FES or FES + tSCS. Swimming with FES support reduced lap times by 15.4 % and 8.7 % on average for subject A and subject B, respectively. Adding further tSCS support yielded even greater mean decreases of 19.3 % and 20.9 % for subjects A and B, respectively. Additionally, both subjects individually reported that swimming with FES + tSCS for 30–45 minutes completely eliminated the spasticity in the lower extremities for up to 4 hours after the swim training – during this time period, it was impossible to trigger extensor spasms or a clonus by inducing postural changes. No spasticity reduction was observed after the first training session of subject A when only FES support was used.

Both subjects fully agreed that FES swimming is more comfortable and enjoyable than swimming without support and that they would like to use such a device for recreational training and

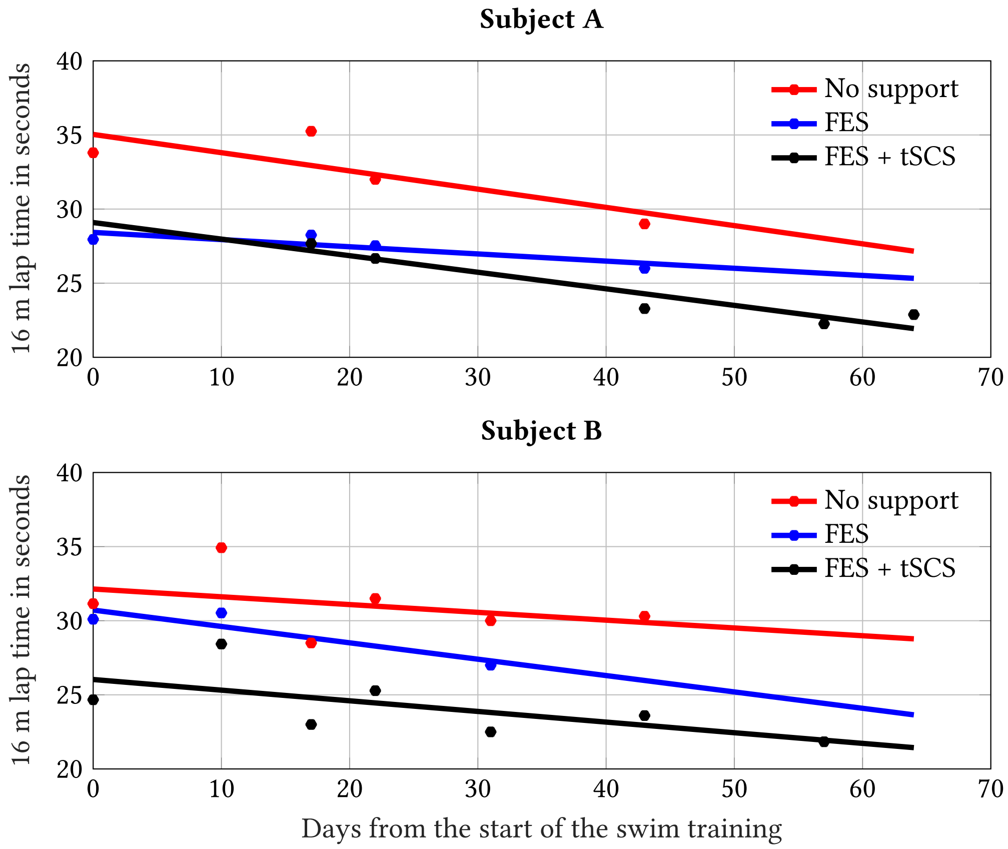

Figure 6.8: Lap times of the two subjects over the swim training phase. The lap times in a single training session have been averaged for each support modality. The solid lines show a fitted progression using linear regression.

	Average 16 m lap time [s]			Reduction [%]	
Day	No support	FES	tSCS + FES	FES	tSCS + FES
0	31.2	30.1	24.7	3.4	20.8
10	34.9	30.5	28.4	12.6	18.6
17	28.5	–	23.0	–	19.3
22	31.5	–	25.3	–	19.7
31	30.0	27.0	22.5	10.0	25.0
43	30.3	–	23.6	–	22.1
57	–	–	21.8	–	–
Average	31.0	29.2	24.2	8.7±4.8%	20.9±2.3%

Table 6.2: Lap times during the swim training phase for subject B. The reduction in lap time with respect to the lab time without support is reported.

rehabilitation in the future. They also fully agreed that swimming with stimulation is more efficient than swimming without support. Subject B states that the additional spinal-cord stimulation has a positive effect on the streamlined position in the water and thus the propulsion through arms and stimulated legs is even more efficient.

The documented donning and doffing time with adhesive electrodes were approximately 10 minutes, where waterproofing the cable-to-electrode connection with 3M Tegaderm film as well as careful detachment of the electrodes and the extra film required large portions of that time. The donning time was reduced to approximately 5 minutes when using the aforementioned silicone electrodes with inherent waterproof cable connection.

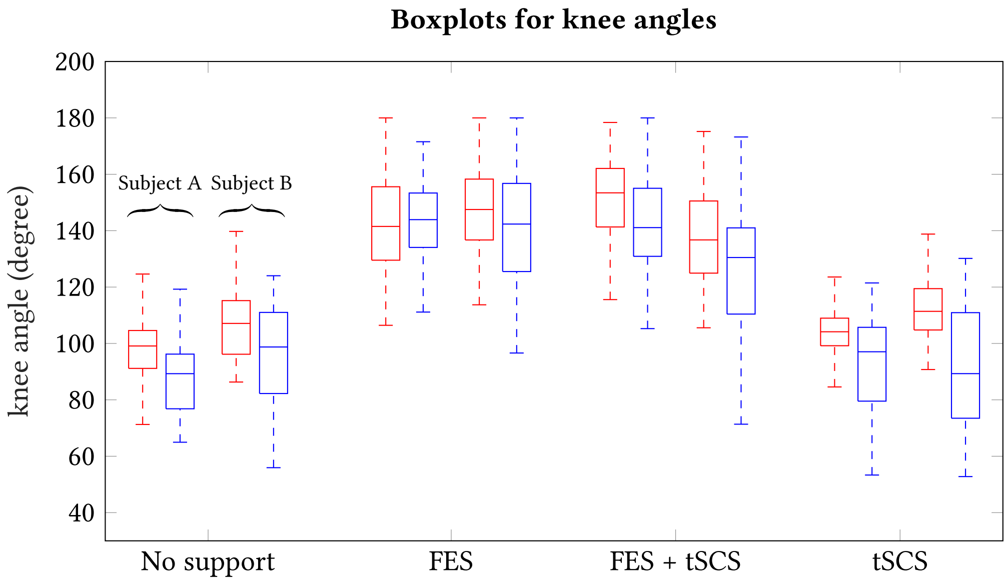

Figure 6.9: Knee-joint angles during swimming without and with different support modalities (left leg – red line, right leg – blue line).

Subject	16 m lap time in seconds				
	No support	FES	tSCS + FES	tSCS	Number of repetitions
A	28	24	22	30	2
B	26	30	31	34	1

Table 6.3: Averaged lap times of the post-training assessment.

For the post-training assessment, in Figs. 6.9 to 6.11, the distribution of the angles for each leg and the back (left – red, right – blue, upper – red, lower – blue) are summarized in boxplots for both subjects. The box corresponds to the range in which the middle 50 % of the data lies. It is therefore bounded by the upper and lower quartiles, and the length of the box corresponds to the interquartile range (IQR). Furthermore, the median is drawn as a continuous line in the box. This line divides the entire chart into two areas, each containing 50% of the data. The whiskers represent the values outside the box that are not considered as outliers. In Fig. 6.10, the plus symbol shows the most distant outliers.

For the knee-joint angles, an increase in extension of up to 60 degrees for FES and the combination of FES + tSCS can be observed compared to swimming without stimulation. But for isolated tSCS, the angular range is not influenced. Regarding the hip-joint angles, there is a minor increase of the median hip angle for subject A and a reduced variance during FES and the combination of FES + tSCS. For subject B no differences for the hip angle can be observed. This is in accordance with the fact that subject B shows a manifested contracture for the hip joint.

Regarding the roll angles, no difference between the support modalities and swimming without support could be measured. The measured mean lap times during the post-training assessment with silicone electrodes are summarized in Table 6.3. Subject A performed every swim support type twice. Subject B fatigued early and conducted every type of swimming only once. Both subjects continued swimming with tSCS + FES after the assessment for another 30 minutes at moderate speed with breaks and experienced a spastic reduction that again lasted for several hours after the swimming.

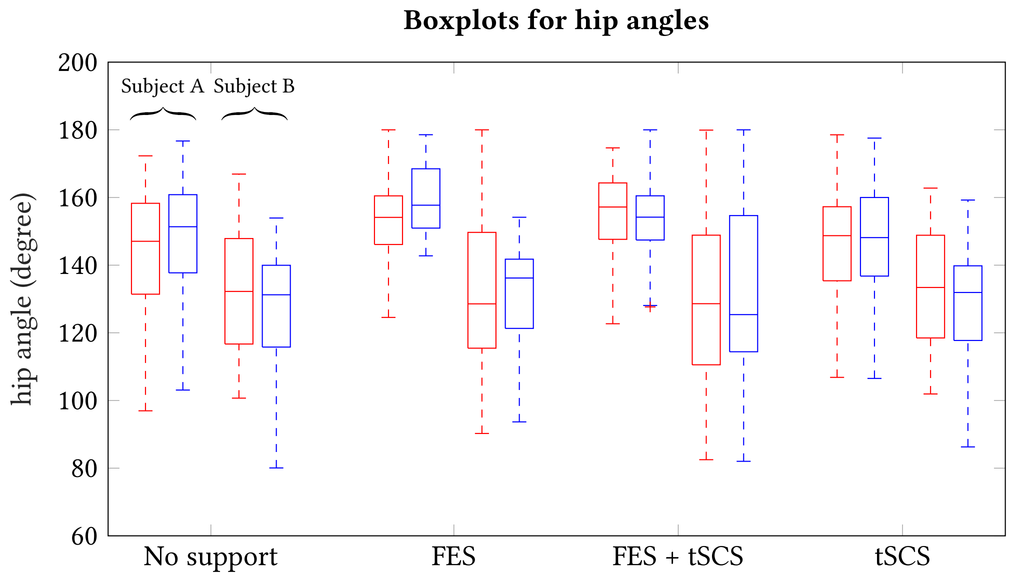

Figure 6.10: Hip-joint angles during swimming without and with different support modalities (left leg – red line, right leg – blue line).

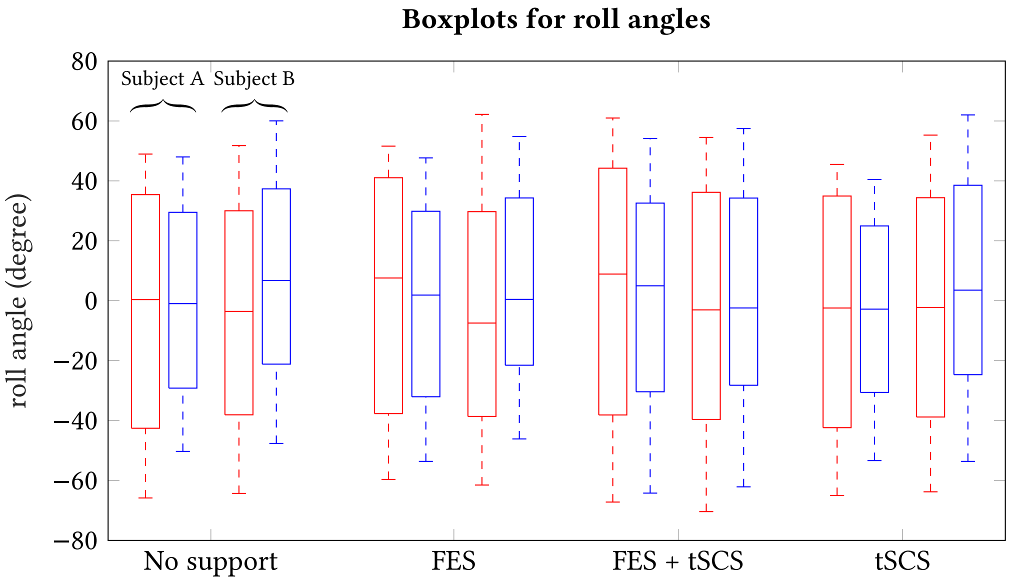

Figure 6.11: Roll angle of the lower and upper back during swimming without and with different support modalities (upper back – red line, lower back – blue line).

6.5 Discussion

For both subjects, a slight training effect over the training period can be recognized for swimming with and without support. This was expected as both subjects are no regular swimmers. Furthermore, the results indicate that FES with and without additional tSCS can enhance the swimming speed in paraplegics during front crawl swimming. So far, the measured lap times suggest for both subjects that the greatest improvement of the swimming speed can be achieved when FES and tSCS are combined. The reasons for this are not fully understood at the moment. The IMU-based motion analysis was a first attempt to investigate this phenomenon. However, lap times for swimming with

FES and with FES + tSCS did not differ to a greater extent in the post-training assessment, as shown in Table 6.3. This might explain why no differences could be observed in the joint and roll angles of the post-training assessment when adding tSCS to swimming without or with FES. The additional post-training tests, therefore, provided no explanation for the tSCS effect.

The large time interval between the swim training and the later assessment with IMUs was certainly too long, but a suitable measurement system was not available before. Subject A, who conducts regular exercises, showed a similar performance as at the end of the swim training, again with minor benefits for the combination of tSCS + FES. Subject B, who previously gained mostly from additional tSCS, did not train at all after the end of the swim training, and was, as a result of it, quickly exhausted already during the first laps. His physical condition at the post-training assessment was certainly not comparable to the one nine months before. The progressing fatigue during the four laps with time taking has probably affected the results. It seems that the improvements made by FES and FES + tSCS have just compensated for the performance losses caused by fatigue.

A possible explanation for the earlier observed positive effects of tSCS during swim training could be that trunk stability continuously improved by tSCS, and as a result, reduced the swimmer's necessary effort to avoid trunk rolling. But also placebo effects can not be ruled out at present, as no sham-tSCS stimulation was applied. Theoretically, subjects may have unconsciously swum much more with their non-paralyzed arms if they knew and felt that tSCS was active.

The use of different electrodes during the training period and the post-training assessment might be interpreted as another weakness of the study design. However, the observed lap times in subject A and spasticity reduction for both subjects with the silicone electrodes indicate, that this simple-to-apply type of electrodes is suitable for stimulation in water and yields comparable effects as with adhesive electrodes.

Major limitations of this feasibility study were the small number of subjects and the not so rigorous training and assessment protocol. The individual contribution of swimming and FES cycling to the observed training effect can also not be quantified. Another weakness of the current study is the way how the swimming speed is assessed. The usage of the lap time is error-prone, especially for short tracks, as the start technique and the occasional presence of extensor spasms at the beginnings of a track have a strong influence. A larger pool would be advisable or better methods, like IMU-based motion analysis, to determine the instantaneous speed during swimming as presented in Chapter 7. Additional IMUs at the arms should have been used to rate the involvement of the arms for propulsion and stabilization of the roll angle. Another important factor is the metabolic efficiency, which has not been studied at all in the present work.

6.6 Conclusions

A new hybrid exercise modality for SCI patients has been proposed that involves the voluntarily moved arms and the artificially stimulated legs and trunk. The swimming exercise can be performed independently by the patient without any additional assistance. The results in two complete ASIA impairment scale A subjects showed that the swimming speed during front crawl could be increased using electrical stimulation either with FES or with the combination of FES + tSCS. The latter yielded better results in both subjects.

The prolonged use of FES and tSCS caused a long-lasting reduction of spasticity in both subjects. To better quantify and document this effect in the future, measurement systems for automatic spasticity assessment are required (e.g., to count the occurrence frequency of a clonus).

In this study, no synchronization was realized between the arm and leg movement. Such a synchronization might help to prevent undesired rolling movements of the swimmer and could have additional effects on the swimming speed. In the case of crawl stroke, the knee extension should be synchronized with the contralateral arm movement to increase swimming speed and effectiveness. A first approach for this synchronization problem of arm and leg movement will be presented in the next chapter.

To further improve the usability of the swimming device, it is planned to incorporate silicone electrodes with all cables inside a neoprene sleeve. This could reduce the donning and doffing time and increase safety, since cables would be less prone to entangle or to slip off the electrodes.

Research on FES swimming is still in an early phase, and further tests with more subjects are needed to quantify, analyze, and improve the training effects for the SCI patients, looking also at the support of backstroke swimming by stimulation for paraplegics and tetraplegics who are not able to perform front crawl swimming. The use of the presented technology for paraplegic scuba diving is another promising recreational application.

7

Inertial-Sensor-Triggered FES Swimming in Paraplegics

7.1 Overview

The results of the STIMSWIM pilot study presented in Chapter 6 were obtained with open-loop control of the stimulation of the lower-limb muscles and thus without synchronization of arm and leg motion. To tap the full potential of FES support, the stimulation timing should be controlled in real-time based on the upper-body motion. In this chapter, the roll angle of the trunk is used to control the quadriceps stimulation and synchronize the leg propulsion with the volitional upper-body movement in front crawl swimming. This yields a more streamlined body posture and increased swimming speed.

Copyright Statement: The methods and results presented in this chapter have been previously published in:

[SWIM1] C. Wiesener, J. Axelgaard, R. Horton, A. Niedeggen, and T. Schauer. "Functional Electrical Stimulation assisted swimming for paraplegics." In: *22th Conference of the International Functional Electrical Stimulation Society*. IFESS. Nottwill, Switzerland, Aug. 2018.

[SWIM2] C. Wiesener, T. Seel, J. Axelgaard, R. Horton, A. Niedeggen, and T. Schauer. "An Inertial Sensor-based Trigger Algorithm for Functional Electrical Stimulation-Assisted Swimming in Paraplegics". In: *IFAC-PapersOnLine* 51.34 (2019), pp. 278–283. DOI: `10.1016/j.ifacol.2019.01.039`.

[SWIM3] C. Wiesener, A. Niedeggen, and T. Schauer. "Electrotactile Feedback for FES-Assisted Swimming". In: *Converging Clinical and Engineering Research on Neurorehabilitation III*. 1st ed. Springer International Publishing, 2019, pp. 922–925. DOI: `10.1007/978-3-030-01845-0_18`.

[SWIM4] C. Wiesener, L. Spieker, J. Axelgaard, R. Horton, A. Niedeggen, N. Wenger, T. Seel, and T. Schauer. “Supporting front crawl swimming in paraplegics using electrical stimulation: A feasibility study”. In: *Journal of NeuroEngineering and Rehabilitation* 17.1 (Apr. 2020), p. 51. DOI: `10.1186/s12984-020-00682-6`.

[SWIM5] C. Wiesener, T. Seel, L. Spieker, A. Niedeggen, and T. Schauer. “Inertial-Sensor-Controlled Functional Electrical Stimulation for Swimming in Paraplegics: Enabling a Novel Hybrid Exercise Modality”. In: *IEEE Control Systems* 40.6 (Dec. 2020), pp. 117–135. DOI: `10.1109/MCS.2020.3019152`.

Therefore, text and figures in this chapter are extracted, with slight modifications, from those publications. The rest of this chapter is structured as follows. In the next section, the methods including the stimulation system, IMU-based motion analysis, and trigger algorithm are addressed. Afterwards, the results for one complete-SCI subject are presented in Section 7.3. Conclusions and future work are remarked finally in Section 7.4.

7.2 Methods

During the STIMSWIM study presented in the previous chapter, no synchronization was realized between the arm and leg movement. Such a synchronization might help to prevent undesired rolling movements of the swimmer and could have additional effects on the swimming speed. Psycharakis and Sanders [126] stated that the alternation between left and right arm strokes in front crawl is always accompanied by angular motion of the trunk about its longitudinal axis, commonly known as body roll. Therefore, Yanai [127] showed in a study with eleven profound swimmers that the main roll movement is produced by the shoulders during propelling of the arms, while the reaction effects of flutter kick of the lower limbs work against the body roll to stabilize the swimmer.

Since the paraplegic swimmer does not realize when her/his legs are artificially extended or flexed it is not possible to synchronize the arms with the leg movement. In [128, 129] methods for electrotactile feedback are described for prostheses feedback in amputees or for gait feedback in patients with peripheral neuropathy. Adapting these methods to paralyzed subjects in FES swimming, each leg stimulation channel was combined with an electrotactile feedback-channel which stimulates synchronously the corresponding sensory unimpaired side of the patients back. In own preliminary tests, the electrotactile feedback was tested with an intensity of 20 mA and a pulse width of 100 µs which did not produce a muscular contraction in this region. Unfortunately, the two swimmers of the STIMWSWIM study could not concentrate on this feedback channel during swimming and had problems to adapt the pace of their arms to the technically dictated pace of the legs.

Therefore, the trunk-roll angle is used to control the quadriceps stimulation and synchronize the leg propulsion with the volitional upper-body movement. In the following, the adapted stimulation system of the previous chapter is briefly introduced and the experimental setting is described. Afterwards, additional IMU-based methods are introduced which are used for motion analysis and for the stimulation-trigger algorithm in the last part of this section.

7.2.1 IMU-Triggered Stimulation System

The same stimulation system as presented in the previous chapter was used, which is shown in Fig. 7.1. Compared to the previous version, only FES support of the paralyzed legs without tSCS was

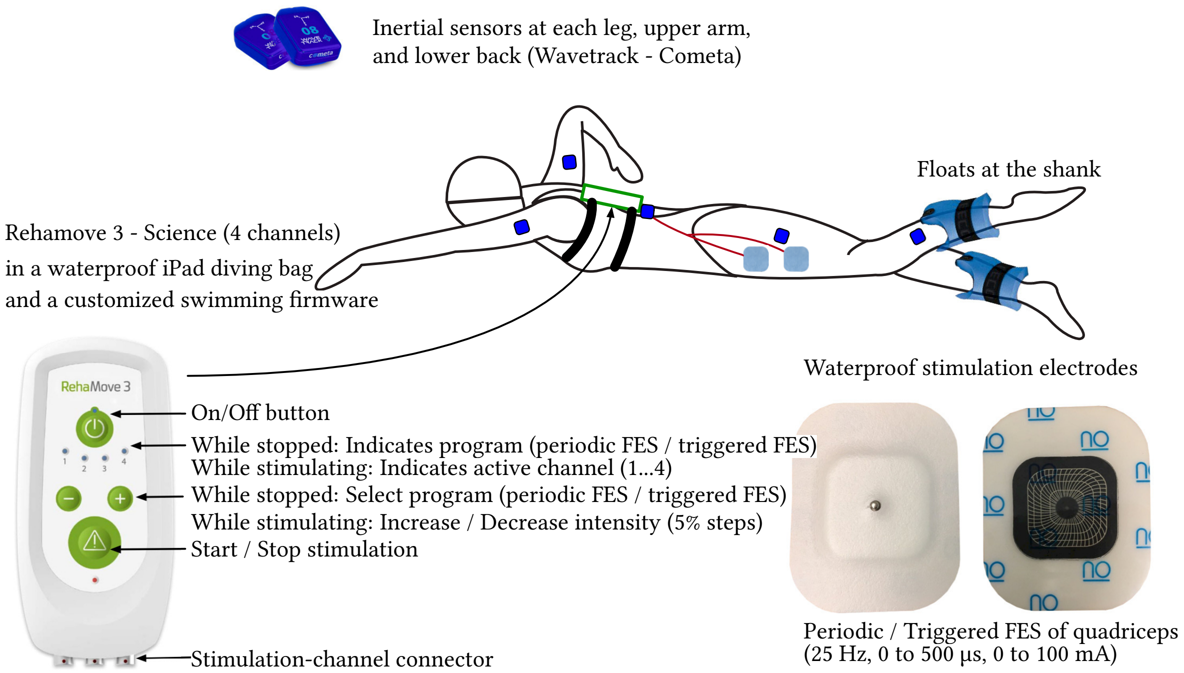
Inertial sensors at each leg, upper arm,
and lower back (Wavetrack - Cometa)
Floats at the shank
Rehamove 3 - Science (4 channels)
in a waterproof iPad diving bag
and a customized swimming firmware
Waterproof stimulation electrodes
RehaMove 3
On/Off button
While stopped: Indicates program (periodic FES / triggered FES)
While stimulating: Indicates active channel (1...4)
While stopped: Select program (periodic FES / triggered FES)
While stimulating: Increase / Decrease intensity (5% steps)
Start / Stop stimulation
Stimulation-channel connector
Periodic / Triggered FES of quadriceps
(25 Hz, 0 to 500 µs, 0 to 100 mA)

Figure 7.1: IMU-triggered stimulation swimming system consisting of the RehaMove3 with a customized firmware, waterproof electrodes and cable connectors, and a wearable inertial sensors. All cable contacts and electric parts are waterproof. On each quadriceps, two waterproof electrodes are placed for FES (©2020 IEEE).

applied. Hence, only the knee extensors were stimulated with charge-balanced biphasic stimulation pulses at a frequency of 25 Hz and pulse width in the range of 0 µs to 500 µs and amplitude of 0 mA to 100 mA. Furthermore, the stimulator incorporates an inertial sensor. This sensor is used to estimate the trunk-roll angle and trunk-roll-angle rate for the trigger algorithm (see Section 7.2.3).

7.2.2 IMU-Based Motion Analysis

As already described in the previous chapter, wearable and wireless inertial sensors (WaveTrack, Cometa srl, Italy) are used to capture the motion of the trunk as well as the upper and lower extremities of the swimmer. These measurements are used for an objective assessment of the swimming motion. Three additional methods are elaborated to estimate the trunk-roll-angle rate, the upper-arm inclination angle, and the instantaneous swimming speed.

The sensor setup is illustrated in Fig. 7.2. As described in Section 6.3.5, one IMU is placed on the lateral aspect of each thigh, on the lateral aspect of each shank, and on the lateral aspect of each upper arm. For each of these IMUs, the intrinsic x-axis is aligned with the longitudinal axis of the body segment and points from proximal to distal, while the intrinsic z-axis always points laterally away from the skin. The IMU that is incorporated in the stimulator is located at the upper back near the thoracic vertebrae with a sensor-to-body orientation that aligns the intrinsic x-axis of the sensor with the spine and lets the intrinsic y-axis point to the right. Since it was not possible to transfer or log the data of this sensor during the experiments, an additional sensor was placed close to the stimulator with the same alignment to measure the trunk-roll angle.

Compared to the previous chapter, only the knee angle and the trunk-roll angle are measured. In addition, the inclination angles of the upper arms are determined. The roll-angle rate is determined

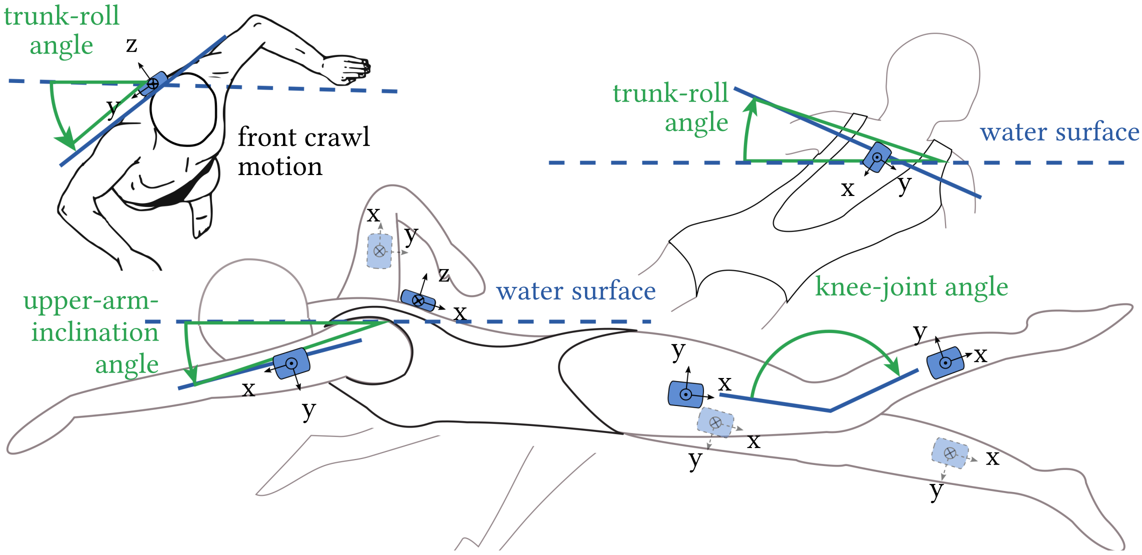

Figure 7.2: Sensor locations and motion parameters during swimming. Seven IMUs are used to capture the characteristics of the motion of the trunk and the extremities during front crawl swimming (©2020 IEEE).

as well, since it also required for the trigger algorithm. Furthermore, the instantaneous swimming speed is estimated to compare the different support modalities.

Upper-arm-inclination angle The motion of the left and right upper arm during front crawl swimming is characterized by the angle between the longitudinal axis of the humerus and the horizontal water surface (see Fig. 7.2). When the arm moves forward above the water surface, that axis is almost horizontal, while it points down during the actual stroke inside the water, as illustrated in Figure 7.2. Recall that the intrinsic x-axes of the upper-arm IMUs are aligned with the longitudinal humerus axes and point from the shoulders to the elbows. Therefore, by analogy with the trunk-roll angle, the angles $\phi_{\mathrm{LA},x}$ and $\phi_{\mathrm{RA},x}$ (LA - left arm, RA - right arm) are determined between these x-axes and the horizontal plane as

$$\phi_{\mathrm{i},y} = \frac{\pi}{2} - \arccos\left({}_{\mathcal{E}_\mathrm{i}}\mathbf{z}^T_{\mathcal{E}_\mathrm{i}} \; {}_{\mathcal{E}_\mathrm{i}}\mathbf{x}_{\mathcal{S}_\mathrm{i}}\right), \tag{7.1}$$

$${}_{\mathcal{E}_\mathrm{i}}\mathbf{x}_{\mathcal{S}_\mathrm{i}} = {}^{\mathcal{S}_\mathrm{i}}_{\mathcal{E}_\mathrm{i}}\mathbf{q} \otimes {}_{\mathcal{S}_\mathrm{i}}\mathbf{x}_{\mathcal{S}_\mathrm{i}} \otimes {}^{\mathcal{E}_\mathrm{i}}_{\mathcal{S}_\mathrm{i}}\mathbf{q}, \quad i = \{\mathrm{LA}, \mathrm{RA}\}, \tag{7.2}$$

where ${}^{\mathcal{S}_\mathrm{i}}_{\mathcal{E}_\mathrm{i}}\mathbf{q}$ are the orientation quaternions that are estimated by the sensor-fusion algorithm. Note that $\phi_{\mathrm{LA},x}$ is negative if the left elbow is below the left shoulder.

Instantaneous swimming speed The average swimming speed per lap can be determined directly from the lap time and the lap length. The instantaneous swimming speed during the lap is determined from the accelerometer readings ${}_{\mathcal{S}_\mathrm{TR}}\mathbf{a}_\mathrm{TR}$ of the trunk IMU. First, the orientation quaternion ${}^{\mathcal{S}_\mathrm{TR}}_{\mathcal{E}_\mathrm{TR}}\mathbf{q}$ is used to transform the intrinsically measured acceleration to the inertial reference frame and the gravitational acceleration ${}_{\mathcal{E}_\mathrm{TR}}\mathbf{g} = [0, 0, 9.81]^T$ is removed, which appears as a vertical upward acceleration in the specific force that is measured by accelerometers. The obtained acceleration

$${}_{\mathcal{E}_\mathrm{TR}}\tilde{\mathbf{a}}_\mathrm{TR} = {}^{\mathcal{S}_\mathrm{TR}}_{\mathcal{E}_\mathrm{TR}}\mathbf{q} \otimes {}_{\mathcal{S}_\mathrm{TR}}\mathbf{a}_\mathrm{TR} \otimes {}^{\mathcal{E}_\mathrm{TR}}_{\mathcal{S}_\mathrm{TR}}\mathbf{q} - {}_{\mathcal{E}_\mathrm{TR}}\mathbf{g} \tag{7.3}$$

describes the instantaneous change of velocity of the trunk IMU with respect to the inertial frame of reference. The inclination angles of the arms and the trunk are used to determine moments t_0 and t_e at which the subject was resting at the pool edge right before and right after swimming the lap, respectively. Between both moments, ${}_{\mathcal{E}_{\mathrm{TR}}}\tilde{\mathbf{a}}_{\mathrm{TR}}$ is integrated over time and the resulting velocity is corrected using the fact that the velocity becomes zero again at the end of the lap

$$ {}_{\mathcal{E}_{\mathrm{TR}}}\mathbf{v}_{\mathrm{TR}} = \frac{1}{f_s} \sum_{\tau_1=t_0}^{t} \left({}_{\mathcal{E}_{\mathrm{TR}}}\tilde{\mathbf{a}}_{\mathrm{TR}}(\tau_1) - \frac{1}{f_s\,(t_e - t_0)} \sum_{\tau_2=t_0}^{t_e} {}_{\mathcal{E}_{\mathrm{TR}}}\tilde{\mathbf{a}}_{\mathrm{TR}}(\tau_2) \right), \ \forall t \in [t_0, t_e], \tag{7.4} $$

where f_s is the sampling frequency of the acceleration readings and the second term inside the parentheses is the accelerometer bias that follows from the zero-end-velocity assumption.

Trunk-roll-angle rate The roll angle was already introduced in Eq. (6.4). The rate of change of this angle $\phi_{\mathrm{TR},y}$, which is the trunk-roll-angle rate, is determined by transforming the measured angular rate ${}_{\mathcal{S}_{\mathrm{TR}}}\mathbf{g}_{\mathrm{TR}}$ into the reference coordinate system and projecting it onto the axis that is orthogonal to the vertical axis and the y-axis of the trunk IMU:

$$ \dot{\phi}_{\mathrm{TR},y} = \frac{\left({}_{\mathcal{E}_{\mathrm{TR}}}\mathbf{y}_{\mathcal{S}_{\mathrm{TR}}} \times {}_{\mathcal{E}_{\mathrm{TR}}}\mathbf{z}_{\mathcal{E}_{\mathrm{TR}}} \right)^T}{\| {}_{\mathcal{E}_{\mathrm{TR}}}\mathbf{y}_{\mathcal{S}_{\mathrm{TR}}} \times {}_{\mathcal{E}_{\mathrm{TR}}}\mathbf{z}_{\mathcal{E}_{\mathrm{TR}}} \|_2} \left({}^{\mathcal{S}_{\mathrm{TR}}}_{\mathcal{E}_{\mathrm{TR}}}\mathbf{q} \otimes {}_{\mathcal{S}_{\mathrm{TR}}}\mathbf{g}_{\mathrm{TR}} \otimes {}^{\mathcal{E}_{\mathrm{TR}}}_{\mathcal{S}_{\mathrm{TR}}}\mathbf{q} \right). \tag{7.5} $$

This roll rate is positive if the trunk rotates such that the right shoulder rises while the left shoulder declines, and it is negative for the opposite direction of rotation. The trunk-roll-angle rate will be used in the algorithm in the next section to segment the individual swimming strokes.

7.2.3 IMU-Based Control of the Stimulation Timing

According to [130] and [131], the synchronization of the leg kick and arm movement in front crawl swimming plays a major role in keeping the body in a streamlined position. Therefore, it is desirable to control the timing of the stimulation phases such that the leg motion is synchronized with the voluntary motion of the upper body. A stimulation control pattern is proposed that activates the knee extensors based on the trunk-roll angle.

During front crawl swimming, this angle typically varies periodically in the range of ±50 ° for expert swimmers and in the range of ±30 ° for non-expert able-bodied swimmers (cf. [132, 133]). In preliminary tests, the trunk-roll angle of a paraplegic subject (cf. Chapter 6, corresponds to subject A of the STIMSWIM study) was measured in combination with the arm-inclination angle. A snapshot of several strokes for a paraplegic subject swimming front crawl without FES support is shown in Fig. 7.3. The arm-inclination angles exhibit a uniform and periodic up and down movement that runs synchronously with the trunk-roll angle. The trunk-roll angle shows a plateau for a rotation to the right side, although the subject used a snorkel. This might be explained by the fact that the subject has a shoulder contracture due to an accident, which limits movements to the left. In preliminary tests, a slow swimming movement was observed of approximately 1.5–2 s for each stroke. To improve the swimming speed and the stability in water, the knee extension of each side should be synchronized to the forward movement of the contralateral arm, which is marked by the arm-inclination angle's steep descent right after reaching the maximum.

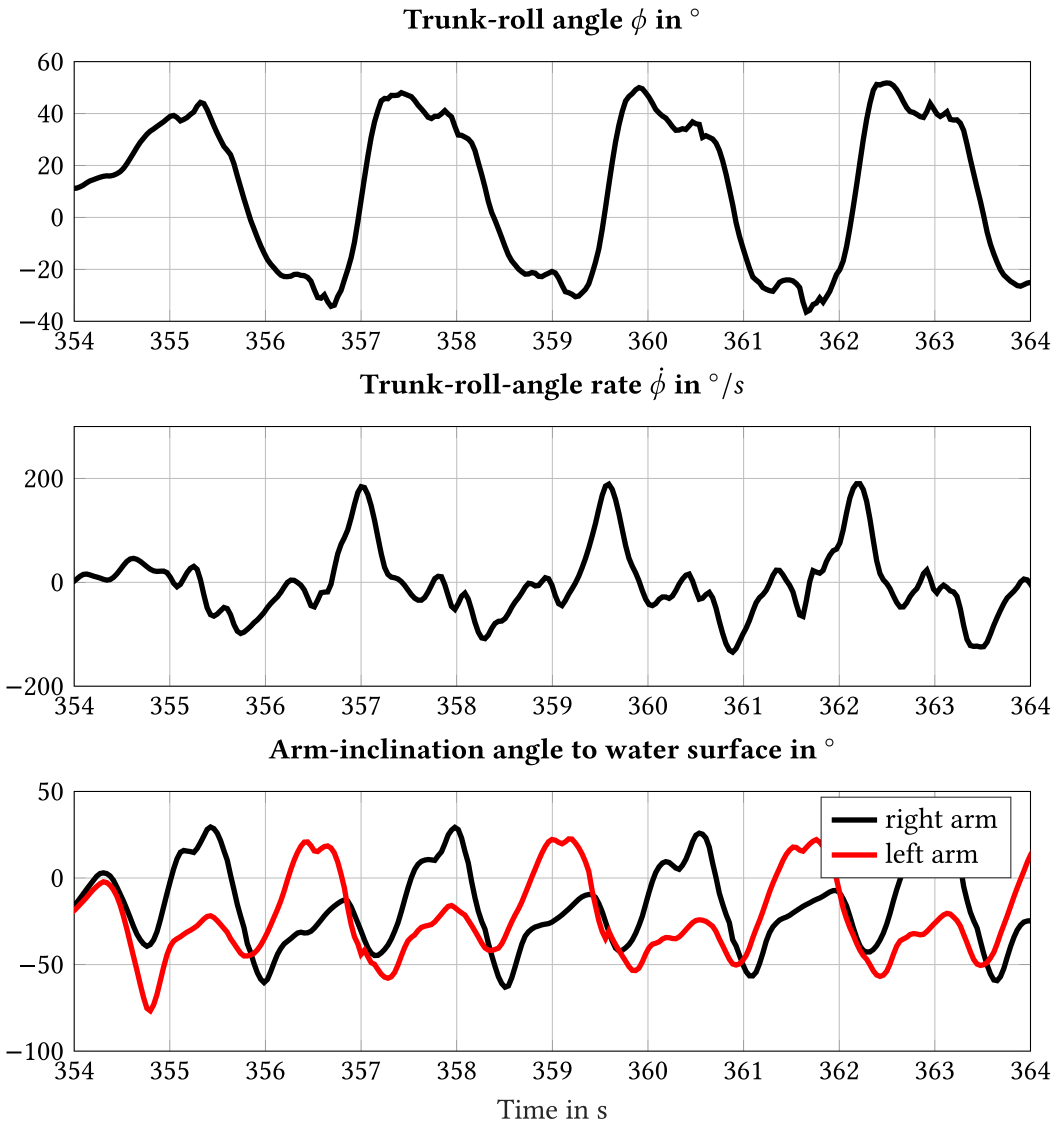

Figure 7.3: Trunk-roll angle and roll rate as well as left and right upper-arm inclination angle during front crawl strokes of a complete-SCI subject without FES. During this measurement, the knee extensors were not stimulated (©2020 IEEE).

To realize the roll-angle-triggered stimulation, the beginning of a stroke has to be detected. This is done using the heuristic rule summarized in Algorithm 1. This procedure is periodically triggered as long as the swimmer is in the correct position so that the z-axis of the trunk sensor points upwards, which is indicated by ${}_{\mathcal{E}_{\mathrm{TR}}}\mathbf{z}^{T}_{\mathcal{S}_{\mathrm{TR}}}\;{}_{\mathcal{E}_{\mathrm{TR}}}\mathbf{z}_{\mathcal{E}_{\mathrm{TR}}} > 0$. After each fully detected stroke, the maximum and minimum of the roll angle are updated and averaged over the last three minima and maxima, where the initial output of the averaging filter is ∞ and $-\infty$, respectively, until three swimming strokes have been detected.

The stimulation of the knee extensors is then triggered based on the state machine in Fig. 7.4. Here, a separate automaton is defined for each leg. For both automata, if the swimmer is in the correct position (${}_{\mathcal{E}_{\mathrm{TR}}}\mathbf{z}^{T}_{\mathcal{S}_{\mathrm{TR}}}\;{}_{\mathcal{E}_{\mathrm{TR}}}\mathbf{z}_{\mathcal{E}_{\mathrm{TR}}} > 0$) and $\phi_{\mathrm{TR},y} < 0$ or $\phi_{\mathrm{TR},y} > 0$, respectively, the state switches from rest to the corresponding idle state. If the trigger criterion for one side is valid, the stimulation intensity I_i with $i \in \{L, R\}$ is set to 1, while the opposite site is at rest or idle. A stimulation intensity of 1

Algorithm 1 Heuristic procedure for detecting a full swim stroke incorporating the left and right arm-crawl movement. $\overline{\max}_{\phi_{\mathrm{TR},y}}$ and $\overline{\min}_{\phi_{\mathrm{TR},y}}$ are the mean maximum and mean minimum of the roll angle averaged over the last three minima and maxima.

```
Require: ${}_{\mathcal{E}_{\mathrm{TR}}}\mathbf{z}^T_{\mathcal{S}_{\mathrm{TR}}}\;{}_{\mathcal{E}_{\mathrm{TR}}}\mathbf{z}_{\mathcal{E}_{\mathrm{TR}}} > 0$
procedure StrokeDetection($\phi_{\mathrm{TR},y}$, $\dot{\phi}_{\mathrm{TR},y}$)
    State := 0
    while State ≠ 3 do
        if $\phi_{\mathrm{TR},y} < 0 \wedge \dot{\phi}_{\mathrm{TR},y} \geq 25\frac{\circ}{s} \wedge \mathrm{State} = 0$ then State := 1
        end if                                                    ▷ Stroke started.
        if $\phi_{\mathrm{TR},y} > 0 \wedge \dot{\phi}_{\mathrm{TR},y} \leq -25\frac{\circ}{s} \wedge \mathrm{State} = 1$ then State := 2
        end if                                                    ▷ Half of stroke done.
        if $\phi_{\mathrm{TR},y} < 0 \wedge \dot{\phi}_{\mathrm{TR},y} \geq 25\frac{\circ}{s} \wedge \mathrm{State} = 2$ then State := 3
        end if                       ▷ New stroke beginning detected → stroke done.
    end while
    Update $\overline{\max}_{\phi_{\mathrm{TR},y}}$ and $\overline{\min}_{\phi_{\mathrm{TR},y}}$
end procedure
```

means that the predefined maximum intensity is set, which is the same for both legs. The maximum intensity can be set via the plus and minus buttons at the stimulator. If the stimulation duration τ_S reaches the maximum duration $\max_{\tau_s}$ or the opposite side switches to active stimulation, the current side switches to rest state. C code was generated from a Stateflow® implementation of the state machine using Simulink Embedded Coder (The Mathworks, Inc., USA) and directly integrated into the stimulator's firmware.

To investigate the effect of closed-loop versus open-loop stimulation timing on swimming performance and speed, the proposed stimulation-trigger algorithm is compared to a periodic stimulation that activates each knee extensor for 0.5 s periodically without synchronization with the upper extremities or the trunk. In the following section, experimental results will be presented.

7.3 Results

During experiments, three different methods have been compared regarding overall and instantaneous swimming velocity, knee, arm, and roll angles:

- No stimulation (unactuated),
- Periodic stimulation (open-loop),
- Triggered stimulation (closed-loop).

The proposed methods have been tested with one completely paralyzed subject (ASIA impairment scale A) who corresponds to subject A of the STIMSWIM study presented in Chapter 6. Each trial consisted of one lap of 16 m length. During the swimming trials, the stimulation intensity was set to 40 mA and 200 µs for both stimulation methods. The tests were executed first with no stimulation, followed by periodic stimulation, and finished with a lap with triggered stimulation. Between each trial there was a break of a few minutes in which the stimulation program was changed and the subject could rest in the water at the pool edge.

First of all, swimming with triggered stimulation achieved the fastest lap time compared to periodic stimulation and to no stimulation, which resulted in the slowest lap time. This result is underlined by

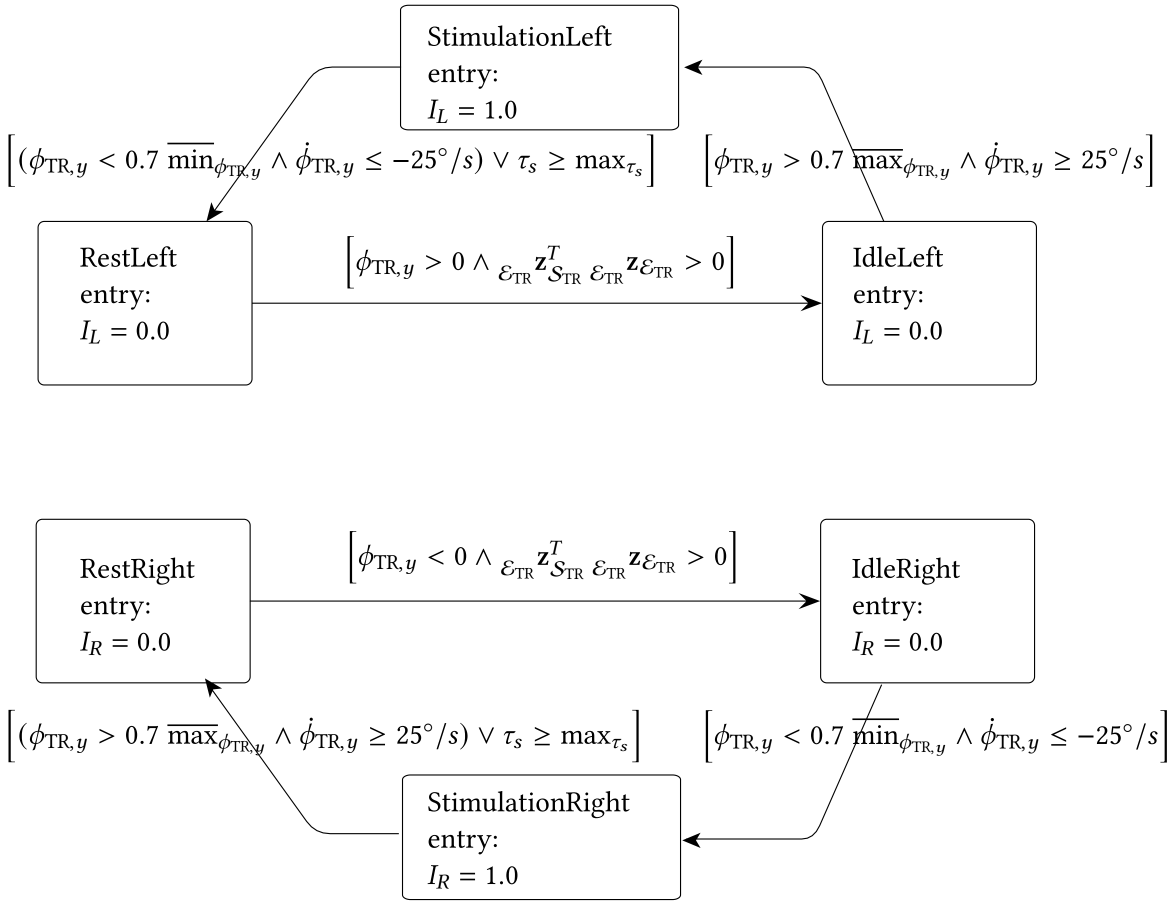
StimulationLeft
entry:
$I_L = 1.0$
$\left[(\phi_{\mathrm{TR},y} < 0.7\,\overline{\min}_{\phi_{\mathrm{TR},y}} \wedge \dot{\phi}_{\mathrm{TR},y} \leq -25^\circ/s) \vee \tau_s \geq \max_{\tau_s}\right]$
$\left[\phi_{\mathrm{TR},y} > 0.7\,\overline{\max}_{\phi_{\mathrm{TR},y}} \wedge \dot{\phi}_{\mathrm{TR},y} \geq 25^\circ/s\right]$
RestLeft
entry:
$I_L = 0.0$
$\left[\phi_{\mathrm{TR},y} > 0 \wedge {}_{\mathcal{E}_{\mathrm{TR}}}\mathbf{z}^T_{\mathcal{S}_{\mathrm{TR}}}\,{}_{\mathcal{E}_{\mathrm{TR}}}\mathbf{z}_{\mathcal{E}_{\mathrm{TR}}} > 0\right]$
IdleLeft
entry:
$I_L = 0.0$
RestRight
entry:
$I_R = 0.0$
$\left[\phi_{\mathrm{TR},y} < 0 \wedge {}_{\mathcal{E}_{\mathrm{TR}}}\mathbf{z}^T_{\mathcal{S}_{\mathrm{TR}}}\,{}_{\mathcal{E}_{\mathrm{TR}}}\mathbf{z}_{\mathcal{E}_{\mathrm{TR}}} > 0\right]$
IdleRight
entry:
$I_R = 0.0$
$\left[(\phi_{\mathrm{TR},y} > 0.7\,\overline{\max}_{\phi_{\mathrm{TR},y}} \wedge \dot{\phi}_{\mathrm{TR},y} \geq 25^\circ/s) \vee \tau_s \geq \max_{\tau_s}\right]$
$\left[\phi_{\mathrm{TR},y} < 0.7\,\overline{\min}_{\phi_{\mathrm{TR},y}} \wedge \dot{\phi}_{\mathrm{TR},y} \leq -25^\circ/s\right]$
StimulationRight
entry:
$I_R = 1.0$

Figure 7.4: State machine implemented in Stateflow®, where entry defines a singular action when the state is entered. The corresponding stimulation intensity I_i with $i \in \{L, R\}$ is set to 0 or 1 depending on the state. A stimulation intensity of 1 means that the predefined maximum intensity is set, which is the same for both legs. The maximum intensity can be set via the plus and minus buttons at the stimulator. τ_S defines the current stimulation duration and $\max_{\tau_s}$ the predefined maximum duration (©2020 IEEE).

the swimming velocity given in Fig. 7.5. Here, the distribution of the maximum, minimum, and mean swimming velocity for each swimming method is shown. For both, periodic and triggered stimulation, a velocity improvement can be observed compared to no stimulation. For triggered stimulation, all values are higher compared to periodic and no stimulation and the distribution is narrower. Further insight is gained by observing the course of the instantaneous velocity in Fig. 7.6. For swimming without stimulation, the minimum velocity reaches zero for nearly all strokes, which is improved for periodic stimulation. Nevertheless, at least for three strokes, the forward movement is interrupted. Only for triggered stimulation, the minimum velocity is always non-zero, which indicates that the sliding phase in between the contralateral arm strokes is improved. Furthermore, the narrowed distribution of the maxima and minima for triggered stimulation also indicates that the swimming movement becomes more homogeneous compared to periodic stimulation. Comparing the knee-joint angles and the stimulation intensity in Figs. 7.7 to 7.9, the improvement of swimming velocity becomes even more apparent. In case of no stimulation, the knee-angle course follows the trunk-roll angle. However, the knee joints are not actively extended and therefore vary in the range of 45 to 130 degrees. A snapshot of the knee motion during left and right arm stroke is shown in Fig. 7.10 A1 and A2, respectively. For periodic stimulation, an increase of the knee angle to the range of 70 to 170 degrees can be observed. However, the knee-angle motion is rarely synchronized with the trunk-roll angle or

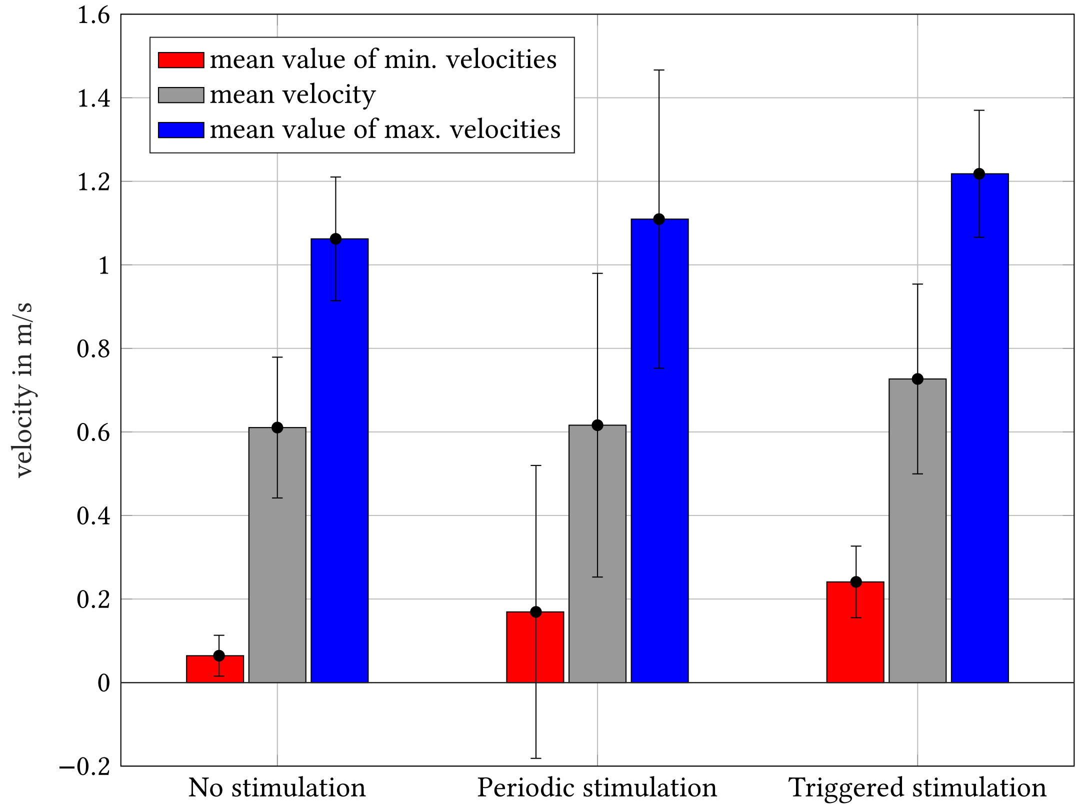

Figure 7.5: Distribution of maximum, minimum, and mean swimming velocity for the three different swimming methods. The whiskers describe the 25th and 75th percentiles, respectively (©2020 IEEE).

the arm movement. Due to that lack of synchronization, the knee extension sometimes takes place during the stroke of the ipsilateral side as shown in Fig. 7.10 B. This causes an undesirable additional roll around the longitudinal body axis, which the swimmer typically counteracts by an extra hand movement. For triggered stimulation, it can be observed that the knee angle is further increased to the range of 100 to 180 degrees. Furthermore, an improved synchronizaton is documented for the triggered stimulation in Fig. 7.9. For both legs, the knee-angle extension follows the rhythm of the stimulation signal and the trunk-roll angle. Furthermore, the mean, maxima, and minima of each knee stroke are increased compared to the periodic stimulation and to no stimulation.

Since the trunk-roll angles show a longer plateau for the rotation to the right side, the stimulation intensity is not a uniform signal. The trigger state-machine does not take a non-uniform roll angle signal into account. Hence, the extension phases for the left knee are longer compared to the right side.

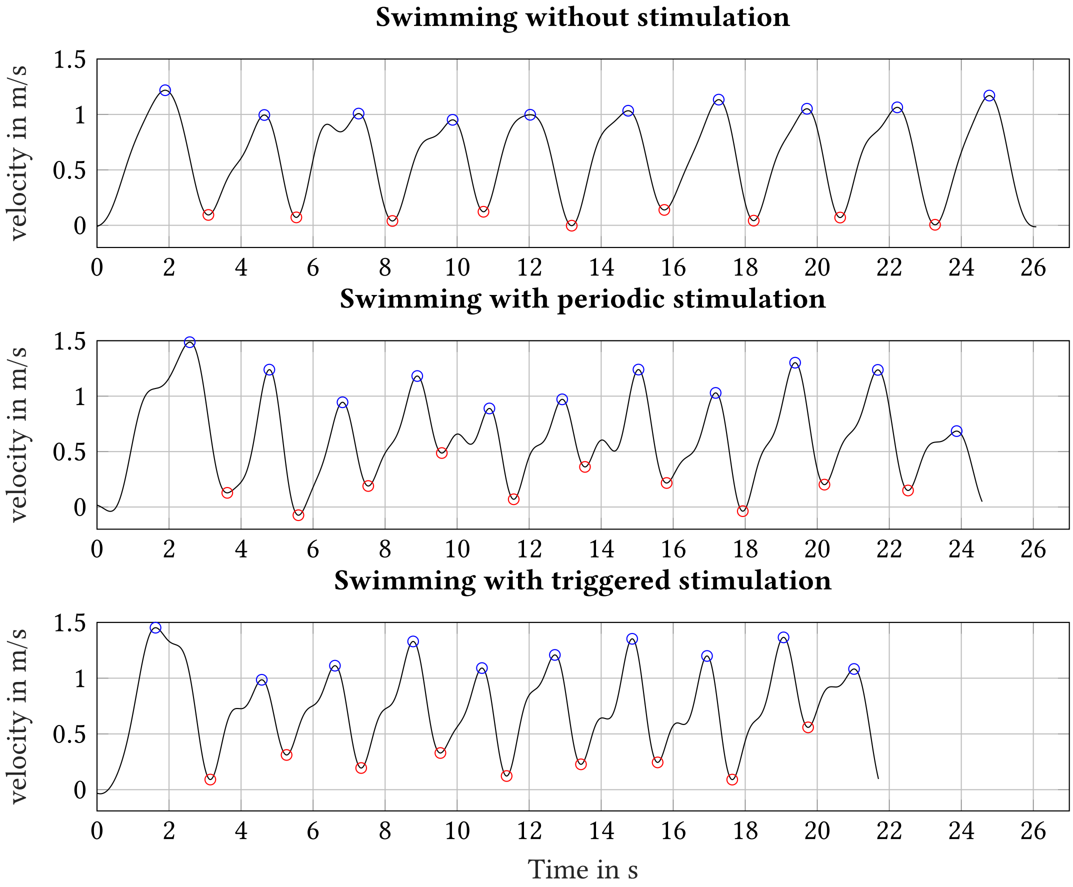

Figure 7.6: Instantaneous swimming velocity for three different swimming methods. Each maximum is labeled with blue and each minimum with a red circle, respectively (©2020 IEEE).

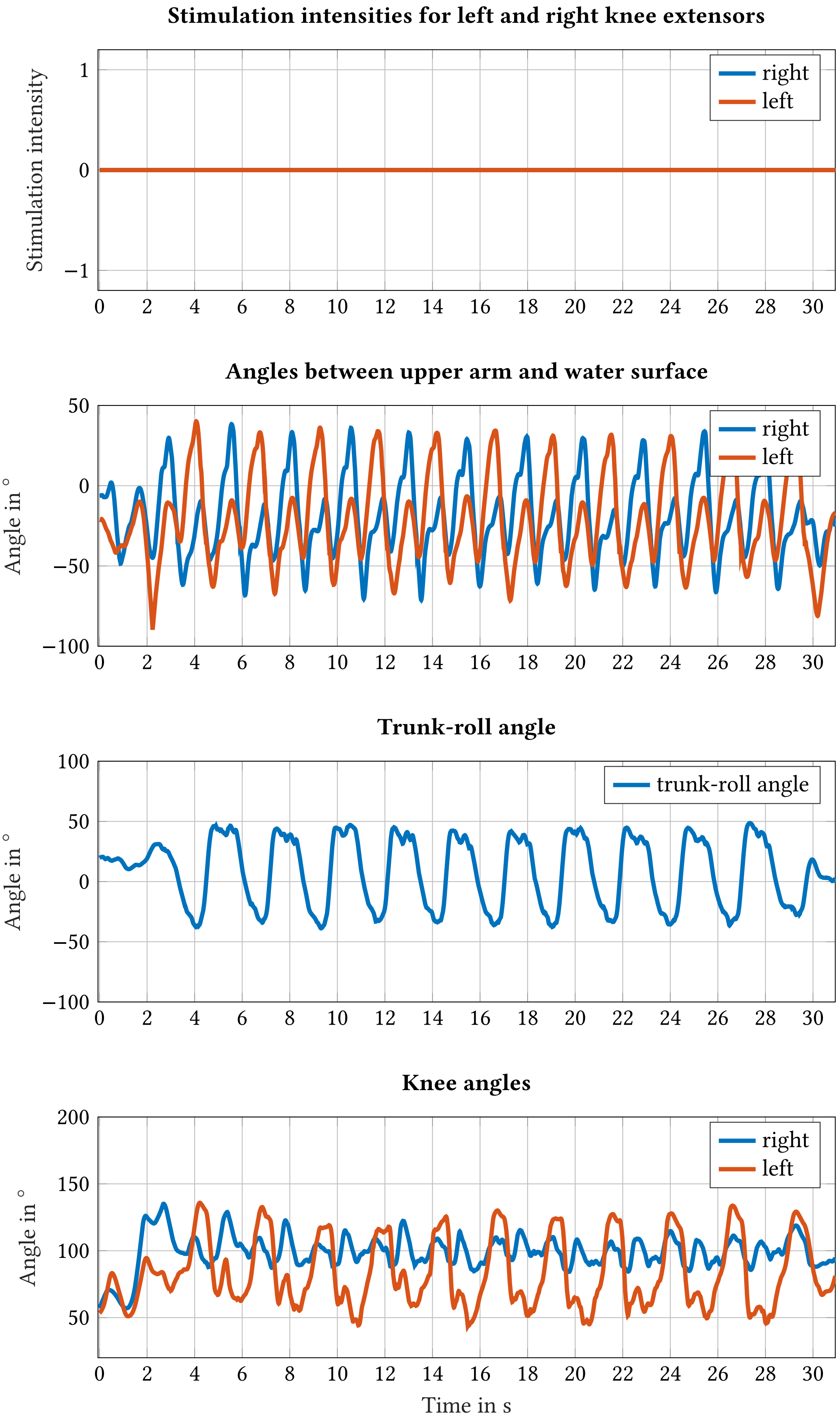

Figure 7.7: Swimming with no stimulation: Stimulation intensity in percentage, where 0 means no stimulation and 1.0 means 40 mA and 200 μs for the right leg and -1.0 means the same intensity for the left leg, respectively (©2020 IEEE).

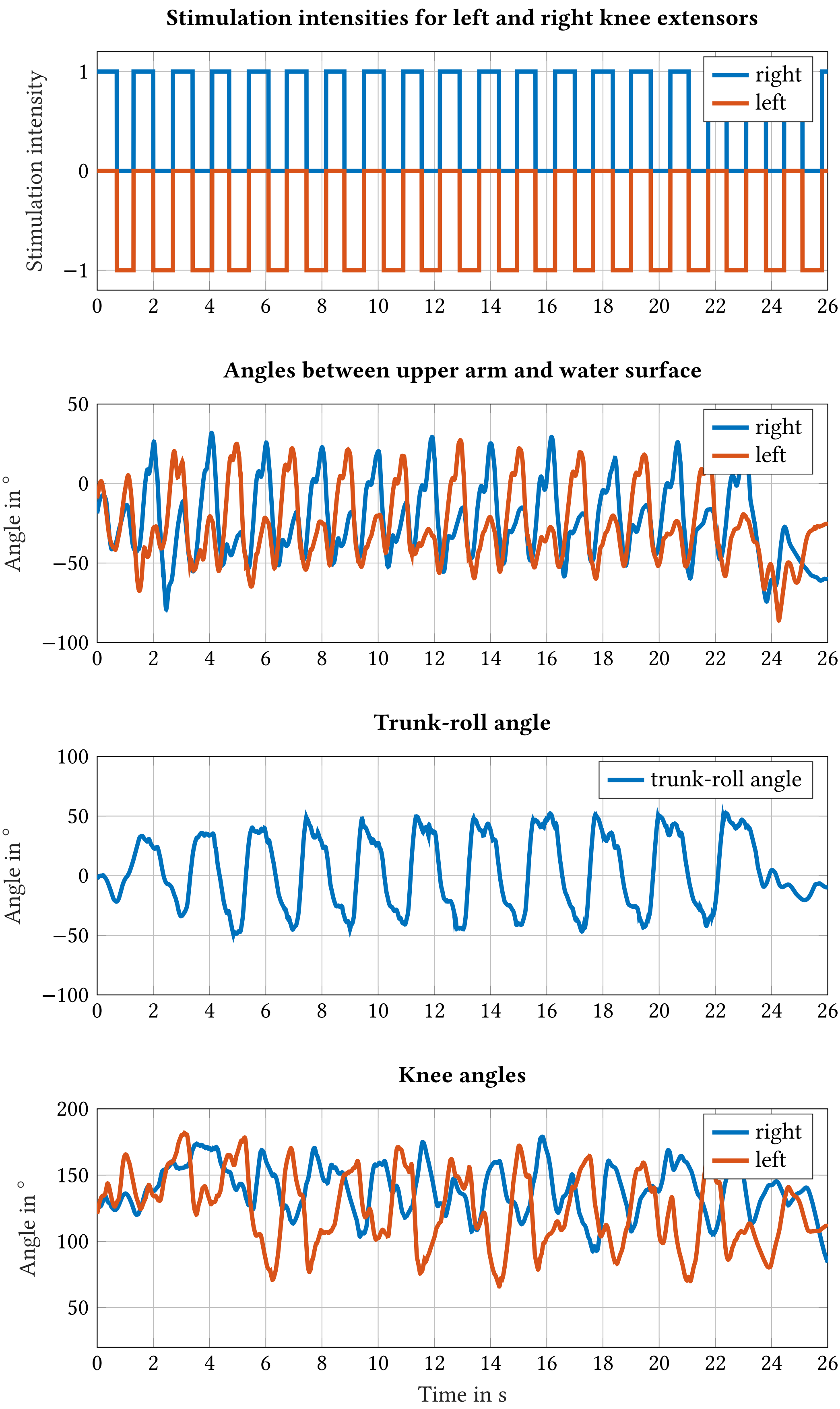

Figure 7.8: Swimming with periodic stimulation: Stimulation intensity in percentage, where 0 means no stimulation and 1.0 means 40 mA and 200 μs for the right leg and -1.0 means the same intensity for the left leg, respectively (©2020 IEEE).

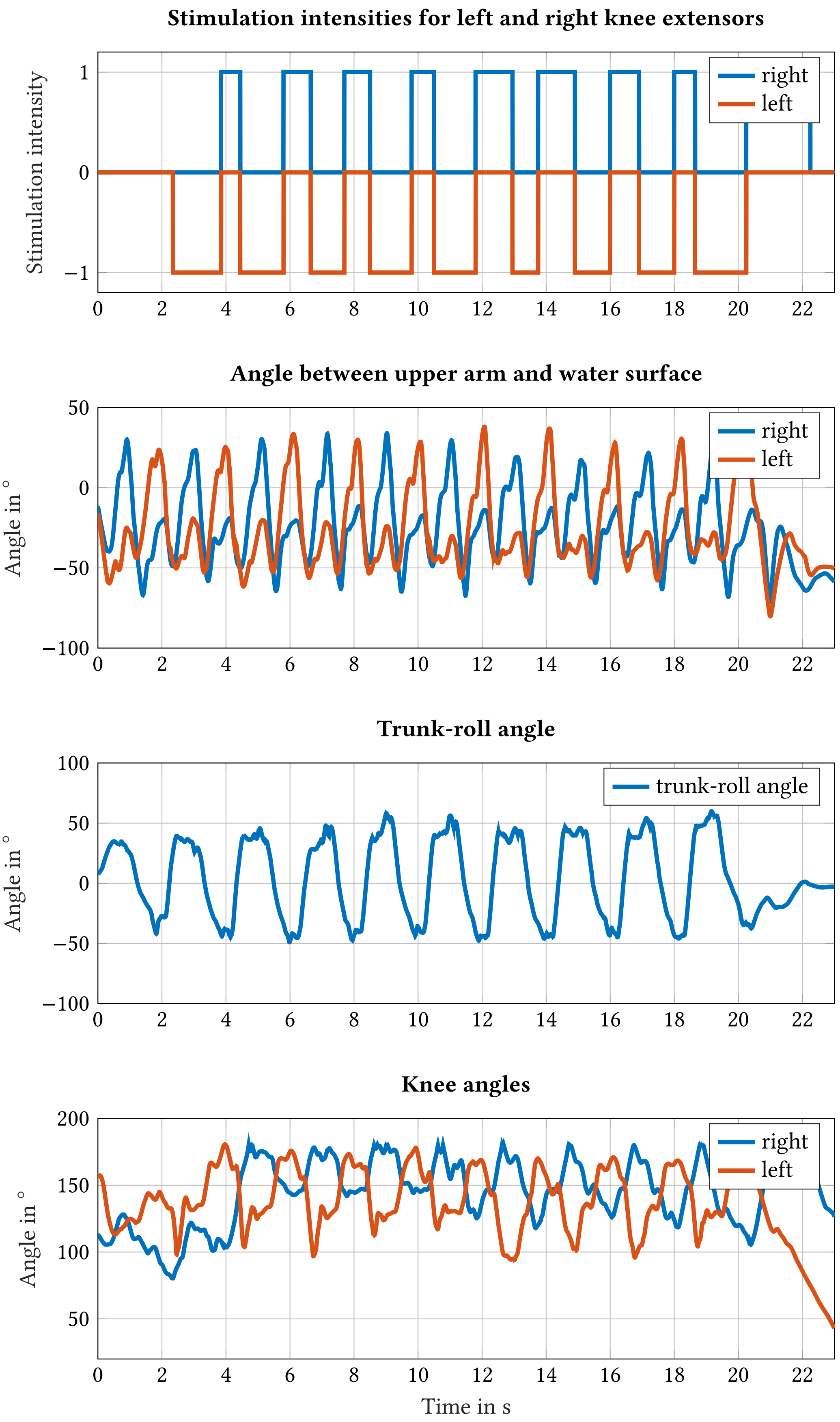

Figure 7.9: Swimming with triggered stimulation: Swimming with periodic stimulation: Stimulation intensity in percentage, where 0 means no stimulation and 1.0 means 40 mA and 200 μs for the right leg and -1.0 means the same intensity for the left leg, respectively (©2020 IEEE).

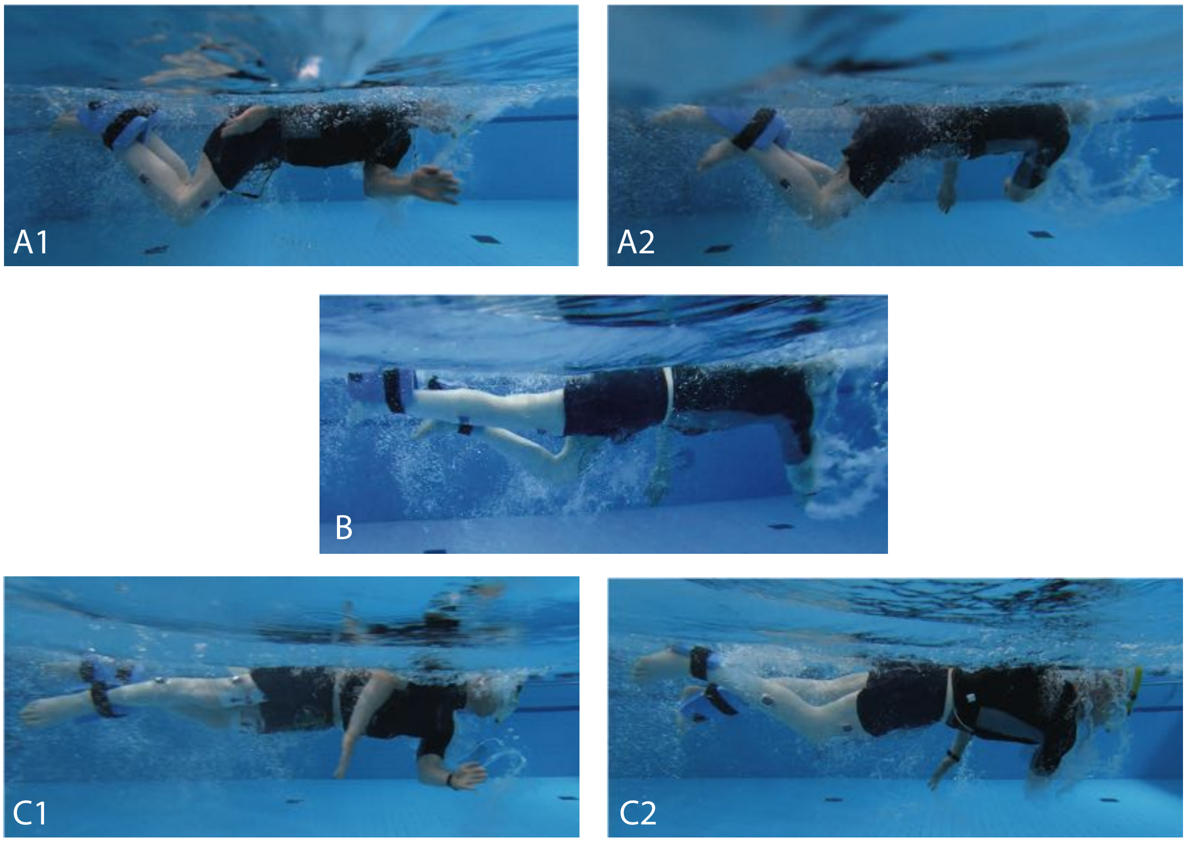

Figure 7.10: Synchronization of arm and leg movement in paraplegic front crawl swimming. A1–A2) Swimming without stimulation and no leg movement. B) Undesired leg extension on the side of arm stroke during non-synchronized stimulation with open-loop stimulation pattern. C1–C2) Roll-angle-triggered stimulation with extension of the contralateral leg during each arm stroke (©2020 IEEE).

As shown in Fig. 7.10 C1–C2, the knee extension is synchronized with the contralateral arm stroke using the roll angle as the trigger signal. Furthermore, the start and stop of the stimulation was initiated by the trunk-roll movement of the subject.

The subject was asked to rate the periodic and triggered FES swimming methods. With the triggered stimulation method, the subject could feel that he was able to trigger the extension of his knee by himself, and he could manually start and stop the stimulation compared to the periodic stimulation. Furthermore, he quoted that it feels like the legs are supporting the swim movement, and he does not have to drag his legs behind him.

7.4 Conclusion and Future Research

A controlled FES system for swimming support in paraplegic patients has been introduced. It realizes the desired knee movement by alternating between FES-induced knee extension and passive knee flexion caused by floats. Moreover, it provides accurate motion assessment and real-time control of the stimulation timing by means of wearable inertial sensors. The system enables a new hybrid exercise modality for SCI subjects that involves the voluntarily moved arms and the artificially stimulated legs. The swimming exercise can be performed independently by the subject without any additional assistance.

The results in one complete-SCI subject showed that the swimming speed can be increased using electrical stimulation, where controlling the stimulation timing based on upper-body motion performed better than periodic open-loop stimulation of the knee extensors. This can be explained by an increased knee-joint angular range and a synchronization of the knee extension to the arm movement. Moreover, the proposed method enables the subject to start and stop the stimulation by initiating the characteristic roll movement of his trunk.

To my best knowledge, this is the first time that closed-loop FES is used under water to generate functional movements in paraplegics. The research is still in a pilot phase, and further tests with more subjects are needed to quantify, analyze, and improve the training effects for the subjects.

FES-based swimming support for paraplegics is a new and very promising application for systems and control methods. The presented initial prototype and results leave a number of challenges open, which should be addressed by future research and by joint efforts of control engineers and clinical SCI experts.

1. At the moment, the trigger criterion is based on heuristically determined symmetric thresholds. In case of a non-uniform trunk-roll angle, this leads to a non-uniform stimulation profile for each side. Future work should aim at optimizing the stimulation pattern to handle also non-uniform trunk-roll angle patterns.

2. Over several consecutive laps within one training day, the muscles fatigued and the stimulation intensity had to be increased to maintain a certain level of muscle recruitment. As a future improvement, an automatic increase of the stimulation intensity could be incorporated into the proposed stimulation method. This would require online observation of the induced muscle contraction and motion level, which in turn requires online communication between the stimulator and inertial or electromyographic sensors on the legs.

3. If such a communication between the four inertial leg sensors and the stimulator can be realized, then closed-loop methods can be applied to control the leg motion with trigger or reference signals based on the arm motion. Numerous existing robust and nonlinear control methods for lower-limb FES motion control could be considered, see for example [78, 134, 135]. However, moving in water is quite different from moving in air, which means that new methods or at least adaptive and self-learning approaches, such as [136–141], might be required to achieve practical results. If feedback control of the leg motion via adaptations of the stimulation intensities can be realized, this will not only yield automatic compensation of fatigue, but it might as well yield further improvement of the swimming performance.

Beyond further technological advancements, future research will include more experimental trials with different subjects to statistically strengthen the initial results and obtain further insights.

8

General Conclusions and Outlook

This dissertation aimed at deriving new methods for the control of functional electrical stimulation based on inertial sensors. These methods can be used for established rehabilitation activities such as FES cycling and novel applications such as FES swimming, focusing on the ease of use of the methods. The subsequent sections briefly summarize and assess the main results of each chapter.

8.1 General Conclusions on the Proposed FES Cycling Methods

In Chapter 3, the state-of-the-art in FES cycling is analyzed in terms of clinical outcomes, stimulation patterns and involved sensors, and stimulated muscle groups. To support and verify the subsequent method development, a simulation model was developed to mimic the biomechanical and physiological properties of the lower extremities during FES cycling. Using this model, new methods for joint-angle-based FES cycling were developed. In a first step, the knee- and hip-joint angles were determined using four inertial sensors attached to each of the upper and lower legs. It was shown that only the longitudinal axis of the sensor and the segment have to be aligned to obtain an accurate estimate of segment-inclination angles compared to an optical reference measurement system. In a second step, the knee-joint angles were converted into a so-called cycle percentage, which was then used as a trigger for FES cycling. It could be shown by means of a proof that the extension and flexion phases of the knee-joint angle can be determined by means of the estimated segment-inclination angles. Furthermore, due to Grashof's condition, the extension of the hip joint must always follow that of the knee joint. In exploratory tests, the stimulation ranges for the quadriceps, hamstrings, and gluteus muscle groups were determined. It was shown in simulations that these joint-angle-based stimulation ranges are not affected by varying the distance and height of the seat with respect to the crank joint. Furthermore, to account for the time delay between stimulation onset and joint-moment generation, a speed-adaptation method of the proposed stimulation pattern is presented. Using a Look-Up Table (LUT), the stimulation pattern is shifted in time by a fixed delay to stimulate the corresponding muscles earlier. This approach also works for strongly varying joint-angle velocities. In simulations the LUT-based method produces a lower cadence variation compared to a simple approach based on mean joint-angle velocity. Therefore, the proposed speed-adaptation method produced a smoother cycling movement with comparable stimulation intensities. In order to compare the joint-angle-based stimulation pattern against crank-angle-based stimulation patterns, a method was developed that allows calculating the crank angle and cadence based on segment-inclination angles. After one complete revolution, it was possible to determine the segment lengths by a nonlinear optimization procedure and thus to calculate the accurate crank angle (RMSE $\approx 4 \cdot 10^{-7}$ rad) and cadence (RMSE $\approx$ 0.58rpm). The combination of all these methods provides a “plug & play” system without the need for initial calibration or manual tuning.

In Chapter 4, the developed methods for the joint-angle-based FES cycling were integrated into the RehaBike of Team Hasomed to participate in the FES cycling race of the very first Cybathlon. The presented tricycle architecture focuses on using as many standard components as possible and enabling easy and autonomous transfer. This allowed the pilot to get on the tricycle without help from a third person. The mechanical components, including the seat, ankle orthosis, electrode sleeves, and the user interface of the bike, were adapted to the needs of the pilot. Particular attention was paid to minimizing the necessary starting torque. In addition, a training regime was developed that consisted of ergometer home training and mobile race training during the last phase of the training. After 18 months of intensive training, the pilot was able to make his personal record right at the small final with a time of 6 min 44 s for the race distance of 750 m. During the race, no problems or malfunctioning of the device occurred. Furthermore, the stimulation pattern produced a very smooth cycling movement and our pilot did not need to push his legs manually during dead zones. Overall, only 7 out of 11 teams completed the full distance.

For the Cybathlon wired sensors have been used for FES cycling. To further improve the usability and to make the technology available in a home-training device, new wireless sensors and a versatile stimulator module have been developed. With a full battery charge, the sensor is capable of transmitting packages with inertial measurements (200 Hz gyroscope measurements, 50 Hz accelerometer and magnetometer measurements) and the estimated orientation (50 Hz) at a sending frequency of 25 Hz for up to ten hours. The orientation estimation thereby exhibits a very low drift without using the magnetometer. This allows the sensor to be used not only for motion against gravity, but also for more complex motion patterns. The presented current-controlled stimulator fulfills all requirements for FES cycling while being ultra-compact. Up to eight stimulation channels can be controlled independently or array electrodes with 16 elements (15 anodes and one cathode) can be accessed. The stimulator can be configured via a standard smart device via Bluetooth Low Energy. The variable high-voltage generation can be used to adjust the stimulation voltage. This method can be used to save power or for applications for which only a low stimulation voltage is needed. For one channel at a load of 1 kΩ, the stimulator can drive up to 100 mA for up to 1 ms per phase at a frequency of 100 Hz, while a pulse onset time of about 1.5 µs can be achieved. When all eight channels are activated, the stimulator can deliver up to 80 mA with a pulse width of 350 µs at a frequency of 25 Hz.

8.2 General Conclusions on the Proposed FES Swimming Methods

Swimming is especially important for people with disabilities: the water allows movement without barriers or aids – an important and in particular free experience. As shown in Chapter 3 and 4, FES is successfully used in SCI rehabilitation and paraplegic sports. But there is no prior work on FES assisted swimming or aquatic therapy for paraplegics.

In Chapter 6 and 7, a new hybrid exercise modality for SCI patients was presented that involves both voluntary arm movements and the artificially stimulated legs and trunk. The swimming exercise can be performed independently by the patient without additional assistance. The results in two complete ASIA scale A subjects showed that the swimming speed during front crawl could be increased by electrical stimulation with either FES or the combination of FES and tSCS. The latter produced better results in both subjects. A prolonged application of FES and tSCS resulted in a long-lasting reduction of spasticity in both subjects. To perform the experiments, a stimulator was integrated into a waterproof swim bag and special waterproof electrodes were used, while the cable connection was additionally sealed. In addition, reusable silicone electrodes were tested with comparable stimulation results.

Following the study, the system was further improved and extended to include an inertial sensor on the swimmer's trunk. In Chapter 7, a method was presented that uses the estimated trunk-roll angle to control the stimulation of the knee extensors. A waterproof inertial sensor system was used to evaluate the dynamics of the swimming motion with and without stimulation. The data of seven inertial sensors were analyzed in terms of the swimmer's arm, knee, hip, and roll angles and instantaneous velocity. The results in one subject with complete SCI showed that swimming speed can be increased by electrical stimulation and that controlling the stimulation timing based on upper body motion worked better than periodic open-loop stimulation of the knee extensors. This can be explained by an increased knee-joint angle range and improved synchronization of knee extension with arm movement. Moreover, the proposed method allowed the subject to start and stop the stimulation by initiating the characteristic rolling motion of his trunk. The subject reported a high acceptance of the swim training and no limitations or negative effects on his constitution or health. With the triggered stimulation method, the subject could feel that he was able to trigger the extension of his knee by himself, and he could manually start and stop the stimulation compared to the periodic stimulation. Furthermore, he quoted that it feels like the legs are supporting the swim movement, and he does not have to drag his legs behind him.

8.3 Future Research

In the respective conclusion sections of the individual chapters, concrete questions regarding further research have already been addressed. At this point, these questions will be discussed in the context of the entire dissertation.

In this thesis, a new joint-angle-based stimulation pattern was presented for stationary and mobile FES cycling of paraplegic subjects which has been successfully employed during the Cybathlon 2016. But, despite this and many other successful studies on FES cycling, these devices are not yet widely available to patients. On the one hand, due to the high costs that have to be borne by the respective healthcare system. On the other hand, the duration of clinical rehabilitation slots is limited. Furthermore, clinicians and patients do not necessarily have the resources to learn complex technical procedures to place sensors and electrodes. To make this possible, it is necessary to transfer the developed procedures to cost-effective devices and make them available to the end users. In addition, the usability and handling must be tailored to the patients, so that they can train independently and in the home environment in the best case, without the need of health care professionals.

Compared to training exercises on land, swimming is often the only activity for which paraplegics do not need aids or support. Due to the buoyancy, a state of weightlessness can be achieved, and they can move in the water very similarly to non-affected persons. The developed hybrid exercise modality for SCI patients involves the voluntarily moved arms and the artificially stimulated legs and trunk. The swimming exercise can be performed independently by the patient without any additional assistance or even self-triggered with an incorporated inertial sensor at the trunk. Hence, this FES-based swimming support is a new and very promising application for systems and control methods. The presented initial prototype and results leave a number of challenges open, which should be addressed by future research and by joint efforts of control engineers and clinical SCI experts. The pilot study so far presented a proof of concept and showed the feasibility of FES in water. Additional tests with more subjects are needed to quantify, analyze, and improve the training effects for the SCI patients. As pointed out throughout the introduction, aquatic therapy is a promising therapy for neurological rehabilitation in incomplete SCI, stroke, or multiples sclerosis patients. Therefore, further studies shall incorporate other neurological disorders and investigate potential benefits of FES and tSCS for gait and balance therapy in water. In an own first study in [142] with an incomplete SCI patient (ASIA impairment scale B, motor complete and sensor incomplete paralysis), an improvement of sensory and motor function in the right leg below the level of lesion could be observed after 14 locomotion training sessions in a rehabilitation pool. Furthermore, the subject's trunk stability increased leading to an improvement in balance during daily routines. A combination of tSCS and FES led to a more upright posture and fully extended knee joints in the stance phase during gait training. Thus, the outcome of this case study indicates that using a combination of tSCS and/or FES might be a useful therapeutic tool for locomotion initiation and gait training in water for patients with neurological disorders.

References

[1] J. Bickenbach, A. Officer, T. Shakespeare, and P. von Groote. *International perspectives on spinal cord injury : summary.* Ed. by WHO. World Health Organization., 2013, p. 250. doi: `10.1002/0470013389.ch14`.

[2] *Statistische Jahrbuch 2017.* Statistisches Bundesamt, 2017, p. 708.

[3] D. J. Newham and N. D. N. Donaldson. "FES cycling". In: *Acta Neurochirurgica, Supplementum* 97.97 PART 1 (2007), pp. 395–402. doi: `10.1007/978-3-211-33079-1-52`.

[4] M. M. Adams and A. L. Hicks. "Spasticity after spinal cord injury". In: *Spinal Cord* 43.10 (Oct. 2005), pp. 577–586. doi: `10.1038/sj.sc.3101757`.

[5] I. Bromley. *Tetraplegia and paraplegia : a guide for physiotherapists.* 6th ed. Churchill Livingstone, 2006, p. 416. doi: `https://doi.org/10.1016/B978-0-443-10180-9.X5001-3`.

[6] D. N. Rushton. "Functional electrical stimulation". In: *Physiological Measurement* 18.4 (Nov. 1997), pp. 241–275. doi: `10.1088/0967-3334/18/4/001`.

[7] F. Dietz, M. Hexamer, F. Kerl, A. Arndt, F. Moscato, D. Schneditz, L. Kramer, O. Simanski, A. Thomas, T. Schauer, H. Vallery, and R. Riener. *Automatisierte Therapiesysteme.* Ed. by J. Werner. Series 9. De Gruyter, May 2014, p. 420. doi: `10.1515/9783110252132`.

[8] E. Rabischong and D. Guiraud. "Determination of fatigue in the electrically stimulated quadriceps muscle and relative effect of ischaemia". In: *Journal of Biomedical Engineering* 15.6 (Nov. 1993), pp. 443–450. doi: `10.1016/0141-5425(93)90056-5`.

[9] T. Kesar and S. Binder-Macleod. "Effect of frequency and pulse duration on human muscle fatigue during repetitive electrical stimulation". In: *Experimental Physiology* 91.6 (Nov. 2006), pp. 967–976. doi: `10.1113/expphysiol.2006.033886`.

[10] M. Laubacher, A. E. Aksöz, R. Riener, S. Binder-Macleod, and K. J. Hunt. "Power output and fatigue properties using spatially distributed sequential stimulation in a dynamic knee extension task". In: *European Journal of Applied Physiology* 117.9 (Sept. 2017), pp. 1787–1798. doi: `10.1007/s00421-017-3675-0`.

[11] L. Z. P. Maneski, N. M. Malešević, A. M. Savić, T. Keller, and D. B. Popović. "Surface-distributed low-frequency asynchronous stimulation delays fatigue of stimulated muscles". In: *Muscle & Nerve* 48.6 (Dec. 2013), pp. 930–937. doi: `10.1002/mus.23840`.

[12] K. Minassian, U. Hofstoetter, and F. Rattay. “Transcutaneous Lumbar Posterior Root Stimulation for Motor Control Studies and Modification of Motor Activity after Spinal Cord Injury”. In: *Restorative Neurology of Spinal Cord Injury* (Dec. 2012), pp. 226–255. doi: `10.1093/acprof:oso/9780199746507.003.0010`.

[13] U. S. Hofstoetter, B. Freundl, H. Binder, and K. Minassian. “Common neural structures activated by epidural and transcutaneous lumbar spinal cord stimulation: Elicitation of posterior root-muscle reflexes”. In: *PLoS ONE* 13.1 (Jan. 2018). Ed. by N. Weidner, e0192013. doi: `10.1371/journal.pone.0192013`.

[14] K. Minassian, W. B. McKay, H. Binder, and U. S. Hofstoetter. “Targeting Lumbar Spinal Neural Circuitry by Epidural Stimulation to Restore Motor Function After Spinal Cord Injury”. In: *Neurotherapeutics* 13.2 (Apr. 2016), pp. 284–294. doi: `10.1007/s13311-016-0421-y`.

[15] B. Domurath, R. Böthig, J. Bremer, A. Kaufmann, and J. Pannek. *Manual zur neuro-urologischen Diagnostik und Therapie Querschnittgelähmter.* www.jachmann-druck.de, 2014. doi: `10.13140/RG.2.1.1571.3046`.

[16] M. P. Galea. “Spinal cord injury and physical activity: Preservation of the body”. In: *Spinal Cord* 50.5 (May 2012), pp. 344–351. doi: `10.1038/sc.2011.149`.

[17] S. L. Stevens, J. L. Caputo, D. K. Fuller, D. W. Morgan, S. L. Stevens, J. L. Caputo, D. K. Fuller, and D. W. Morgan. “Physical activity and quality of life in adults with spinal cord injury”. In: *Journal of Spinal Cord Medicine* 31.4 (2008), pp. 373–378. doi: `10.1080/10790268.2008.11760739`.

[18] K. A. Martin Ginis, J. W. van der Scheer, A. E. Latimer-Cheung, A. Barrow, C. Bourne, P. Carruthers, M. Bernardi, D. S. Ditor, S. Gaudet, S. de Groot, K. C. Hayes, A. L. Hicks, C. A. Leicht, J. Lexell, S. Macaluso, P. J. Manns, C. B. McBride, V. K. Noonan, P. Pomerleau, J. H. Rimmer, R. B. Shaw, B. Smith, K. M. Smith, J. D. Steeves, D. Tussler, C. R. West, D. L. Wolfe, and V. L. Goosey-Tolfrey. “Evidence-based scientific exercise guidelines for adults with spinal cord injury: an update and a new guideline”. In: *Spinal Cord* 56 (Oct. 2017), pp. 308–321. doi: `10.1038/s41393-017-0017-3`.

[19] P. Jacobs and M. Nash. “Exercise recommendations for individuals with spinal cord injury”. In: *Sports Med.* 34.11 (2004), pp. 727–751. doi: `10.2165/00007256-200434110-00003`.

[20] L. D. Duffell, N. De N. Donaldson, and D. J. Newham. “Why is the metabolic efficiency of FES cycling low?” In: *IEEE Transactions on Neural Systems and Rehabilitation Engineering* 17.3 (June 2009), pp. 263–269. doi: `10.1109/TNSRE.2009.2016199`.

[21] B. W. Sport. *Wheelchair Sport and Physical Activity Survey 2016.* Tech. rep. British Wheelchair Sport, 2016, pp. 4–6.

[22] O. J. Woodman. *An Introduction to Inertial Navigation.* 2007. doi: `10.1119/1.3081061`.

[23] D. K. Shaeffer. “MEMS inertial sensors: A tutorial overview”. In: *IEEE Communications Magazine* 51.4 (Apr. 2013), pp. 100–109. doi: `10.1109/MCOM.2013.6495768`.

[24] J. Lenz and A. S. Edelstein. “Magnetic sensors and their applications”. In: *IEEE Sensors Journal* 6.3 (June 2006), pp. 631–649. doi: `10.1109/JSEN.2006.874493`.

[25] K. Shoemake. “Quaternions: "A Classic of Science"”. In: *The Science News-Letter.* Vol. 23. 621. Sofia, Bulgaria: Coral Press Scientific Publishing, 1933, p. 139. DOI: `10.2307/3909157`.

[26] T. Seel and S. Ruppin. “Eliminating the Effect of Magnetic Disturbances on the Inclination Estimates of Inertial Sensors”. In: *IFAC-PapersOnLine* 50.1 (July 2017), pp. 8798–8803. DOI: `10.1016/j.ifacol.2017.08.1534`.

[27] J. S. Petrofsky, H. Heaton, and C. A. Phillips. “Outdoor bicycle for exercise in paraplegics and quadriplegics”. In: *Journal of Biomedical Engineering* 5.4 (Oct. 1983), pp. 292–296. DOI: `10.1016/0141-5425(83)90003-1`.

[28] T. Schauer. “Feedback Control of Cycling in Spinal Cord Injury Using Functional Electrical Stimulation”. PhD thesis. University of Glasgow, 2006.

[29] R. Berkelmans, M. Arns, and J. Duysens. “The development of a hybrid outdoor FES bike”. In: *Rehabilitation: Mobility, Exercise and Sports.* Vol. 26. Maroochydore, 2003, pp. 329–331. DOI: `10.3233/978-1-60750-080-3-329`.

[30] C. W. Peng, S. C. Chen, C. H. . Lai, C. J. Chen, C. C. Chen, J. Mizrahi, and Y. Handa. “Review: Clinical benefits of functional electrical stimulation cycling exercise for subjects with central neurological impairments”. In: *Journal of Medical and Biological Engineering* 31.1 (2011), pp. 1–11. DOI: `10.5405/jmbe.718`.

[31] K. J. Hunt, J. Fang, J. Saengsuwan, M. Grob, and M. Laubacher. “On the efficiency of FES cycling: A framework and systematic review”. In: *Technology and Health Care* 20.5 (2012), pp. 395–422. DOI: `10.3233/THC-2012-0689`.

[32] K. J. Hunt, M. Laubacher, R. Riener, M. Baumberger, S. Binder-Macleod, A. K. Brust, and E. A. Aksoez. “Stimulation of paralysed quadriceps muscles with sequentially and spatially distributed electrodes during dynamic knee extension”. In: *Journal of NeuroEngineering and Rehabilitation* 16.1 (2019), pp. 1–12. DOI: `10.1186/s12984-018-0471-y`.

[33] H. R. Berry, T. H. Kakebeeke, N. Donaldson, C. Perret, and K. J. Hunt. “Energetics of paraplegic cycling: Adaptations to 12 months of high volume training”. In: *Technology and Health Care* 20.2 (2012), pp. 73–84. DOI: `10.3233/THC-2011-0656`.

[34] M. Kent. *Oxford Food and Fitness: A Dictionary of Diet and Exercise.* 1st ed. Oxford University Press, 2003. DOI: `10.1093/acref/9780191803239.001.0001`.

[35] D. H. Thijssen, R. Ellenkamp, P. Smits, and M. T. Hopman. “Rapid vascular adaptations to training and detraining in persons with spinal cord injury”. In: *Archives of Physical Medicine and Rehabilitation* 87.4 (Apr. 2006), pp. 474–481. DOI: `10.1016/j.apmr.2005.11.005`.

[36] H. L. Gerrits, A. De Haan, A. J. Sargeant, H. Van Langen, and M. T. Hopman. “Peripheral vascular changes after electrically stimulated cycle training in people with spinal cord injury”. In: *Archives of Physical Medicine and Rehabilitation* 82.6 (2001), pp. 832–839. DOI: `10.1053/apmr.2001.23305`.

[37] D. J. Allison, B. Chapman, D. Wolfe, K. Sequeira, K. Hayes, and D. S. Ditor. “Effects of a functional electrical stimulation-assisted cycling program on immune and cardiovascular health in persons with spinal cord injury”. In: *Topics in Spinal Cord Injury Rehabilitation* 22.1 (2016), pp. 71–78. DOI: `10.1310/sci2201-71`.

[38] S. P. Hooker, A. M. Scremin, D. L. Mutton, C. F. Kunkel, and G. Cagle. "Peak and submaximal physiologic responses following electrical stimulation leg cycle ergometer training". In: *Journal of Rehabilitation Research and Development* 32.4 (1995), pp. 361–366.

[39] D. Mutton, A. Scremin, T. Barstow, M. Scott, C. Kunkel, and T. Cagle. "Physiologic responses during functional electrical stimulation leg cycling and hybrid exercise in spinal cord injured subjects". In: *Archives of Physical Medicine and Rehabilitation* 78.7 (July 1997), pp. 712–718. DOI: `10.1016/s0003-9993(97)90078-2`.

[40] H. R. Berry, C. Perret, B. A. Saunders, T. H. Kakebeeke, N. D. N. Donaldson, D. B. Allan, and K. J. Hunt. "Cardiorespiratory and power adaptations to stimulated cycle training in paraplegia". In: *Medicine and Science in Sports and Exercise* 40.9 (Sept. 2008), pp. 1573–1580. DOI: `10.1249/MSS.0b013e318176b2f4`.

[41] N. N. Kahn, S. P. Feldman, and W. A. Bauman. "Lower-extremity functional electrical stimulation decreases platelet aggregation and blood coagulation in persons with chronic spinal cord injury: A pilot study". In: *Journal of Spinal Cord Medicine* 33.2 (2010), pp. 150–158. DOI: `10.1080/10790268.2010.11689690`.

[42] P. J. Pacy, R. Hesp, D. A. Halliday, D. Katz, G. Cameron, and J. Reeve. "Muscle and bone in paraplegic patients, and the effect of functional electrical stimulation". In: *Clinical Science* 75.5 (1988), pp. 481–487. DOI: `10.1042/cs0750481`.

[43] A. R. Alashram, G. Annino, and N. B. Mercuri. "Changes in spasticity following functional electrical stimulation cycling in patients with spinal cord injury: A systematic review". In: *Journal of Spinal Cord Medicine* 14 (2020), pp. 1–14. DOI: `10.1080/10790268.2020.1763713`.

[44] P. B. Arnold, P. P. McVey, W. J. Farrell, T. M. Deurloo, and A. R. Grasso. "Functional electric stimulation: Its efficacy and safety in improving pulmonary function and musculoskeletal fitness". In: *Archives of Physical Medicine and Rehabilitation* 73.7 (1992), pp. 665–668. DOI: `10.5555/uri:pii:000399939290133H`.

[45] S. C. Chen, C. H. Lai, W. P. Chan, M. H. Huang, H. W. Tsai, and J. J. J. Chen. "Increases in bone mineral density after functional electrical stimulation cycling exercises in spinal cord injured patients". In: *Disability and Rehabilitation* 27.22 (2005), pp. 1337–1341. DOI: `10.1080/09638280500164032`.

[46] J. S. Petrofsky. "Functional Electrical Stimulation, a Two-Year Study". In: *The Journal of Rehabilitation* 58.3 (July 1992), p. 29.

[47] L. Griffin, M. J. Decker, J. Y. Hwang, B. Wang, K. Kitchen, Z. Ding, and J. L. Ivy. "Functional electrical stimulation cycling improves body composition, metabolic and neural factors in persons with spinal cord injury". In: *Journal of Electromyography and Kinesiology* 19.4 (Aug. 2009), pp. 614–622. DOI: `10.1016/j.jelekin.2008.03.002`.

[48] S. Gualdi, A. Salghetti, C. DeConti, E. Trevisi, and S. Ferrante. "Cycling induced by functional electrical stimulation (FES-cycling) in children affected by cerebral palsy: A pilot study". In: *Gait & Posture* 30.June (Oct. 2009), pp. 31–32. DOI: `10.1016/j.gaitpost.2009.07.017`.

[49] E. Trevisi, S. Gualdi, C. De Conti', A. Salghetti, A. Martinuzzi, A. Pedrocchi, and S. Ferrante. "Cycling induced by functional electrical stimulation in children affected by cerebral palsy: Case report". In: *European Journal of Physical and Rehabilitation Medicine* 48.1 (2012), pp. 135–145.

[50] S. S. Alabdulwahab. "Electrical stimulation improves gait in children with spastic diplegic cerebral palsy". In: *NeuroRehabilitation* 29.1 (2011), pp. 37–43. DOI: `10.3233/NRE-2011-0675`.

[51] J. Szecsi, C. Krewer, F. Müller, and A. Straube. "Functional electrical stimulation assisted cycling of patients with subacute stroke: Kinetic and kinematic analysis". In: *Clinical Biomechanics* 23.8 (2008), pp. 1086–1094. DOI: `10.1016/j.clinbiomech.2008.05.001`.

[52] S. Ferrante, A. Pedrocchi, G. Ferrigno, and F. Molteni. "Cycling induced by functional electrical stimulation improves the muscular strength and the motor control of individuals with post-acute stroke." In: *European journal of physical and rehabilitation medicine* 44.2 (2008), pp. 159–67. DOI: `10.1016/j.ejca.2010.05.007`.

[53] E. Ambrosini, S. Ferrante, A. Pedrocchi, G. Ferrigno, and F. Molteni. "Cycling induced by electrical stimulation improves motor recovery in postacute hemiparetic patients: A randomized controlled trial". In: *Stroke* 42.4 (Apr. 2011), pp. 1068–1073. DOI: `10.1161/STROKEAHA.110.599068`.

[54] E. Ambrosini, S. Ferrante, G. Ferrigno, F. Molteni, and A. Pedrocchi. "Cycling induced by electrical stimulation improves muscle activation and symmetry during pedaling in hemiparetic patients". English. In: *IEEE Transactions on Neural Systems and Rehabilitation Engineering* 20.3 (May 2012), pp. 320–330. DOI: `10.1109/TNSRE.2012.2191574`.

[55] G. Alon, V. M. Conroy, and T. W. Donner. "Intensive Training of Subjects with Chronic Hemiparesis on a Motorized Cycle Combined with Functional Electrical Stimulation (FES): A Feasibility and Safety Study". In: *Physiotherapy Research International* 16.2 (June 2011), pp. 81–91. DOI: `10.1002/pri.475`.

[56] D. G. de Sousa, L. A. Harvey, S. Dorsch, J. Leung, and W. Harris. "Functional electrical stimulation cycling does not improve mobility in people with acquired brain injury and its effects on strength are unclear: a randomised trial". In: *Journal of Physiotherapy* 62.4 (Oct. 2016), pp. 203–208. DOI: `10.1016/j.jphys.2016.08.004`.

[57] T. W. J. Janssen, M. Bakker, A. Wyngaert, K. H. L. Gerrits, and A. de Haan. "Effects of stimulation pattern on electrical stimulation-induced leg cycling performance". In: *The Journal of Rehabilitation Research and Development* 41.6 (2004), p. 787. DOI: `10.1682/JRRD.2004.03.0030`.

[58] C. Fornusek, G. M. Davis, P. J. Sinclair, and B. Milthorpe. "Development of an Isokinetic Functional Electrical Stimulation Cycle Ergometer". In: *Neuromodulation* 7.1 (Jan. 2004), pp. 56–64. DOI: `10.1111/j.1525-1403.2004.04007.x`. arXiv: `1309.7937`.

[59] K. J. Hunt, C. Ferrario, S. Grant, B. Stone, A. N. McLean, M. H. Fraser, and D. B. Allan. "Comparison of stimulation patterns for FES-cycling using measures of oxygen cost and stimulation cost". In: *Medical Engineering and Physics* 28.7 (2006), pp. 710–718. DOI: `10.1016/j.medengphy.2005.10.006`.

[60] J. Hongyuan, M. Changbo, L. Nianli, and A. Hongrui. “Study on automatic power control in FES cycling”. In: *2008 2nd International Symposium on Systems and Control in Aerospace and Astronautics, ISSCAA 2008* (2008), pp. 1–4. DOI: `10.1109/ISSCAA.2008.4776193`.

[61] N. A. Hakansson and M. L. Hull. “Muscle Stimulation Waveform Timing Patterns to Increase Muscular Endurance in Functional Electrical Stimulation Pedaling Using a Forward Dynamic Model”. In: *ASME 2009 Summer Bioengineering Conference, Parts A and B* 56.9 (2009), p. 1221. DOI: `10.1115/SBC2009-206785`.

[62] R. Shalaby, T. Schauer, W. Liedecke, and J. Raisch. “Amplifier design for EMG recording from stimulation electrodes during functional electrical stimulation leg cycling ergometry”. In: *Biomedizinische Technik* 56.1 (Jan. 2011), pp. 23–33. DOI: `10.1515/BMT.2010.055`.

[63] T. Watanabe, Y. Karasawa, and Y. Handa. “A test of controlling different muscles in FES cycling with cycling wheelchair ’Profhand’”. In: *2014 IEEE 19th International Functional Electrical Stimulation Society Annual Conference, IFESS 2014 - Conference Proceedings* (Sept. 2014), pp. 1–4. DOI: `10.1109/IFESS.2014.7036742`.

[64] J. Szecsi, A. Straube, and C. Fornusek. “A biomechanical cause of low power production during FES cycling of subjects with SCI”. In: *Journal of NeuroEngineering and Rehabilitation* 11.1 (2014), p. 123. DOI: `10.1186/1743-0003-11-123`.

[65] A. S. Gorgey, H. J. Poarch, D. D. Dolbow, T. Castillo, and D. R. Gater. “Effect of adjusting pulse durations of functional electrical stimulation cycling on energy expenditure and fatigue after spinal cord injury”. In: *Journal of Rehabilitation Research and Development* 51.9 (2014), pp. 1455–1468. DOI: `10.1682/JRRD.2014.02.0054`.

[66] R. K. Tong, X. Wang, K. W. Leung, G. T. Lee, C. C. Lau, H. W. Wai, P. M. Pang, and H. C. Leung. “How to prepare a person with complete spinal cord injury to use surface electrodes for FES trike cycling”. In: *IEEE International Conference on Rehabilitation Robotics* (2017), pp. 801–805. DOI: `10.1109/ICORR.2017.8009346`.

[67] K. W. W. Leung, R. K. Tong, X. Wang, G. T. Lee, P. M. Pang, H. W. Wai, and H. C. Leung. “The Effectiveness of Functional Electrical Stimulation (FES) in On-Off Mode for Enhancing the Cycling Performance of Team Phoenix at 2016 Cybathlon.” In: *European journal of translational myology* 27.4 (Dec. 2017), pp. 302–307. DOI: `10.4081/ejtm.2017.7132`.

[68] B. Sijobert, C. Fattal, A. Daubigney, and C. Azevedo-Coste. “Participation to the first Cybathlon: an overview of the FREEWHEELS team FES-cycling solution”. In: *European Journal of Translational Myology* 27.4 (Dec. 2017), pp. 289–294. DOI: `10.4081/ejtm.2017.7120`.

[69] A. Metani, L. Popovic-Maneski, S. Mateo, L. Lemahieu, V. Bergeron, L. Popović-Maneski, S. Mateo, L. Lemahieu, V. Bergeron, L. Popovic-Maneski, S. Mateo, L. Lemahieu, and V. Bergeron. “Functional electrical stimulation cycling strategies tested during preparation for the First Cybathlon Competition - a practical report from team ENS de Lyon.” In: *European journal of translational myology* 27.4 (Dec. 2017), pp. 279–288. DOI: `10.4081/ejtm.2017.7110`.

[70] J. McDaniel, L. M. Lombardo, K. M. Foglyano, P. D. Marasco, and R. J. Triolo. “Cycle Training Using Implanted Neural Prostheses: Team Cleveland”. In: *European Journal of Translational Myology* 27.4 (Dec. 2017), pp. 289–294. DOI: `10.4081/ejtm.2017.7087`.

[71] M. Laubacher, E. A. Aksöz, I. Bersch, and K. J. Hunt. “The road to Cybathlon 2016 - Functional electrical stimulation cycling Team IRPT/SPZ”. In: *European Journal of Translational Myology* 27.4 (Dec. 2017), pp. 259–264. DOI: `10.4081/ejtm.2017.7086`.

[72] A. Bo, L. da Fonseca, J. Guimaraes, E. Fachin-Matins, M. Paredes, G. Brindeiro, A. de Sousa, M. Dorado, and F. Ramos. “Cycling with Spinal Cord Injury: A Novel System for Cycling Using Electrical Stimulation for Individuals with Paraplegia, and Preparation for Cybathlon 2016”. In: *IEEE Robotics & Automation* 24.November (4 2017), pp. 58–65. DOI: `10.1109/MRA.2017.2751660`.

[73] J. Araujo Guimarães, L. Oliveira da Fonseca, A. C. De Sousa, M. E. Gutierrez Paredes, G. A. Brindeiro, A. Padilha Lanari Bó, and E. Fachin-Martins. “FES Bike Race preparation to Cybathlon 2016 by EMA team: a short case report”. In: *European Journal of Translational Myology* 27.4 (Dec. 2017), pp. 272–278. DOI: `10.4081/ejtm.2017.7169`.

[74] R. Berkelmans and B. Woods. “Strategies and performances of Functional Electrical Stimulation Cycling using the BerkelBike with Spinal Cord Injury in a competition context (CYBATHLON).” In: *European journal of translational myology* 27.4 (Dec. 2017), pp. 255–258. DOI: `10.4081/ejtm.2017.7189`.

[75] J. Arnin, T. Yamsa-ard, P. Triponyuwasin, and Y. Wongsawat. “Development of practical functional electrical stimulation cycling systems based on an electromyography study of the Cybathlon 2016”. In: *European Journal of Translational Myology* 27.4 (Dec. 2017), pp. 295–301. DOI: `10.4081/ejtm.2017.7111`.

[76] M. Gföhler and P. Lugner. “Dynamic simulation of FES-cycling: Influence of individual parameters”. In: *IEEE Transactions on Neural Systems and Rehabilitation Engineering* 12.4 (Dec. 2004), pp. 398–405. DOI: `10.1109/TNSRE.2004.836778`.

[77] R. Riener and T. Fuhr. “Patient-driven control of FES-supported standing up: a simulation study”. In: *Rehabilitation Eng, IEEE Trans on* 6.2 (1998), pp. 113–124. DOI: `10.1109/86.681177`.

[78] C. Lynch and M. Popovic. “Functional Electrical Stimulation”. In: *IEEE Control Systems Magazine* 28.2 (Apr. 2008), pp. 40–50. DOI: `10.1109/MCS.2007.914689`.

[79] T. Seel, T. Schauer, and J. Raisch. “Joint axis and position estimation from inertial measurement data by exploiting kinematic constraints”. In: *Proceedings of the IEEE International Conference on Control Applications* (2012), pp. 45–49. DOI: `10.1109/CCA.2012.6402423`.

[80] J. S. Furtado, H. H. T. Liu, G. Lai, H. Lacheray, and J. Desouza-Coelho. “Comparative Analysis of OptiTrack Motion Capture Systems”. In: 2019, pp. 15–31. DOI: `10.1007/978-3-030-17369-2_2`.

[81] R. L. Williams and C. F. Reinholtz. “Proof of Grashof’s law using polynomial discriminants”. In: *Journal of Mechanical Design, Transactions of the ASME* 108.4 (1986), pp. 562–564. DOI: `10.1115/1.3258770`.

[82] C. Azevedo Coste and P. Wolf. “FES-Cycling at Cybathlon 2016: Overview on Teams and Results”. In: *Artificial Organs* 42.3 (2018), pp. 336–341. DOI: `10.1111/aor.13139`.

[83] M. Sojka, P. Pisa, and P. Píša. “Usable Simulink Embedded Coder Target for Linux”. In: *16th Real Time Linux Workshop.* 2014, pp. 1–6.

[84] F. Heinrich, C. Wiesener, and T. Schauer. “Control and Optimization of FES-Cycling with Differential Evolution: A Computer Model-based Study”. In: *Autsym 2017, 8th International Symposium on AUTOMATIC CONTROL.* Vol. 8. 2017.

[85] F. Hoflinger, J. Muller, R. Zhang, L. M. Reindl, and W. Burgard. “A wireless micro inertial measurement unit (IMU)”. In: *IEEE Transactions on Instrumentation and Measurement* 62.9 (2013), pp. 2583–2595. DOI: `10.1109/TIM.2013.2255977`.

[86] J. Barton, A. Gonzalez, J. Buckley, B. O’Flynn, and S. C. O’Mathuna. “Design, fabrication and testing of miniaturised wireless Inertial Measurement Units (IMU)”. In: *Proceedings - Electronic Components and Technology Conference* (2007), pp. 1143–1148. DOI: `10.1109/ECTC.2007.373939`.

[87] C. Wiesener, E. Ambrosini, L. Blankenfeld, S. Schneider, B. Grzywacz, and T. Schauer. “Wireless IMU- and EMG-Sensors for Controlled Functional Electrical Stimulation”. In: *Converging Clinical and Engineering Research on Neurorehabilitation III.* 1st ed. Springer International Publishing, 2018, pp. 16–20. DOI: `10.1007/978-3-030-01845-0_4`.

[88] M. Valtin, K. Kociemba, C. Behling, B. Kuberski, S. Becker, and T. Schauer. “RehaMovePro: A versatile mobile stimulation system for transcutaneous FES applications”. In: *Eur J Transl Myol* 26.263 (2016), pp. 203–208. DOI: `10.4081/ejtm.2016.6076`.

[89] H. P. Wang, Z. G. Wang, X. Y. Lu, Z. H. Huang, and Y. X. Zhou. “Design of a pulse-triggered four-channel functional electrical stimulator using complementary current source and time division multiplexing output method”. In: *Proceedings of the Annual International Conference of the IEEE Engineering in Medicine and Biology Society, EMBS.* Vol. 2015-Novem. IEEE, Aug. 2015, pp. 1671–1674. DOI: `10.1109/EMBC.2015.7318697`.

[90] A. Tamtrakarn. “A 115V bi-phasic pulse electrical muscle stimulator by using inductor-sharing dual-output boost converter with supply-stepping switch driver”. In: *2017 24th IEEE International Conference on Electronics, Circuits and Systems (ICECS).* IEEE, Dec. 2017, pp. 410–413. DOI: `10.1109/ICECS.2017.8291997`.

[91] R. Thorsen and M. Ferrarin. “Battery powered neuromuscular stimulator circuit for use during simultaneous recording of myoelectric signals”. In: *Medical Engineering and Physics* 31.8 (Oct. 2009), pp. 1032–1037. DOI: `10.1016/j.medengphy.2009.06.006`.

[92] S. C. Huerta, M. Tarulli, A. Prodic, M. R. Popovic, and P. W. Lehn. “A universal functional electrical stimulator based on merged flyback-SC circuit”. In: *15th International Power Electronics and Motion Control Conference and Exposition, EPE-PEMC 2012 ECCE Europe.* IEEE, Sept. 2012, LS5a.3–1–LS5a.3–5. DOI: `10.1109/EPEPEMC.2012.6397471`.

[93] S. Simcox, G. Davis, A. Barriskill, J. Middleton, I. Bruinsma, M. Duncan, and R. Smith. “A portable, 8-channel transcutaneous stimulator for paraplegic muscle training and mobility-A technical note”. In: *The Journal of Rehabilitation Research and Development* 41.1 (2004), p. 41. DOI: `10.1682/JRRD.2004.01.0041`.

[94] M. Valtin, T. Schauer, C. Behling, M. Daniel, and M. Weber. “Combined stimulation and measurement system for array electrodes”. In: *BIODEVICES 2012 - Proceedings of the International Conference on Biomedical Electronics and Devices.* 2012, pp. 345–349. DOI: `10.5220/0003786303450349`.

[95] *Low Charge Injection 16-Channel High Voltage Analog Switch.* HV2801. Supertex Inc. 2013, pp. 1–9.

[96] *N-channel 200 V, 1.1 Ω, 1 A SOT-223 STripFET Power MOSFET.* STN1NF20. STMicroelectronics. Nov. 2011, pp. 1–12.

[97] International Electrotechnical Commission. *IEC 60601-2-10:2012 Medical electrical equipment - Part 2-10: Particular requirements for the basic safety and essential performance of nerve and muscle stimulators.* 2012.

[98] J. Martin. “The Halliwick method”. In: *Physiotherapy* 67.10 (1981), pp. 288–291.

[99] A. Pachalski and T. Mekarski. “Effect of swimming on increasing of cardio-respiratory capacity in paraplegics”. In: *Paraplegia* 18.3 (June 1980), pp. 190–196. DOI: `10.1038/sc.1980.33`.

[100] T. J. Ellapen, H. V. Hammill, M. Swanepoel, and G. L. Strydom. “The benefits of hydrotherapy to patients with spinal cord injuries.” In: *African journal of disability* 7.0 (2018), a450. DOI: `10.4102/ajod.v7i0.450`.

[101] C. Li, S. Khoo, A. Adnan, L. Chunxiao, S. Khoo, A. Adnan, C. Li, S. Khoo, and A. Adnan. “Effects of aquatic exercise on physical function and fitness among people with spinal cord injury”. In: *Medicine (United States)* 96.11 (Mar. 2017), e6328. DOI: `10.1097/MD.0000000000006328`.

[102] A. C. Recio, S. A. Stiens, and E. Kubrova. “Aquatic-Based Therapy in Spinal Cord Injury Rehabilitation: Effective Yet Underutilized”. In: *Current Physical Medicine and Rehabilitation Reports* 5.3 (2017), pp. 108–112. DOI: `10.1007/s40141-017-0158-5`.

[103] N. Kesiktas, N. Paker, N. Erdogan, G. Gülsen, D. Biçki, and H. Yilmaz. “The Use of Hydrotherapy for the Management of Spasticity”. In: *Neurorehabilitation and Neural Repair* 18.4 (Dec. 2004), pp. 268–273. DOI: `10.1177/1545968304270002`.

[104] B. E. Becker. “Aquatic Therapy: Scientific Foundations and Clinical Rehabilitation Applications”. In: *PM and R* 1.9 (Sept. 2009), pp. 859–872. DOI: `10.1016/j.pmrj.2009.05.017`.

[105] S. Van Houtte, Y. Vanlandewijck, and R. Gosselink. “Respiratory muscle training in persons with spinal cord injury: A systematic review”. In: *Respiratory Medicine* 100.11 (Nov. 2006), pp. 1886–1895. DOI: `10.1016/j.rmed.2006.02.029`.

[106] J. Jung, E. Chung, K. Kim, B.-H. Lee, and J. Lee. “The Effects of Aquatic Exercise on Pulmonary Function in Patients with Spinal Cord Injury”. In: *Journal of Physical Therapy Science* 26.5 (May 2014), pp. 707–709. DOI: `10.1589/jpts.26.707`.

[107] E. M. Gass and G. C. Gass. “Thermoregulatory responses to repeated warm water immersion in subjects who are paraplegic”. In: *Spinal Cord* 39.3 (2001), pp. 149–155.

[108] M. Howard. *Electric Bath.* Patent. United States, US1193018A. Aug. 1916.

[109] T. Nakamura, M. Katoh, T. Hachisu, R. Okazaki, M. Sato, and H. Kajimoto. “Localization Ability and Polarity Effect of Underwater Electro-Tactile Stimulation”. In: *International Conference on Human Haptic Sensing and Touch Enabled Computer Applications, EuroHaptics 2014*. Lecture Notes in Computer Science. Springer, Berlin, Heidelberg, Oct. 2014, pp. 216–223. DOI: `10.1007/978-3-662-44193-0_28`.

[110] L. Seifert, H. Leblanc, D. Chollet, and D. Delignières. “Inter-limb coordination in swimming: Effect of speed and skill level”. In: *Human Movement Science* 29.1 (Feb. 2010), pp. 103–113. DOI: `10.1016/j.humov.2009.05.003`.

[111] L. Seifert, M. L’Hermette, L. Wattebled, J. Komar, F. Mell, D. Gomez, and Y. Caritu. “Use of Inertial Central to Analyse Skill of Inter-Limb Coordination in Sport Activities”. In: *BIO Web of Conferences* 1 (Dec. 2011), pp. 1–4. DOI: `10.1051/bioconf/20110100082`.

[112] U. S. Hofstoetter, W. B. McKay, K. E. Tansey, W. Mayr, H. Kern, and K. Minassian. “Modification of spasticity by transcutaneous spinal cord stimulation in individuals with incomplete spinal cord injury”. In: *The Journal of Spinal Cord Medicine* 37.2 (Mar. 2014), pp. 202–211. DOI: `10.1179/2045772313Y.0000000149`.

[113] W. M. Silvers and D. G. Dolny. “Comparison and reproducibility of sEMG during manual muscle testing on land and in water”. In: *Journal of Electromyography and Kinesiology* 21.1 (2011), pp. 95–101. DOI: `10.1016/j.jelekin.2010.05.004`.

[114] R. D. Benfield, E. R. Newton, and T. Hortobágyi. “Waterproofing EMG instrumentation”. In: *Biological Research for Nursing* 8.3 (Jan. 2007), pp. 195–201. DOI: `10.1177/1099800406293313`.

[115] J. Axelgaard. *Current-Controlling Electrode with Adjustable Contact Area*. Patent. United States, US 6,745,082. June 2004.

[116] J. Axelgaard. *Moisture Resistant Electrode with Edge Protection*. Patent. United States, US 7,697,999. Apr. 2010.

[117] J. Favre, R. Aissaoui, B. M. Jolles, J. A. de Guise, and K. Aminian. “Functional calibration procedure for 3D knee joint angle description using inertial sensors”. In: *Journal of Biomechanics* 42.14 (2009), pp. 2330–2335. DOI: `https://doi.org/10.1016/j.jbiomech.2009.06.025`.

[118] A. Cutti, A. Ferrari, P. Garofalo, M. Raggi, A. Cappello, and A. Ferrari. “’Outwalk’: A protocol for clinical gait analysis based on inertial and magnetic sensors”. In: *Medical & biological engineering & computing* 48 (2009), pp. 17–25.

[119] D. Laidig, P. Mueller, and T. Seel. “Automatic Anatomical Calibration for IMU-based Elbow Angle Measurement in Disturbed Magnetic Fields”. In: *Current Directions in Biomedical Engineering* 3.2 (2017), pp. 167–170. DOI: `10.1515/cdbme-2017-0035`.

[120] B. Taetz, G. Bleser, and M. Miezal. “Towards self-calibrating inertial body motion capture”. In: *Proceedings of the 19th International Conference on Information Fusion*. Heidelberg, Germany, July 2016, pp. 1751–1759.

[121] D. Graurock, T. Schauer, and T. Seel. “User-Adaptive Inertial Sensor Network for Feedback-Controlled Gait Support Systems”. In: *Proc. of the 20th Annual International FES Society Conference*. La Grande Motte, France, 2016, pp. 1–4.

[122] D. Graurock, T. Schauer, and T. Seel. “Automatic Pairing of Inertial Sensors to Lower Limb Segments – A Plug-and-Play Approach”. In: *Current Directions in Biomedical Engineering* 2.1 (2016), pp. 715–718. DOI: `10.1515/cdbme-2016-0155`.

[123] D. Laidig, D. Lehmann, and and T. Seel. “Magnetometer-free Realtime Inertial Motion Tracking by Exploitation of Kinematic Constraints in 2-DOF Joints”. In: *41st IEEE International Engineering in Medicine and Biology Conference (EMBC).* Berlin, Germany, 2019.

[124] D. Laidig, T. Schauer, and T. Seel. “Exploiting Kinematic Constraints to Compensate Magnetic Disturbances when Calculating Joint Angles of Approximate Hinge Joints from Orientation Estimates of Inertial Sensors”. In: *Proc. of 15th IEEE Conference on Rehabilitation Robotics (ICORR).* London, UK, 2017, pp. 971–976. DOI: `10.1109/ICORR.2017.8009375`.

[125] D. Lehmann, D. Laidig, and T. Seel. “Magnetometer-free motion tracking of one-dimensional joints by exploiting kinematic constraints”. In: *14th Symposium on Automation in Medical Engineering (AUTOMED).* 27. Lübeck, Germany, 2020. DOI: `10.18416/AUTOMED.2020`.

[126] S. G. Psycharakis and R. H. Sanders. “Body roll in swimming: A review”. In: *Journal of Sports Sciences* 28.3 (Feb. 2010), pp. 229–236. DOI: `10.1080/02640410903508847`.

[127] T. Yanai. “What causes the body to roll in front-crawl swimming?” In: *Journal of Applied Biomechanics* 17.1 (Feb. 2001), pp. 28–42. DOI: `10.1123/jab.17.1.28`.

[128] M. Isaković, M. Belić, M. Štrbac, I. Popović, S. Došen, D. Farina, and T. Keller. “Electrotactile Feedback Improves Performance and Facilitates Learning in the Routine Grasping Task.” In: *European journal of translational myology* 26.3 (June 2016), p. 6069. DOI: `10.4081/ejtm.2016.6069`.

[129] J. W. Schroeder, V. N. Dubey, T. Hickish, J. Cole, T. Hickish, and J. Cole. “Wearable Electrocutaneous Feedback System: A Smart Device to Compensate for Sensation Loss”. In: *Journal of Medical Devices* 6.1 (Mar. 2012), p. 017515. DOI: `10.1115/1.4026693`.

[130] R. H. Sanders, J. T. Andersen, and H. Takagi. “The Segmental Movements in Front Crawl Swimming”. In: *Handbook of Human Motion.* Springer, Cham, 2017, pp. 1–15. DOI: `10.1007/978-3-319-30808-1_132-1`.

[131] J. V. Deschodt, L. M. Arsac, and A. H. Rouard. “Relative contribution of arms and legs in humans to propulsion in 25-m sprint front-crawl swimming”. In: *European Journal of Applied Physiology and Occupational Physiology* 80.3 (July 1999), pp. 192–199. DOI: `10.1007/s004210050581`.

[132] A. J. Callaway, J. E. Cobb, and I. Jones. “A Comparison of Video and Accelerometer Based Approaches Applied to Performance Monitoring in Swimming”. In: *International Journal of Sports Science & Coaching* 4.1 (Mar. 2009), pp. 139–153. DOI: `10.1260/1747-9541.4.1.139`.

[133] M. Bächlin, K. Förster, and G. Tröster. “SwimMaster: A Wearable Assistant for Swimmer”. In: *Proceedings of the 11th international conference on Ubiquitous computing.* UbiComp ’09. New York, NY, USA: ACM Press, 2009, pp. 215–224. DOI: `10.1145/1620545.1620578`.

[134] J. Quintern, R. Riener, and S. Rupprecht. "Comparison of Simulation and Experiments of Different Closed-Loop Strategies for Functional Electrical Stimulation: Experiments in Paraplegics". In: *Artificial Organs* 21.3 (1997), pp. 232–235. DOI: `10.1111/j.1525-1594.1997.tb04656.x`.

[135] M. O. Ibitoye, N. A. Hamzaid, M. Hayashibe, N. Hasnan, and G. M. Davis. "Restoring prolonged standing via functional electrical stimulation after spinal cord injury: A systematic review of control strategies". In: *Biomedical Signal Processing and Control* 49 (2019), pp. 34–47. DOI: `https://doi.org/10.1016/j.bspc.2018.11.006`.

[136] A. Hughes, C. Freeman, J. Burridge, P. Chappell, P. Lewin, and E. Rogers. "Feasibility of Iterative Learning Control Mediated by Functional Electrical Stimulation for Reaching After Stroke". In: *Neurorehabilitation and Neural Repair* 23.6 (2009). PMID: 19190087, pp. 559–568. DOI: `10.1177/1545968308328718`.

[137] C. T. Freeman, E. Rogers, A. Hughes, J. H. Burridge, and K. L. Meadmore. "Iterative Learning Control in Health Care: Electrical Stimulation and Robotic-Assisted Upper-Limb Stroke Rehabilitation". In: *IEEE Control Systems Magazine* 32.1 (Feb. 2012), pp. 18–43. DOI: `10.1109/MCS.2011.2173261`.

[138] H. Dou, K. K. Tan, T. H. Lee, and Z. Zhou. "Iterative learning feedback control of human limbs via functional electrical stimulation". In: *Control Engineering Practice* 7.3 (1999), pp. 315–325. DOI: `https://doi.org/10.1016/S0967-0661(98)00191-9`.

[139] M. Valtin, T. Seel, J. Raisch, and T. Schauer. "Iterative learning control of drop foot stimulation with array electrodes for selective muscle activation". In: *Preprints of the 19th World Congress, The International Federation of Automatic Control.* Cape Town, South Africa, 2014, pp. 6586–6592. DOI: `10.3182/20140824-6-ZA-1003.01991`.

[140] N. A. Alibeji, N. A. Kirsch, and N. Sharma. "A Muscle Synergy-Inspired Adaptive Control Scheme for a Hybrid Walking Neuroprosthesis". In: *Frontiers in Bioengineering and Biotechnology* 3 (2015), p. 203. DOI: `10.3389/fbioe.2015.00203`.

[141] T. Seel, D. Laidig, M. Valtin, C. Werner, J. Raisch, and T. Schauer. "Feedback Control of Foot Eversion in the Adaptive Peroneal Stimulator". In: *Proceedings of the 22nd IEEE Mediterranean Conference on Control and Automation.* Palermo, Italy, 2014, pp. 1482–1487. DOI: `10.1109/MED.2014.6961585`.

[142] L. Spieker, C. Wiesener, A. Niedeggen, N. Wenger, and T. Schauer. "Motor and sensor recovery in a paraplegic by transcutaneous spinal cord stimulation in water". In: *Proceedings on Automation in Medical Engineering* 1.1 (Feb. 2020), pp. 022–022. DOI: `10.18416/AUTOMED.2020`.

A

ASIA Impairment Scale (AIS) Questionnaire

Figure A.1: The international standards for neurological classification of spinal cord injury comprising motor and sensory testing. The spinal cord injury is classified according to the level of injury and an impairment scale. American Spinal Injury Association: International Standards for Neurological Classification of Spinal Cord Injury `http://asia-spinalinjury.org/wp-content/uploads/2016/02/International_Stds_Diagram_Worksheet.pdf`

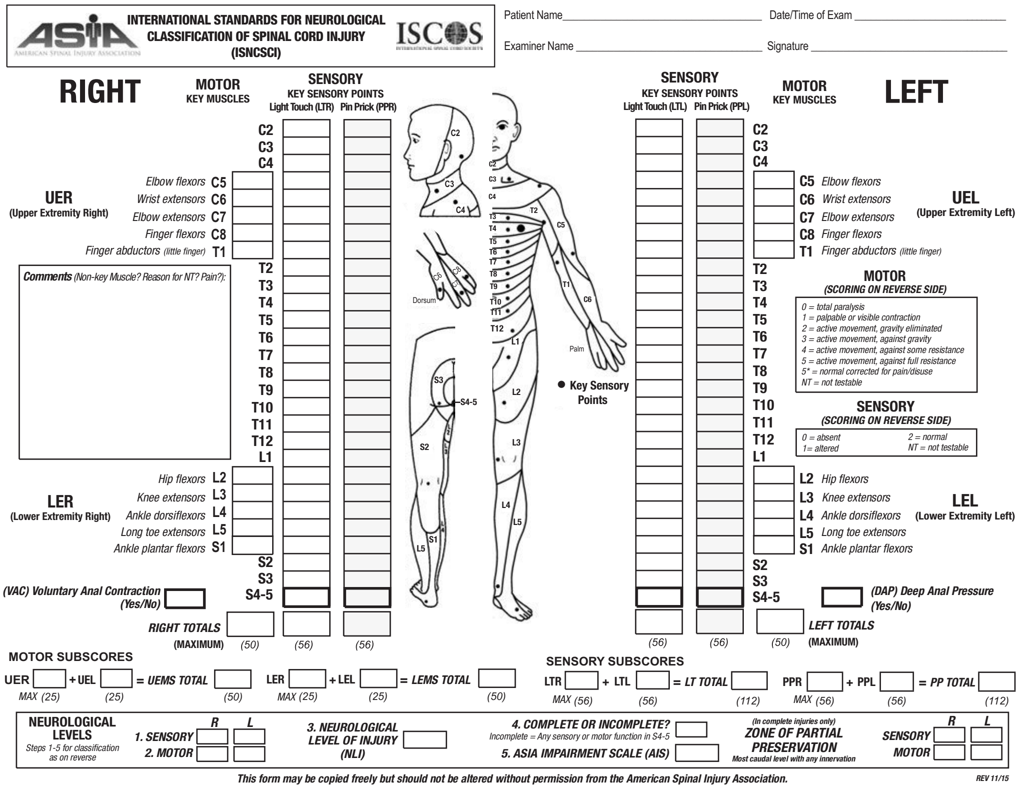

C2
C3
C4
C2
C3
C4
T2
T3
T4
T5
T6
T7
T8
T9
T10
T11
T12
L1
C5
T1
C6
C6
C7
C8
Dorsum
Palm
S3
S4-5
S2
L2
L3
L4
L5
S1
L5
● Key Sensory Points

INTERNATIONAL STANDARDS FOR NEUROLOGICAL CLASSIFICATION OF SPINAL CORD INJURY (ISNCSCI)

Patient Name________________ Date/Time of Exam ________________

Examiner Name ________________ Signature ________________

RIGHT

	MOTOR KEY MUSCLES			SENSORY KEY SENSORY POINTS Light Touch (LTR)	Pin Prick (PPR)
		C2			
		C3			
		C4			
UER (Upper Extremity Right)	Elbow flexors	C5			
	Wrist extensors	C6			
	Elbow extensors	C7			
	Finger flexors	C8			
	Finger abductors (little finger)	T1			
		T2			
		T3			
		T4			
		T5			
		T6			
		T7			
		T8			
		T9			
		T10			
		T11			
		T12			
		L1			
LER (Lower Extremity Right)	Hip flexors	L2			
	Knee extensors	L3			
	Ankle dorsiflexors	L4			
	Long toe extensors	L5			
	Ankle plantar flexors	S1			
		S2			
		S3			
(VAC) Voluntary Anal Contraction (Yes/No) ☐		S4-5			
	RIGHT TOTALS				
	(MAXIMUM)		(50)	(56)	(56)

Comments (Non-key Muscle? Reason for NT? Pain?):

LEFT

SENSORY KEY SENSORY POINTS Light Touch (LTL)	Pin Prick (PPL)		MOTOR KEY MUSCLES		
		C2			
		C3			
		C4			
		C5		Elbow flexors	UEL (Upper Extremity Left)
		C6		Wrist extensors	
		C7		Elbow extensors	
		C8		Finger flexors	
		T1		Finger abductors (little finger)	
		T2			
		T3			
		T4			
		T5			
		T6			
		T7			
		T8			
		T9			
		T10			
		T11			
		T12			
		L1			
		L2		Hip flexors	LEL (Lower Extremity Left)
		L3		Knee extensors	
		L4		Ankle dorsiflexors	
		L5		Long toe extensors	
		S1		Ankle plantar flexors	
		S2			
		S3			
		S4-5		(DAP) Deep Anal Pressure (Yes/No) ☐	
				LEFT TOTALS	
(56)	(56)		(50)	(MAXIMUM)	

MOTOR
(SCORING ON REVERSE SIDE)

0 = total paralysis
1 = palpable or visible contraction
2 = active movement, gravity eliminated
3 = active movement, against gravity
4 = active movement, against some resistance
5 = active movement, against full resistance
5 = normal corrected for pain/disuse*
NT = not testable

SENSORY
(SCORING ON REVERSE SIDE)

0 = absent
1= altered
2 = normal
NT = not testable

MOTOR SUBSCORES

UER ☐ + UEL ☐ = ***UEMS TOTAL*** ☐
MAX (25) (25) (50)

LER ☐ + LEL ☐ = ***LEMS TOTAL*** ☐
MAX (25) (25) (50)

SENSORY SUBSCORES

LTR ☐ + LTL ☐ = ***LT TOTAL*** ☐
MAX (56) (56) (112)

PPR ☐ + PPL ☐ = ***PP TOTAL*** ☐
MAX (56) (56) (112)

NEUROLOGICAL LEVELS
Steps 1-5 for classification as on reverse

	R	L
1. SENSORY		
2. MOTOR		

3. NEUROLOGICAL LEVEL OF INJURY (NLI) ☐

4. COMPLETE OR INCOMPLETE? ☐
Incomplete = Any sensory or motor function in S4-5

5. ASIA IMPAIRMENT SCALE (AIS) ☐

(In complete injuries only)
ZONE OF PARTIAL PRESERVATION
Most caudal level with any innervation

	R	L
SENSORY		
MOTOR		

This form may be copied freely but should not be altered without permission from the American Spinal Injury Association.

REV 11/15

Figure A.2: Second page of the impairment scale.

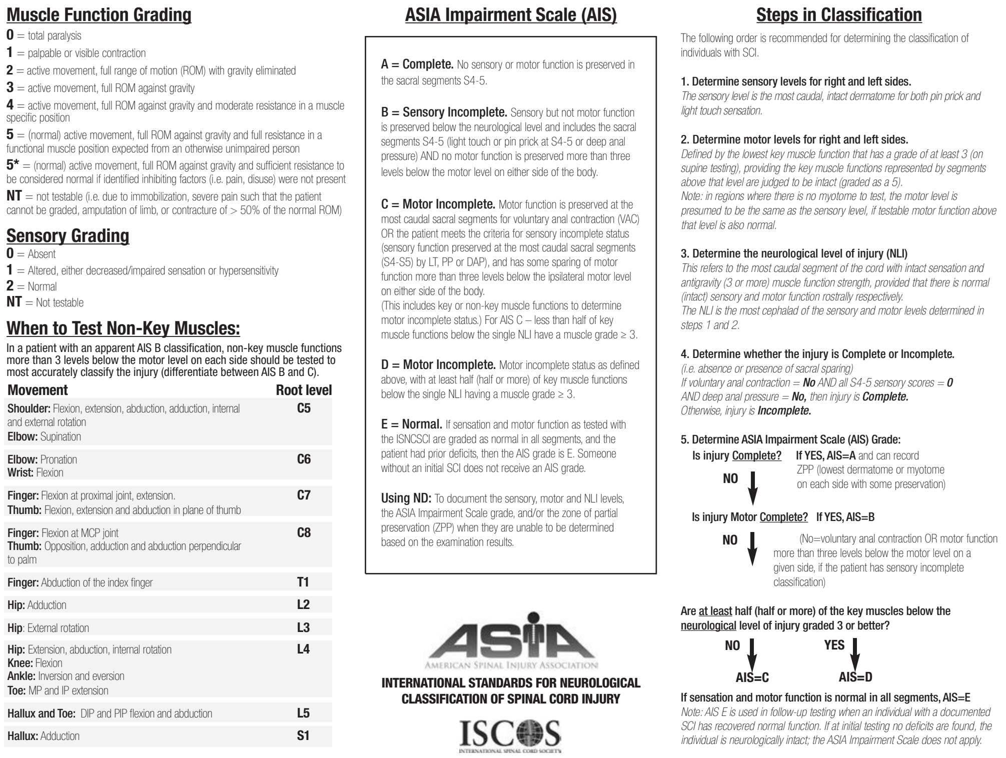

Muscle Function Grading

0 = total paralysis
1 = palpable or visible contraction
2 = active movement, full range of motion (ROM) with gravity eliminated
3 = active movement, full ROM against gravity
4 = active movement, full ROM against gravity and moderate resistance in a muscle specific position
5 = (normal) active movement, full ROM against gravity and full resistance in a functional muscle position expected from an otherwise unimpaired person
5* = (normal) active movement, full ROM against gravity and sufficient resistance to be considered normal if identified inhibiting factors (i.e. pain, disuse) were not present
NT = not testable (i.e. due to immobilization, severe pain such that the patient cannot be graded, amputation of limb, or contracture of > 50% of the normal ROM)

Sensory Grading

0 = Absent
1 = Altered, either decreased/impaired sensation or hypersensitivity
2 = Normal
NT = Not testable

When to Test Non-Key Muscles:

In a patient with an apparent AIS B classification, non-key muscle functions more than 3 levels below the motor level on each side should be tested to most accurately classify the injury (differentiate between AIS B and C).

Movement	Root level
Shoulder: Flexion, extension, abduction, adduction, internal and external rotation **Elbow:** Supination	**C5**
Elbow: Pronation **Wrist:** Flexion	**C6**
Finger: Flexion at proximal joint, extension. **Thumb:** Flexion, extension and abduction in plane of thumb	**C7**
Finger: Flexion at MCP joint **Thumb:** Opposition, adduction and abduction perpendicular to palm	**C8**
Finger: Abduction of the index finger	**T1**
Hip: Adduction	**L2**
Hip: External rotation	**L3**
Hip: Extension, abduction, internal rotation **Knee:** Flexion **Ankle:** Inversion and eversion **Toe:** MP and IP extension	**L4**
Hallux and Toe: DIP and PIP flexion and abduction	**L5**
Hallux: Adduction	**S1**

ASIA Impairment Scale (AIS)

A = Complete. No sensory or motor function is preserved in the sacral segments S4-5.

B = Sensory Incomplete. Sensory but not motor function is preserved below the neurological level and includes the sacral segments S4-5 (light touch or pin prick at S4-5 or deep anal pressure) AND no motor function is preserved more than three levels below the motor level on either side of the body.

C = Motor Incomplete. Motor function is preserved at the most caudal sacral segments for voluntary anal contraction (VAC) OR the patient meets the criteria for sensory incomplete status (sensory function preserved at the most caudal sacral segments (S4-S5) by LT, PP or DAP), and has some sparing of motor function more than three levels below the ipsilateral motor level on either side of the body.
(This includes key or non-key muscle functions to determine motor incomplete status.) For AIS C – less than half of key muscle functions below the single NLI have a muscle grade ≥ 3.

D = Motor Incomplete. Motor incomplete status as defined above, with at least half (half or more) of key muscle functions below the single NLI having a muscle grade ≥ 3.

E = Normal. If sensation and motor function as tested with the ISNCSCI are graded as normal in all segments, and the patient had prior deficits, then the AIS grade is E. Someone without an initial SCI does not receive an AIS grade.

Using ND: To document the sensory, motor and NLI levels, the ASIA Impairment Scale grade, and/or the zone of partial preservation (ZPP) when they are unable to be determined based on the examination results.

AMERICAN SPINAL INJURY ASSOCIATION

INTERNATIONAL STANDARDS FOR NEUROLOGICAL CLASSIFICATION OF SPINAL CORD INJURY

ISCOS
INTERNATIONAL SPINAL CORD SOCIETY

Steps in Classification

The following order is recommended for determining the classification of individuals with SCI.

1. Determine sensory levels for right and left sides.
The sensory level is the most caudal, intact dermatome for both pin prick and light touch sensation.

2. Determine motor levels for right and left sides.
Defined by the lowest key muscle function that has a grade of at least 3 (on supine testing), providing the key muscle functions represented by segments above that level are judged to be intact (graded as a 5).
Note: in regions where there is no myotome to test, the motor level is presumed to be the same as the sensory level, if testable motor function above that level is also normal.

3. Determine the neurological level of injury (NLI)
This refers to the most caudal segment of the cord with intact sensation and antigravity (3 or more) muscle function strength, provided that there is normal (intact) sensory and motor function rostrally respectively.
The NLI is the most cephalad of the sensory and motor levels determined in steps 1 and 2.

4. Determine whether the injury is Complete or Incomplete.
(i.e. absence or presence of sacral sparing)
If voluntary anal contraction = ***No*** *AND all S4-5 sensory scores =* ***0***
AND deep anal pressure = ***No,*** *then injury is* ***Complete.***
Otherwise, injury is ***Incomplete.***

5. Determine ASIA Impairment Scale (AIS) Grade:
Is injury Complete? **If YES, AIS=A** and can record ZPP (lowest dermatome or myotome on each side with some preservation)
NO ↓
Is injury Motor Complete? **If YES, AIS=B**
NO ↓ (No=voluntary anal contraction OR motor function more than three levels below the motor level on a given side, if the patient has sensory incomplete classification)

Are at least half (half or more) of the key muscles below the neurological level of injury graded 3 or better?
NO ↓ **AIS=C**
YES ↓ **AIS=D**

If sensation and motor function is normal in all segments, AIS=E
Note: AIS E is used in follow-up testing when an individual with a documented SCI has recovered normal function. If at initial testing no deficits are found, the individual is neurologically intact; the ASIA Impairment Scale does not apply.

B

Proof: Hip Extension Always Follows Knee Extension in Cycling

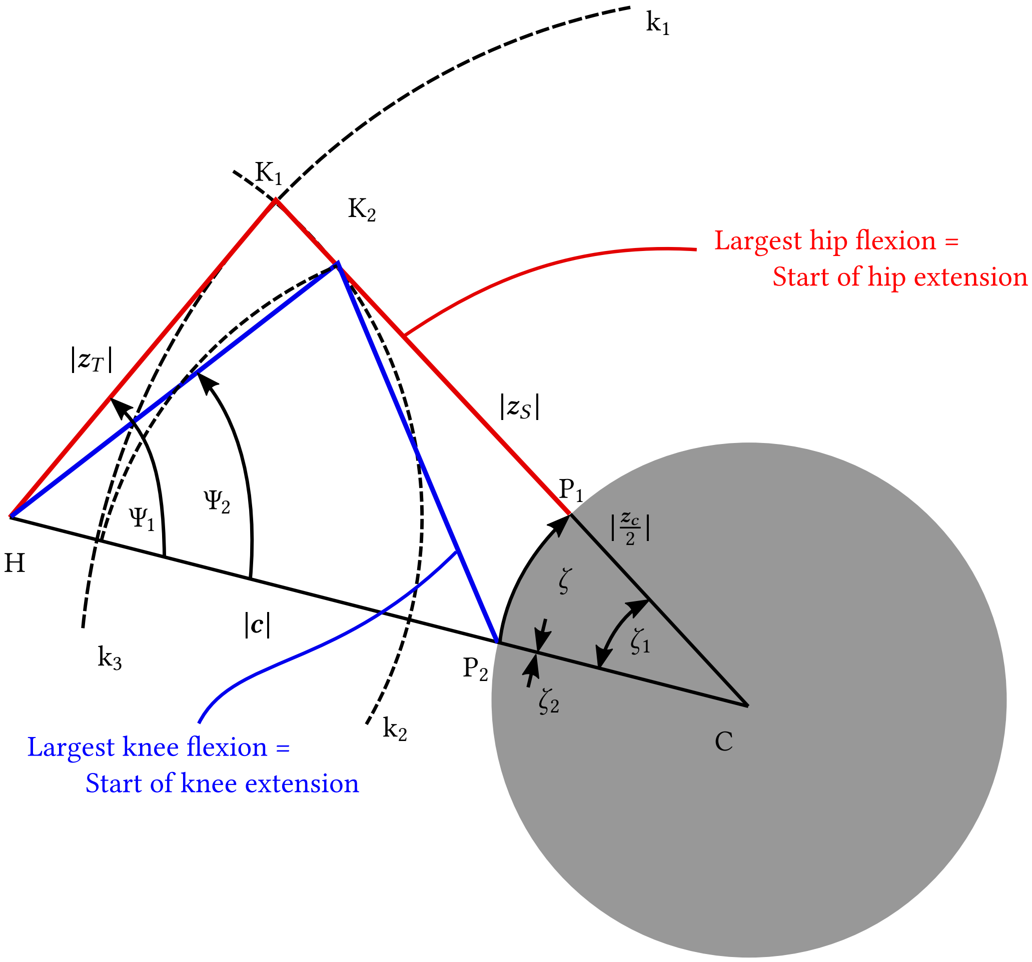
k$_1$
K$_1$
K$_2$
Largest hip flexion =
Start of hip extension
$|z_T|$
$|z_S|$
Ψ_2
Ψ_1
P$_1$
$|\frac{z_c}{2}|$
H
ζ
ζ_1
$|c|$
k$_3$
P$_2$
ζ_2
k$_2$
C
Largest knee flexion =
Start of knee extension

Figure B.1: Simplified configuration for one leg, where H denotes the hip joint, K$_1$, P$_1$, Ψ_1, and ζ_1 the knee-joint, pedal-joint, thigh-inclination angle and ζ angle for the blue configuration, and K$_2$, P$_2$, Ψ_2, and ζ_2 the knee-joint, pedal-joint, thigh-inclination angle and ζ angle for the red configuration. $|\boldsymbol{z}_S|$, $|\boldsymbol{z}_T|$, $|\frac{\boldsymbol{z}_c}{2}|$, and $|\boldsymbol{z}_l|$ describe the lengths of shank, thigh, crank (for one leg), and distance between hip and crank joint. k$_1$, k$_2$, and k$_3$ denote different auxiliary circle lines.

The configuration of four segments (thigh, shank, crank, and $\boldsymbol{c}$) is generally known as a crank-rocker mechanism. This mechanism is circumferential, which means that the crank can rotate around C, if the following Grashof conditions are fulfilled [81]:

1. The circumferential element $\frac{\boldsymbol{z}_c}{2}$ must be the shortest of the four segments.
2. The sum of this shortest element and the longest element must be smaller than the sum of the two remaining elements, where $\boldsymbol{z}_S$, $\boldsymbol{z}_T$, and $\boldsymbol{c}$ can be the longest element.

These rules are well fulfilled for a bicycle if the rider can cycle. It was already shown in (3.24) that for $\zeta = 0$ the minimum knee-joint angle is reached, which corresponds with ζ_2 of the blue configuration in Figure B.1. To find the value for ζ where the hip joint is maximum flexed, auxiliary circle lines are needed. The circle k_1 desribes the farthest possible position of the knee joint with respect to the crank joint C with the radius $|\boldsymbol{z}_S| + |\frac{\boldsymbol{z}_c}{2}|$. Furthermore, it is evident that the position of the knee joint must lie along a circular path around the hip joint with radius $|\boldsymbol{z}_T|$ which shows the circle k_2 assuming that the hip joint is approximated as hinge joint for cycling. Both circle lines intersect in the upper part (The second intersection would result in a knee joint > 180°.), which results in the position of the knee with the maximum distance of the crank joint. Hence, the shank and the crank are in line with $\zeta = \zeta_1$, which is shown for the red configuration in Figure B.1. The circle k_3 describes the distance from the pedal joint P_2 to the knee joint for the blue configuration which has to intersect with k_2 in K_2. Based on cosine law the following equations for Ψ_1 and Ψ_2 can be formulated with

$$\Psi_1 = \arccos\left(\frac{-(|\boldsymbol{z}_S| + |\frac{\boldsymbol{z}_c}{2}|)^2 + |\boldsymbol{z}_T|^2 + |\boldsymbol{c}|^2}{2|\boldsymbol{z}_T||\boldsymbol{c}|}\right) \quad \text{and} \tag{B.1}$$

$$\Psi_2 = \arccos\left(\frac{-|\boldsymbol{z}_S|^2 + |\boldsymbol{z}_T|^2 + (|\boldsymbol{c}| - \frac{|\boldsymbol{z}_c|}{2})^2}{2|\boldsymbol{z}_T|(|\boldsymbol{c}| - \frac{|\boldsymbol{z}_c|}{2})}\right). \tag{B.2}$$

Now it shall be shown, that the following inequality is fulfilled

$$\Psi_1 > \Psi_2 \tag{B.3}$$

$$\arccos\left(\frac{-(|\boldsymbol{z}_S| + |\frac{\boldsymbol{z}_c}{2}|)^2 + |\boldsymbol{z}_T|^2 + |\boldsymbol{c}|^2}{2|\boldsymbol{z}_T||\boldsymbol{c}|}\right) > \arccos\left(\frac{-|\boldsymbol{z}_S|^2 + |\boldsymbol{z}_T|^2 + (|\boldsymbol{c}| - \frac{|\boldsymbol{z}_c|}{2})^2}{2|\boldsymbol{z}_T|(|\boldsymbol{c}| - \frac{|\boldsymbol{z}_c|}{2})}\right). \tag{B.4}$$

With Ψ_1 and Ψ_2 being in the range $[0, \pi[$ applying cos on both sides of the inequality, flips the direction of the inequality to

$$\frac{-(|\boldsymbol{z}_S| + |\frac{\boldsymbol{z}_c}{2}|)^2 + |\boldsymbol{z}_T|^2 + |\boldsymbol{c}|^2}{2|\boldsymbol{z}_T||\boldsymbol{c}|} < \frac{-|\boldsymbol{z}_S|^2 + |\boldsymbol{z}_T|^2 + (|\boldsymbol{c}| - \frac{|\boldsymbol{z}_c|}{2})^2}{2|\boldsymbol{z}_T|(|\boldsymbol{c}| - \frac{|\boldsymbol{z}_c|}{2})}. \tag{B.5}$$

With the first part of Grashof conditions both divisors are always > 0 and hence the inequality can be simplified to

$$(|\boldsymbol{z}_S| + |\frac{\boldsymbol{z}_c}{2}|)^2 + |\boldsymbol{c}|^2 < 2|\boldsymbol{c}|(|\boldsymbol{z}_S| + |\frac{\boldsymbol{z}_c}{2}|) + |\boldsymbol{z}_T|^2. \tag{B.6}$$

This inequality is always true if it is guaranteed that

$$|\boldsymbol{z}_S| + |\frac{\boldsymbol{z}_c}{2}| - |\boldsymbol{z}_T| < |\boldsymbol{c}| < |\boldsymbol{z}_S| + |\frac{\boldsymbol{z}_c}{2}| + |\boldsymbol{z}_T|. \tag{B.7}$$

The left part of this inequality is always true due to Grashofs second condition despite $|\boldsymbol{z}_S|$ or $|\boldsymbol{z}_T|$ being the longest segment. The right side of the inequality is as well always true since otherwise the basic inequality of a general square that the sum of three sides are always bigger than the fourth side is not fulfilled. Since $|\boldsymbol{c}|$, $|z_S|$, $|\frac{z_c}{2}|$, and $|z_T|$ form a general square for any configuration fulfilling the Grashof conditions. From this it follows directly that Ψ_1 is always greater than Ψ_2, which means that hip extension always starts after the beginning of knee extension. Similarly, hip extension always ends after the end of knee extension.

C

User Requirements Specifications for the Neuromuscular Stimulator

Introduction

Document Overview

This document presents the user requirements specifications of the neuromuscular stimulator development project. It describes:

- Requirements of functionalities, performances, interfaces, environment,
- Tests principles and definitions of validation methods of requirements,
- The compliance of requirements to customer needs,
- The relative importance and precedence of requirements.

Standard and Regulatory References

#	Document Identifier	Document Title
[STD1]	IEC 60601-2-10	Particular requirements for the basic safety and essential performance of nerve and muscle stimulators
[STD2]	IEC 62304	Medical device software - Software life-cycle processes

Functionalities and Performance

Stimulator Unit

The stimulator unit consists of a high-voltage source, a demultiplexer, and a current controller.

ID	Requirement	Priority	Status
URS_001	**Current controller:** The setting time of the current at a load of 1 kΩ shall be less than 10 µs and with a steady-state error of less than +/-2%.	high	proposed
URS_003	**Pulse characteristics:** It shall be possible to generate biphasic and monophasic pulses with a maximum current of 100 mA at 1 kΩ with maximum Pulse width 1 ms at a frequency of 1 - 100 Hz.	high	proposed
URS_004	**Channels:** It shall be possible to stimulate up to 8 channels synchronously with a switching time less than 50 µs while only one channel is stimulated at the same time.	high	proposed
URS_005	**Electrode error:** The stimulator shall be able to detect a unconnected electrode and then disable the one channel as long as the error is active after one pulse.	high	proposed
URS_006	**Communication to Stimulator Unit:** The communication between application and stimulator unit shall be realized via a serial interface.	medium	proposed

Battery Charger

The battery charger is needed to charge the internal battery.

ID	Requirement	Priority	Status
URS_018	**Maximum charge current:** The maximum charge current shall be 1.5 A.	high	proposed
URS_019	**Cable connector:** The battery charger shall be USB compliant.	high	proposed

Battery

The battery is used to power all parts of the device.

ID	Requirement	Priority	Status
URS_023	**Battery capacity:** It shall be possible to run the stimulator for at least 30 minutes with all channels stimulating with maximum rating and while communicating with the maximum number of sensors and smart devices.	high	proposed
URS_024	**Charge time:** The battery shall be charged in less than 5h.	medium	proposed
URS_025	**Battery certification:** The battery shall be certified for medical use.	medium	proposed

Sensor Interface

The stimulator communicates with external sensors and the orientation of the stimulator itself can be used during operation.

ID	Requirement	Priority	Status
URS_026	**Internal IMU:** It shall be possible to get the orientation of the stimulator during operation.	high	proposed
URS_027	**External sensors:** It shall be possible to connect up to 2 external sensors at the same time via a wireless communication.	high	proposed

Communication Interface

There are two use cases for communicating with the stimulator device:

- Smart device for normal user. Setting parameters, loading applications, and starting and stopping stimulation,
- Firmware updates.

ID	Requirement	Priority	Status
URS_033	**Wireless communication:** There shall be a wireless communication between a smart device and the stimulator.	high	proposed
URS_034	**Number of communication channels:** It shall be only possible to communicate with one smart device at the same time.	high	proposed

Protocol

The protocol describes the communication between smart device and the stimulator.

ID	Requirement	Priority	Status
URS_035	**Unique protocol:** There shall be a unique protocol for wireless communication.	high	proposed
URS_036	**Low-level protocol:** There shall be a low-level protocol for stimulation without applications. Comment: Here only the parameters can be set and the stimulation can be switched on or off.	high	proposed
URS_037	**Mid-level protocol:** There shall be a mid-level protocol, where the user can transfer exercises in combination with sensors. Comment: The exercises are created with a workbench where a subset of tasks is defined and can be customized.	medium	proposed
URS_038	**High-level protocol:** There shall be a high-level protocol for ready applications e.g. massage, cycling, or walking. Comment: Here only parameters concerning the application can be set, but the application cannot be customized.	high	proposed
URS_040	**Wireless Firmware update:** The firmware update of all included micro-controllers shall be possible without opening the device via a wireless communication.	medium	proposed

Housing

With housing the enclosure of the device is meant, which incorporates all parts of the device, e.g., PCB, battery etc.

ID	Requirement	Priority	Status
URS_028	**IP - ingress protection:** The housing of the stimulator shall be submergible in water. Comment: A combination with a diving bag can be an option too.	medium	proposed
URS_029	**Cable connectors:** All cable connectors shall be submergible in water.	medium	proposed
URS_030	**Different cable connectors:** There shall be different cable connectors for different applications e.g. 2, 4, 8 channel version.	medium	proposed
URS_031	**Size:** The size shall be smaller than 30 mm x 70 mm x 120 mm.	medium	proposed
URS_032	**Weight:** The device shall be lighter than 250g.	medium	proposed

User Interface

The user interface is intended to be minimal. The main interface is planned to be realized via a smart device.

ID	Requirement	Priority	Status
URS_013	**LED indicator stimulation unit:** There shall be a LED indicator for error state, idle state, and active stimulation. Comment: Could be realized with one RGB LED.	high	proposed
URS_014	**On/off, start/stop Button:** There shall be button for switching on/off the device and starting/stopping the stimulation or application.	high	proposed
URS_016	**Stimulation-intensity Manipulator:** There shall be manipulator for in- or decreasing the stimulation intensity / frequency. Comment: The parameter which shall be manipulated depends on the application.	high	proposed
URS_015	**Battery-charge indicator:** There shall be a LED for indicating the battery charge state.	high	proposed

Safety

There are several mechanisms implemented for safety issues.

ID	Requirement	Priority	Status
URS_020	**No stimulation while charging:** The stimulation shall be disabled during charging by hardware.	high	proposed
URS_021	**Unique Stimulator cable connector:** It should be impossible to plug the connector incorrectly.	high	proposed
URS_022	**Maximum stimulation time:** The maximum stimulation time shall be limited in all applications. After the maximum time is reached the stimulation shall be switched off automatically and can be only switched on again after a manual button press.	high	proposed